

Electromagnetic Modeling and Optimization of Through Silicon Vias

Vom Promotionsausschuss der
Technischen Universität Hamburg-Harburg
zur Erlangung des akademischen Grades
Doktor-Ingenieur (Dr.-Ing.)
genehmigte Dissertation

von
David Dahl

aus
Mölln

2017

1. Gutachter:

Prof. Dr. sc. techn. Christian Schuster

2. Gutachter:

Prof. Dr. Klaus-Dieter Lang

3. Gutachter:

Dr.-Ing. Ivan Ndip

Vorsitzender des Prüfungsausschusses:

Prof. Dr.-Ing. Gerhard Bauch

Tag der mündlichen Prüfung:

13.12.2017

DOI: <https://doi.org/10.15480/882.1713>

URN: urn:nbn:de:gbv:830-88221817

Summary

This thesis presents work in the area of electromagnetic modeling of through silicon vias (TSVs). TSVs are vertical interconnects in silicon wafers and an important component for the three-dimensional integration that is required for the further increase in performance of integrated circuits and integrated systems.

Major parts of this thesis discuss the adaptation of the physics-based modeling approach from the original application for the modeling of vias in printed circuit boards to the application in interposers with a sufficient amount of metallizations of the substrate. Adaptations are necessary because the substrate can show significant conductivity and has to be regarded as a layered medium. The latter is due to the required dielectric insulators and due to oxide layers that results from the TSV fabrication process. Further layers need to be included in the analysis if the depletion layer effects due to the metal-oxide-insulator interface are to be considered.

The adaptations consist in the adaptation of a far field model for which an effective wave number of radial wave propagation in the layered medium is computed. They consist also in the computation of a near field model for the mode conversion at the junction between coaxial ports at the top and bottom of the interposer and the inner radial ports that connect to the far field model. In conjunction, the adaptations lead to an efficient and exact modeling over a large parameter range.

The efficient modeling is further applied to large scale crosstalk analysis. A measure for the effective total crosstalk of uncorrelated signal alongs the channels for single-ended links is defined and analyzed for several parameter variations. This measure allows for the investigation of the influence of several important design parameters of silicon interposers on the crosstalk.

Several test structures with TSVs have been fabricated and measured. Using full-wave simulations, the measurement results have been validated.

Acknowledgment

This thesis presents the results of my work carried out as a research assistant at the Institute of Electromagnetic Theory at Hamburg University of Technology in the time from October 2012 to April 2017. Most of the work was part of the project “Electrical Modeling and Design of Through Silicon Vias for Integrated Systems”. This project, funded by the DFG (Deutsche Forschungsgemeinschaft), was a collaboration between the Institute of Electromagnetic Theory, the Fraunhofer Institute of Reliability and Microintegration (IZM) located in Berlin, and the Technical University Berlin (TUB).

First of all, I am very grateful to my doctoral adviser Prof. Dr. sc. techn. Christian Schuster for giving me the opportunity to work on this interesting topic. His continuous guidance and advice, honest feedback, dedication, and the inspiration regarding the opportunities greatly inspired this work.

I would like to thank Prof. Dr. Klaus-Dieter Lang and Dr.-Ing. Ivan Ndip for serving as second and third examiner of this thesis and the fruitful cooperation throughout the project. The feedback during regular teleconferences and the organization of the test wafer fabrication are highly appreciated. I would also like to thank Anne Beyreuther for the work at IZM during the first part of the project, especially the organization related to test structure design and fabrication.

I am grateful for the pleasant and motivating working atmosphere at the institute. Special thanks go to Dr.-Ing. Xiaomin Duan for mentoring the beginning of my research by introducing me to several subjects of modeling and simulation and for the continued collaboration as a member of IZM later in the project. I would like to thank Dr.-Ing. Miroslav Kotzev for introducing me to high-frequency measurement techniques and consulting on many practical aspects. I want to express my gratitude to my former fellow student and colleague Dr.-Ing. Alexander Vogt for encouraging me to apply for the PhD position. I would like to thank my former colleagues Dr.-Ing. Andreas Hardock and Dr.-Ing. Sebastian Müller for fruitful discussions and support. I am thankful to Katharina Scharff, Dr.-Ing. Heinz-Dietrich Brüns, Dr.-Ing. Jan Preibisch, Torsten Reuschel, and Ömer Yildiz for numerous helpful discussions and proof-reading parts of my thesis. The administrative and technical support of Heike Herder, Angela Freiberg, Stefan Conradi, and Volker Paulsen is highly appreciated.

Finally, I want to thank my parents, Eva and Peter, and my brother Jonas for their support and encouragement. I am indebted to Katharina for great motivation and support, especially during the final months of work for this thesis. Thank you!

Contents

1	Introduction	1
1.1	Motivation and Context of this Work	1
1.2	Organization of this Work	5
1.3	Conference and Journal Contributions	6
2	Application and Modeling of Through Silicon Vias	7
2.1	Application in 2.5D- and 3D-Integration	7
2.2	Fabrication and Process Technologies	8
2.3	Idealizations of TSVs for Efficient Modeling	10
2.4	Classification and Overview over Modeling Approaches	11
2.4.1	Physical Effects to Account for by Modeling Approaches	12
2.4.2	General Purpose Full-Wave Simulations	14
2.4.3	Methods That Focus on Propagation Along Barrels	14
2.4.4	Models That Focus on Propagation Along Planes	15
2.5	Comparison of TSVs with PBC Vias	16
2.6	Modeling of Coaxial Through Silicon Vias	18
2.7	Summary and Outlook	19
3	Physics-Based Modeling of TSVs	21
3.1	Boundary Conditions for Applicability of PBV Modeling	22
3.2	Decomposition into Near and Far Fields for PBV Modeling	24
3.3	Port Definitions	27
3.4	Composition of Model Parts	27
3.5	Near Field Modeling	29
3.5.1	Discussion of Applicable Simplifications	29
3.5.2	Near Field Modeling Approaches	31
3.5.3	Outlook on Adaptations for Layered Fillings	33

3.6	Far-Field Modeling	34
3.6.1	Radial Waveguide Method	34
3.6.2	Cavity Resonator Method	34
3.6.3	Contour Integral Method for Planar Circuits	35
3.6.4	Outlook on Adaptations for Layered Fillings	37
3.7	Embedding of the Physics-Based Via Model	37
3.8	De-embedding of the Physics-Based Via Model	38
3.9	Summary of the Physics-Based Modeling	38
3.10	Modeling of Coaxial TSVs	39
4	Far Field TSV Modeling	41
4.1	Parallel Plate Waveguide Modes	41
4.2	Classification of Wave Solutions	42
4.2.1	Classifications of Parallel Plate Structures	43
4.3	Characteristic TRM-Equations for TM-modes and N Layers	45
4.3.1	Derivation of the Transfer Matrix	45
4.3.2	Characteristic Equation for Perfect Electric Conductor Boundaries .	49
4.3.3	Characteristic Equation for Bounding Half-Spaces of Finite Conduc- tivity	50
4.3.4	Approximations for Cases with PEC boundaries	52
4.4	Solution of Characteristic Equations	53
4.5	Determination of the Fields	53
4.6	Application of the TRM to Silicon Interposer Stackups	54
4.6.1	Modes of Propagation in Si–SiO ₂ -Structures	54
4.6.2	Application Details of the TRM Methods	56
4.6.3	Validation with Full-Wave Simulation Results	57
4.6.4	Application to Arbitrary Layered Structures	61
4.7	Application to Computation of Planar Microwave Circuits	61
4.7.1	Application with the CIM	61

4.7.2	Application with Radial Line Segment	63
4.7.3	Adaptation of Wave Impedances and Characteristic Impedances to Inhomogeneous Fillings	64
4.8	Summary and Conclusions	64
5	Near Field TSV Modeling	65
5.1	Finite-Difference Frequency Domain Method (FDFD)	65
5.1.1	Motivation	65
5.2	Adaptation of a BOR FDFD Method for Near Field Modeling	66
5.2.1	Finite Difference Equations	68
5.2.2	Relations at Dielectric Interfaces	71
5.2.3	Port Excitations and Port Responses	73
5.3	Approximate Methods for Near Field Modeling	76
5.3.1	Coaxial-to-Radial Junction Model by Williamson	76
5.3.2	Quasi-static Near Field Modeling Using an Effective Admittance . .	78
5.4	Comparison and Validation	80
5.4.1	Convergence Behavior and Conclusions	83
5.5	Application in Physics-Based Via Modeling	84
5.6	Conclusions	92
6	Application to Large Scale Crosstalk Analysis of TSV Arrays	93
6.1	Adaptations and Optimizations for Large Scale Analysis	93
6.1.1	Derivation of Optimized Solution	94
6.1.2	Discussion of Savings	95
6.2	Validation of the PBV Model for Mid-Scale TSV Arrays	96
6.2.1	Numerical Performance	101
6.3	Time and Frequency Domain Superposition Techniques for Total Uncorre- lated Crosstalk	102
6.3.1	Computation of Total Uncorrelated Crosstalk	104
6.4	Total Uncorrelated Crosstalk in Large Arrays	116

6.5	Analysis of Design Parameter Variation using WPSXT	121
6.6	Summary and Conclusions	122
7	Validation of Modeling Approaches	125
7.1	Modeling Techniques for Wave Propagation Along the Via barrels	125
7.1.1	Rigorous Modeling of Two-Wire Lines Using the Multipole Expansion Method	126
7.1.2	Modeling Based on Quasi-Static Analysis	126
7.1.3	Per Unit Length Parameter Computation Based on a Fourier Method	128
7.1.4	Per Unit Length Parameter Computation Based on Thin-Wire Approximation	128
7.1.5	Computation of Network Parameters from Per Unit Length Parameters	130
7.2	Comparison of Modeling Approaches	131
7.2.1	Modeling using FEM Full-Wave Simulations	132
7.2.2	Simulation of Several Stackups	133
7.2.3	Conclusions Regarding Model Comparisons	140
7.3	Correlation of Measurements and Full-Wave Simulations	140
7.3.1	Motivation and Challenges	141
7.3.2	Designed and Fabricated Structures for TSV Characterization . . .	141
7.3.3	Measurement Setups	146
7.3.4	Practical Challenges of the Measurement Execution	147
7.3.5	Measurement and Simulation Results	147
7.3.6	Summary and Conclusions Regarding Measurements	154
8	Conclusion and Outlook	161
A	Numerical Methods	163
A.1	Root Search Techniques for the Complex Domain	163
A.1.1	Newton's Method	163
A.1.2	Halley's method	164
A.1.3	Argument Principle Method	164

A.2	Numerical Integration using Gauss Quadrature	165
B	Parallel-Plate Waveguides	167
B.1	Parallel Plate Waveguide With Homogeneous, Isotropic, Lossless Dielectric and Perfect Conductor Plates	167
B.2	Characteristic Equation for a Single Intermediate Layer	167
B.3	Application to Radial Waveguides	168
B.3.1	Derivation of the General Transfer Matrix	168
B.3.2	Characteristic Equation for Two Layers	175
B.3.3	Adaptations for Modes with Azimuthal Variations	176
B.3.4	Approximate Solution for a PEC-bounded Single Layer	177
B.4	Analytical Derivatives for the TRM	177
B.4.1	First Derivative of the Transfer Matrix	178
B.4.2	First Derivative of the Characteristic Function	179
B.5	Characteristic Impedance and Wave Impedances of Parallel Plate Waveguides	179
B.5.1	Impedances of the Homogeneously Filled Waveguide	179
B.5.2	Impedances of the Layered Waveguide	180
C	Computation of Waveguides Based on Cylindrical Wave Functions	183
C.1	Computation of Wave Numbers of Propagation in Coaxial TSVs	183
C.1.1	Adaptation of a Matrix Method for Radially Layered Coaxial TSVs	184
C.1.2	Quasi-static First Order Approximation	187
C.1.3	Application to Coaxial TSV Structures	188
C.2	TM_{0n} -Modes of the Radial Waveguide	189
D	The Contour Integral Method for Planar Circuits	195
D.1	Theoretical Foundations of the Contour Integral Method	195
D.1.1	Original Formulation for Line Ports	198
D.1.2	Extensions to Isotropic Modes on Circular Ports	198
D.1.3	Extensions to Anisotropic Modes on Circular Ports	201

D.2	Adaptation to Layered Substrates	203
D.3	Radial Waveguide Example for Low Frequencies	204
D.4	Practical Application of the CIM	204
D.4.1	Suggestions for Efficient Implementation	204
D.4.2	Principal Steps of the CIM Application	206
E	Derivations for Multiconductor Transmission Line Models	209
E.1	Two-Conductor Transmission Lines	209
E.1.1	Network Parameters	209
E.1.2	Determination of Wave Number From Network Parameters	210
E.2	Internal Impedance of Circular Cylindrical Conductors	211
E.2.1	Exact Solution for Single Circular Cylindrical Conductor	211
E.2.2	Approximate Solutions for Single Circular Cylindrical Conductor	212
E.2.3	Incorporation of Internal Parts Into Resistivity and Inductance Matrices	213
E.3	Complex Analytical Capacitance and Effective Permittivity of Two Circular TSVs	213
E.4	Exact Capacitance for Two Circular Conductors in Homogeneous Medium	214
E.5	Fourier Method for Exact Capacitance Calculation	214
E.5.1	Basic Formulation of the Quasi-Static Analysis	215
E.5.2	Solution Inside the Silicon Region	216
E.5.3	Assembly of the Descriptions for Oxide and Silicon Areas	221
E.5.4	Inclusion of Complex Permittivities	224
E.5.5	Proof of Equivalence With TWA	224
E.6	Generalized Capacitance Matrix	226
E.7	Network Parameters of Transmission Lines	227
E.7.1	Chain Parameter Matrix for the General Case	227
E.7.2	Approximations for Short Transmission Lines	228
E.7.3	Assignment of Several Reference Conductors	230

F Mathematical Appendix	235
F.1 Derivatives in 2D Cartesian Coordinates	235
F.1.1 Directional Derivative of Scalar Field	235
F.1.2 Normal Derivative of Euclidean Norm	235
F.1.3 Gradient of Euclidean Norm	235
F.2 Symmetries of Harmonic Functions for Complex Arguments	236
F.3 Derivatives of Bessel Functions	236
G Network Parameters	237
G.1 Concatenation of Admittance Parameters	237
G.1.1 General case	237
G.2 Concatenation of Impedance Parameters	239
G.2.1 General Case	239
G.2.2 Concatenation of Single Series Impedances Per Port	240
G.2.3 Concatenation of a Common Series Impedance	240
G.2.4 Concatenation of Per Port and Common Series Impedances	241
G.3 Conversion Between Single-Ended and Mixed-Mode Network Parameters	242
G.3.1 On the Use of Block-Diagonal Matrices	242
G.3.2 Scattering Parameter Conversion for Uncoupled, Balanced Port Pairs	244
H Additional Discussions and Data Related to Measurements	245
H.1 Design for Practical Measurability	245
H.2 Details on the Test Structures and Measurement Setups	247
H.3 Fabricated Structures	249
References	253
Curriculum Vitea	269

Notation, Symbols and Acronyms

Notation

a	Scalar
\boldsymbol{r}	Vector
$\hat{\boldsymbol{r}}$	Unit vector in direction of \boldsymbol{r}
\boldsymbol{e}_ξ	Unit vector along coordinate ξ
\boldsymbol{M}	Matrix

Symbols

$\mathbf{1}$	Identity matrix
α	Attenuation constant (Np/m)
β	Phase constant (rad/m)
C	Capacitance (F)
E	Electric field strength (V m ⁻¹)
ε	Permittivity
$\underline{\varepsilon}$	Complex permittivity ($\underline{\varepsilon} = \varepsilon_r \varepsilon_0 - j\sigma/\omega$)
ε_r	Relative permittivity
ε_0	Permittivity of free space ($\varepsilon_0 \approx 8.854\,188 \times 10^{-12}$ F m ⁻¹)
η	Wave impedance (Ω)
G	Conductance (S)
γ	Propagation constant (m ⁻¹)
H	Magnetic field strength (A m ⁻¹)
$H_n^{(1)}(\cdot)$	Hankel function of the first kind and order n
$H_n^{(2)}(\cdot)$	Hankel function of the second kind and order n
I	Electric current (A)
\Im	Imaginary part
j	Imaginary unit
\mathbf{J}	Matrix of ones
k	Complex wave number (m ⁻¹)

L	Inductance (H)
μ_r	Relative permeability of a medium
μ_0	Permeability of free space ($\mu_0 = 4\pi \times 10^{-7} \text{ H m}^{-1}$)
∇	Nabla operator
ω	Angular frequency (rad s^{-1})
R	Resistance (Ω)
\Re	Real part
$S_{n,o}$	Scattering parameter from port o to port n (normalized to 50Ω if not stated otherwise)
σ	Electrical conductivity (S/m)
σ_{SD}	Standard deviation
$\tan \delta$	Dielectric loss tangent
V	Electric voltage (V)
Y	Admittance (S)
$Y_{n,o}$	Admittance parameter from port o to port n
Z	Impedance (Ω)
$Z_{n,o}$	Impedance parameter from port o to port n
\mathbb{Z}	Set of all integer numbers

Acronyms

2D	two-dimensional
3D	three-dimensional
AC	alternating current
APM	argument principle method
BCB	benzocyclobutene
BOR	body of revolution
CIM	contour integral method
CPU	central processing unit
CTE	coefficient of thermal expansion
CVD	chemical vapor deposition
DUT	device under test
FDFD	finite difference frequency domain
FEM	finite element method
FEXT	far-end cross talk

FFT	fast Fourier transform
FWHM	full width at half maximum
GND	ground
GPIO	General Purpose Interface Bus
GSG	ground–signal–ground
IC	integrated circuit
ISI	inter symbol interference
ITRS	International Technology Roadmap for Semiconductors [1]
LRM	line–reflect–match (calibration)
MEM	multipole expansion
MEMS	micro–electro–mechanical systems
MOS	metal–oxide–semiconductor
MTL	multi–conductor transmission lines
MtM	more–than–Moore
NEXT	near end cross talk
PC	personal computer
PCB	printed circuit board
PDF	probability density function
PEC	perfect electrically conducting
PI	power integrity
PMC	perfect magnetically conducting
PMF	probability mass function
PRBS	pseudo random bit sequence
PSXT	power of cross talk
PUL	per–unit–length
RAM	random–access memory
RDL	redistribution layer
SACVD	sub-atmospheric chemical vapor deposition
SI	signal integrity
Si	silicon
SiO ₂	silicon dioxide
SiP	system in package
SIW	substrate integrated waveguide
SoP	system on package
TEM	transverse electromagnetic
TM	transverse magnetic
TRM	transverse resonance method
TSV	through silicon via

TWA	thin wire approximation (→ Section 7.1.4)
UI	unit interval
USB	universal serial bus
via	vertical interconnect access
VNA	vector network analyzer
WPR	wafer photo resist (used as trade name, cf. Fig. 7.9)
WPSXT	weighted power sum of crosstalk
XTALK	crosstalk

Chapter 1

Introduction

1.1 Motivation and Context of this Work

The development of integrated circuits (ICs) is one of the main driving forces behind the performance of today's systems in terms of computing power. The miniaturization leads to faster switching of these circuits and allows for a reduction of consumed electrical power. One of the difficulties that arises with the miniaturization is the proper electrical interconnection of system parts. For one, the power has to be supplied to all consuming devices of an electrical circuit. Also, the number of required interconnections increases with the number of interconnected systems parts. Certain signal paths can become relatively long and a scaling of interconnecting lines including a reduction of their cross-sections leads to increasing losses in the interconnect.

The packaging of integrated circuits has the following principal aims: Establishing a mechanical and electrical connection between an integrated system and the remainder of the system, e.g., other components that are located on a printed circuit boards (PCB). The electrical connection is in general used for both exchange of information with the integrated circuit in form of electrical signals and provision of electrical power to the circuit. Ensuring the quality of the signaling as well as the quality of the supplied electrical power is commonly referred to as signal integrity (SI) and power integrity (PI), respectively.

Two important established technologies that are used in the packaging of ICs are illustrated in Fig. 1.1. Figs. 1.1a and 1.1b depict the perspective and side view, respectively, of an illustration of the wire bond interconnect. The integrated circuit is placed on a package substrate or printed circuit board (shown in green) with the active chip area on the top, i.e. pointing away from the substrate. The electrical connection to the active chip area is established through metallic wires (e.g. made of gold, or aluminum [2, Ch. 19], [3]). These wires are known to introduce an inductance which reduces the interconnect performance of

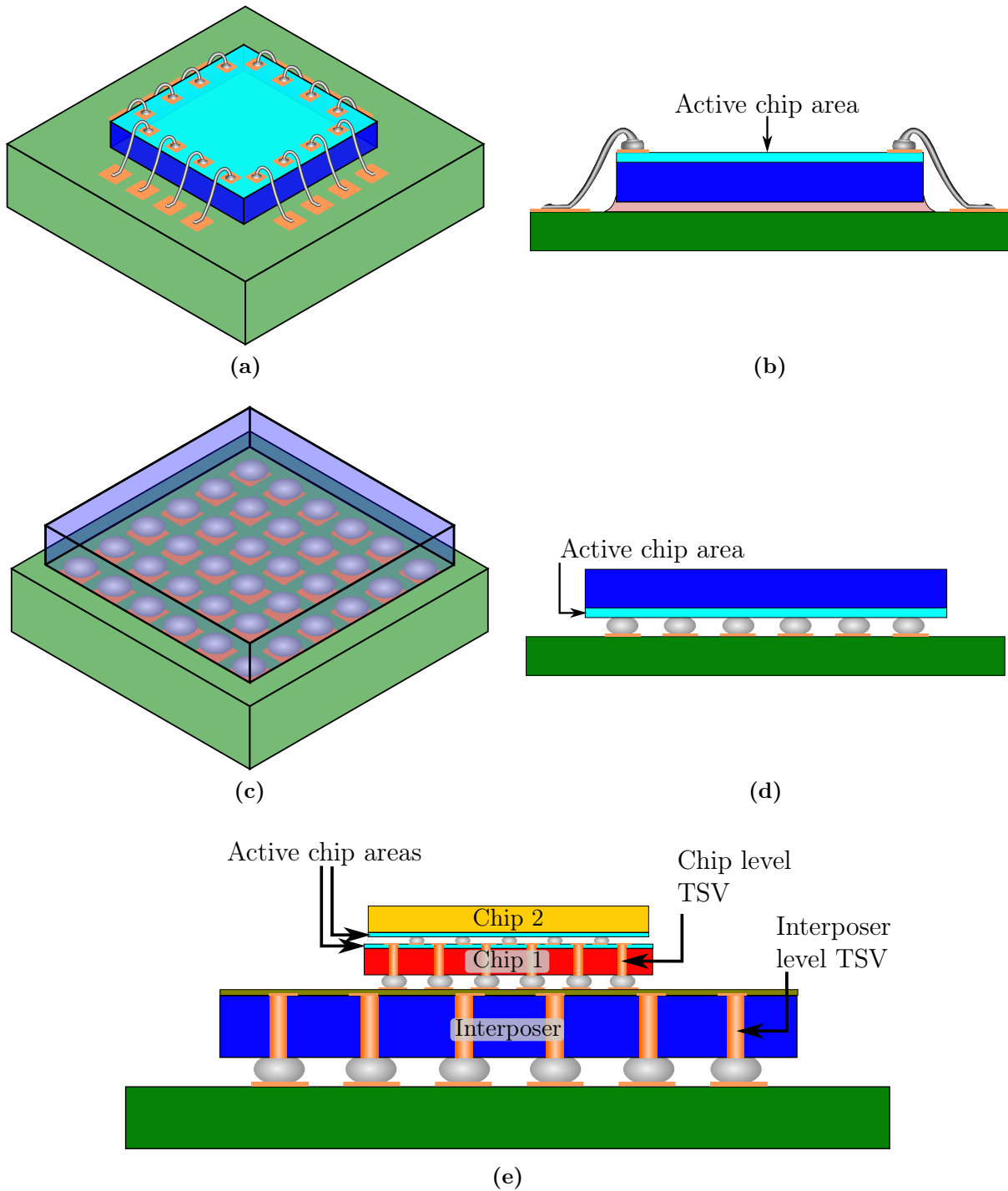


Figure 1.1: Established and emerging technologies used in packaging of integrated circuits to establish the electrical and mechanical interconnection with other system parts: (a) perspective view and (b) side view of an example for wire bonding. (c) perspective view and (d) side view of an example for flip-chip technology. (e) side view an example stackup of two stacked chips on an interposer.

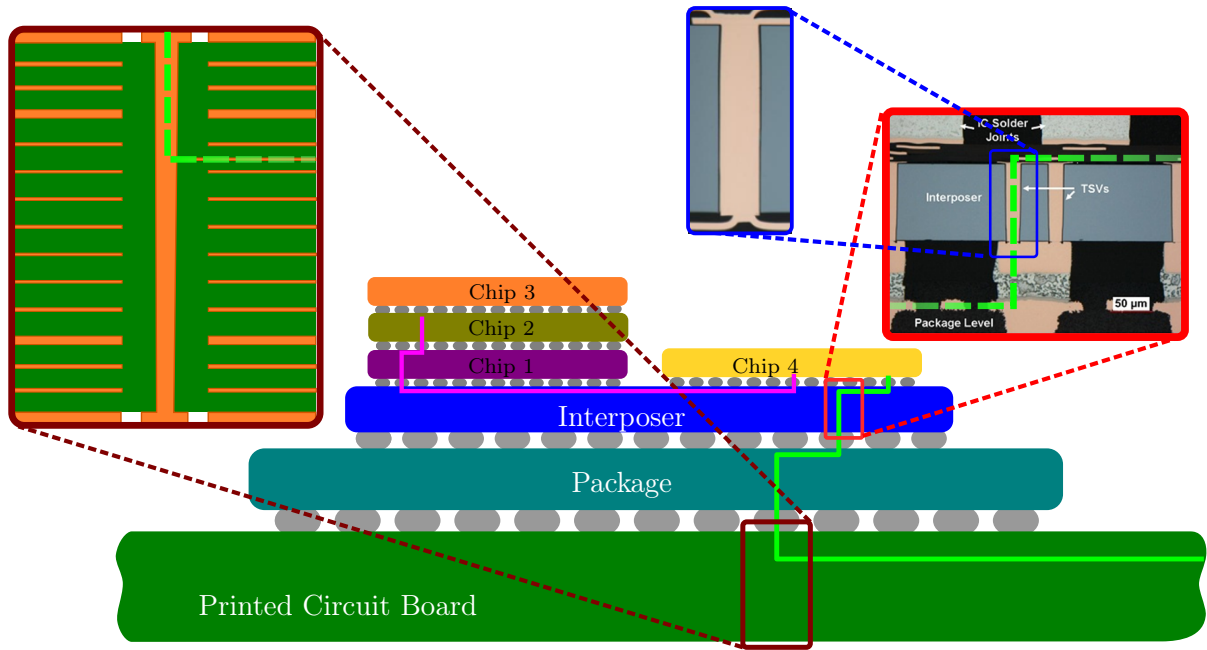
wire bonds at high frequencies [4, Ch. 4.5], [5,6]. An illustration of the flip-chip technology is depicted in Figs. 1.1c and 1.1d. The active chips are flipped towards the package substrate or printed circuit board and connected through metallic bumps. These bumps represent a much smaller inductance and therefore a smaller discontinuity in the signal path than the wire bonds. Another important advantage is that the complete chip area can potentially be used for the interconnection with the flip chip, while a connection is only possible from one of the four sides with wire-bonds.

The term 3D integration describes technologies which allow for the interconnection of components in integrated systems using all three spatial directions. Traditionally, integrated devices are fabricated in processes where the contacts are planar and the connection between sub-components is also established horizontally with respect to devices, e.g., by the wire-bonding described before. This has several disadvantages including the limitation of the number of connections, long interconnection paths and potentially many discontinuities if many sub-circuits need to be connected.

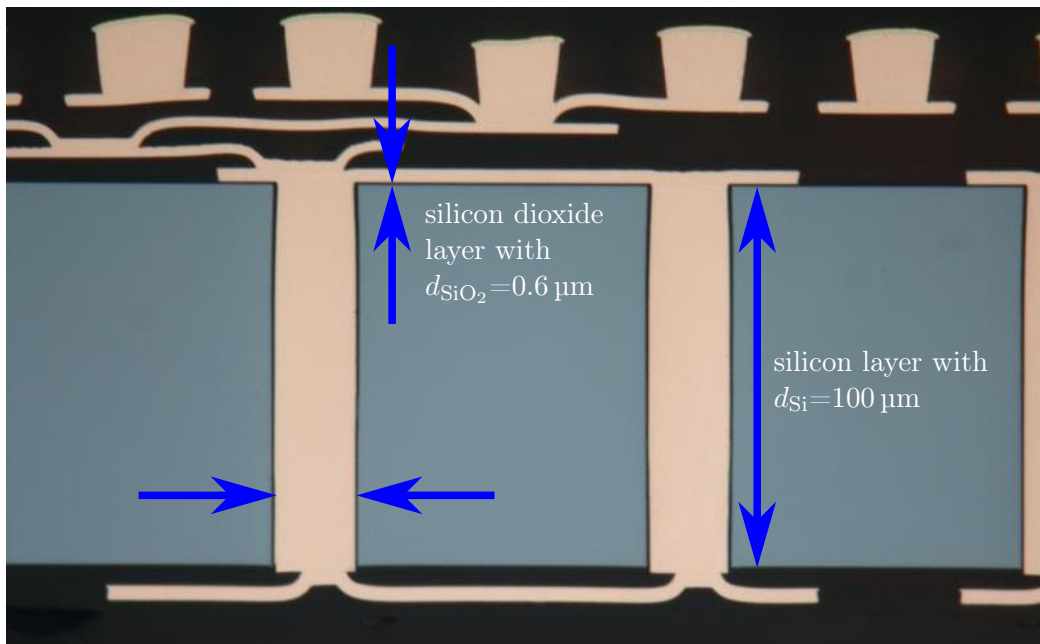
The 3D approach mainly aims at decreasing the interconnect lengths and, at the same time, enabling larger numbers of connections between sub-circuits. One long-term goal in 3D integration is to use all three spatial dimension for the fabrication of active devices. The connections between the devices is implemented along these dimensions during the process of device fabrication. An already more established way to fabricate cost-effective integrated systems consists in connecting the planar chips vertically by stacking chips and establishing electrical connections among them. When using dies manufactured with silicon technology the through connection called vertical interconnect access (via), which electrically connects the top and bottom side of a chip, is called through silicon via (TSV). TSVs and their applications are illustrated in Figs. 1.1e and 1.2a.

The TSV establishes short interconnections compared to connected chips placed next to each other in the same plane. Also, the theoretical interconnect density is higher for connections through chips. When stacking multiple chips to obtain very compact systems, one major limitation, if compared to the placement side by side, is the cooling of active devices which becomes more challenging [7]. Fig. 1.2a gives an example for the environment in which TSVs are applied. They can be part of a silicon interposer to connect a package and several chips. The vertical interconnects in the silicon have a similar structures as those found in printed circuit boards. Differences in their electrical properties are briefly discussed in Sec. 2.5.

Apart from the also very challenging fabrication of such systems consisting of stacked chips, the interconnects have to be designed with care. The starting point of the investigations is the single via and its electrical properties in the typical interposer environment. This



(a)



(b)

Figure 1.2: (a) Example for the environment of a silicon interposer. (b) Microsection of a silicon interposer. (Photos embedded in both figures courtesy of Fraunhofer Institute for Reliability and Microintegration (IZM), Berlin.)

environment includes the silicon substrate through which the TSVs establish the connection. Further structures contribute to the overall electromagnetic properties such as other signal TSVs, TSVs connected to ground, conducting redistribution structures on the top and bottom sides of the silicon substrate, and neighboring system components. The investigation of the properties is complicated by the layered nature of the substrates. Especially the thin oxide layers, which electrically isolate all metal components (via barrels, redistribution metallizations) from the conducting silicon, have to be taken into account when modeling interposer structures for a large frequency range.

Fig. 1.2b shows a cross-section photo with typical dimensions of a silicon interposer. Two vias with nearly circular cross-sections connect the upper and lower side of the silicon layer. On both sides of the silicon layer, the routing of signals is enabled by metallic redistribution layers which are embedded in benzocyclobutene (BCB).

1.2 Organization of this Work

The presented work is organized as follows:

- **Chapter 2** presents application areas of TSVs, the principal fabrication steps, some fundamental material properties, and the most important physical effects that occur in structures with TSVs. Further, it gives an overview over some of the most important modeling approaches.
- **Chapter 3** is an introduction to the main modeling approach of this work, namely the physics-based modeling: After discussing the boundary conditions for the applicability, the interconnection of the constituents and the fundamental properties of the constituents are discussed.
- **Chapter 4** discusses one of the most important parts of the physics-based modeling which is the modeling of the propagation inside a parallel-plate structure. This propagation is governed by an effective wave number that can be obtained from a technique known as transverse resonance method (TRM) and by the multiple scattering of radial waves between parallel metallic plates that is computed from a contour integral method (CIM) for planar microwave circuits.
- **Chapter 5** discusses the second constituent which is the near field modeling of TSVs. It describes the transitions between the ports towards the structures connected to the interposer cavity and the ports that connect to the propagating field models.

The main approach that is presented is based on a local full-wave modeling using a finite-difference frequency domain method.

- **Chapter 6** presents an application of the proposed physics-based modeling approach to the modeling of large via arrays. Based on investigations of a total uncorrelated crosstalk, design guidelines are derived for a certain parameter range.
- **Chapter 7** shows how the proposed modeling approach compares to a complementary modeling approach based on multi-conductor transmission line theory and concludes the applicability of both modeling approaches. It further presents correlations of full-wave simulations with measurements that aim at the electrical characterization of TSVs from the measurement of structures with only a few TSVs.
- **Chapter 8** discusses conclusions from the investigations of TSV properties and numerical techniques and gives an outlook on possible extensions of the modeling approach to cover a larger parameter space.

1.3 Conference and Journal Contributions

Major parts of the presented work have already been published in several conference papers [8–12] and journal publications [13, 14]. In the related fields of modeling of vias and striplines in (multilayer) printed circuit boards further contributions have been published [15–17]. Several Bachelor’s theses and one Master’s thesis have been supervised on related subjects [18–21].

Most of the work has been part of a project funded by the German Research Foundation (Deutsche Forschungsgemeinschaft, DFG) entitled “Electrical Modeling and Design of Through Silicon Vias for Integrated Systems”. It was carried out as a collaboration between the Hamburg University of Technology (TUHH), the Technical University of Berlin (TUB), and the Fraunhofer Institute for Reliability and Microintegration (IZM), Berlin. Complementary modeling approaches for TSVs have been published during this project in [22, 23] and investigations on material characterization have been presented in [24, 25].

Chapter 2

Application and Modeling of Through Silicon Vias

2.1 Application in 2.5D- and 3D-Integration

Much of the functionality of today's electronic systems is related to the use of integrated circuits (ICs). In purely electronic systems, devices such as transistors, capacitors, inductors, and resistors are integrated. The scaling has been governed in the past by the empirical law known as Moore's law [26]. In micro-electro-mechanical system (MEMS), additional devices such as mechanical switches and sensors are used. Adding functionality in various ways that are not related to the scaling of the traditional IC components (CPUs, RAM, logical circuitry) is often named more-than-Moore (MtM). MtM is defined by ITRS as "Incorporation into devices of functionalities that do not necessarily scale according to 'Moore's Law', but provide additional value in different ways. The 'More-than-Moore' approach allows for the non-digital functionalities to migrate from the system board-level into the package (SiP) or onto the chip (SoC).", cf. Appendix A of [27].

The main advantages of these new systems are the reduced size which is relevant, e.g., in numerous mobile devices for communication and medical applications, the potential of cost reductions, and the potential of increased energy efficiency. Drawbacks are thermal challenges due to the narrower spacing of dissipating components and a potentially reduced yield (which is then comparable to the monolithic circuit) if tests for proper functioning of the single die are omitted. The latter problem is further discussed in [28, Sec. 2.2], [29, Sec. 3.3.4].

From an electrical point of view, the closer spacing of system parts could reduce the average path length of the interconnects and thereby also reduce signal loss and crosstalk. On the other hand, the routing requires the extended use of the third dimension which potentially introduces (additional) discontinuities in the signal path.

2.2 Fabrication and Process Technologies

The fabrication of TSVs requires advanced process technologies that differ in a few ways from the process steps that are used for the ICs. TSVs can be part of dies with or without active devices. The principal steps of an exemplary fabrication process are depicted in Fig. 2.1 for a silicon wafer on which active devices have already been fabricated (via last approach), cf. [30].

The first step is the etching of the TSV holes. The result is typically not a cylindrical hole. The diameter decreases with depth and a hole with the form of a truncated cone is formed. This hole does not traverse the complete silicon layer which can still be comparatively thick. After etching the holes for the TSVs, isolation layers are grown. In most cases, a silicon dioxide layer is used which has a more or less constant thickness on the TSV holes. In the next step the remaining holes are filled with a conductive material, e.g., copper. The TSVs can then be electrically connected to the existing redistribution layers and components on the top side. For the subsequent steps an auxiliary handling wafer is temporarily bonded to the top side of the silicon wafer. This allows for a processing of the bottom side of the wafer which consists in a thinning of the wafer by which the ends of the vias are exposed. Then, isolation layers can also be applied on the bottom side and contacts can be formed on this side. After the bottom side processing, the auxiliary wafer can finally be removed. The fabrication methods mentioned above lead to specific characteristic geometries that are discussed in section 2.3.

Alternatively, the vias can be formed before the active layers on an integrated circuit are processed (via first approach). Active devices are not part of an interposer whose purpose is to establish the mechanical and electrical connection between several chips (with active components, MEMS-components etc.) and another integration level, e.g. a package or a printed circuit board. An interposer can include redistribution layers for the signal routing that are necessary for the electrical connection. It also establishes the size transformation that is required in many cases between the different pitches at different system levels.

Further discussion of fabrication technologies can be found, e.g., in [31, 32].

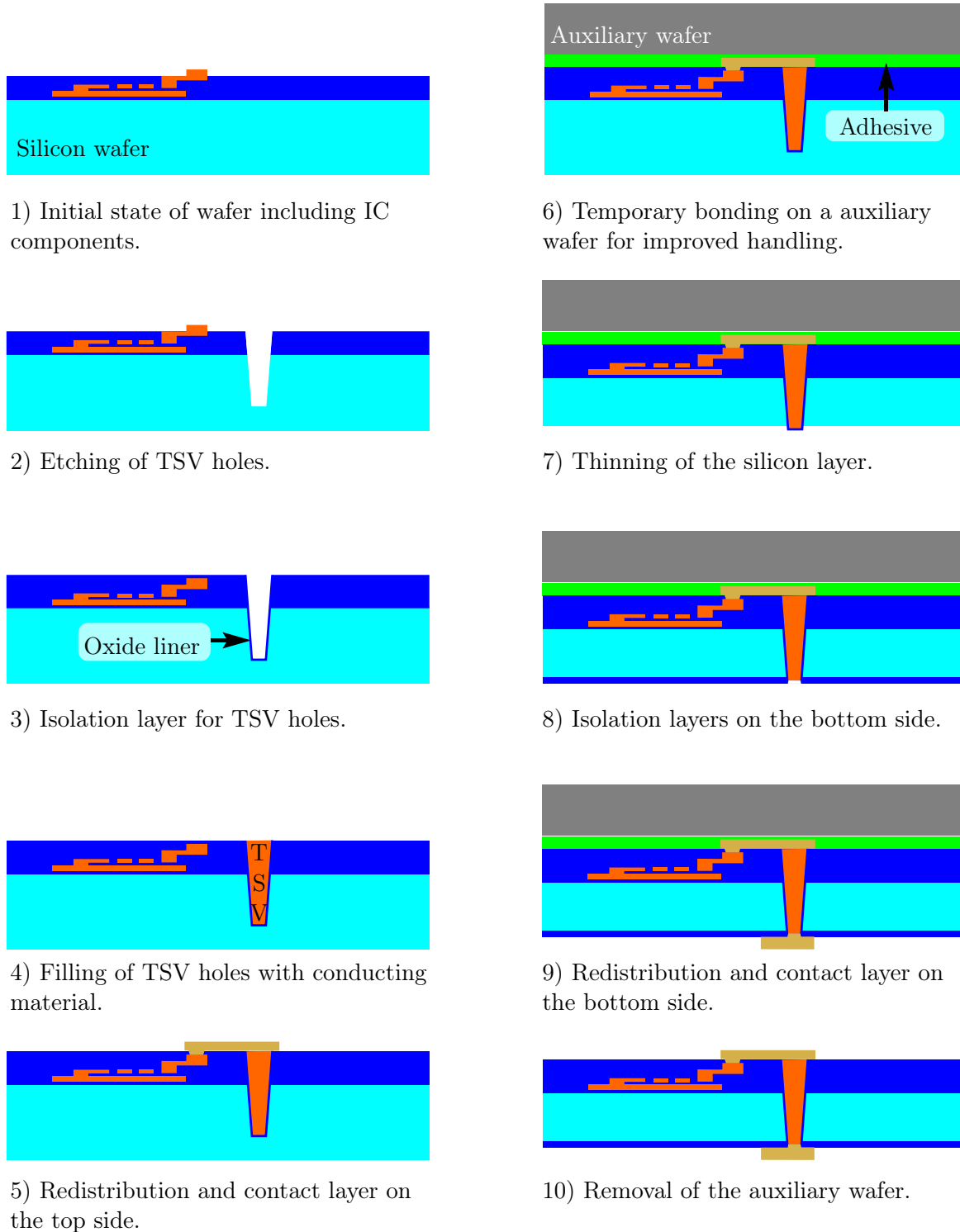


Figure 2.1: Principle TSV fabrication steps as carried out by Fraunhofer IZM–ASSID (All-Silicon System Integration Dresden). Figure adapted from [30].

2.3 Idealizations of TSVs for Efficient Modeling

In the following, the main differences with regard to the geometry between real TSVs as found in silicon interposers and the structures for which modeling approaches are presented in this thesis are pointed out. The most important differences with regard to the included physical effects will be pointed out in section 2.4. Figure 2.2a shows many of the features that can be found in real TSVs, while Figs. 2.2b and 2.2c illustrate the simplified structures that are actually modeled in this work.

As illustrated in Figure 2.2a, real TSV barrels have approximately the geometry of a diffracted cone which relates to a dominantly trapezoidal cross-section as sketched in the figure by the dashed lines. The surface is not even but shows different kinds of surface waviness and roughness which depend on the used fabrication process. In contrast, the barrels of the idealized TSVs have the shape of a circular cylinder with a perfectly smooth surface. Its geometry can therefore be characterized by only a radius.

The exact configuration of the structure that surrounds the via can be diverse. In the example given in Figure 2.2a, the environment in the horizontal directions of the via barrels is composed of a substrate and electrically insulating oxide layers. On the top side, there is an electric insulation, either silicon oxide or a polymer dielectric. Above that, there are redistribution layers (RDLs) for rerouting and size transformation for the connected chips embedded in a dielectric. On the bottom side of the substrate there can also be metallic structures in a dielectric layer for a rerouting of signals. Below the substrate, the interposer can be connected to a printed circuit board using metallic bumps. These connections through an array of solder joint interconnects is often embedded in an underfill dielectric for an improved mechanical connection. It is required because differing coefficients of thermal expansion (CTEs) lead to mechanical stress in case of temperature cycling [33]. The need for an underfill material for the connection to ICs is discussed, e.g., in [34].

The idealized TSVs in Fig. 2.2b are in a stackup with more metallic components than the example given in Figure 2.2a. These metallizations extend over the complete substrate area except for the locations where TSVs connect to the adjacent structures. There, a circular coaxial cutout allows for a connection. The customary naming from the printed circuit board context is adopted by referring to these clearances as “antipads”. The shape of the antipad hints at the type of field distribution that will dominate in this area, i.e., depending on the connected structures outside the cavity that is constituted by the metallizations, the fundamental coaxial mode will dominate the field behavior. The metallizations are again electrically insulated, e.g., with silicon dioxide layers. TSVs can also be connected

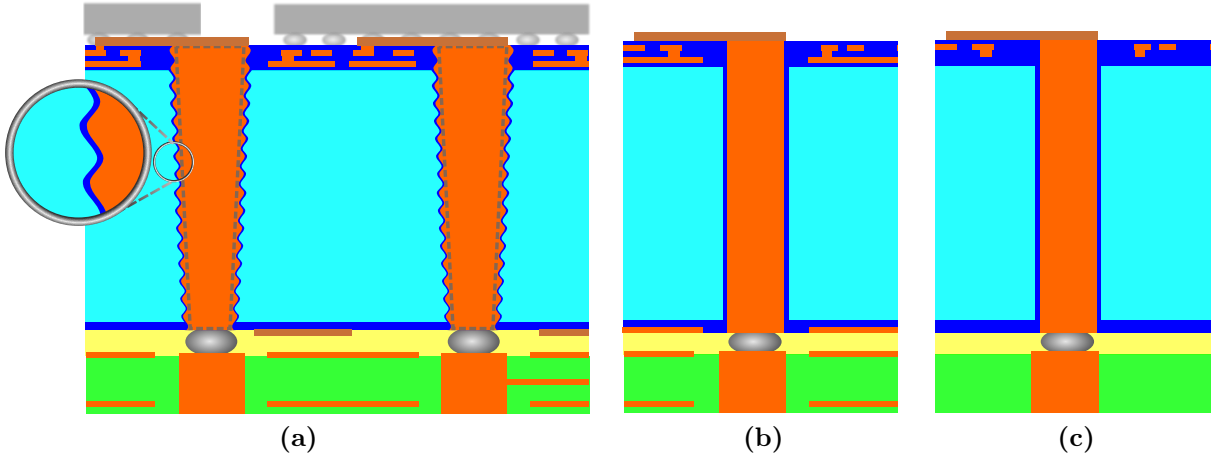


Figure 2.2: (a) Realistic geometry and electromagnetic environment (stackup) of a silicon interposer. (b) Simplified, ideal structure with metal layers (c) Simplified, ideal structure without metal layers.

to the metallizations, thereby enforcing the same electric potential at their location. As customary in the PCB context, the latter type of TSV is named ground via.

The idealized TSVs in Fig. 2.2c are in a stackup with fewer metal components than the example given in Figure 2.2a. As will be discussed in the course of this thesis, this leads to a fundamentally different field behavior for high-frequency signals. The modeling in this case assumes a dominant behavior with wave propagation along the via barrels and the electric and magnetic field components mostly transverse to the via axis, which can thus be described as a multi-conductor transmission line.

2.4 Classification and Overview over Modeling Approaches

The electromagnetic modeling and simulation of microwave components has numerous aims, some of which are as follows:

- Designing components for specific needs, e.g., to fulfill given specifications.
- Optimizing components with respect to defined figures of merit through variation of all geometrical and material parameters that can be varied in reality.
- Developing simpler equivalent models that represent the actual behavior of components over a large parameter range.

- Developing an understanding of the underlying physics and determining the dominant effects.

Different applications of electromagnetic modeling and simulation have different needs regarding accuracy and efficient simulation, i.e. comparatively low memory and computation time requirements. The required accuracy also depends on the investigated quantities and the system boundaries. For example, modal network parameters represent an integral quantity with respect to the corresponding fields and therefore often have lower relative errors than the maximum field errors that can be observed throughout the considered volume. The system boundaries can be relevant since not every part of a structure contributes in the same way to the total error that is observed for the complete structure after concatenation of the system parts.

2.4.1 Physical Effects to Account for by Modeling Approaches

This section lists several aspects that should potentially be taken into account by modeling approaches when dealing with the simulation of TSVs. It is discussed in this section and the following ones, which of the aspects are considered by modeling approaches that are available in the form of computer software or that have been published in the past.

Inclusion of Full-Wave Effects

The principal classification judges to which extend the wave behavior of signal propagation in the structures under investigation is taken into account. If no assumptions are made or can be made regarding the nature of the problem that describes the EM properties of these structures, the most general solution methods are applied that solve Maxwell's equations for electromagnetic fields for all three spatial dimensions in the time or frequency domain. They are called full-wave solutions and are obtained through full-wave methods. Non full-wave methods are usually based on assumptions regarding the size of the geometries along all spatial dimensions relative to the wavelength along these dimensions.

Inclusion of Slow-Wave and Skin-Effect Modes of Propagation

Due to physical effects discussed in section 4.6.1, the consideration of a large parameter range of the layered structure with silicon and comparatively thin oxide layers reveals that, apart from a quasi-TEM mode, two other modes of propagation can be observed which are qualitatively different. One mode is characterized by a low phase velocity and consequently named slow-wave mode, the other one shows a strong skin-effect in the silicon layer and is therefore named skin-effect mode. Due to these phenomena, the consideration of these structures is in general more complex than in the case of other materials because for the latter only a quasi-TEM mode has to be considered, cf. section 4.2.

Inclusion of Surface Roughness

High levels of surface roughness of metallic conductors are known to have an impact on the signal propagation. In this work, it is assumed that the surface roughness has a minor effect and therefore is not considered in any of the methods considered in this thesis.

Inclusion of MOS-Effects

It has to be noted that a modeling is dependent on the substrate voltage if the MOS-effect needs to be taken into account. In this sense, the modeling is nonlinear if the substrate voltage is regarded as applied through one or multiple port(s). In contrast, neglecting the MOS-effect results in a fully linear and voltage independent description, e.g., using network parameters.

Inclusion of Carrier Dynamics and Thermal Effects

The interactions between physical effects of semiconductors such as silicon can be very intricate. In general, the dynamics of carrier generation and combination have to be considered and also the dissipated energy in the form of ohmic heating has effects on the semiconductor behavior. It is clear that configurations where these effects are relevant lead to multi-physical problems that are relatively complicated to solve. Only by limitation to configurations where these effects can be neglected is it possible to study structures of realistic sizes and realistic geometrical complexity and to gain insight into dominant physical effects.

2.4.2 General Purpose Full-Wave Simulations

The constraints of full-wave simulations are typically with regard to the grid resolution and size, the resulting sizes of the matrices that contain the data for the system of equations, the required memory, and the required time for the solution including setup times and post-processing times. This results in limitations with regard to the geometrical size of the structures, the resolution of structure details (especially those portions that do not align with the mesh/grid), and the frequency bandwidth for which simulations can be carried out. Most general purpose full-wave simulators can be classified as employing either volume or surface meshing methods [35]. The most important approximation is due to the meshing of the volumes, interfaces, and surfaces, i.e., to what degree the actual geometry can be represented by the mesh. It depends on the actual problem under investigation how much impact these approximations have on the overall results [35, Sec. 5.1].

2.4.3 Methods That Focus on Propagation Along Barrels

The first part of modeling approaches is characterized by the fact that the dominant wave propagation is assumed to be along the via barrels. This is the assumption made by the majority of publications.

Multi-Conductor Transmission Line Models

In the following, methods are classified as multi-conductor transmission line (MTL) techniques which are based on the computation of per-unit-length parameters for capacitance, conductance, inductance, and resistance. Scalar values are sufficient for pairs of vias, and matrices for the description of more than two TSVs. Due to the inhomogeneous medium — in this case the inhomogeneity in the horizontal directions orthogonal to the via axes is relevant — the parameters are in general frequency-dependent. It is conventionally acknowledged that the TSV is short in comparison to the guided wavelength (along the via barrel) and a lumped element representation is therefore constructed from elements that are obtained through multiplication of the per-unit-length parameters with the length. This type of modeling has been presented in [36–42].

Polarization Mode Basis Functions

An alternative formulation, which also accounts for the effects due to close spacing, is based on polarization mode basis functions. First applications to TSV modeling have been presented in [43,44]. The MOS-effect has been included in the investigations in [45,46] and effects due to the finite thickness of the silicon layer in [47]. Results for this modeling have been combined with FDFD-modeling of signal paths in [48].

2.4.4 Models That Focus on Propagation Along Planes

In printed circuit boards (PCBs), plane metallization are conventionally used as power and ground planes or, more generally, as reference planes in high-speed layouts. Therefore, the modeling of this type of structure is already well studied in the PCB context where a homogeneous medium can be assumed. In the context of multi chip modules with mesh-shaped planes, the effects due to partially broken reference planes are known to lead to similar behavior [49]. Two important approaches that aim at the simulation of the dominant effects of radial wave propagation are known as the multi-scattering methods and the physics-based methods.

Multi-Scattering

The multi-scattering methods are based on Green's functions for the cylindrical waves excited by circular magnetic current frills between the two parallel plates. The antipads represent apertures with coaxial field excitations. These can be replaced by the current frills in order to obtain an equivalent "interior" problem. The multi-scattering which is also known as Foldy-Lax approach has been applied to the case of homogeneous substrates, e.g., in [50,51]. An application to TSV modeling has been proposed in [52,53] and presented in [54,55]. The Foldy-Lax computation considers propagating and localized field in a conforming way and, as pointed out in [56, Sec. 2.2], leads thereby to some redundancy which is discussed in the following comparison with the PBV approach.

Physic-Based Modeling of Vias

The physics-based via (PBV) modeling performs a decomposition of the problem into building blocks for near field and far field. The former models the localized field due to coupling from the coaxial apertures to the cavity, the latter models the field propagation and scattering within this cavity. Theory and application in the PCB context can be found in [57–64]. Further discussions on this method, of which the adaptation to the modeling of TSV constitutes a major part of the work presented in this thesis, is given in the following chapters.

Comparison

Compared to the PBV modeling, the multi-scattering approach considers propagating and localized fields in the same part of the model. Every coaxial aperture is considered as a separate port, whereas the PBV model uses additional radial ports as interfaces between the near and far field models. The multi-scattering method therefore results (in general) in a higher numerical complexity because all interactions, even those with comparatively small impact on the effective properties, are taken into account. The latter is the case for coupling with distant ports due to localized fields, which is negligible in most practical cases. On the other hand, the coupling with directly neighboring vias due to localized field is of relevance in more practical cases and supported by the multi-scattering theory. An improvement of the physics-based modeling through extraction of only the relevant terms from the multi-scattering and inclusion in the PBV for cases with narrow spacing of vias has been presented in [65].

2.5 Comparison of TSVs with PBC Vias

It can be interesting to compare the metal-clad interposer with TSVs to a printed circuit board (PCB) structure with the same layout and each structure with its respective typical dimensions. Such a comparison is shown in Fig. 2.3 together with results for a modified simulation of the silicon interposer where a depletion layer for the fully depleted case is included. Using [39, Eq. 6], a layer thickness of $2.2\,\mu\text{m}$ is computed. A layer of non-conductive silicon is included both around each via barrel (between radial oxide layer and conductive silicon substrate) and next to every plate metallization (between planar oxide layer and the conductive silicon substrate). The expected influence on the parallel plate mode propagation is as follows (skin-effect mode excluded): At lower frequencies, i.e.

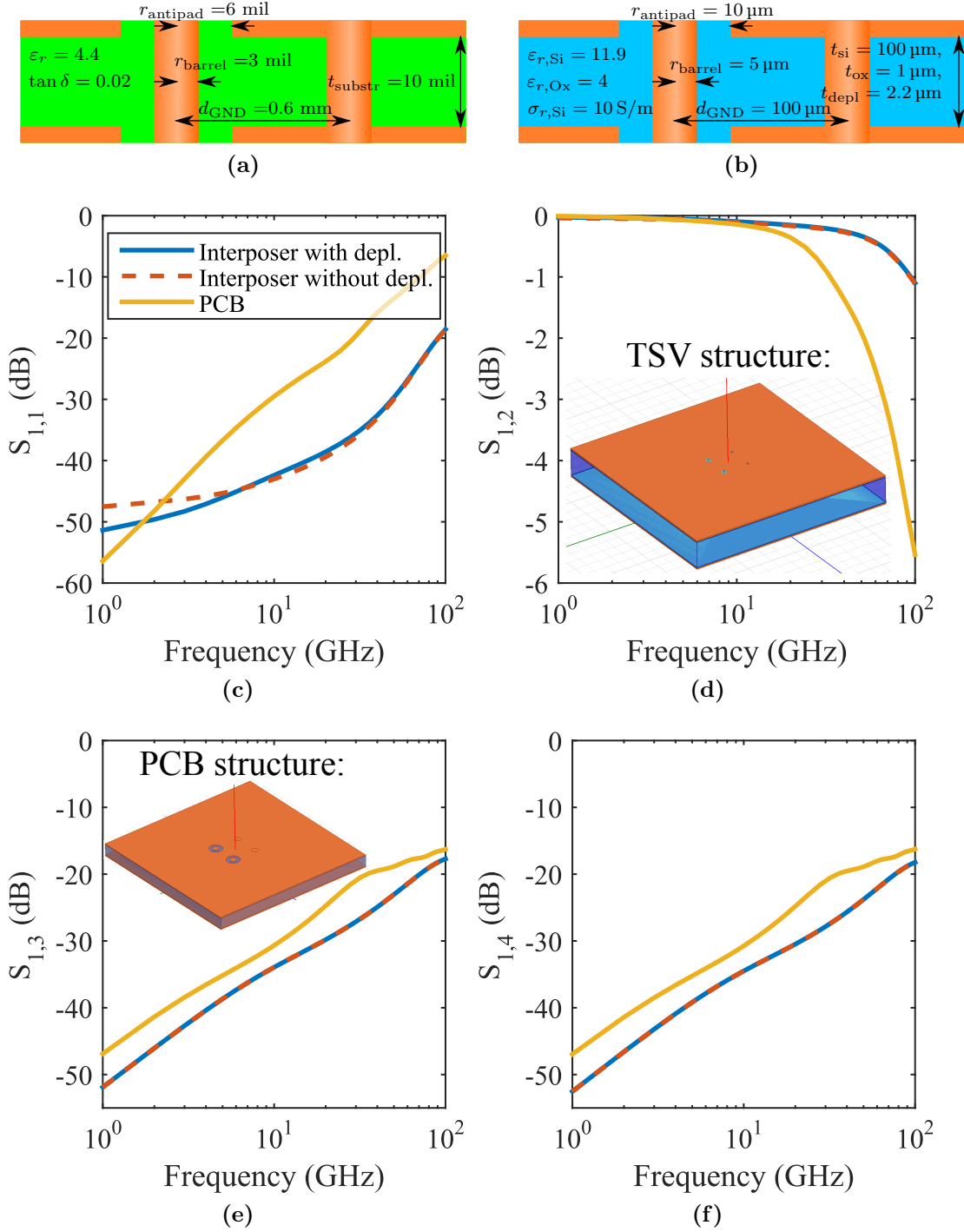


Figure 2.3: Configuration of (a) the PCB structure and (b) the interposer structure. (c)-(f) Comparison of a TSV-interposer and a printed circuit board structure in terms of magnitudes of scattering parameters normalized to 50Ω that are obtained from FEM full-wave simulations [66]. For the interposer, one variant with depletion layers and one without depletion layers is simulated.

in the slow-wave regime, the electrically insulating silicon layer represents a capacitance in series to the oxide capacitance. The overall reduced capacitance translates to a less pronounced slow-wave effect. At higher frequencies, i.e. in the quasi-TEM regime, the absence of conductivity for a small layer of the silicon can be expected to be quite small. The TSV data and cross-section are given in Fig. 2.3b and the perspective view in the inset of Fig. 2.3d. For the PCB structure, data and cross-section are given in Fig. 2.3a and the perspective view is shown in the inset of Fig. 2.3e.

The TSV structure and the PCB structure can be observed to exhibit the same qualitative behavior: A high transmission which decreases slowly up to several Gigahertz which then decreases faster and a transmission which is dominated by a linear behavior in the log-log scaling. The quantitative behavior however is different in that this significant drop in transmission occurs for higher frequencies for the Interposer than for the PCB structure. Both structures show an increase in near end crosstalk (NEXT) and far end crosstalk (FEXT) with frequency with only very small differences between NEXT and FEXT of any pair ports on a via. The quantitative differences are in the level which is higher for the PCB structure than for the interposer over the complete frequency range. Also, the characteristics of the slight changes of slope in these log-log plots are different for the structures. Significant influences of the depletion layer cannot be observed. Visible differences in the used representation can only be observed for the reflection in the lower Gigahertz range.

2.6 Modeling of Coaxial Through Silicon Vias

Another type of TSV that can be of interest due to the benefit of very low coupling of channels is the coaxial through silicon via. A cylindrical via barrel of circular cross-section constitutes the inner conductor. It is inside a hollow cylinder of annular cross-section that is the outer conductor. If the inner and outer conductor are exactly concentric, the overall magnetic fields due to the currents in both conductors are zero outside each coaxial structure. Even if they are not perfectly concentric, negligible field coupling can be achieved with a neighboring coaxial TSV if the outer conductor is highly conductive. Depending on the considered filling material, the properties can be very simple for homogeneous fillings or more complicated as in the case of layered dielectric. If the layering consists of silicon and silicon dioxide layers, slow-wave effects can be observed. Coaxial TSVs have been considered in several publications [37, 67–72] and a patent [73]. A discussion of the exact analytical computation of the wave number of the fundamental mode along a coaxial TSV with inhomogeneous, radially layered filling consisting of oxide and silicon dioxide layers is presented in [10] and Appendix C.1.1.

2.7 Summary and Outlook

In this chapter, the relevant properties of TSVs with respect to geometry and material have been discussed. It has been described which physical effects occur due to the structure and the typical modes of operation. Several modeling techniques have been classified. In the following chapters, the physics-based modeling and its adaptation to the modeling of TSVs is discussed in greater detail. To provide an orientation for the methods discussed in the following chapters of this thesis, an outlook is given in Fig. 2.4.

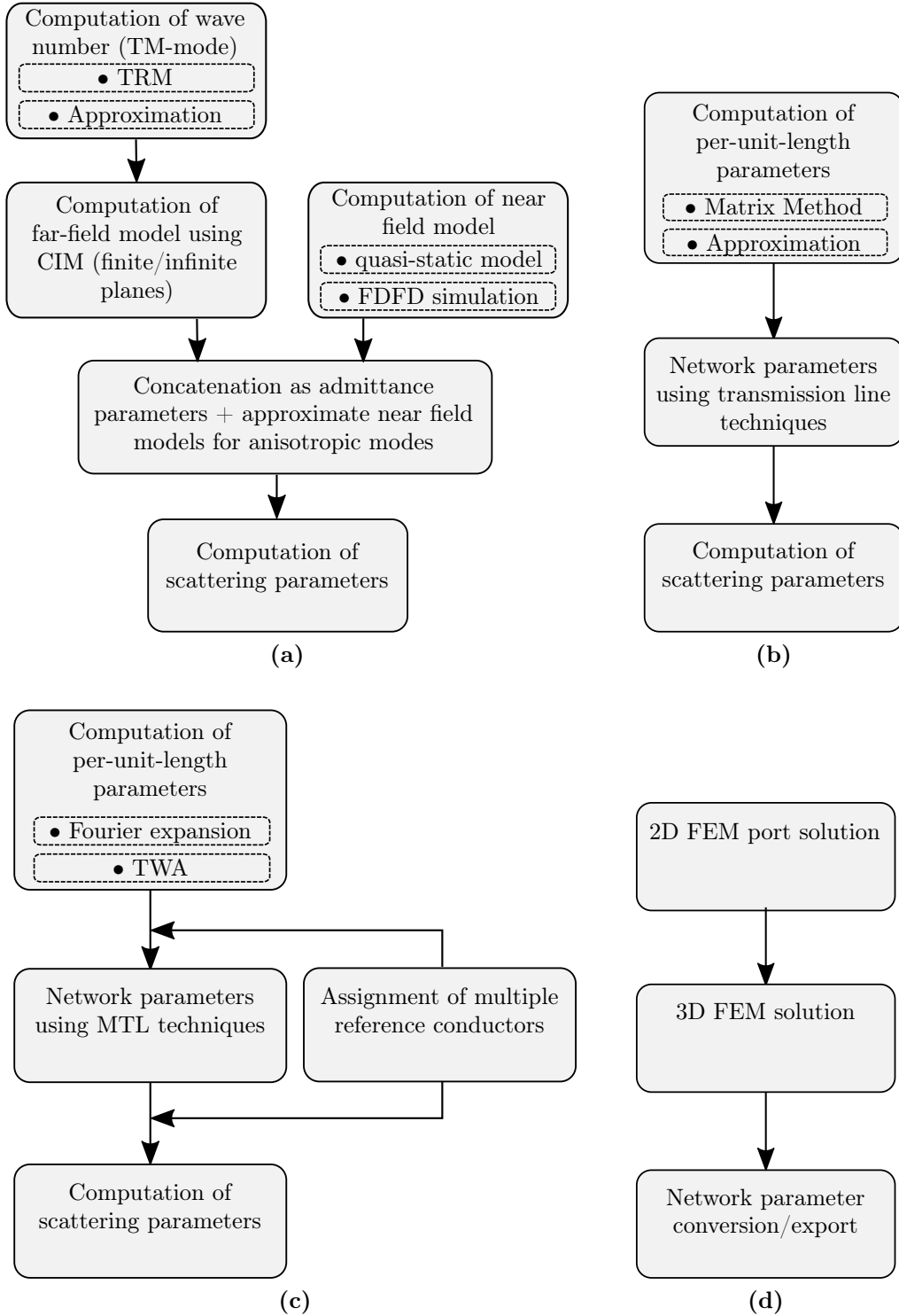


Figure 2.4: Outlook on the modeling approaches used throughout this thesis: (a) physics-based via (PBV) modeling (b) coaxial via modeling (c) multi-conductor transmission line (MTL) modeling (d) FEM full-wave simulations.

Chapter 3

Physics-Based Modeling of TSVs

The physics-based via (PBV) modeling can be motivated by the observation that, for the electromagnetic behavior of vias in cavities constituted by parallel metallic planes, dominant physical effects can be determined. The PBV model was originally developed for the efficient simulation and phenomenological analysis of vias in printed circuit boards [58, 60, 63]. As discussed in the previous chapter, the identification of the dominant effects allows for a more efficient description and computation of the electromagnetic properties if adapted methods are used compared to the use of general purpose 3D numerical techniques. Depending on the specific building blocks of the physics-based modeling various degrees of numerical efficiency and accuracy can be achieved.

The PBV model has been developed for a frequency domain characterization by network parameters. In the following, admittance parameters are mostly used. As will be discussed later, they allow for an efficient concatenation of near and far field models if the simplified near field model is used. By using network parameters, the complex electromagnetic properties are reduced to the integral parameters of modal currents and voltages defined at the ports. For many practical applications, these parameters provide sufficient information for the investigations of structures in which the via is only one of several building blocks, e.g., via arrays and signal links constituted by multiple vias of different levels and other connecting components in series.

This chapter gives an introduction to the PBV modeling in the following order: First, the structures for which it is applicable and the observations regarding the dominant effects of electromagnetic (EM) signal propagation are detailed. Then, using a description in terms of waveguide modes, a general model of a junction with coaxial and radial ports defined for a via is considered. It is used to derive a simplified junction model which is in the following applied as a near field model. The overall system behavior that is given by a concatenation of near field models with propagating field models is first described in a general way, subsequently for the case of a homogeneous substrate, and finally for a layered substrate.

Several options that are relevant for the determination of the near field models and the far field models for both the homogeneous substrate and the layered substrate are outlined. The detailed analysis for the layered structures that are relevant for the TSV modeling are then given in the following chapters.

3.1 Boundary Conditions for Applicability of PBV Modeling

Fig. 3.1 shows three important cases of via modeling. For each case, a perspective view and a cross-sectional view are given with illustrations of the surface currents on metal components and the electric field inside the dielectric layers. Both are related to a signal propagation from a port at the top side of the structure to a port at the bottom of the structure with a small reflection of the signal, the latter only in case of AC-signals.

Figs. 3.1a and 3.1b illustrate the DC case for a structure with top and bottom metallizations of the dielectric which is homogeneous. The current return part is established through a so-called ground via which short circuits the top and bottom metallizations at some distance from the signal via. The currents on both vias distribute themselves uniformly around the circumferences. The field lines of current flow on the top and bottom metallizations are distributed analog to the electric field lines of two parallel circular wires with opposite charge.

For the same structure, Figs. 3.1c and 3.1d illustrate the behavior for excitations with alternating currents. A signal applied to the coaxial top port leads to the excitation of radial waves inside the cavity that is constituted by the top and bottom metallizations. This can be interpreted as a mode conversion between coaxial and radial modes. The return current is established partially as a displacement current between the top and bottom metallizations and partially by conduction currents along the ground via barrels. The physics of wave propagation inside the parallel plate cavity can be interpreted as a superposition of radial waves with reflections from cavity edges and other vias. In the illustrated example, the reflection causes a radial wave front that originates from the single ground via.

The structure depicted in Figs. 3.1e and 3.1f is different from the structure considered before in that no plane metallizations are present. Depending on the length of the vias and the type of excitation, different field patterns are possible but only the fundamental mode of this structure of parallel conductors is considered here. While, in the case of substrate metallizations, the wave propagation that is related to the current return path is orthogonal

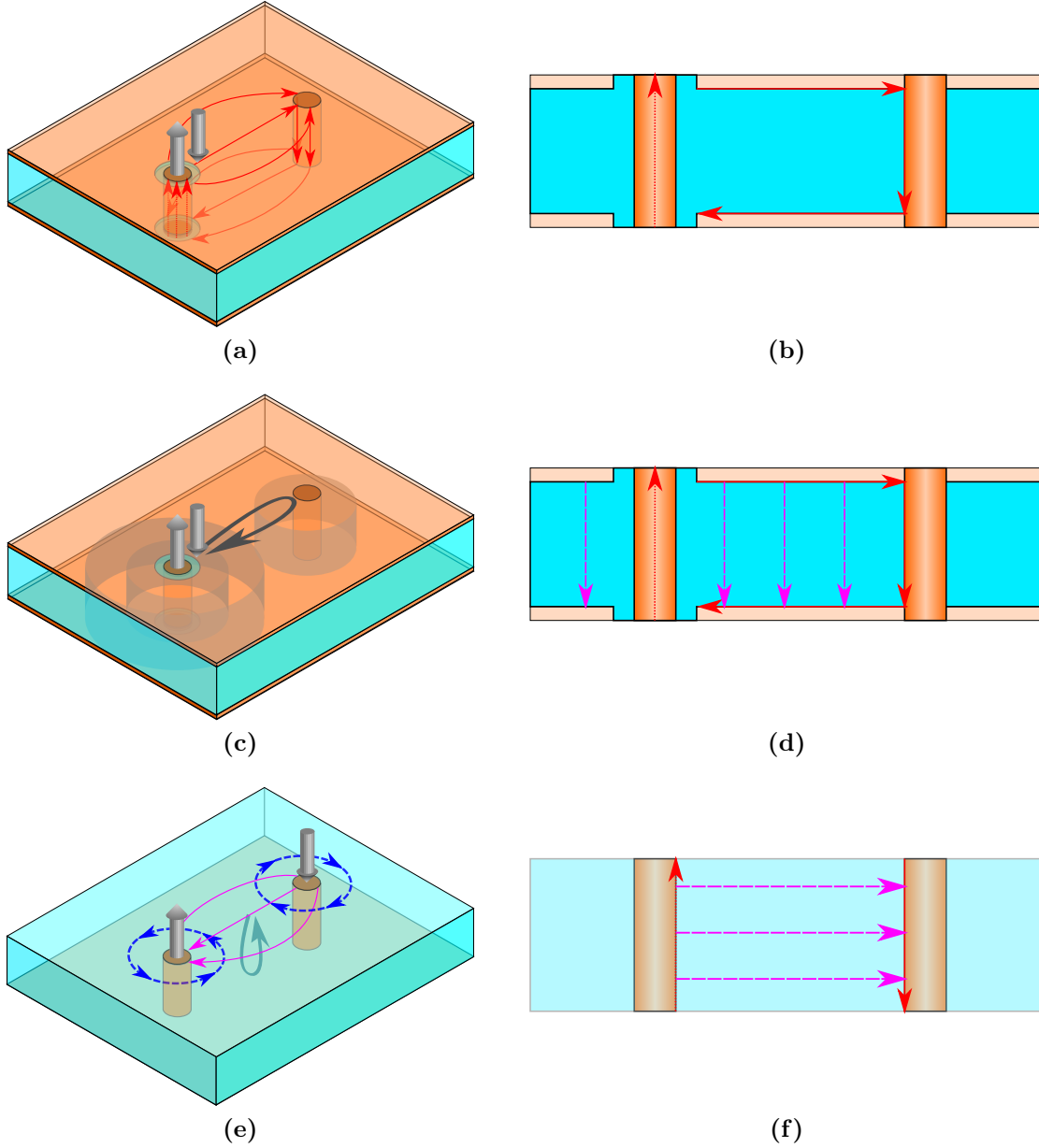


Figure 3.1: Illustration of three important cases of via modeling with currents entering and exiting the excited ports shown in light gray. Conduction currents are illustrated with red arrows, magnetic fields with blue arrows, and displacement currents with purple arrows. Directions of signal propagation including reflection are indicated with arrows in dark gray. (a,b) As only conduction current flows in the DC case shown here, the total current flows each of the planes and on the ground via barrel that connects the two metallic planes. (c,d) Wave propagation inside a parallel plate environment for a high-frequency signal: The far-field interaction is dominated by radially propagating parallel plate modes. Parts of the wave fronts of an isotropic fundamental mode emanating from the leftmost via are illustrated between the parallel plates. (e,f) Signal propagation in case of the absence of plane metallizations: The structure can be modeled as a multi-conductor transmission line problem.

to the via axes, the signal and wave propagation is only parallel to the via axes in this case.

From comparison of the electric fields it can be seen that these two structures exhibit signal propagation-, reflection- and scattering- physics which have fundamental differences. Both types of structures are considered for the AC case in this thesis, the first one with the PBV model in this and the following chapters, and the second one with a multi-conductor transmission line model in Section 7.1.

3.2 Decomposition into Near and Far Fields for PBV Modeling

The signal path along which an electromagnetic wave is guided in the structure of Fig. 3.1c includes several discontinuities to the wave. These discontinuities lead to partial reflections. The vertical path starts at the plane at the top end of the barrel with a short coaxial section and it ends at the plane at the bottom end of the barrel with a short coaxial section. The following intermediate section of the barrel can be described as an oxide-coated conductor inside the silicon region. The vertical propagation along the barrel is related to a horizontal wave propagation along the planes inside the parallel plate structure. The parallel plate structure is also referred to as a cavity.

Figure 3.2 illustrates the physics of signal and wave propagation inside a metal-clad planar circuit in terms of electric field lines. The total field can be decomposed into a near field and a far field which enables, by the identification of symmetries and the use of adapted methods of reduced dimensionality, a more efficient description. Close to each via, there is a superposition of the near field which consists of the localized field parts related to the discontinuity and the far field which relates to the propagating field parts. Under certain conditions, roughly speaking sufficient distances, coupling between vias only occurs due to the far field. Then, the near field can be treated independently for each via. For the near field, the description is often sufficient which assumes azimuthally symmetric fields. In such cases the number of spatial dimensions to consider in a numerical computation is reduced to two. For the far field, it can be observed that the field is independent of the transverse z -coordinate for the homogeneously filled cavity. The effective number of spatial dimensions of the problem then also reduces to two. The reduction of the effective number of spatial dimension leads in general to an improved numerical efficiency of simulations. It can therefore be seen how, by decomposing the overall electromagnetic field into near and far field parts, the identification of dominant physical effects and symmetries leads to an efficient modeling.

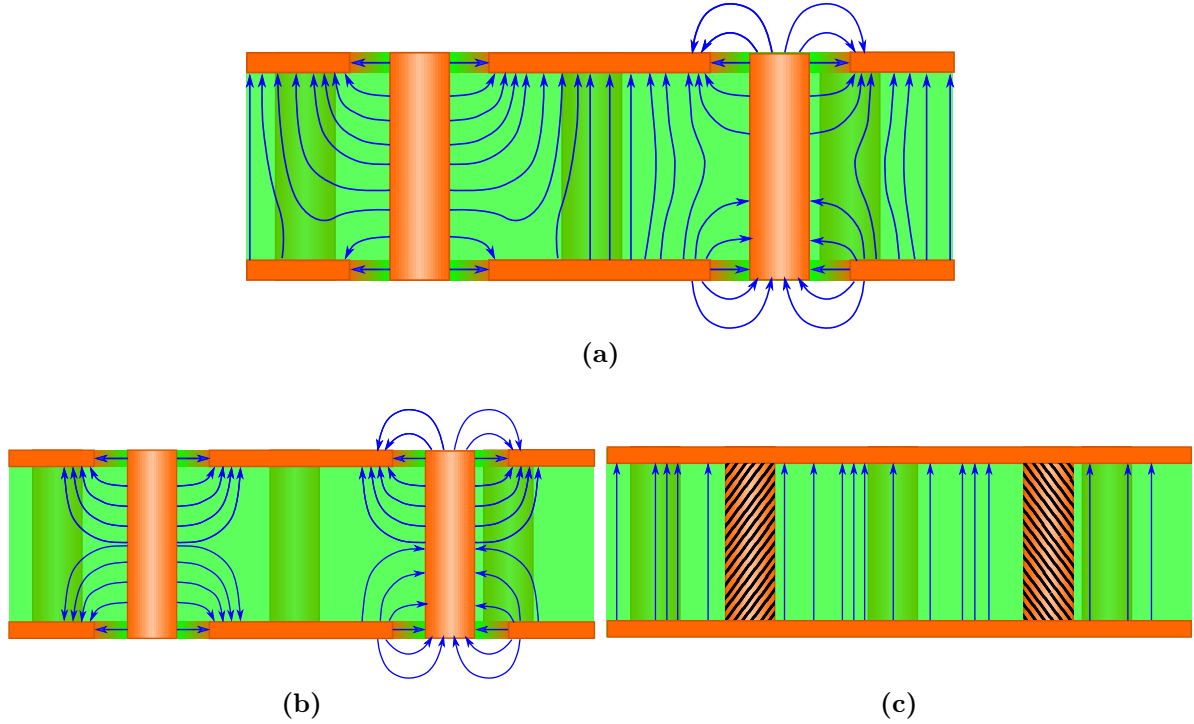


Figure 3.2: (a) Illustration of the overall electric field with excitation at the left top port. It can be decomposed into (b) localized fields and (c) propagating fields. Fields in the coaxial regions and fringing fields at open circuited coaxial ports are also shown. Under certain simplifying conditions, the near fields are similar to electrostatic fields and can be modeled using static capacitances. The far field interaction can be considered as a 2D problem for which the ports are defined at the lateral surfaces of the via barrels. These ports are marked by hatched areas.

The far field propagation and the reflections from the chip edges, other discontinuities, and other vias are represented by the parallel plate impedance. The parallel plate impedance extends the description of a microwave device with a single port for which to describe magnitude and phase of the reflected signal to multiple ports on a microwave device: Measurements of the ratio of modal voltage and current at the single port of a single pair of metal planes will reveal frequency dependent behavior with resonance effects at specific frequencies. Correspondingly for multiple ports of the same device, voltage to current ratios with equal or differing index of voltage and current can be defined which entail the same information as, e.g., the scattering parameters of a corresponding measurement.

In the following, results for the regions are computed independently. Even though near and far field regions are in general overlapping with respect to the space in which the corresponding fields are physically located, ports can be defined at which the field models are connected. On these ports, one or several modes can be defined and the near and far

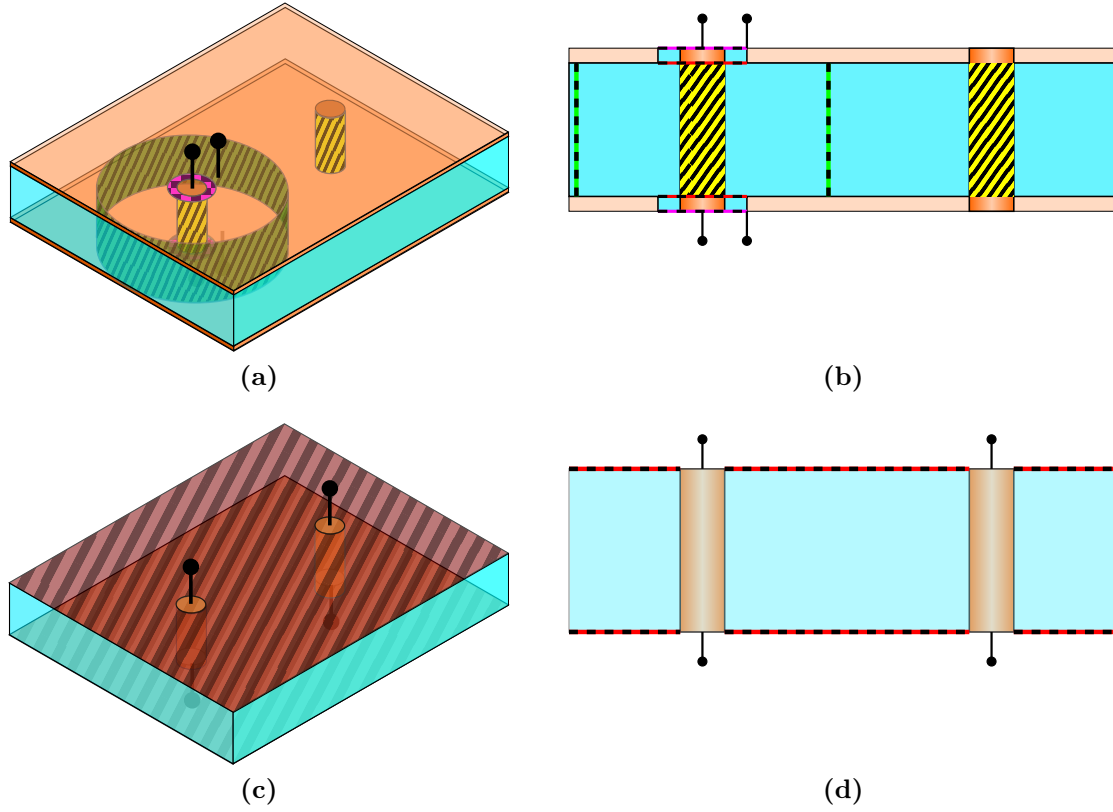


Figure 3.3: Illustration of the ports of the modeling approaches. The corresponding terminals are marked with black lines and circles. (a,b) Ports of the physics-based modeling with outer coaxial ports and several inner ports. The ports are marked with patterned areas and dashed lines in the perspective view and in the side view. The outer ports can be used for concatenation of models for adjacent structures, the inner ports are used for the concatenation of the model building blocks. (c,d) The multi-conductor uses only outer ports. The multi-conductor ports are marked with hatched areas in the perspective view and with dashed line in the side view.

field region results are obtained as the concatenation in terms of the network parameters for these modes. Due to the overlapping of near and far field regions, a de-embedding step is required in some cases.

3.3 Port Definitions

The port and terminal definitions for the case with metallizations (PBV modeling) and the case without metallizations (MTL modeling) are illustrated in Fig. 3.3.

For the PBV modeling, the ports are illustrated in Figs. 3.3a and 3.3b. The outer coaxial ports are defined at the coaxial clearances (antipads) at the outermost plane of each metallic plate (purple dashed line). An inner coaxial port can be defined at the respective inner plane of each metallization (red dashed line). Inner radial ports are defined at different positions within the cavity. As illustrated, they are defined concentrically to the TSVs and either on the lateral barrel surface of the cylindrical barrel (marked in yellow) or with a larger radius, i.e. at some distance from the TSV (marked in green).

For the MTL model, several terminals that are assigned to the conductors on one side of the substrate share a port area, as illustrated in Figs. 3.3c and 3.3d. In the idealized models, each multi-conductor port extends over an infinite area. In contrast, in reality and in many numerical methods, the port area is finite which results in no significant differences as long as it is large compared to the distances between the TSVs.

3.4 Composition of Model Parts

The way in which the corresponding model parts of a PBV model structure as the one depicted in Fig. 3.4a can be composed or decomposed is illustrated in Figs. 3.4b and 3.4c. As depicted in Fig. 3.4b, the near field models that relate to the via junctions have two coaxial ports and one radial port. The near field models are connected to models for the coaxial sections through coaxial ports with several modes defined each. They are also connected to the far field model through a radial port with several modes defined on it. Every mode on a port is illustrated here as a port within this port, i.e., one modal port is illustrated with its two terminals. Each terminal is visualized by a straight line and a circle. The modes on one port are drawn in this figure behind each other foster the understanding that they belong to the same port and hence are defined for the same physical location.

The far field model is also labeled as parallel plate impedance Z_{pp} . Even though other types of network parameter descriptions of the EM properties of planar structures are in general equally suited for the description¹, the impedance type description is the most common one in discussions of these structures. For a single port, this impedance describes the effective

¹E.g., the admittance proves to be advantageous for the low-frequency model, see Section 3.7

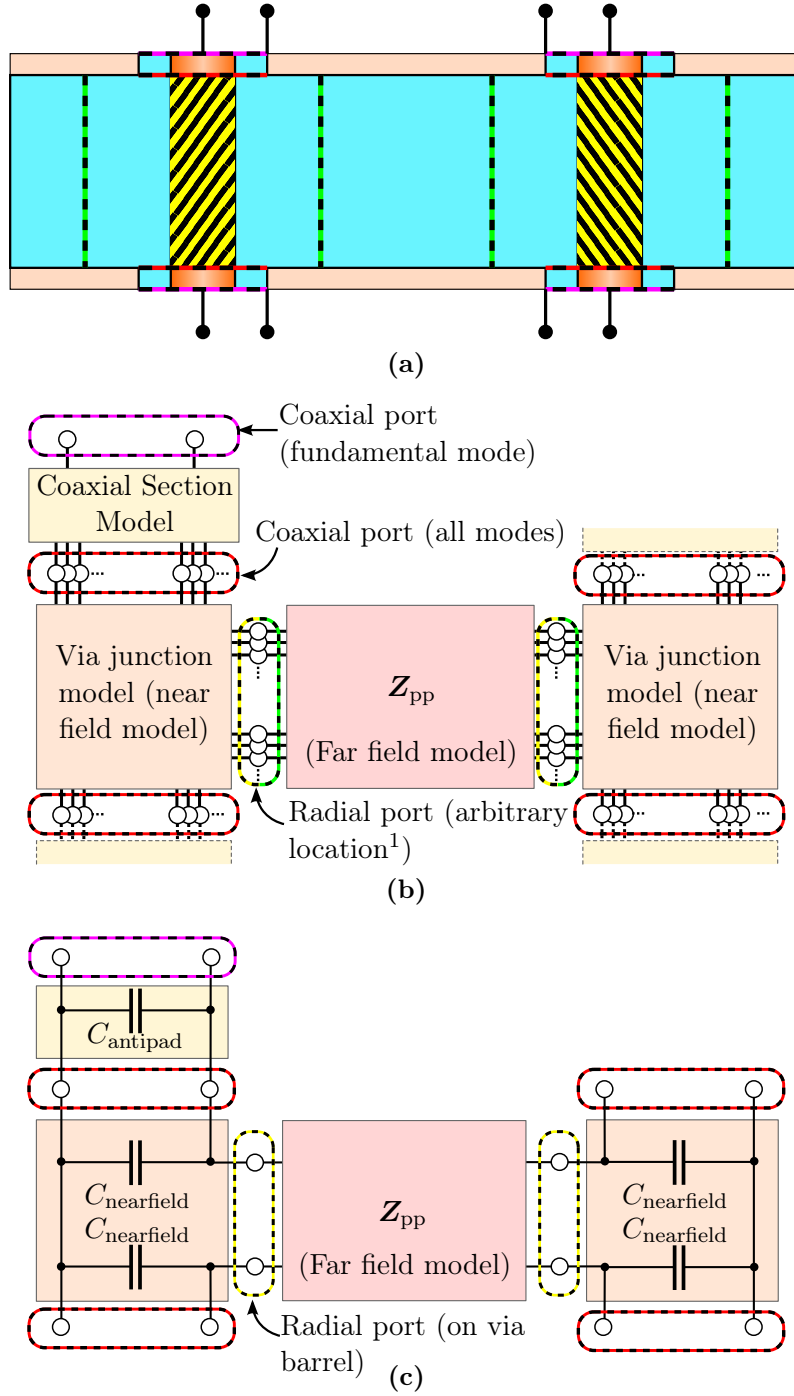


Figure 3.4: Network representations of the PBV Model. (a) Illustration of the corresponding cross-section. (b) General model for a pair of signal vias. In general, all modes on the respective port have to be included. (c) Simplified model that is applicable for cases without losses and homogeneous filling at relatively low frequencies.

¹The arbitrary location must have the same axis as the via barrel for a simple de-embedding.

impedance measured at the radial port due to signal propagation and reflection within the cavity. For several ports, it describes also the transfer impedances between different ports. In many practical situations, only one mode is required on each radial port of the parallel plate impedance. This is illustrated in Fig. 3.4c. As will be discussed later in more detail, at relatively low frequencies, the anisotropic modes on radial ports that account for the azimuthal anisotropy, i.e. non-uniformity, of the fields along the ports can be neglected.

The near field model describes the properties of the junction with corresponding electromagnetic fields and can be relatively complicated for the most general cases. An efficient simulation of these case is therefore difficult. In most practical situations however, the dominant properties can be described with limited effort. The near field can, e.g., be approximated as being azimuthally symmetric. At relatively low frequencies and for cavities filled with a homogeneous, low-loss dielectric, the near field can be described with good accuracy by capacitances between the via barrel and each of the parallel plates. Therefore, it is modeled by admittances parallel to the coaxial ports in a topology depicted in Fig. 3.4c.

3.5 Near Field Modeling

In this section, the applicable simplifications are derived and an overview of the most relevant model options is given.

3.5.1 Discussion of Applicable Simplifications

In the following it is discussed how the general description of the junction with two coaxial ports and one radial port constituted by the via and its parallel plate environment can be simplified. The most general model regarding the network parameter block and the considered modal ports is depicted in Fig. 3.5a. On both coaxial ports (one at the top and one at the bottom) several modes are in general required to fully describe the fields present close to and at the port surfaces. By definition, all modes of a port are orthogonal meaning that each corresponds to a solution with a distinct eigenvalue of the corresponding eigenvalue problem. In terms of the fields which relate to the eigen-vectors, no modal field can be represented by linear combinations of other modal fields.

As a first step, it can be made use of the property that not every mode can couple with any other mode if the structure itself is azimuthally symmetric. In the symmetric case only modes with the same azimuthal variation can couple. Therefore, the junction model is split into models for each type of orthogonal azimuthal variation and the coaxial ports for each

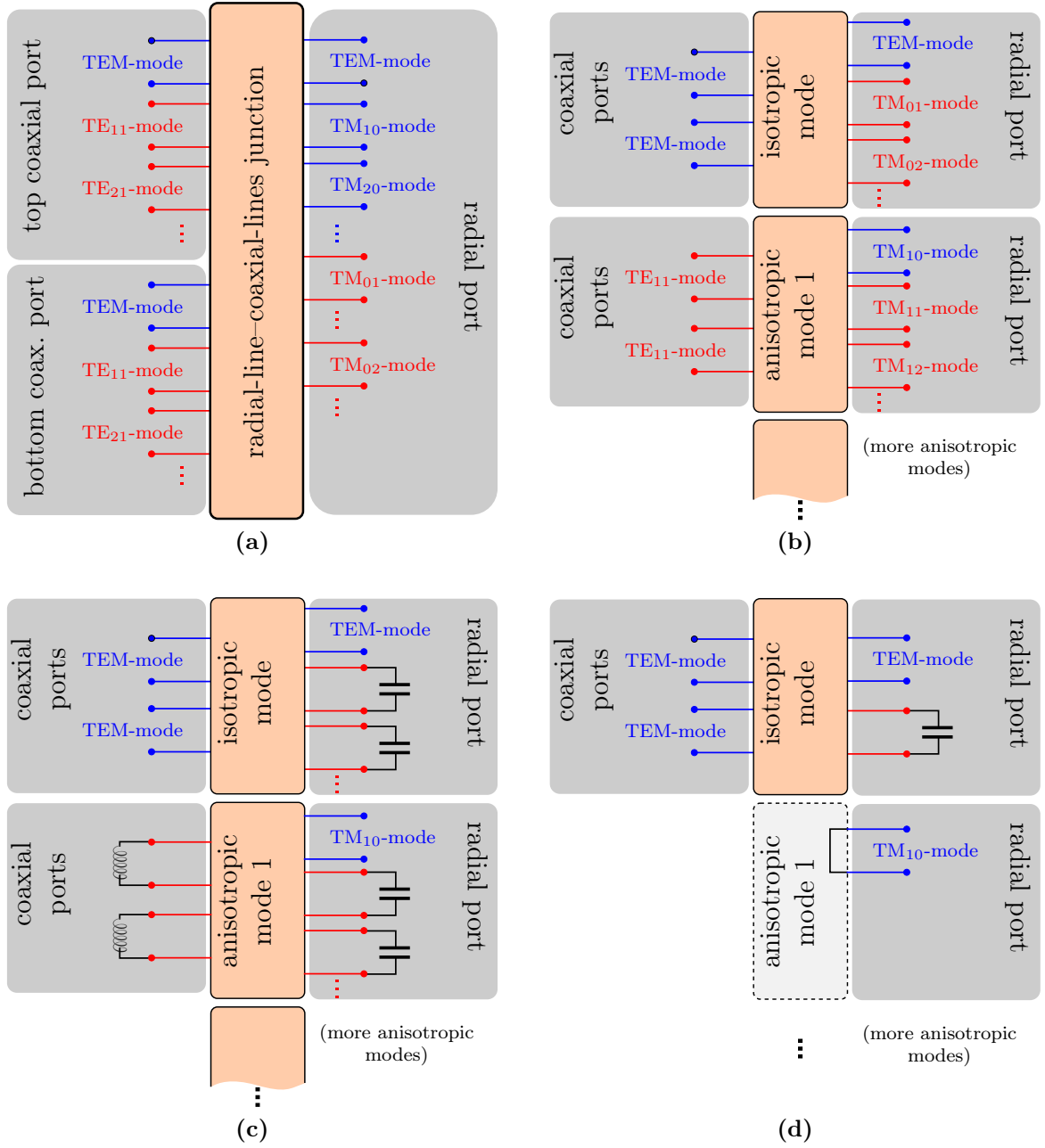


Figure 3.5: Derivation of a physics-based near field model for vias (a) Most general description of the coaxial line–radial line junction with ordering by physical ports and marking of modes as either **propagating** (with blue color) or **non-propagating** (in red color) for the typical configurations considered throughout this work. (b) As before but with ordering according to the azimuthal anisotropy. (c) As before but with port for non-propagation modes terminated with appropriate impedances. (d) As before but with neglected anisotropic modes on coaxial ports and approximation of the mode termination for the anisotropic modes on radial ports for frequencies well below the cutoff of the higher order modes on the coaxial ports.

variation are grouped. The types of azimuthal variation are isotropy, i.e. uniformity with no angular variation, or sinusoidal variations with different periodicities which correspond to anisotropic modes of different order. It can further be taken into account as a relevant simplification that modes on the coaxial ports with field nodes along the radial direction (such as the TM_{01} -mode [74, Fig. 2.8]) can be neglected because these are well below cutoff. Both these simplifications are summarized in Fig. 3.5b.

Next, the remaining modes which are below cutoff, but not as far below cutoff as the previously mentioned ones, should be suitably terminated. Each termination must represent the type of field in which the reactive energy is stored in this part of the localized field. The relevant cutoff modes on the coaxial ports are TE-modes which, below cutoff, store the reactive energy in the magnetic field [75, Sec. V.B]. The impedance seen by the junction connected to the coaxial line section is therefore of inductive type and an inductance is, in general, used to model the appropriate termination. For the radial port, the relevant modes are TM-modes. Below cutoff there is an electric reactive field storage that can be modeled by a capacitance. These discussed terminations are used in Fig. 3.5c.

Finally, the following further simplifications are used: For the isotropic mode, all capacitances of the localized fields are combined to one. For the anisotropic modes, no model for the junction is available in the theory used for this thesis. It is anticipated that the model should be similar to the one for the isotropic modes. Because the inductive termination at the coaxial port can be approximated as short-circuits well below the cutoff of the corresponding modes, the near field model is approximated by a short-circuit of the corresponding radial port. It can be seen that the capacitances on the radial ports are thereby also short-circuited in this approximation.

3.5.2 Near Field Modeling Approaches

In the following, several near field modeling approaches for waveguides filled with a homogeneous medium are presented and an outlook on possible adaptations for modeling of more general cases is given. The near field domain is illustrated again in Fig. 3.6a.

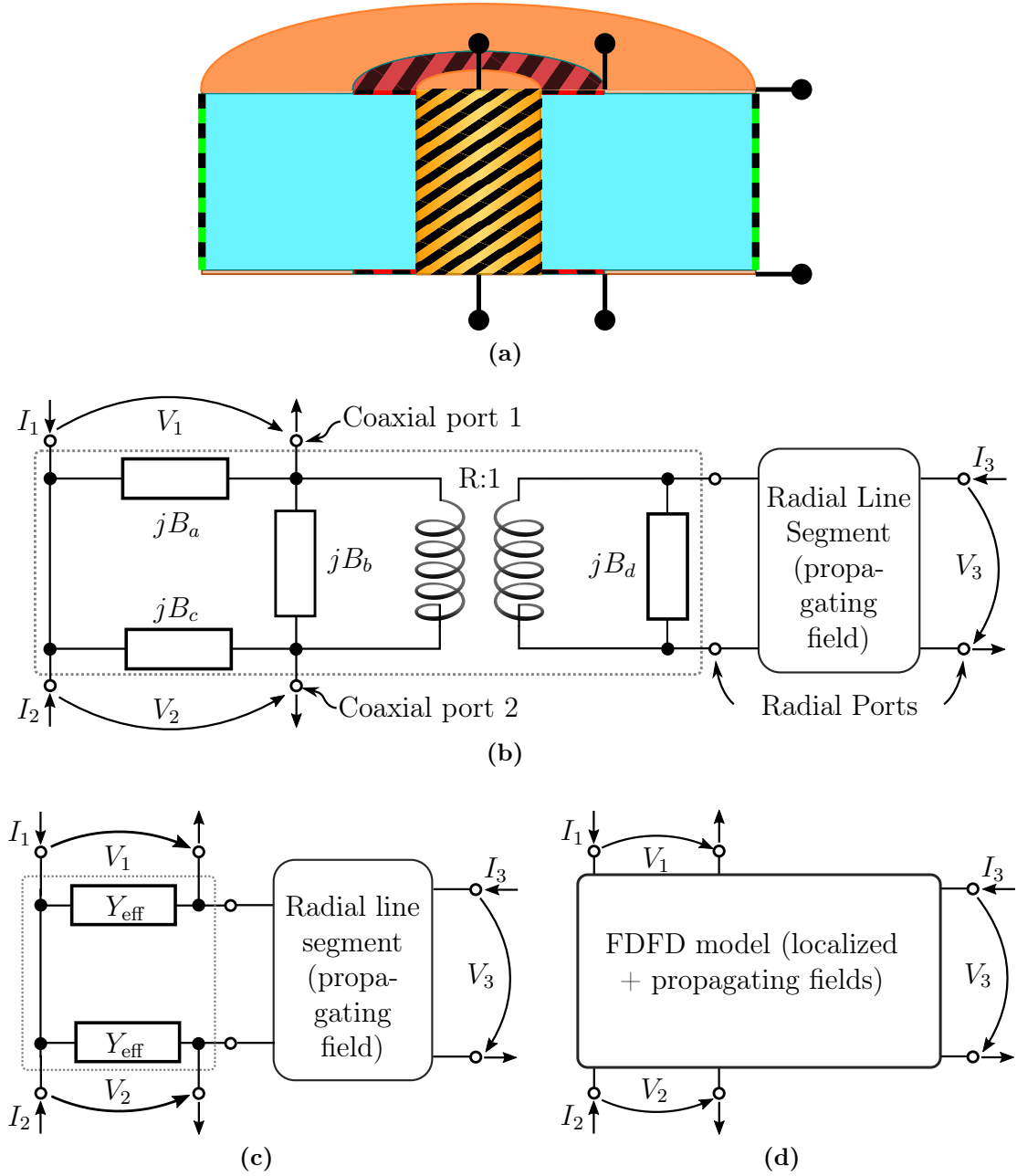


Figure 3.6: (a) Illustration of the physical near field domain. (b) Equivalent element representation of a model for the approximate analytical description of the coaxial to radial line junction by Williamson [76] inside the area marked with the dotted line. Drawing for the case with two coaxial ports adapted from [76]. (c) Equivalent circuit applied in the second, mostly analytical model as described in last paragraph of Section 5.3.2. The near field is modeled by Y_{eff} parallel to each coaxial port. (d) Corresponding representation of the FDFD model. Figures and text adapted from [13].

Relevant Modeling Approaches for Homogeneous Fillings

The first type of near field model uses a quasi-static modeling. For comparatively low frequencies, the field parts in the junction that are in general identified as cut-off modes are in this case identified as the (static) capacitances between the via barrel and the reference planes. The static definition results in a frequency independent value for all cases where it represents a sufficient approximation. For this approximation, the static capacitance definitions require the barrel and the reference planes to have each a uniform potential. This type of approximation has been studied for PCB vias with various techniques [77–83].

The second type of near field model takes into account the wave properties. The models neglect fields with azimuthal variations but include the effects of reactive field of the cutoff modes and an impedance transformation at the junction. The model of this type that is considered in the following is the model first proposed in this form by Williamson [76,84,85]. An equivalent circuit is depicted in Fig. 3.6b. The admittances jB_a , jB_b , jB_c , and jB_d model parts of the capacitive near field, while the transformer models the impedance transformation between radial port and coaxial ports. For many practical applications in PCBs, it has been found that several simplifications are possible, e.g., the transformer ratio is relatively close to 1. A related near field model is known as the intrinsic via model and has been discussed in [63,86]

3.5.3 Outlook on Adaptations for Layered Fillings

For the case with layered fillings, the detailed discussion of all adaptations is given in Chapter 5. A short outlook is given in the following.

The first type of model assumes that an admittance parallel to each port provides a near field model for the quasi-static case. In the model depicted in Fig. 3.6c, the admittances Y_{eff} represent effective values of via barrel to plate conductance and capacitance. Due to the frequency-dependent complex permittivity of the silicon $\underline{\varepsilon} = \varepsilon_0 \varepsilon_r - j\sigma_{\text{si}}/\omega$, the values are not constant with frequency as is the case for a medium without conductivity. A relatively simple approximation based on static field computations is presented in Section 5.3.2. More accurate results could be obtained by adapting a contour integral method for quasi-static capacitance calculation as in [16,87]. This has not been done but instead development of the full-wave approach has been pursued.

The full-wave approach used in this work performs a local full-wave modeling of the area around a via barrel using a finite-difference frequency domain (FDFD) method in cylinder coordinates. This is the main subject of Chapter 5. As labeled in Fig. 3.6d, this local full-

wave model gives results for both the localized near field and the propagating far field in a modeled region around the via barrel. In order to enable the comparison of all near field modeling approaches, one option is to add radial line segments to the modeling approaches which model only the localized field as is depicted in Figs. 3.6b and 3.6c.

3.6 Far-Field Modeling

As already discussed, the far field model considers a 2D problem of wave propagation in the cavity. Either through the concatenation of the near field models or directly, it also describes the scattering, i.e. the overall field, due to incident fields from every signal via and reflected fields from all vias (signal vias and ground vias) and other terminated ports such as the plane contours. The “direct” description of scattering refers to the property that the reflection at ground vias and plane contours can typically be simplified to simple boundary conditions of the planar problem and therefore mostly have simpler near field models. Some important modeling approaches that are mostly applied for homogeneously filled cavities are discussed in the following. Adaptation to the inhomogeneously filled cavity are outlined in the following and presented in detail in Chapter 4.

3.6.1 Radial Waveguide Method

In the radial waveguide method, the radial wave propagation is considered without reflections from scatterers such as ground vias and plane edges, see [88, 89]. The formulation considers a finite size of the radial port for which a field is evaluated but neglects the size of the source port [61, Sec. 4.3.2]. Using image theory the case of finite planes with open boundary condition can also be computed [88].

3.6.2 Cavity Resonator Method

The cavity resonator method is applicable to planar circuits with simple shapes and includes the reflection from either open-circuited boundaries [90], [91, Sec. 2.4.1]. The original formulation defines rectangular ports but adaptations to circular ports are also available [92, Sec. III], [56, Appendix B]. The accuracy of the method can be controlled by the number of modes that are used. The method can be implemented relatively easily and provides a good accuracy if a large enough number of modes is ensured by observing the

convergence behavior. The cavity resonator method has proven itself to be a good reference for the validation of techniques for arbitrarily shaped contours such as the contour integral method discussed in the following.

3.6.3 Contour Integral Method for Planar Circuits

The method of choice for this thesis is the contour integral method (CIM) for planar circuits because it provides a good trade-off between the generality of its application and the achievable numerical efficiency. This numerical technique includes both the scattering from arbitrarily shaped contours with arbitrary terminations and finite port sizes of both source and observation ports. The CIM is a frequency-domain method for microwave and optical frequencies for the computation of the N -port network parameters and field information of planar circuits [91, 93]. Circuits are considered planar if only two spatial dimensions are larger than the guided wavelength in these structures while the third dimension, which is referred to as the height, is significantly shorter. This leads to the assumption for homogeneous fillings that the transverse field components are constant across the height. Thus, the electromagnetic fields propagating in this structure can be described by a 2D Helmholtz equation.

The method has numerous possible applications and extensions. The typical general field is the application for signal and power integrity analysis. Coupling of the method with descriptions for connected devices (e.g. decoupling capacitors) is possible and can be used for the optimal placement of decoupling capacitors for reduction of simultaneous switching noise [93]. The method can further be used to investigate the resonant frequencies of planar circuits [91]. Also, as an advanced application, the numerical efficiency allows application in optimal circuit pattern synthesis [91, Ch. 7].

Because the CIM is a frequency domain method, the properties of the circuit at discrete frequencies are determined. Continuous wave problems where the structure is excited with a time-harmonic signal can directly be investigated. Therefore, time domain analysis can in general only be performed after Fourier transformation of the frequency domain information. Nonlinearities in form of the dependence of the electromagnetic properties on the amplitudes of the fields are not included. This would need to be considered in the most general case of modeling of the silicon properties but is not further considered here.

A single computational domain of the CIM consists of a planar structure of which the stackup is invariant with respect to the directions which span the plane. In the most simple case, a planar stackup consists of only a dielectric of a certain thickness and real permittivity which is bounded by perfect electric conductor (PEC) layers. Thus no dielec-

tric losses and conductivity are considered for the dielectric and no losses through limited conductivity of the conducting layers. The fundamental mode which can propagate in this parallel plate structure is TEM.

For the application with realistic structures, such as silicon interposers, PCBs, and package substrates, a finite conductivity of the bounding metal layers and dielectric and conductive losses in the dielectrics need to be considered. As is discussed further in the following chapter, the fundamental mode which can propagate in these structures is not a true TEM mode because the electric field does not vanish at the interfaces of bounding layers and dielectric layers and also has a component in propagation direction. If these effects are relatively small, this component in propagation direction is still small and the mode is qualified as “quasi-TEM”. In contrast to the parallel plate structure with homogeneous filling, even the fundamental mode of the layered lossless structure has longitudinal field components. In the presented work it is aimed at extending the CIM to the treatment of structures with a larger variety of stackups with a focus on those found in TSV structures.

The “classical” CIM considers piecewise linear contours which are segmented into linear ports. This is illustrated in Fig. D.1a of Appendix D. The planar circuit is treated as an N -port where N is the number of segments: the ports at the outer contour are typically considered to be open circuited which corresponds to a perfect magnetic conductor (PMC) boundary condition of the corresponding electromagnetic problem and models the typically small radiation resistance. The CIM interrelates the electric and magnetic fields, i.e., their tangential components, of all boundary ports. By assuming the fields to be constant on each port, the fields can be replaced with modal currents and voltages which are defined as integral quantities of the fields. Self impedance is defined as the ratio of voltage and current at one port and transfer impedances for voltages and currents at different ports.

The extended CIM is based on both line ports from which waves emanate that are decomposed and approximated by one or more isotropic radial waves and circular ports on which both isotropic modes with azimuthal symmetry and anisotropic modes with azimuthally varying fields are defined:

- The fundamental isotropic mode features constant fields along the port perimeter. This mode is dominant in many practical applications and its sole consideration is justified in many cases where ports are sufficiently distant from each other. The sufficient distance depends on the geometrical and material properties.
- The higher-order anisotropic modes feature an azimuthal variation, i.e. a functional dependence on angle, of the fields on the circular port. Their application is significant for cases of closely spaced vias or vias close the plane edges. They can also be relevant due to specific excitations of the fields at the ports, e.g., the excitation of a via by

a micro-strip line [94]. Very closely spaced ground vias can lead to a significant alteration of the local field of a via along which a signal is guided and may invalidate the assumptions of the PBV modeling.

More details on the CIM and a collection of the most relevant formulas are given in Appendix D.

3.6.4 Outlook on Adaptations for Layered Fillings

The adaptation required for the discussed 2D methods consist in the use of an effective wave number of propagation or the radial parallel plate waveguide modes in the layered structure. This is presented in the following chapter. In the context of via modeling only the properties of TEM- and TM-modes are of interest, so only these will be discussed. For layered dielectric this leads to the requirement of the definition of an effective characteristic impedance which is discussed further in Section 4.7.3. For the proposed methods, the permeability must be constant for all parts of the structure ($\mu_r = 1$) which is the case for all considered and practical cases.

3.7 Embedding of the Physics-Based Via Model

For the embedding, two methods can be distinguished, one general technique, and one that is adapted to the case where the structure is symmetric with respect to a central plane. Based on the latter case, the near field can be represented by a lumped parallel element for relatively low frequencies.

The general technique consists in the concatenation of a three-port for the radial-line-coaxial-lines junction to every radial line port of the network parameter matrix \mathbf{Z}_{pp} for the parallel plate propagation. Assuming that the ports which correspond to ground vias are already terminated in terms of the network parameters for the planar circuit, the number of ports is thereby doubled as a top and a bottom port is assigned to every via. The general concatenation procedure for this case is described in Appendix G.

The adapted method for the low-frequency case consists in the construction of an expanded admittance matrix from the parallel plate admittance or impedance matrix. This expansion reflects the property that the coaxial ports are in series and due to the symmetry must, except for a sign, have the same “connection” in the thereby constructed multi-port. The difference in sign is due to the terminal voltage and current definitions with the voltages

being defined from outer to inner antipad rim (plane to via barrel) and the current entering at the outer antipad rim (plane) and exiting at the inner antipad rim (via barrel). The overall admittance matrix is then obtained by addition of the impedance $Y^{(vp)}$ of the respective lumped elements that represent the near field effects to the diagonal of the expanded (parallel plate) admittance matrix as [60,61]:

$$\mathbf{Y}^{(PBV)} = \underbrace{\begin{bmatrix} \mathbf{Y}_{pp} & -\mathbf{Y}_{pp} \\ -\mathbf{Y}_{pp} & \mathbf{Y}_{pp} \end{bmatrix}}_{\mathbf{Y}^{(pp,exp)}} + \begin{bmatrix} Y^{(vp)} & \mathbf{0} & \cdots & \mathbf{0} \\ \mathbf{0} & Y^{(vp)} & \cdots & \mathbf{0} \\ \vdots & \vdots & \ddots & \mathbf{0} \\ \mathbf{0} & \mathbf{0} & \mathbf{0} & Y^{(vp)} \end{bmatrix} = \begin{bmatrix} \mathbf{Y}_{pp} + \mathbf{1} \cdot Y^{(vp)} & -\mathbf{Y}_{pp} \\ -\mathbf{Y}_{pp} & \mathbf{Y}_{pp} + \mathbf{1} \cdot Y^{(vp)} \end{bmatrix} \quad (3.1)$$

where $\mathbf{1}$ is an identity matrix and an identical near field model for the identical vias is assumed. The port ordering of (3.1) is block-wise with the ports on one side of the cavity (e.g., on the top side) followed by the ports for the same vias on the other side of the cavity (e.g., on the bottom side). It should be noted that the near field model contained in $Y^{(vp)}$ only influences the diagonal elements of the admittance matrix which relate modal current and voltage at the same respective port.

3.8 De-embedding of the Physics-Based Via Model

A de-embedding procedure is also possible. The general case requires the knowledge of the near field model and a general de-concatenation procedure which is given, e.g., in [95]. In the simplified case, near and far field models can be separated due to the specific structures of the admittance matrix which can be seen in (3.1). Thus, with the assumption of this case to apply for the modeling, the far field model \mathbf{Y}_{pp} can be extracted from the overall network parameters of the structure as the negative of the off-diagonal blocks of $\mathbf{Y}^{(PBV)}$. Then the near field $Y^{(vp)}$ can be computed by subtraction of \mathbf{Y}_{pp} from the diagonal blocks.

3.9 Summary of the Physics-Based Modeling

The adopted PBV model can be summarized as illustrated in Fig. 3.7 and described as follows: The overall network parameter description at the top and bottom via ports, e.g., in terms of admittance parameters, is obtained by concatenation of a near field to each port of the admittance matrix \mathbf{Y}_{pp} which corresponds to the isotropic mode. The termination of the anisotropic modal ports with short-circuits represents an approximation of the true

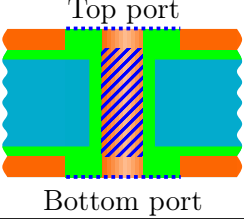
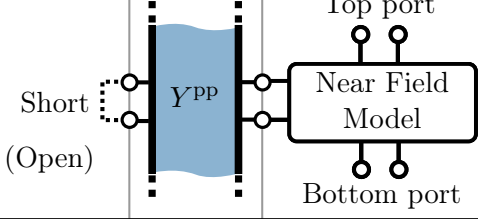
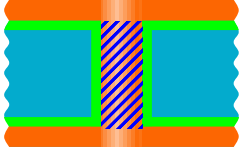
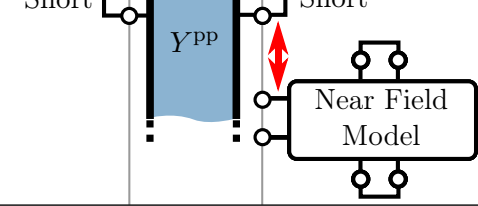
Via type	Topology of via connection	Connection/Termination of Modes		
		Anisotropic		Isotropic
Signal Via				
Ground Via				

Figure 3.7: Geometrical topology and equivalent network connection of model components in the PBV model for the two types of vias: coaxial top and bottom signal via ports (dashed lines) are created by concatenation of a near field model to the ports of the isotropic modes of the parallel-plate admittance (port surfaces are the hatched area around the via barrel). Text taken and figure adapted from [14].

admittances that correspond to the reactive fields of cut-off modes at these frequencies. To show the relevance of the latter terminations, the open circuit terminations will be shown in some of the validations to follow. As further discussed and validated later, a near field model is not required for ground vias, as they can be included in the form of short circuiting terminations for the 2D parallel plate results.

3.10 Modeling of Coaxial TSVs

As will be seen later in this thesis, conventional TSVs have to be operated in specific ways in order to limit the coupling between vias and to minimize the crosstalk between channels assigned to vias. This includes the use of differential signaling and a sufficiently large number of ground vias in metal clad interposers or reference vias in interposers without metallizations. An alternative to the conventional TSVs are coaxial TSVs. In these, every via barrel of circular cross-section is surrounded by a hollow concentric metallic cylinder. The electromagnetic field that is excited, e.g. at either of the ends, is completely contained between these metallic structures. Therefore, no coupling between individual coaxial TSVs needs to be considered. The theory and the discussion of several examples results are

presented in Appendix C. It is shown how an efficient matrix method can be applied, similar to the transverse resonance method presented in the following chapter. Further an approximation is given which is applicable in the quasi-TEM and slow-wave regimes of wave propagation. With respect to the signal integrity the results show that due to slow-wave effects and the transition regions a significant frequency dispersion of the phase velocity can occur for signals with large bandwidth. Operation of the coaxial TSV can be of interest because, as seen in Appendix C.1, the attenuation is relatively low.

Chapter 4

Far Field TSV Modeling

In this chapter, the modeling of the far-field part of the physics-based modeling is discussed. It is based on parallel plate propagation for which a wave number is computed that accounts for the presence of a layered substrate consisting of electrically isolating and conducting layers. Based on that, the corresponding network parameters are obtained using 2D-methods. In this thesis, the contour integral method (CIM) for planar circuits is applied.

In the first part of this chapter, the parallel plate modes for single layer and layered dielectrics are discussed. Next, the transverse resonance method (TRM) is discussed and wave numbers for several example stackups are presented. The solutions are applicable for both plane waves in the parallel plate structure and for the cylindrical waveguides which are of interest for the PBV modeling. Conclusively, the adaptations in the 2D-methods to the modeling of layered structures are explained.

4.1 Parallel Plate Waveguide Modes

A parallel plate waveguide consists of two planar, parallel, and conducting plates. This type of structure can be found in those interposers which have a sufficiently high coverage of the top and bottom surfaces with metallizations. If present, these metallizations support propagation of parallel plate modes governing the far-field coupling that occurs in the directions along the planes. The parallel plate structure supports both planar and radial waves. A formulation in terms of radial waves has advantages for the application with planar circuits if line sources or radial ports are used. The formulation used for determination of effective wave numbers which are eigenvalues of the corresponding eigenvalue problem are independent of the choice of mode basis (plane or radial waves) [96, Ch. 5]. In the

following, the derivations are presented for the plane wave case; analogous derivations for radial waves are given in Appendix B.3.

4.2 Classification of Wave Solutions

The types of waves supported by the structures under investigation can be classified as follows [89, 96]:

- Waves having magnetic and electric field components only in the transverse direction(s) with respect to the direction of propagation are called transverse electromagnetic (TEM) waves. They are only supported by structures with at least two disjoint perfectly conducting bodies embedded in a homogeneous medium. TEM waves in a parallel plate guide or those guided between two wires have the same propagation velocity (phase velocity) as an unguided wave in the medium (filling or background material, respectively). Moreover, there is no dispersion caused by the waveguide in this case.
- Waves with only small electric or magnetic field components in the longitudinal direction (direction of propagation) are often characterized as quasi-TEM, as they show properties very similar to the TEM modes, e.g., phase velocities close to those of the medium in which they propagate.
- For most of the modes that are supported by (homogeneously filled) parallel plate waveguides, the wave has either magnetic or electric field components in the longitudinal direction. These modes are called transverse electric (TE) or transverse magnetic (TM), respectively, specifying which component is orthogonal to the direction of propagation. In general the phase velocity is frequency dependent.
- For parallel plate waveguides with layered fillings, the modes have in general both electric and magnetic field components along the direction of propagation. A classification as TM or TE is possible in many cases if it refers to the transverse coordinate instead of the direction of propagation. Multilayer-dielectrics, including the cases which also take into account losses, can be calculated using the transverse resonance method (TRM) presented in the following.

4.2.1 Classifications of Parallel Plate Structures

The most simple parallel plate structure is the one of a homogeneous, isotropic and lossless dielectric with perfect electric conductor (PEC) boundary conditions that is depicted in Fig. 4.1a. This structure supports a true transverse electromagnetic wave and the guided wave number is equal to the wave number of the dielectric filling.

The structure depicted in Fig. 4.1b is only different from the previous one in that the dielectric is assumed to have polarization or conduction losses. This structure also supports a TEM-mode [97, Sec. 4.1], [98, Sec. 1.4], and can therefore also be analyzed analytically without approximations.

Next, the PEC boundaries are replaced by half spaces of finite conductivity, see Fig. 4.1c. The conductivity must still be sufficiently high in order to support a guided mode. Independent of the properties of the dielectric, a TEM-mode is not supported. This structure supports no TEM-mode, but (among others) a TM-mode. If the losses in the conducting half-spaces are relatively small, i.e., the conductivity is high, the TM-mode shows properties similar to a TEM-mode and can then be classified as a quasi-TEM mode.

The case depicted in Fig. 4.1d already represents the situation encountered in PCBs. The difference from the before case is that the half spaces have been replaced by layers of finite thickness. A guided wave exists if the conductivity of the bounding layers is sufficiently high. A quasi-TEM classification is justified if the losses are small. The corresponding wave number for the case in which the skin-depth in the conductor r is at most about as high as the thickness of the bounding layers d is given by [91, Appendix A2.1]

$$k = \omega \sqrt{\varepsilon_0 \varepsilon_r \mu} [1 - j(\tan \delta + r/d)/2], \quad (4.1)$$

where ω is the angular frequency, ε_r is the relative permittivity, and $\tan \delta$ is the loss tangent of the medium (combining conductive and polarization losses). It is clear that, using the above approximation, this case is effectively treated as the case in Fig. 4.1c.

Next, layered substrates are introduced, see Figs. 4.1e and 4.1f, consisting of layers with equal permeability and different (complex) permittivity. All interfaces are planar and parallel to the parallel bounding layers. Even in the lossless case and with bounding PEC conditions, no true TEM-mode exist. A quasi-TEM mode exists if losses are small and the contrasts of material properties of the layers is not too high.

Structures of the types depicted in Figs. 4.1e and 4.1f are mainly of interest in the following as they are constituted by the layering of a metal-clad silicon interposer.

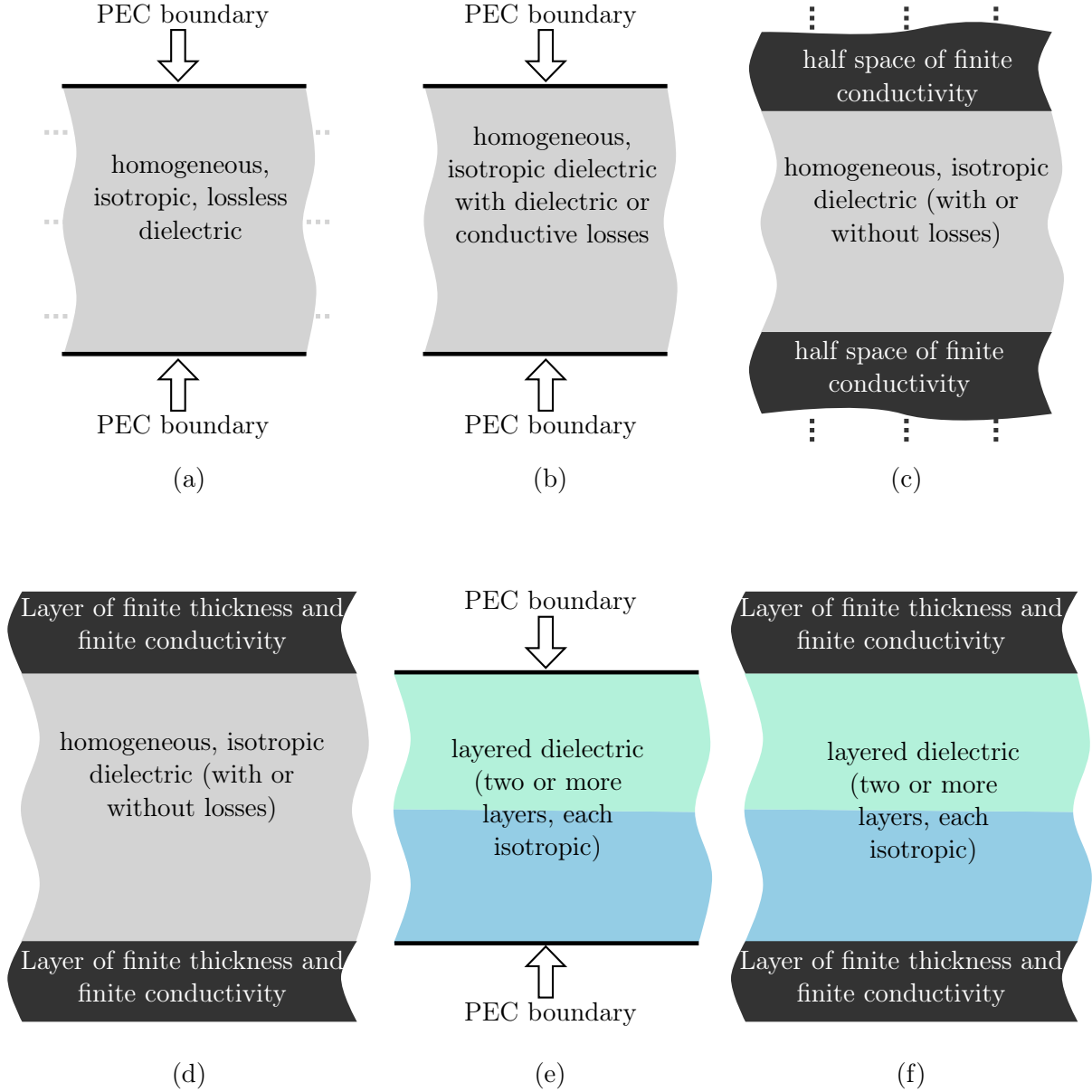


Figure 4.1: Cases of parallel plate structures to consider, sorted approximately in ascending order of complexity of the theoretical treatment. Depending on the real structure, these cases can be appropriate models. (a)-(b) Parallel plate structures with losses only in the homogeneous dielectric support a TEM-mode in addition to TE- and TM-modes. (c)-(d) Parallel plate guides with losses due to the finite conductivity of the bounding layers do not support a TEM mode but a quasi-TEM mode with similar properties as a TEM-mode if losses are low. (e)-(f) Parallel plate waveguides with layered/stratified dielectric also support a quasi-TEM-mode if the overall losses are relatively low.

4.3 Characteristic TRM-Equations for TM-modes and N Layers

In the following, the parallel plate structures depicted in Fig. 4.2 are considered. The direction of the stack-ups (layerings) along which the properties change in sections is the transverse z -direction. The propagation is chosen to be along the x -direction. Due to the symmetries, the computed wave number applies to all horizontal directions of wave propagation parallel to the plates. The following derivations are based on theory presented in [96, Ch. 4], [99, Sec. 2.3.3], [100, Ch. 11]. The method is often referred to as TRM because the formulation is analog to the resonance condition in a circuit which is a concatenation of transmission line sections, cf. Fig. 4.2.

4.3.1 Derivation of the Transfer Matrix

With the definitions in Fig. 4.2, a scalar potential can be given for the modes which propagate along the x -direction and which only have magnetic components along the y - and x -directions. They are therefore transverse magnetic (TM) with respect to the transverse direction of layering which is the z -direction. For the n th layer this scalar potential can be expressed in cosinusoidal form to express the standing wave property as

$$\Psi_n = C_n \cos(k_{z,n}(z - z_{0,n})) e^{-jk_x x}, \quad (4.2)$$

where C_n is an arbitrary (in general complex) constant and $z_{0,n}$ is the z -coordinate of the lower boundary of the n th layer. For the further derivation it is more convenient to use exponential functions. The following scalar potential is used

$$\Psi_n = C_n \left(\tilde{A} e^{-jk_{z,n} z} + \tilde{B} e^{jk_{z,n} z} \right) e^{-jk_x x}, \quad (4.3)$$

where \tilde{A} and \tilde{B} are constants which are in general complex. The wave number of the medium k , the transverse wave number $k_{z,n}$, and the longitudinal wave number of guided wave propagation k_x which all partial waves in the layers have in common are interrelated for each layer by

$$k^2 = \omega^2 \mu_n \varepsilon_n = k_{z,n}^2 + k_x^2. \quad (4.4)$$

Here, μ and ε^* are, respectively, the permittivity and the in general complex permittivity of the layer with index n .

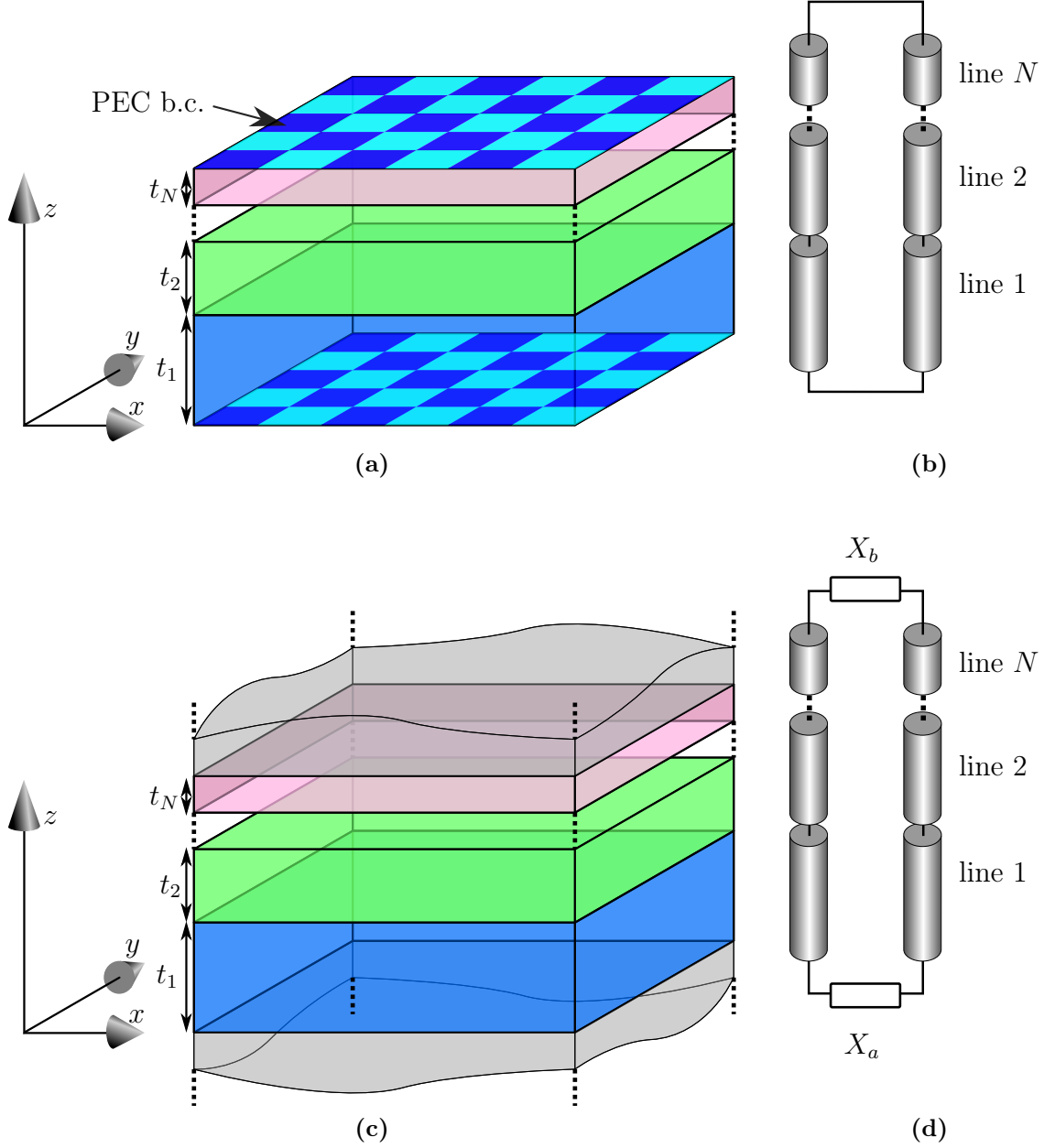


Figure 4.2: (a) Illustration of the case with N layers with PEC boundary conditions at the top and the bottom of the stackup and (b) the corresponding TRM circuit. (c) Illustration of the case with infinite bounding layers and (d) the corresponding TRM circuit. In the used coordinate system, the layering is in the z -direction and the planar layers extend along the x - and y -directions. The propagation is along the x -direction. The structure and the fields are invariant with respect to the y -direction.

The electric field components are given by [96, Eq. 3-86]

$$E(x, z)_x = \frac{1}{\hat{y}} \frac{\partial^2 \Psi_n}{\partial x \partial z} \quad (4.5a)$$

$$E(x, z)_y = \frac{1}{\hat{y}} \frac{\partial^2 \Psi_n}{\partial y \partial z} \quad (4.5b)$$

$$E(x, z)_z = \frac{1}{\hat{y}} \left(\frac{\partial^2}{\partial z^2} + k^2 \right) \Psi_n \quad (4.5c)$$

and the components of the magnetic fields are given by

$$H(x, z)_x = \frac{\partial \Psi_n}{\partial y} \quad (4.5d)$$

$$H(x, z)_y = -\frac{\partial \Psi_n}{\partial x} \quad (4.5e)$$

$$H(x, z)_z = 0 \quad (4.5f)$$

where $\hat{y} = j\omega\epsilon^* = j\omega(\epsilon_0\epsilon_r - j\sigma/\omega) = \sigma + j\omega\epsilon_0\epsilon_r$ for nonmagnetic dielectrics. Using (4.3), the corresponding field components can be derived as

$$E(x, z)_x = \frac{1}{\hat{y}} \frac{\partial^2 \Psi_n}{\partial x \partial z} = \frac{1}{\hat{y}} (-jk_{z,n}) C_n \left(\tilde{A} e^{-jk_{z,n}z} - \tilde{B} e^{jk_{z,n}z} \right) (-jk_x) e^{-jk_x x}, \quad (4.6a)$$

$$E(x, z)_y = \frac{1}{\hat{y}} \frac{\partial^2 \Psi_n}{\partial y \partial z} = 0, \quad (4.6b)$$

$$E(x, z)_z = \frac{1}{\hat{y}} \left(\frac{\partial^2}{\partial z^2} + k^2 \right) \Psi_n = \frac{1}{\hat{y}} \underbrace{(-k_{z,n}^2 + k^2)}_{k_x^2} C_n \left(\tilde{A} e^{-jk_{z,n}z} + \tilde{B} e^{jk_{z,n}z} \right) e^{-jk_x x}, \quad (4.6c)$$

and the components of the magnetic fields are

$$H(x, z)_x = \frac{\partial \Psi_n}{\partial y} = 0, \quad (4.6d)$$

$$H(x, z)_y = -\frac{\partial \Psi_n}{\partial x} = -C_n \left(\tilde{A} e^{-jk_{z,n}z} + \tilde{B} e^{jk_{z,n}z} \right) (-jk_x) e^{-jk_x x}, \quad (4.6e)$$

$$H(x, z)_z = 0. \quad (4.6f)$$

For the field components that are tangential to the layer interfaces one can write

$$E(x, z)_x = \frac{jk_{z,n}}{\hat{y}} \left(A e^{-jk_{z,n}z} - B e^{jk_{z,n}z} \right), \quad (4.7a)$$

$$H(x, z)_y = A e^{-jk_{z,n}z} + B e^{jk_{z,n}z}, \quad (4.7b)$$

in which A and B include the longitudinal dependence which these field components have in common. This can be evaluated for $z = 0$ and gives

$$\frac{\hat{y}}{jk_{z,n}} E(z=0)_x = (A - B), \quad (4.8a)$$

$$H(z=0)_y = (A + B). \quad (4.8b)$$

From the sum and difference of (4.8) one infers that

$$A = \frac{1}{2} \left(\frac{\hat{y}}{jk_{z,n}} E(z=0)_x + H(z=0)_y \right), \quad (4.9a)$$

$$B = \frac{1}{2} \left(H(z=0)_y - \frac{\hat{y}}{jk_{z,n}} E(z=0)_x \right). \quad (4.9b)$$

Inserting this into (4.7b) with an upper index (0) for the values at $z = 0$ gives

$$\begin{aligned} E(x, z)_x &= \frac{jk_{z,n}}{\hat{y}} (Ae^{-jk_{z,n}z} - Be^{jk_{z,n}z}) \\ &= \frac{jk_{z,n}}{\hat{y}} \left(\frac{1}{2} \left(\frac{\hat{y}}{jk_{z,n}} E_x^{(0)} + H_y^{(0)} \right) e^{-jk_{z,n}z} - \frac{1}{2} \left(H_y^{(0)} - \frac{\hat{y}}{jk_{z,n}} E_x^{(0)} \right) e^{jk_{z,n}z} \right) \\ &= \cos(k_{z,n}z) E_x^{(0)} + \frac{jk_{z,n}}{\hat{y}} (-j) \sin(k_{z,n}z) H_y^{(0)} \\ &= \cos(k_{z,n}z) E_x^{(0)} + \frac{k_{z,n}}{\hat{y}} \sin(k_{z,n}z) H_y^{(0)}. \end{aligned} \quad (4.10)$$

Insertion into (4.7a) gives

$$\begin{aligned} H(x, z)_y &= Ae^{-jk_{z,n}z} + Be^{jk_{z,n}z} \\ &= \frac{1}{2} \left(\frac{\hat{y}}{jk_{z,n}} E_x^{(0)} + H_y^{(0)} \right) e^{-jk_{z,n}z} + \frac{1}{2} \left(H_y^{(0)} - \frac{\hat{y}}{jk_{z,n}} E_x^{(0)} \right) e^{jk_{z,n}z} \\ &= \frac{\hat{y}}{jk_{z,n}} (-j) \sin(k_{z,n}z) E_x^{(0)} + \cos(k_{z,n}z) H_y^{(0)} \\ &= -\frac{\hat{y}}{k_{z,n}} \sin(k_{z,n}z) E_x^{(0)} + \cos(k_{z,n}z) H_y^{(0)}. \end{aligned} \quad (4.11)$$

Using the impedance definition

$$\eta_n^{(TM)} = \frac{k_{z,n}}{\omega \varepsilon_n}, \quad (4.12)$$

the following matrix notation can be used that is analog to the well-known transmission line transformation matrix that relates the voltages and currents at the beginning of the

line (left hand side) to those at the end of the line (right hand side):

$$\begin{pmatrix} E(x)_x \\ H(x)_y \end{pmatrix} = \underbrace{\begin{bmatrix} \cos(k_{x,n}t_n) & -j\eta_n^{(TM)} \sin(k_{x,n}t_n) \\ -j \sin(k_{x,n}t_n)/\eta_n^{(TM)} & \cos(k_{x,n}t_n) \end{bmatrix}}_{\mathbf{T}_n} \begin{pmatrix} E_x^{(0)} \\ H_y^{(0)} \end{pmatrix}. \quad (4.13)$$

This gives the relation between the tangential field components at the lower end of a layer to those at the upper end of this layer. The latter must equal the tangential field components at the lower end of the subsequent layer:

$$\begin{pmatrix} E(t_n, y)_{z,n+1} \\ H(t_n, y)_{x,n+1} \end{pmatrix} = \mathbf{T}_n \begin{pmatrix} E(0, y)_{z,n} \\ H(0, y)_{x,n} \end{pmatrix}. \quad (4.14)$$

For a total number of N layers, the relation between the fields at the outermost layer interfaces is therefore given by

$$\begin{pmatrix} E(t_N, y)_{z,N} \\ H(t_N, y)_{x,N} \end{pmatrix} = \underbrace{\mathbf{T}_N \cdot \mathbf{T}_{N-1} \cdot \dots \cdot \mathbf{T}_2 \cdot \mathbf{T}_1}_{\mathbf{T} = \begin{bmatrix} T_{1,1} & T_{1,2} \\ T_{2,1} & T_{2,2} \end{bmatrix}} \begin{pmatrix} E(0, y)_{z,1} \\ H(0, y)_{x,1} \end{pmatrix}, \quad (4.15)$$

where the dot refers to the conventional matrix multiplication.

Note that (4.4) only implicitly gives $k_{x,n}$ as a function of k_z and k . Taking the (complex) square root of (4.4) one obtains

$$k_{x,n} = \pm \sqrt{\omega^2 \mu \varepsilon_n - k_z^2}. \quad (4.16)$$

Both signs in (4.16) are admitted. This can be seen, e.g., from the even symmetry of both the cosine function and the function $x \cdot \sin(x)$ applied to (4.13).

4.3.2 Characteristic Equation for Perfect Electric Conductor Boundaries

Consider first the case where the outermost layers are bounded by perfectly conducting (e.g. idealized metal) layers, see Fig. 4.2a. This imposes the following boundary conditions

$$E(t_N, y)_{x,N} = 0, \quad (4.17)$$

$$E(0, y)_{x,1} = 0. \quad (4.18)$$

Then it follows from (4.15) that one needs to solve for the (in general complex) roots of a characteristic function F given by

$$0 = F(k_z) = T_{1,2}. \quad (4.19)$$

The first step in the solution for a TM-mode is now carried out by solving (4.19) in conjunction with (4.16). The equal longitudinal wave number k_z of all layers can be interpreted (for propagating modes) as ensuring that all field parts propagate in the same manner along the propagation direction.

4.3.3 Characteristic Equation for Bounding Half-Spaces of Finite Conductivity

Next, consider the case where the wave is guided due to decaying field amplitudes in the outermost layers in z -direction. In the topmost layer extends from the topmost layer interface towards infinity. The potential from which the fields are derived is given by

$$\Psi_u = C_u e^{-\gamma_{z,u} z} e^{-jk_x x} \quad (4.20)$$

with

$$\gamma_{z,u} = \pm \sqrt{\omega^2 \mu \varepsilon^* - k_x^2}. \quad (4.21)$$

In (4.21) only the sign is admitted which leads to a positive real part of $\gamma_{z,u}$ such that the fields decay in the respective directions away from the waveguide.

Then, the electric field components are

$$E(x, z)_x = \frac{1}{\hat{y}} \frac{\partial^2 \Psi_n}{\partial x \partial z} = \frac{1}{\hat{y}} (-\gamma_{z,u}) C_u e^{-\gamma_{z,u} z} (-jk_x) e^{-jk_x x}, \quad (4.22a)$$

$$E(x, z)_y = \frac{1}{\hat{y}} \frac{\partial^2 \Psi_n}{\partial y \partial z} = 0, \quad (4.22b)$$

$$E(x, z)_z = \frac{1}{\hat{y}} \left(\frac{\partial^2}{\partial z^2} + k^2 \right) \Psi_n = \frac{1}{\hat{y}} (\gamma_{z,u}^2 + k^2) C_u e^{-\gamma_{z,u} z} e^{-jk_x x}, \quad (4.22c)$$

and the components of the magnetic field are

$$H(x, z)_x = \frac{\partial \Psi_n}{\partial y} = 0, \quad (4.22d)$$

$$H(x, z)_y = -\frac{\partial \Psi_n}{\partial x} = -C_u e^{-\gamma_{z,u} z} (-jk_x) e^{-jk_x x}, \quad (4.22e)$$

$$H(x, z)_z = 0 \quad (4.22f)$$

The ratio of the field components parallel to the layer interfaces is given by

$$\frac{E_{x,u}}{H_{y,u}} = \frac{\gamma_{z,u}}{\hat{y}} = \frac{-j\gamma_{z,u}}{\omega\varepsilon_u^*}. \quad (4.23)$$

In the same manner, one can obtain the relation for the field components in the lowest layer at the lowest layer interface which is given by

$$\frac{E_{x,l}}{H_{y,l}} = \frac{-\gamma_{z,l}}{\hat{y}} = \frac{j\gamma_{z,l}}{\omega\varepsilon_l^*}. \quad (4.24)$$

To obtain the overall relation for the wave number, we divide the first by the second row of (4.15), rearrange and equate with the field ratios of the bounding layers given in (4.23) and (4.24):

$$\begin{aligned} \frac{E(t_N, y)_{x,N}}{H(t_N, y)_{y,N}} &= \frac{T_{1,1}E(0, y)_{x,1} + T_{1,2}H(0, y)_{y,1}}{T_{2,1}E(0, y)_{x,1} + T_{2,2}H(0, y)_{y,1}} \\ &= \frac{T_{1,1}E(0, y)_{x,1}/H(0, y)_{y,1} + T_{1,2}}{T_{2,1}E(0, y)_{x,1}/H(0, y)_{y,1} + T_{2,2}}, \\ \frac{-j\gamma_{z,u}}{\omega\varepsilon_u^*} &= \frac{T_{1,1}\frac{j\gamma_{z,l}}{\omega\varepsilon_l^*} + T_{1,2}}{T_{2,1}\frac{j\gamma_{z,l}}{\omega\varepsilon_l^*} + T_{2,2}}. \end{aligned} \quad (4.25)$$

This can finally be rewritten as a function F for which the roots need to be determined in order to find the guided wave number:

$$0 \stackrel{!}{=} F(k_z) = jT_{1,1}\frac{\gamma_{z,l}}{\omega\varepsilon_l^*} - T_{2,1}\frac{\gamma_{z,l}}{\omega\varepsilon_l^*}\frac{\gamma_{z,u}}{\omega\varepsilon_u^*} + jT_{2,2}\frac{\gamma_{z,u}}{\omega\varepsilon_u^*} + T_{1,2} \quad (4.26)$$

The result in (4.26) in conjunction with (4.13) and (4.15) is in consistency with [101, Ch. 2 (TM case)] and [99, Sec. (2.3.3, TM Modes)]. Note that the signs in some intermediate steps differ, but the overall results are equivalent. From comparison with these references, it can be seen that a representation without ω is possible. When applied to stackups that include layers with non-zero conductivity such as silicon, there is still a frequency dependence due to the frequency dependent complex permittivity. For a single intermediate layer with index n the characteristic equation becomes

$$F(k_z) = \cos(k_{x,n}t_n)\frac{\gamma_{z,l}}{\varepsilon_l^*} + \sin(k_{x,n}t_n)\frac{\varepsilon_n}{k_{z,n}}\frac{\gamma_{z,l}}{\varepsilon_l^*}\frac{\gamma_{z,u}}{\varepsilon_u^*} + \cos(k_{x,n}t_n)\frac{\gamma_{z,u}}{\varepsilon_u^*} - \sin(k_{x,n}t_n)\frac{k_{z,n}}{\varepsilon_n}. \quad (4.27)$$

4.3.4 Approximations for Cases with PEC boundaries

An electrical length θ_i is defined as the product for layer i of layer thickness Δz_i and the transverse wave number in the respective layer $k_{z,i}$. If θ_i is small, then approximations for the transfer matrix in (B.42) can be used. This condition is fulfilled in the following situations:

- For lossless layers: For cases in which the layer is thin compared to the free space wavelength in the material.
- For layers with losses: For cases in which the layer is thin compared to the skin-depth.

Using the series expansions of the harmonic functions, the transfer matrix is given by

$$\begin{pmatrix} E_\rho(z_{e,i}) \\ H_\phi(z_{e,i}) \end{pmatrix} = \begin{pmatrix} (1 - \frac{1}{2!}\theta_i^2 + \dots) & \frac{k_{z,i}}{\hat{y}} (\theta_i - \frac{1}{3!}\theta_i^3 + \dots) \\ -\frac{\hat{y}}{k_{z,i}} (\theta_i - \frac{1}{3!}\theta_i^3 + \dots) & (1 - \frac{1}{2!}\theta_i^2 + \dots) \end{pmatrix} \begin{pmatrix} E_\rho(z_{0,i}) \\ H_\phi(z_{0,i}) \end{pmatrix}. \quad (4.28)$$

Using only the respective first terms, the relation is given by

$$\begin{pmatrix} E_\rho(z_{e,i}) \\ H_\phi(z_{e,i}) \end{pmatrix} = \underbrace{\begin{pmatrix} 1 & k_{z,i}^2 \Delta z_i / \hat{y}_i \\ -\hat{y}_i \Delta z_i & 1 \end{pmatrix}}_{\mathbf{T}_i} \begin{pmatrix} E_\rho(z_{0,i}) \\ H_\phi(z_{0,i}) \end{pmatrix}. \quad (4.29)$$

The transfer matrix of two adjacent layer with indices 1 and 2 is then given by

$$\begin{aligned} \mathbf{T}_{\{1,2\}} &= \mathbf{T}_2 \mathbf{T}_1 = \begin{pmatrix} 1 & k_{z,2}^2 \Delta z_2 / \hat{y}_2 \\ -\hat{y}_2 \Delta z_2 & 1 \end{pmatrix} \begin{pmatrix} 1 & k_{z,1}^2 \Delta z_1 / \hat{y}_1 \\ -\hat{y}_1 \Delta z_1 & 1 \end{pmatrix} \\ &= \begin{pmatrix} 1 - k_{z,2}^2 \Delta z_2 \hat{y}_1 \Delta z_1 / \hat{y}_2 & k_{z,2}^2 \Delta z_2 / \hat{y}_2 + k_{z,1}^2 \Delta z_1 / \hat{y}_1 \\ -\hat{y}_2 \Delta z_2 - \hat{y}_1 \Delta z_1 & 1 - k_{z,1}^2 \Delta z_1 \hat{y}_2 \Delta z_2 / \hat{y}_1 \end{pmatrix} \\ &\approx \begin{pmatrix} 1 & k_{z,2}^2 \Delta z_2 / \hat{y}_2 + k_{z,1}^2 \Delta z_1 / \hat{y}_1 \\ -\hat{y}_2 \Delta z_2 - \hat{y}_1 \Delta z_1 & 1 \end{pmatrix}. \end{aligned} \quad (4.30)$$

In an analogous way, one obtains the entry $T_{1,2}$ of the overall transfer matrix that is of interest for the case with PEC boundaries at the outermost layers as

$$T_{1,2} = \{\mathbf{T}_{\{1,2,\dots,N\}}\}_{1,2} = \sum_{n=1}^N \frac{k_{z,n}^2 \Delta z_n}{\hat{y}_n} = \sum_{n=1}^N \frac{(k_n^2 - k_\rho^2) \Delta z_n}{j\omega \underline{\epsilon}_n}, \quad (4.31)$$

where $\mathbf{T}_{\{1,2,\dots,N\}}$ is the overall transfer matrix for all layers and $\underline{\varepsilon}_n = \varepsilon_0 \varepsilon_{r,n} - j\sigma\omega$. For the PEC bounded case, $T_{1,2}$ must equal zero. Enforcing this condition and inserting $k_n^2 = \omega^2 \mu \underline{\varepsilon}_n$, (4.31) can be rearranged to

$$k_\rho = \omega \sqrt{\mu \frac{\sum_{n=1}^N \Delta z_n}{\sum_{n=1}^N (\Delta z_n / \underline{\varepsilon}_n)}} = \beta_\rho - j\alpha_\rho. \quad (4.32)$$

This approximation has been found to give a good accuracy in [9, 102].

4.4 Solution of Characteristic Equations

While the problem form of a characteristic equation for which the complex roots have to be determined is relatively simple, finding the solution numerically can in general be a complex task. Mostly, iterative, gradient-based numerical techniques are used to solve this problem, see e.g. [101]. One of the principal reasons for this problem to be complex in general is that one typically wants to obtain one specific solution (i.e. the wave number for a specific mode) out of the multitude of solutions. Using start values for the iterative techniques which are close to the exact solution increases in most practical cases the probability to obtain the desired solution but does not guarantee it. Also, good approximations may be difficult to obtain. In other situations, it may also be of interest to obtain all solutions within a specific range, e.g., all modes with attenuation below a certain limit. An introduction to some techniques that are available to partly overcome these limitations is given in Appendix A.1.

4.5 Determination of the Fields

The matrix formulation can be used not only to compute the characteristic function which determines the longitudinal wave number. As soon as the wave number has been computed, the magnitudes of the field components can also be determined. The magnitudes are normalized to one of the field components. Here, only the case of perfectly conducting outer boundaries is considered. In this case the electric field component tangential to this perfectly conducting plane is zero while the magnetic field can be set to a normalization value of one. The value inside the adjacent dielectric layer are then determined with the help of the transfer matrix where the coefficients are now known: The transverse propagation

constant of every layer is given by the condition of separability

$$k_{x,n} = \pm \sqrt{\omega^2 \varepsilon_n \mu_n - k_z^2}, \quad (4.33)$$

where the signs can again be chosen arbitrarily because of the discussed symmetries, cf. (4.16). To determine the field values at a distance x_i from an interface, this distance is used instead of the d_i in the transfer matrices.

4.6 Application of the TRM to Silicon Interposer Stackups

In this section, the expected modes of propagation in the structures consisting of a silicon layer between metallic plates and intermediate oxide layers are briefly discussed. Then, the methods for computation of the dispersion relation discussed in the previous sections are carried out for several silicon interposer stackups with silicon and silicon dioxide layers, including one stackup with a large number of layers. Major parts of the data have been presented already in [8]. The results are validated through correlation with results from a finite-element (FEM) based full-wave solver [103]. A good agreement with reference results is obtained while significantly shorter calculation times are feasible. The approximation that is applicable for the fundamental mode presented in Section 4.3.4 is also applied and validated.

4.6.1 Modes of Propagation in Si–SiO₂-Structures

The considered structure consists of silicon and oxide layers between metallic plates. Three principal modes can be distinguished and are commonly named as slow-wave, quasi-TEM, and skin-effect mode [104]. The three modes are three different manifestations of the fundamental TM-mode that propagates in the layered substrate between the parallel plates and are differentiated because of their differences in the dominant physical effects and resulting phenomena, especially regarding phase velocity and attenuation. In [104] domains for each of these modes are defined which are separated by transition regions between the modes. With all other parameters fixed, the transition regions can be given for certain ranges of frequency and conductivity of the silicon layer and represented in a frequency–resistivity-chart as the one depicted in Fig. 4.6. Even though a structure with a single oxide layer was studied in [104], the principal findings also apply to the cases with (different) oxide layers to both sides of the silicon layer and to other insulation materials. The discussions in [104] are based on a analytic derivation including several approximations. In the following, some

of the findings are validated using the exact numerical solutions, but for the subsequent applications in this thesis, similar approximations as in [104] are used.

Slow-wave Mode

A mode which is of high practical relevance is the slow-wave mode because it appears at low frequencies for all practical silicon conductivities [104, Eq. 8]. An equivalent circuit from [104] for the propagation along the parallel plate structure is illustrated in Fig. 4.3a. The slow-wave mode is characterized by a magnetic field that is, for lower conductivities, very similar to the magnetic field of an empty waveguide. This is reflected in the inductance L . For higher conductivities, a frequency-dependent resistance R_d accounts for the losses. The silicon layer mainly acts as a conductor which is represented by the conductance G_s . This leads to an electric field that is concentrated in the oxide layers and can be modeled by a relatively large capacitance C_1 . This large capacitance leads to a phase velocity which is lower than the one of a waveguide filled with either conductive silicon or electrically insulating silicon dioxide. As pointed out in [104, Sec. II.C], the power is mainly transmitted in the thin oxide layer with an exchange of reactive power between the layers. This leads to a very low attenuation in this mode compared to the other two modes.

Quasi-TEM Mode

For relatively low conductivities of the silicon layer and high frequencies, the displacement currents in the silicon layer are more important than they are in the slow-wave mode. An equivalent circuit from [104] for this mode is shown in Fig. 4.3b. The magnetic field is again almost the same as in the empty waveguide. Dominated by the displacement currents, the electric field concentrates in the areas with higher permittivity, here the silicon layer. The waveguide then shows a phase velocity that is between those of waveguides with one of the involved materials. As will be seen in the following and has also been stated in [104, Fig. 4c], the attenuation in this mode is constant with frequency.

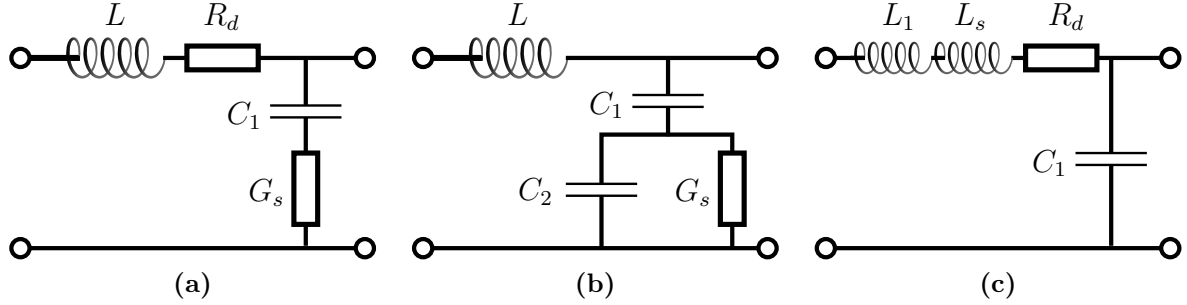


Figure 4.3: Equivalent circuits for the three principal modes of propagation in the structures with layering of silicon and thin oxide layers: (a) slow-wave mode, (b) quasi-TEM mode, and (c) skin-effect mode. Figures adapted from [104] where explicit formulas for the circuit elements can be found.

Skin-Effect Mode

For high conductivities and elevated frequencies, the skin-effect mode occurs. An equivalent circuit from [104] is depicted in Fig. 4.3c. In this mode, the magnetic field cannot fully penetrate the silicon layer due to the skin-effect which increases with both frequency and conductivity. The inductance of the model that is attributed to the silicon layer L_s is a function of the skin-depth and therefore of frequency. The silicon dioxide layer can then be regarded as a dielectric layer between one good conductor (metallic plate) and one lossy conductor due to the still significantly lower conductivity of the silicon layer. This leads to the dominance of the capacitance of the oxide layer. As can be seen in the equivalent circuit, the losses can be modeled by a series resistance which is related to the skin-effect and also frequency-dependent.

4.6.2 Application Details of the TRM Methods

The equation in (4.19) is applied in the following and the options to solve this equation need to be discussed. The following investigations are limited to frequencies below 100 GHz. For typical interposer dimensions it is then sufficient to consider only the fundamental mode for the propagating field model. By fundamental mode it is referred to the mode (plane or radial waves) which has no field nodes along the transverse direction.

4.6.3 Validation with Full-Wave Simulation Results

Configuration

A finite-element (FEM) based full-wave simulator [103] is applied for validation of the presented methods. An example setup is shown in Fig. 4.4. The software provides both 2D port solutions in terms of modal propagation constants and 3D results in terms of modal scattering parameters. The 2D port solutions can be directly used for the comparison. Certain characteristics are checked for the mode results, i.e., the transverse field distributions should show the expected behavior of invariance with respect to the coordinate along the width of the port. An appropriate boundary condition is the PMC boundary for the faces next to the port areas, as TE^z -modes and modes of the corresponding rectangular waveguide (obtained through a PEC boundary condition) are thereby excluded. A PEC boundary condition is used at the top and bottom layers for the considered cases. For the 3D simulation, the structure is excited from the two wave ports at the opposite sides which extend over the all faces of the stackup between the bounding PEC-layers. The structure can in theory be chosen arbitrarily short, but a length of the structure which is approximately twice the height is used here. This prevents the coupling through any fields which do not correspond to the investigated mode. A limiting to the size reduces the required 3D simulation time and therefore seems appropriate if simulation times should be compared. Effects of the width of the port have also been investigated by variation in the range from $100\text{ }\mu\text{m}$ to 20 mm . As expected no significant influence could be observed. From the 3D results in terms of the scattering parameters, the wave number can be obtained with the known geometrical length of the waveguide section as given in Appendix E.1.2.

Correlation

For reference, structure A from Table 4.1 with a silicon conductivity of $10\text{ }\Omega\text{ cm}$ (10 S/m) is used which corresponds to the example from the publication by Hasegawa *et al.* [104]. This structure serves here as a reference of the implemented TRM including the used root search algorithm. The results obtained for the normalized phase velocity and for the attenuation constant are shown in Figs. 4.5a and 4.5b, respectively. For comparison, the constant normalized phase velocity in bulk silicon is shown. Two configurations have been simulated which differ in their length and in the solution frequency for which the adaptive mesh is created. The shorter structure with a higher solution frequency (config. 1) shows a good agreement with the port solutions except for frequencies below 10^{-4} GHz . Using the results for the longer structure with a lower solution frequency (config. 2), the range of agreement is extended down to near 10^{-6} GHz .

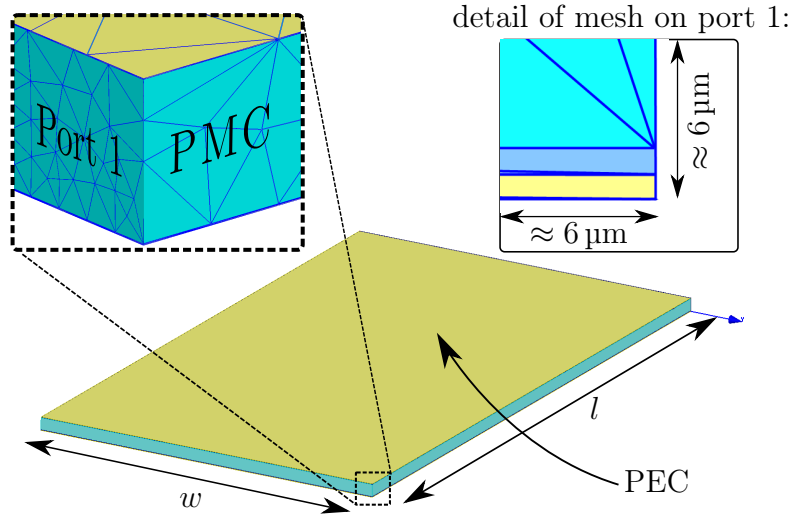


Figure 4.4: Considered layout for full-wave simulation [10]: Width and length are set to $200\text{ }\mu\text{m}$ (approximately twice the structure thickness) to obtain reliable results for the propagation constant. Figure and text adapted from [8].

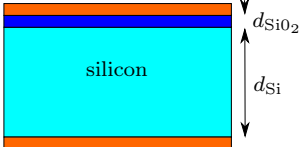
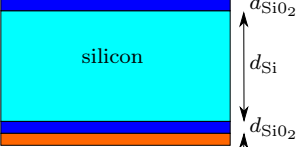
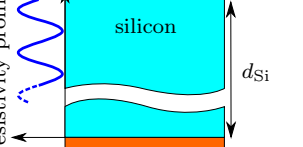
	Structure A	Structure B	Structure C
d_{SiO_2}	$1\text{ }\mu\text{m}$	$0.6\text{ }\mu\text{m}$	-
SiO ₂ layers	1 st	1 st ; 3 rd	-
d_{Si}	$200\text{ }\mu\text{m}$	$100\text{ }\mu\text{m}$	$100\text{ }\mu\text{m}$
Si layers	2 nd	2 nd	1 st
			

Table 4.1: Configurations of the considered structures. Perfect conductor boundary conditions are assumed. Therefore the thickness of the modeled metal layers is not relevant. Embedded figures and data adapted from [8].

A good agreement of the port results of the FEM solutions with the results obtained from the TRM is observed for both the normalized phase velocity and for the attenuation constant. The behavior with frequency that is expected from theory [104] can be observed: for low frequencies, a slow-wave propagation occurs, with increasing frequency it transitions towards the quasi-TEM mode which is found above about 100 GHz . As the oxide layer is very thin, the normalized phase constant is almost the same as the one of the bulk silicon in the quasi-TEM mode.

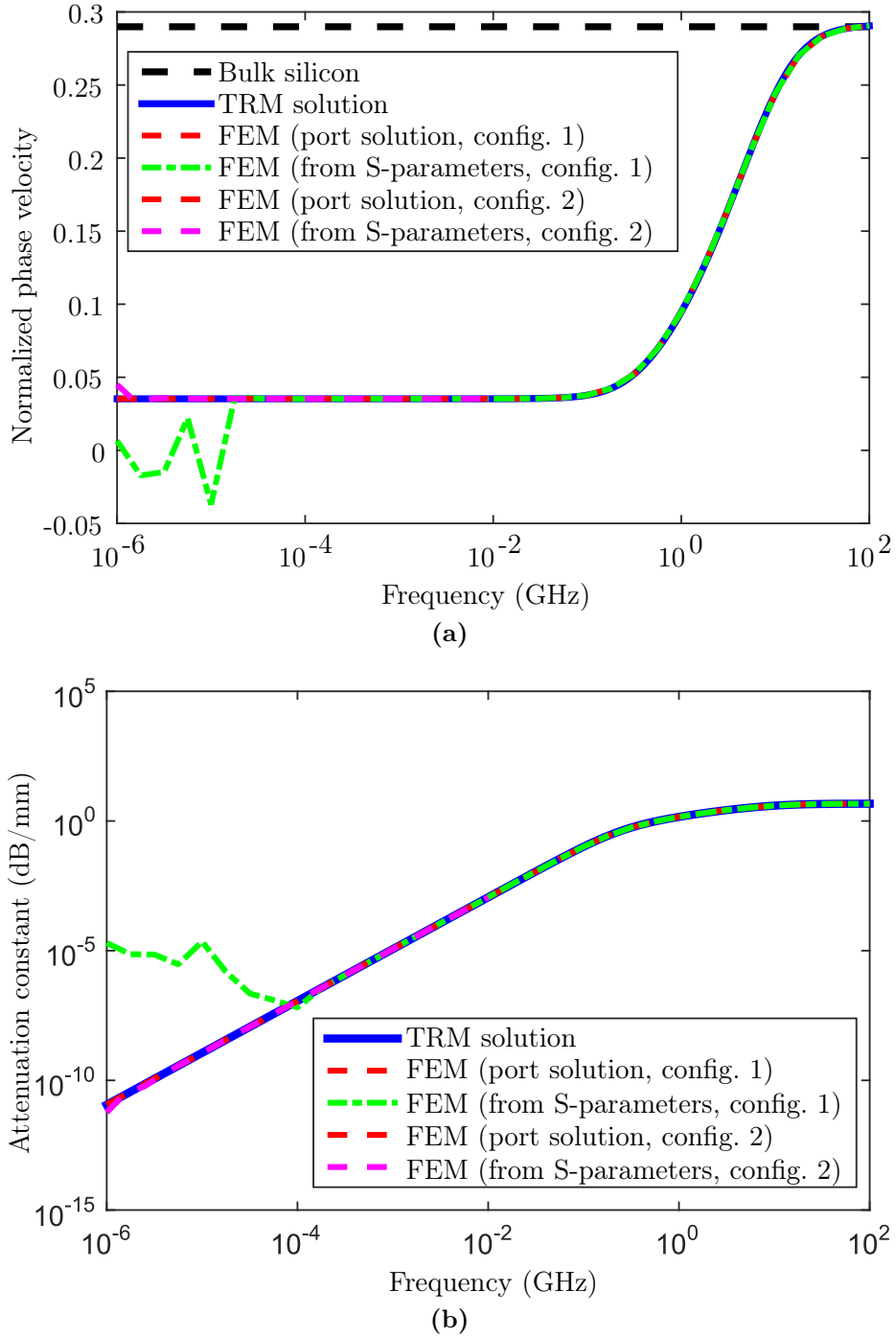


Figure 4.5: (a) Phase velocities normalized to the free space phase velocity and (b) attenuation constants for comparison of results for structure A with a silicon resistivity of $10 \Omega \text{ cm}$ (10 S/m). FEM results have been obtained with [103]. The FEM configurations differ in the length of the simulated waveguide and the frequency of adaptive solution and meshing. Over most of the frequency range, all curves are on top of each other. Figures adapted from [8].

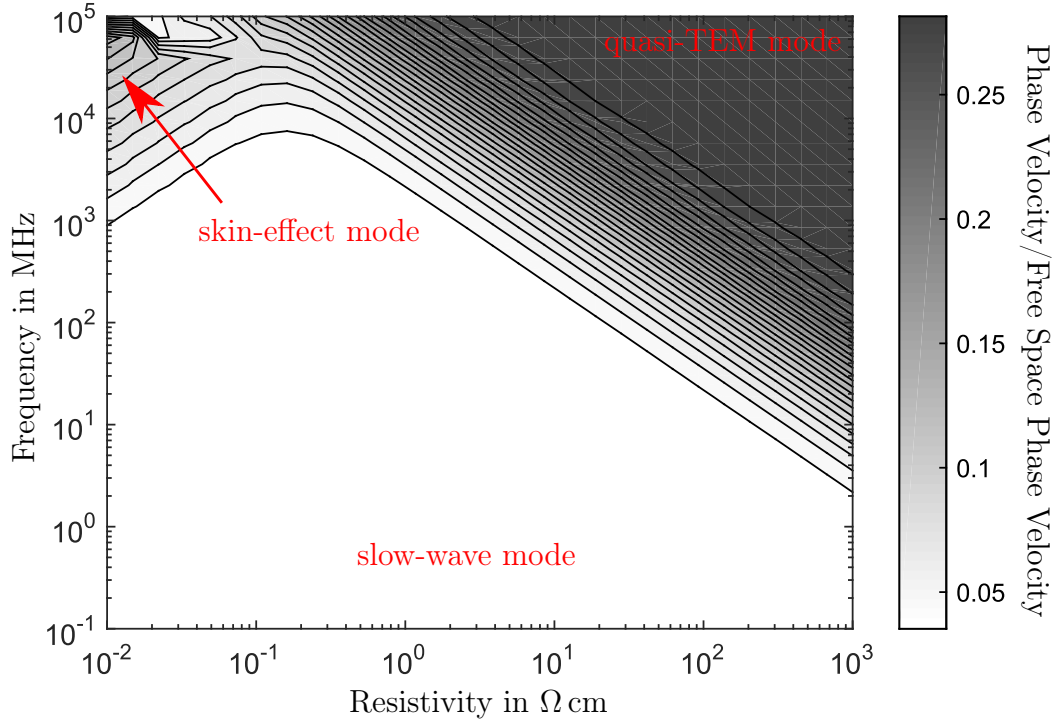


Figure 4.6: Frequency-Resistivity-chart for phase velocity of example structure A. All 900 points are calculated by the TRM in 5.8 seconds. Figure and text adapted from [8].

Comparison of Simulation Times

The TRM results can be obtained in relatively short time depending on the efficient computation of the characteristic function of the TRM and fast root search algorithms. An implementation of the characteristic function in MATLAB [105] and root search algorithms provided by MATLAB have been used. The results for frequencies up to 30 GHz have been obtained in less than 8 ms, those for frequencies in the range 30 GHz–100 GHz in less than 23 ms. The computation time differences can be attributed to a sensitivity of the solvers to the exact configuration of convergence criteria and to the start value. A frequency–resistivity-chart for structure A has also been computed with this implementation and is presented in Fig. 4.6. The total number of 900 values have been obtained in less than 5.8 s. A FEM full-wave simulation is estimated to take at least 30 minutes.

4.6.4 Application to Arbitrary Layered Structures

In many practical cases, the transverse propagation constant is small. In these cases, the approximation from Section 4.3.4 can be applied. As pointed out in [24], it is applicable over a large parameter range. This parameter range is given by the configurations and frequencies which lead to only quasi-TEM and slow-wave propagation.

Next, structure B which has two oxide layers and dimensions similar to a typical interposer is investigated. The results are shown in Fig. 4.7. They are very similar to the results for structure A when using the same silicon conductivity which is to be expected from the approximate formula. When using a very large resistivity of $500 \, \Omega \text{ cm}$ (0.02 S/m), the transition region is shifted towards lower frequencies by about two decades. The effect of a oxide layer of only 10 nm for structure B is also shown. The main effect is an even stronger slow-wave effect and an increased width (frequency range) of the transition region.

As a further demonstration of the applicability of the TRM, a structure with a larger number of layers is investigated. Structure C has a sinusoidal resistivity profile with 25 complete periods of variation of the resistivity between $1 \, \Omega \text{ cm}$ and $100 \, \Omega \text{ cm}$. A discretization of the $100 \, \mu\text{m}$ thick substrate into 500 layers, each with constant resistivity, is used. An average of about 143 ms per frequency point is needed for the computation of the wave number in this case. As can be observed in Fig. 4.7a, slow-wave and quasi-TEM mode can also be observed but the transition region is significantly larger than in the cases considered before. The results in Fig. 4.7b show that the attenuation at low frequencies is significantly higher. In all considered examples it can be observed that the proposed methods, i.e., the TRM and the simplified calculation of the wave number/propagation constant are in good agreement.

4.7 Application to Computation of Planar Microwave Circuits

4.7.1 Application with the CIM

The CIM is the adopted approach for the determination of network parameters of the parallel plate structures. As already mentioned, the wave number computed with the transverse resonance method can be used to adapt the CIM to compute the properties of planar circuits with either infinite planes or finite planes and with arbitrarily shaped contours. Some details of the CIM are given in Appendix D. Instructions on where the adaptations need to be applied are discussed in Section 4.7.3

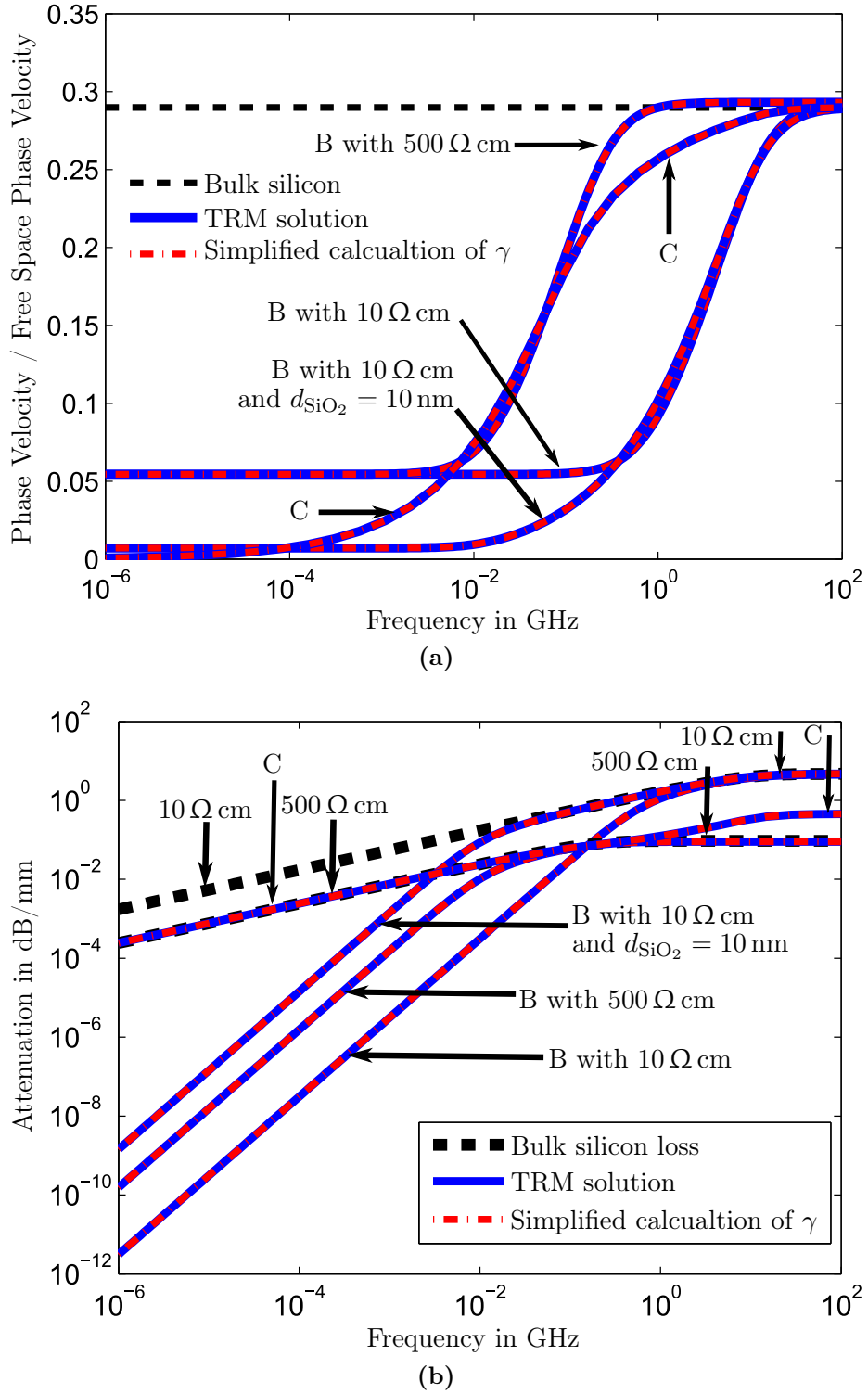


Figure 4.7: (a) Results for phase velocity of structures B and C. (b) Results for attenuation of structures B and C. Figure and text taken from [8].

4.7.2 Application with Radial Line Segment

Another propagating field model that is of interest in the following is the radial line. In the near field modeling technique presented in the following chapter that is based on a finite-difference frequency domain method, the superposition of localized and propagating field is computed. In order to separate the near and far field models, a de-embedding is required which uses a radial line segment and the network parameter description in terms of the fundamental isotropic mode.

Solution for Homogeneous Filling

The following two-port description of a homogeneously filled waveguide from [13] can be derived with the help of [96, Ch. 5]. For two radial ports with index 1 of the inner port at the smaller radius and with index 2 at the outer radial port with the larger radius, an admittance parameter matrix that relates the fundamental isotropic modes can be given as

$$\mathbf{Y}^{(R)} = \frac{2\pi}{h\eta D} \begin{bmatrix} r_1 & -r_1 \\ -r_2 & r_2 \end{bmatrix} \circ \left(\begin{bmatrix} H_1^{(2)}(a) \\ H_1^{(2)}(b) \end{bmatrix} \begin{bmatrix} H_0^{(1)}(b) & H_0^{(1)}(a) \end{bmatrix} - \begin{bmatrix} H_1^{(1)}(a) \\ H_1^{(1)}(b) \end{bmatrix} \begin{bmatrix} H_0^{(2)}(b) & H_0^{(2)}(a) \end{bmatrix} \right), \quad (4.34)$$

where \circ denotes the Hadamard product, i.e. an element-wise multiplication of matrices, and

$$D = H_0^{(2)}(b)H_0^{(1)}(a) - H_0^{(2)}(a)H_0^{(1)}(b) \quad (4.35a)$$

$$a = k_{\text{TM}}r_1, \quad (4.35b)$$

$$b = k_{\text{TM}}r_2, \quad (4.35c)$$

$$k_{\text{TM}} = 2\pi f \sqrt{\mu_0 \varepsilon}, \quad (4.35d)$$

$$\eta = \frac{k_{\text{TM}}}{2\pi f \varepsilon}. \quad (4.35e)$$

h is the thickness of the substrate that is equal to the plane separation, k_{TM} is the wave number of the (transverse magnetic) mode, r_1 and r_2 are the inner and outer radius, respectively, of the waveguide.

4.7.3 Adaptation of Wave Impedances and Characteristic Impedances to Inhomogeneous Fillings

As has been shown in Appendix B.3, the wave number of propagation in the radial direction is equal to that of the planar waveguide with plane wave propagation and the same stackup. An effective wave impedance is defined in the following which allows the application of the CIM and (4.35e) with inhomogeneously filled waveguides. It is defined analogously to the approximation of the wave number in Section 4.3.4 as

$$\eta_{\text{eff}} = \frac{k_x}{\omega \underline{\varepsilon}_{\text{eff}}}. \quad (4.36)$$

where

$$\underline{\varepsilon}_{\text{eff}} = \frac{\sum_{i=1}^3 t_i}{\sum_{i=1}^3 (t_i / \underline{\varepsilon}_i)}, \quad (4.37)$$

The derivation is presented in Appendix B.5.2.

It is known that the values of the wave impedances and characteristic impedances in the case of inhomogeneous media depend on the definition [106]. In the applications that follow, waveguides with the same stackup are concatenated in terms of their network parameters and completely equivalent definitions are applied in all cases. Therefore, the concatenation corresponds to enforcing the continuity of the tangential field components at the interfaces. Any influence of the definition vanishes because the overall results of the characterizations are given at the coaxial via ports on homogeneously filled antipads for which the usual definitions of characteristic impedance can be applied.

4.8 Summary and Conclusions

Two methods have been presented and validated for the computation of the wave number of fundamental mode propagation in the parallel plate structure that is identified as relevant for the wave propagation in metal clad silicon interposers, an exact method based on the TRM and an approximation that is valid in the typical parameter ranges of interest. Further, the adaptations of the 2D techniques for planar wave propagation and the limitations thereof have been briefly introduced.

Chapter 5

Near Field TSV Modeling

In this chapter, the modeling of the near fields of TSVs in metal-clad interposers is discussed. The techniques for modeling of the homogeneous structures have already been shortly discussed in Section 3.5.2. Here, a few simple adaptations of some of these methods are considered. The main subject of this chapter is a local full-wave model using a finite-difference frequency domain (FDFD) method which represents a good tradeoff between numerical efficiency, generality, and ease of implementation. It is used because analytical techniques can only be found in the literature for homogeneously filled junctions for which the near field is to be computed.

5.1 Finite-Difference Frequency Domain Method (FDFD)

5.1.1 Motivation

The numerical method presented in the following is an FDFD method for rotationally symmetric geometries. The latter property is sometimes referred as body of revolution (BOR). Due to the rotational symmetry, the number of effective dimensions of the problem to compute is two instead of the general three spatial dimensions. It will be shown that this method is applicable and leads to results of good accuracy for the considered TSV structures with lossy silicon and thin oxide layers. Even though the presented method achieves a good numerical efficiency, the near field model results should be re-used for every via with the same geometry of a via array.

Fig. 5.1 shows again the cross-section of the modeled structure. The modeled near field region is bounded by the “FDFD Domain Boundary” in the direction of the planes, and by the planes and the inner coaxial ports (marked as A2 and B2) in the z -direction.

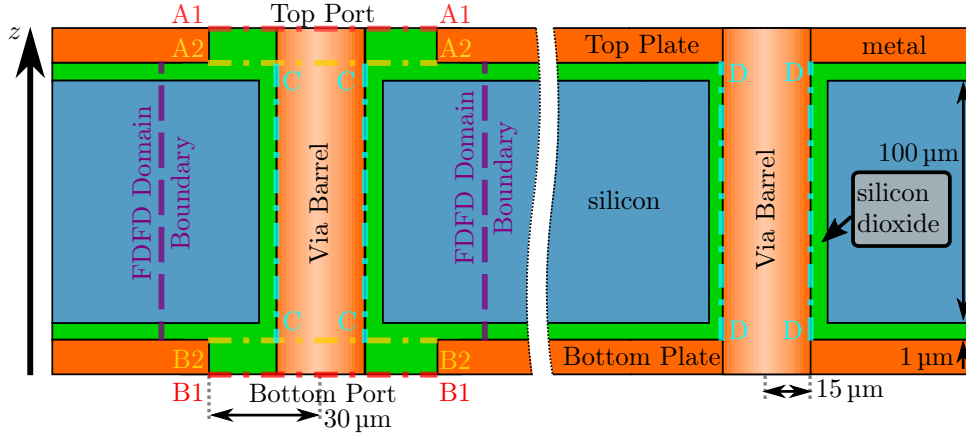


Figure 5.1: Schematical drawing of the considered types of TSVs in interposers with the considered dimensions. A signal via (left side) and a ground via (right side) are embedded in a structure consisting of parallel metallic plates on a silicon substrate which is electrically isolated. A1, A2, B1, and B2 denote coaxial ports of the modeling. C and D denote the desired radial ports in terms of which the near field models can be connected to the far field interaction to compute the overall electromagnetic properties. Figure and text taken from [13].

5.2 Adaptation of a BOR FDFD Method for Near Field Modeling

Because the FDFD methods are discussed in little detail compared to the related finite-difference time domain methods (the latter for example in [107]), the proposed method is discussed in greater detail in the following section, thereby replicating the derivations from [13]. The theory is based on the methods presented in [108] and extends the technique to the case with inhomogeneous substrates and also considers the case of non-equidistant grid-spacings. The latter is of interest, as the oxide layers are typically very thin compared to the silicon layers. The non-equidistant grid can be adapted exactly to the interfaces between layers without increasing the grid in the silicon layers to an equal extent.

For the FDFD with rotational symmetry, only the following three field components are relevant: the magnetic field component in azimuthal direction, the electric field component in axial direction, and the electric field component in radial direction. The 2D computational domain is depicted in Fig. 5.2. It corresponds to a modeled 3D domain which has the shape of a circular cylindrical ring.

An approximation is made by assuming the metal components of the structures, i.e. the vias and the bounding metal layers, to correspond to a PEC boundary condition. This assumption has been validated in [13], where it has been found from FEM full-wave sim-

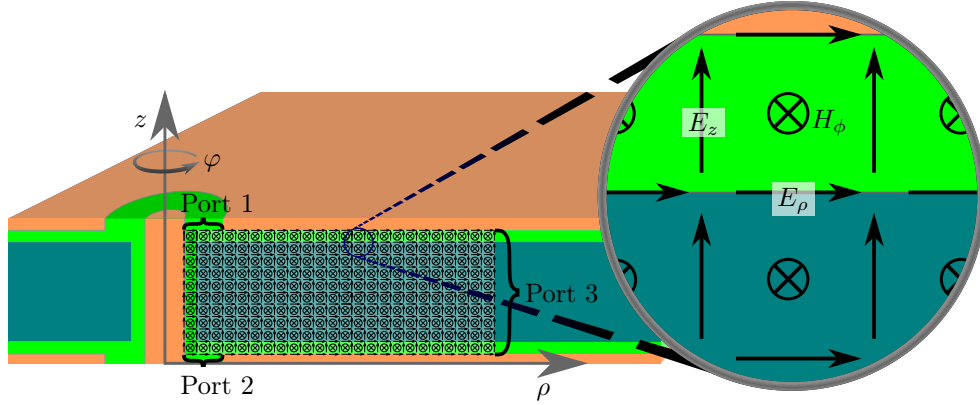


Figure 5.2: Cut view of the considered structure with FDFD grid for near field modeling. The radial port (port 3) must be placed sufficiently far from the via barrel such that almost all localized fields of this via are inside the computational domain. Reasonable distances are in the order of the substrate thickness. Figure taken and text adapted from [13].

ulations using [66] that results differ little from the PEC case if, e.g., aluminum with a specific conductivity $\sigma = 3.4 \times 10^7 \text{ S/m}$ is used at frequencies above 100 MHz.

In the proposed FDFD, several interrelated grids are defined as depicted in Fig. 5.3. A primary and a secondary grid are defined for both the radial and the axial direction. The different field components are located on nodes defined at different intersections of these four grids. In case of the non-equidistant grid, the distances between grid points on the primary and secondary grid differ. The azimuthal magnetic field grid points are located on the nodes of the secondary grids of both the axial and radial direction. The radial electric field points are on the nodes of the secondary grid of the radial direction and the primary grid of the axial direction. The axial electric field points are on the nodes of the primary grid of the radial direction and the secondary grid of the axial direction.

The computational domain coincides with primary grid points. Therefore, only tangential electric field components are located on its boundaries. For dielectric interfaces which are along the axial direction, the primary radial grid is configured such that it coincides with the interfaces. For dielectric interfaces which are along the radial direction, the primary axial grid is configured such that it coincides with the interfaces. In both cases, this leads to a configuration with only tangential electric field grid points on the dielectric interface

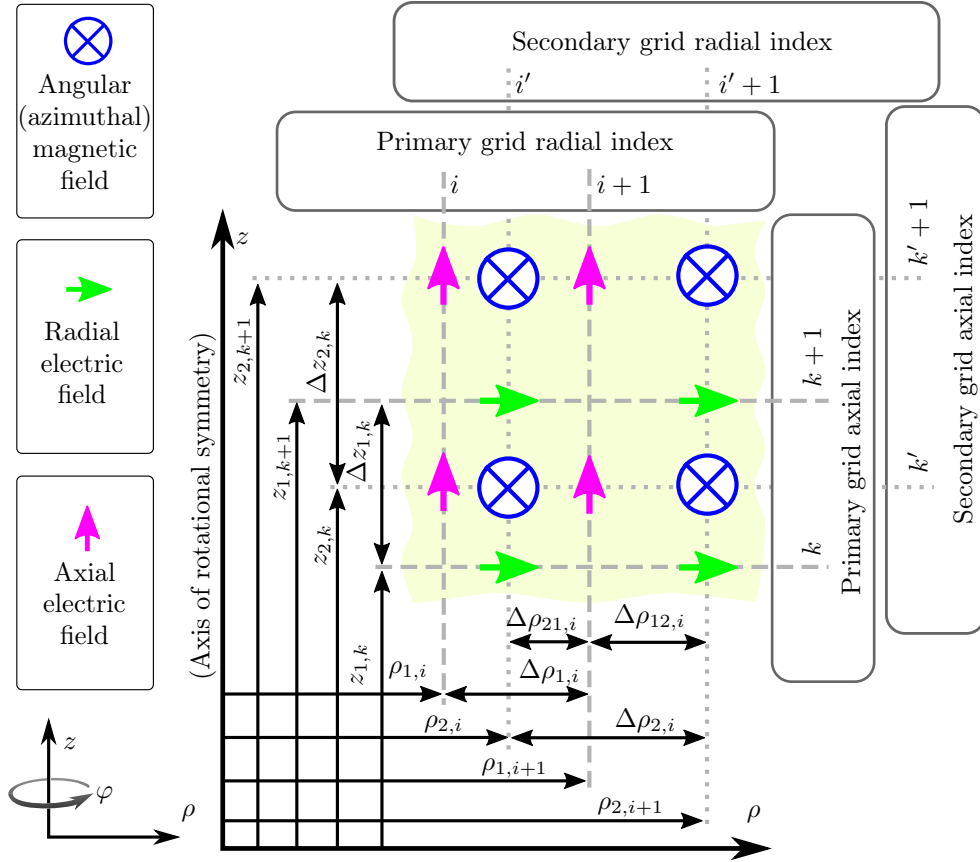


Figure 5.3: Definition of the grid coordinates: a primary and a secondary grid are defined for the radial direction with indices i and i' , respectively. For the axial direction they are named k and k' , respectively. Figure taken from [13].

5.2.1 Finite Difference Equations

In the following, it is discussed how the relations presented in [108, Eqs. 7–9] have been adapted to varying grid distances. The curl equations (Gauss's law and Ampère's circuital law, both in differential form) govern the interdependence of the electric and magnetic field components in the source free regions and are given by

$$\nabla \times \mathbf{E} = -\frac{\partial}{\partial t} \mu_0 \mathbf{H}, \quad (5.1a)$$

$$\nabla \times \mathbf{H} = \frac{\partial}{\partial t} \underline{\varepsilon} \mathbf{E}, \quad (5.1b)$$

where $\underline{\varepsilon}$ is the complex relative permittivity of the (homogeneous) medium given by $\underline{\varepsilon} = \varepsilon_0 \varepsilon_r - j\sigma/\omega$. The curl of a vector field \mathbf{A} in cylindrical coordinates is given by

$$\nabla \times \mathbf{A} = \mathbf{e}_\rho \left(\frac{1}{\rho} \frac{\partial A_z}{\partial \phi} - \frac{\partial A_\phi}{\partial z} \right) + \mathbf{e}_\phi \left(\frac{\partial A_\rho}{\partial z} - \frac{\partial A_z}{\partial \rho} \right) + \mathbf{e}_z \frac{1}{\rho} \left(\frac{\partial}{\partial \rho} (\rho A_\phi) - \frac{\partial A_\rho}{\partial \phi} \right), \quad (5.2)$$

where \mathbf{e}_ρ , \mathbf{e}_ϕ , and \mathbf{e}_z are the unit vectors of radial, azimuthal, and axial directions, respectively. Due to the symmetries, only components E_ρ , E_ϕ , and H_ϕ exist. For the rotationally symmetric case ($\partial/\partial\phi = 0$) and a harmonic time dependence ($\partial/\partial t = j\omega$), the equations in (5.1) reduce to

$$\mathbf{e}_\phi \left(\frac{\partial E_z}{\partial \rho} - \frac{\partial E_\rho}{\partial z} \right) = j\omega\mu_0 \mathbf{H}, \quad (5.3a)$$

$$-\mathbf{e}_\rho \frac{\partial H_\phi}{\partial z} + \mathbf{e}_z \left(\frac{H_\phi}{\rho} + \frac{\partial H_\phi}{\partial \rho} \right) = j\omega\epsilon \mathbf{E}. \quad (5.3b)$$

For the implementation of the finite differences, the first derivative expressions in (5.3) are replaced by their first order approximations. In (5.3b), the coordinate ρ refers to the location of the axial electric field component. Therefore, for the finite difference relation, a linear interpolation is used with the azimuthal magnetic field at neighboring grid points for this location. The latter modification is the only one required for the non-equidistant grids compared to the equidistant grids if first order finite differences are used.

The grid indexing as defined in Fig. 5.3 is applied in the following. The discretized representations of the relevant equations are then given by

$$j\omega\mu_0 H_\phi^{i',k'} = \frac{E_z^{i+1,k'} - E_z^{i,k'}}{\Delta\rho_{1,i}} - \frac{E_\rho^{i',k'+1} - E_\rho^{i',k}}{\Delta z_{1,k}}, \quad (5.4a)$$

$$j\omega\epsilon E_\rho^{i',k'+1} = - \frac{H_\phi^{i',k'+1} - H_\phi^{i',k'}}{\Delta z_{2,k}}, \quad (5.4b)$$

$$j\omega\epsilon E_z^{i+1,k'} = \left(\frac{\Delta\rho_{21,i}}{\rho_{1,i+1}\Delta\rho_{2,i}} + \frac{1}{\Delta\rho_{2,i}} \right) H_\phi^{i'+1,k'} + \left(\frac{\Delta\rho_{12,i}}{\rho_{1,i+1}\Delta\rho_{2,i}} - \frac{1}{\Delta\rho_{2,i}} \right) H_\phi^{i',k'}, \quad (5.4c)$$

where H_ϕ is the magnetic field in the angular direction, E_z is the axial component of the electric field, and the radial electric field component E_ρ as shown in Fig. 5.3. The superscript used with the field components are discussed below.

The equations in (5.4) can be written for the complete grid in matrix equations form as

$$\mathbf{H}_\phi = \mathbf{A}\mathbf{E}_\rho + \mathbf{B}\mathbf{E}_z + \mathbf{C}\mathbf{E}_{\text{boundary}}, \quad (5.5a)$$

$$\mathbf{E}_\rho = \mathbf{D}\mathbf{H}_\phi, \quad (5.5b)$$

$$\mathbf{E}_z = \mathbf{E}\mathbf{H}_\phi. \quad (5.5c)$$

Here, \mathbf{A} , \mathbf{B} , \mathbf{C} , \mathbf{D} , and \mathbf{E} are all sparsely populated matrices with at most 2 entries per row. The non-zero elements of the matrices \mathbf{A} , \mathbf{B} , and \mathbf{D} are given as

$$A_{\{i',k'\},\{i',k\}} = \frac{+1}{j\omega\mu_0\Delta z_{1,k}}, \quad (5.6a)$$

$$A_{\{i',k'\},\{i',k+1\}} = \frac{-1}{j\omega\mu_0\Delta z_{1,k}}, \quad (5.6b)$$

$$B_{\{i',k'\},\{i,k'\}} = \frac{-1}{j\omega\mu_0\Delta\rho_{1,i}}, \quad (5.6c)$$

$$B_{\{i',k'\},\{i+1,k'\}} = \frac{+1}{j\omega\mu_0\Delta\rho_{1,i}}, \quad (5.6d)$$

$$D_{\{i',k\},\{i',k'\}} = \frac{-1}{j\omega\varepsilon\Delta z_{2,k}}, \quad (5.6e)$$

$$D_{\{i',k\},\{i',k'-1\}} = \frac{+1}{j\omega\varepsilon\Delta z_{2,k}}. \quad (5.6f)$$

The non-zero elements of matrix \mathbf{E} are given as

$$E_{\{i,k'\},\{i',k'\}} = \frac{1}{j\omega\varepsilon} \left(\frac{\Delta\rho_{21,i-1}}{\rho_{1,i}\Delta\rho_{2,i-1}} + \frac{1}{\Delta\rho_{2,i-1}} \right), \quad (5.7a)$$

$$E_{\{i,k'\},\{i'-1,k'\}} = \frac{1}{j\omega\varepsilon} \left(\frac{\Delta\rho_{12,i-1}}{\rho_{1,i}\Delta\rho_{2,i-1}} - \frac{1}{\Delta\rho_{2,i-1}} \right). \quad (5.7b)$$

In the above equations, the notations for A , B , D , and E use an indexing with a subscript of the form $\{\tilde{\rho}_1, \tilde{z}_1\}$, $\{\tilde{\rho}_2, \tilde{z}_2\}$. This denotes a first and second part of the index, each of the form $\{\tilde{\rho}, \tilde{z}\}$. The latter denotes a linear index computed from radial index $\tilde{\rho}$ and the index for the axial direction \tilde{z} . The relation between the subscript indices $\tilde{\rho}$ and \tilde{z} and the linear index $\{\tilde{\rho}, \tilde{z}\}$ depends on the shape of the computational domain and the ordering of grid points inside it.

The above equation (5.6) and (5.7) can readily be applied for homogeneous regions with complex permittivity ε . The modifications required for electric field grid points on dielectric contours are discussed in Section 5.2.2.

The matrix \mathbf{C} establishes the relation between the non-zero electric field values on the

boundary of the computational domain and the respective neighboring magnetic field points. The only non-zero electric field values are those of the excitations on the ports. Therefore, the non-zero entries of \mathbf{C} are of the same form as the non-zero entries of either \mathbf{A} or \mathbf{B} . For a radial port parallel to the z -coordinate, the entries are of same form as the entries of \mathbf{B} . For a coaxial port parallel to the ρ -coordinate, the entries are of the same form as the entries of \mathbf{A} .

One can insert (5.5b) and (5.5c) into (5.5a) and rearrange for the vector \mathbf{H}_ϕ to obtain as an intermediate results the magnetic field related to the tangential electric field values on the ports

$$\mathbf{H}_\phi = \underbrace{(\mathbf{1} - \mathbf{AD} - \mathbf{BE})^{-1}}_{\mathbf{S}} \mathbf{CE}_{\text{boundary}}, \quad (5.8)$$

where $\mathbf{1}$ is an identity matrix of a size given by the squared total number of secondary grid points. The system matrix named \mathbf{S} and defined in (5.8) is a relatively sparse matrix with dominating diagonals.

5.2.2 Relations at Dielectric Interfaces

In the following, dielectric interfaces are considered which are aligned with either the radial or the axial coordinate axis. Because non-equidistant grids are used, it is possible for the structures of interest, to align the interfaces such that only electric field components are on the interfaces which are tangential to it. The finite-difference relations from the previous section need to be adapted, accordingly.

Interfaces Parallel to the z -Axis

This interface is parallel to the z -axis and shows a difference in material properties for different radial coordinates and indices. The integral form of Ampere's law, which is applied in the following, can be stated as

$$j\omega \iint_A \underline{\varepsilon} \mathbf{E} \, d\mathbf{A} = \oint_{\partial A} H \, d\mathbf{l}. \quad (5.9)$$

It is applied to a region that has the shape of a circular ring. A part of this ring is the area between the dotted lines that is illustrated in Fig. 5.4. The electric field component is tangential at the interface and therefore continuous across it. Due to the fine discretization near the dielectric interfaces, it can further be assumed to be constant in the considered domain. Therefore, the integration in polar coordinates over the areas gives a weighting

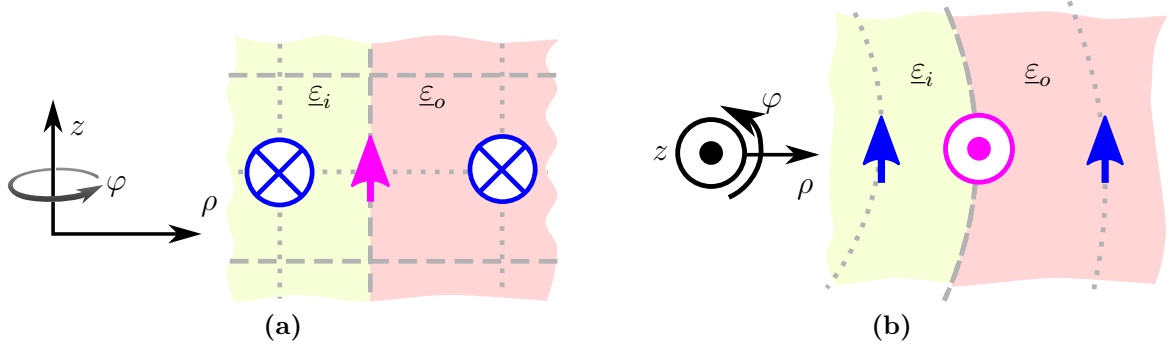


Figure 5.4: Illustration of the relevant field components of dielectric interfaces parallel to the z -axis. Magnetic field components are shown in blue and the electric field components in purple. (a) Side view in positive azimuthal direction. (b) Top view in negative axial direction.

with the areas of circular rings. The integration along the contours gives a weighting with the corresponding circumferences. Therefore, one obtains

$$\begin{aligned} j\omega \left(((\rho_1 + \Delta\rho_{21})^2 - \rho_1^2) \varepsilon_o + (\rho_1^2 - (\rho_1 - \Delta\rho_{12})^2) \varepsilon_i \right) \pi E_z \\ = H_\phi^{(i)} 2\pi(\rho_1 - \Delta\rho_{12}) - H_\phi^{(o)} 2\pi(\rho_1 + \Delta\rho_{21}). \end{aligned} \quad (5.10)$$

Here, ρ_1 is the radial coordinate of the interface, $\Delta\rho_2$ is the distance between the magnetic field grid points, $\Delta\rho_{12}$ is the distance between the secondary grid of the second region and the primary grid on the interface, $\Delta\rho_{21}$ is the distance between the secondary grid of the first region and the primary grid on the interface. ε_i is the permittivity in the first region (inner) and ε_o is the permittivity in the second (outer) region. Division of (5.10) by $-2\pi\rho_1\Delta\rho_2$ gives

$$\begin{aligned} j\omega \frac{-1}{2\rho_1\Delta\rho_2} \left(((\rho_1 + \Delta\rho_{21})^2 - \rho_1^2) \varepsilon_o + (\rho_1^2 - (\rho_1 - \Delta\rho_{12})^2) \varepsilon_i \right) E_z \\ = -H_\phi^{(i)} \frac{1}{\rho_1\Delta\rho_2} (\rho_1 - \Delta\rho_{12}) + H_\phi^{(o)} \frac{1}{\rho_1\Delta\rho_2} (\rho_1 + \Delta\rho_{21}), \end{aligned} \quad (5.11)$$

which can be rewritten as

$$\begin{aligned} -j\omega E_z \left(\left(\frac{\Delta\rho_{21}^2}{2\rho_1} + \Delta\rho_{21} \right) \frac{\varepsilon_o}{\Delta\rho_2} - \left(\frac{\Delta\rho_{12}^2}{2\rho_1} - \Delta\rho_{12} \right) \frac{\varepsilon_i}{\Delta\rho_2} \right) \\ = H_\phi^{(i)} \left(\frac{\Delta\rho_{12}}{\rho_1\Delta\rho_2} - \frac{1}{\Delta\rho_2} \right) + H_\phi^{(o)} \left(\frac{\Delta\rho_{21}}{\rho_1\Delta\rho_2} + \frac{1}{\Delta\rho_2} \right). \end{aligned} \quad (5.12)$$

From comparison of (5.12) with (5.4c) it can be concluded that an effective permittivity can be used for the electric field point on the dielectric interface. This effective permittivity

is used in (5.4c) only for the grid points on dielectric interfaces and is given by [13]

$$\varepsilon_{12} = \frac{\varepsilon_1}{\Delta\rho_2} \left(\frac{(\Delta\rho_{12})^2}{2\rho_1} - \Delta\rho_{12} \right) - \frac{\varepsilon_2}{\Delta\rho_2} \left(\frac{(\Delta\rho_{21})^2}{2\rho_1} + \Delta\rho_{21} \right), \quad (5.13)$$

where the naming has been modified to ε_1 for the permittivity in the first region (inner) and ε_2 for the permittivity in the second (outer) region.

Interfaces Parallel to the ρ -Axis

This interface is parallel to the ρ -axis and shows a difference in material properties for different axial coordinates and indices. In this case, a simple average have been found to enable accurate results for typical grids. The following relative permittivity is therefore inserted into (5.4b) for all radial electric field grid points on dielectric interfaces:

$$\varepsilon_{12} = \frac{\varepsilon_1 + \varepsilon_2}{2}. \quad (5.14)$$

where ε_1 and ε_2 are the complex permittivities to both sides of the interface.

5.2.3 Port Excitations and Port Responses

The final goal of the presented FDFD method is to obtain network parameters for the three-port structure with two coaxial and one radial port. On these three ports the respective fundamental mode on each port is excited by imposing the corresponding tangential electric field on the corresponding boundary grid points. The port response is evaluated by correlation of the tangential magnetic fields on the port with the modal fields. As discussed in the following, the magnetic field is only available on grid points close to the port and therefore needs to be extrapolated.

Organization of Port Excitations

The electric field values on the port areas of the of excitation are assembled in vectors and inserted as columns of an overall excitation matrix $\mathbf{E}^{\text{boundary}}$ as

$$E_{m,n}^{\text{boundary}} = \begin{cases} E_{\rho}^{\text{boundary}}, & \text{if } m \in q1, \\ E_z^{\text{boundary}}, & \text{if } m \in q2, \\ 0, & \text{else,} \end{cases} \quad (5.15)$$

where $q1$ and $q2$ are the index sets for tangential electric field grid points on coaxial and radial ports, respectively, of port $n \in \{1, 2, 3\}$.

Port Excitations on Coaxial Ports

The coaxial ports are assigned on the homogeneous antipad regions. There, the fundamental mode is a TEM-mode of which the electrical field is given as

$$E_\rho(\rho) = \frac{1}{\rho} \frac{V_0}{\log(r_{\text{antipad}}/r_{\text{barrel}})}, \quad (5.16)$$

where r_{antipad} and r_{barrel} are the radius of antipad and via barrel, respectively, and V_0 is a normalization voltage of, e.g., 1 V.

Port Excitations on Radial Ports

The proposed methods aims at modeling the parameter ranges of quasi-TEM mode and the slow-wave mode. For these two modes of propagation, the transverse electric field components of the respective fundamental mode are given with good accuracy by [13]

$$E_z(z) = \begin{cases} V_0 Y'_{\text{total}} / (t_{\text{oxide}} Y'_{\text{oxide}}), & \text{in the oxide,} \\ V_0 Y'_{\text{total}} / (t_{\text{silicon}} Y'_{\text{silicon}}), & \text{in the silicon,} \end{cases} \quad (5.17)$$

where

$$Y'_{\text{total}} = j\omega \left(2 \frac{t_{\text{oxide}}}{\varepsilon_{\text{oxide}}} + \frac{t_{\text{silicon}}}{\varepsilon_{\text{silicon}}} \right)^{-1}, \quad (5.18a)$$

$$Y'_{\text{oxide}} = j\omega \varepsilon_{\text{oxide}} / t_{\text{oxide}}, \quad (5.18b)$$

$$Y'_{\text{silicon}} = j\omega \varepsilon_{\text{silicon}} / t_{\text{silicon}}. \quad (5.18c)$$

Here, t_{oxide} and t_{silicon} are the thickness of oxide and silicon layer, respectively, and $\varepsilon_{\text{oxide}}$ and $\varepsilon_{\text{silicon}}$ are the corresponding (complex) relative permittivities.

Evaluation of Port Responses

With the proposed grid structure, the choice was made to have the electric field grid points on the boundaries of the computational domain. The magnetic field values are then not available exactly on the port but only at grid point near the ports. The values on the contour are extrapolated using a 1D extrapolation step which is formulated as a matrix multiplication presented in the following. The presented relations assume a constant grid spacing for the three rows of the grid which are closest to the respective port. The evaluation matrix \mathbf{J} for the port responses is formulated as

$$J_{m,n} = \pm \begin{cases} (7/4) \cdot 2\pi\rho/N, & n \in p1, \\ (-1) \cdot 2\pi\rho/N, & n \in p2, \\ (1/4) \cdot 2\pi\rho/N, & n \in p3, \\ 0, & \text{else,} \end{cases} \quad (5.19)$$

where the plus sign has to be chosen for outer radial ports (at largest ρ -coordinates) and top coaxial ports, and the minus sign for bottom coaxial ports and inner radial ports (at smallest ρ -coordinates). N is the number of grid points on the respective port, and ρ is the radial coordinate of the respective grid point. $p1$, $p2$, and $p3$ are the index sets of the first, second and third row or column, respectively, inside of the computational domain and next to the port m . The operation carried out by the multiplication of the magnetic field vector with the evaluation matrix \mathbf{J} can be interpreted as an averaging or as a correlation with the modal field distribution.

Admittance Matrix Formulation

A three-port admittance matrix description of the structure under consideration can be obtained by combining (5.8), (5.15) and (5.19) as

$$\mathbf{Y} = \mathbf{J}(\mathbf{1} - \mathbf{A}\mathbf{D} - \mathbf{B}\mathbf{E})^{-1}\mathbf{C}E_{\text{boundary}}/V_0. \quad (5.20)$$

Interpretation in Terms of Relevant Waveguide Modes

The proposed evaluation of admittance parameters as summarized in (5.20) requires no absorbing boundary. On all ports, there are, in general, higher order modes both with and without azimuthal variations of the fields. As illustrated in Fig. 5.5, only the modes without azimuthal variation are considered in this method. The remaining modes are the fundamental TEM modes and all higher order modes without azimuthal variation of the fields. In the proposed formulation, the admittance parameters are evaluated by implicit computation of the fundamental mode currents if on one port the fundamental mode is excited and all other ports are short-circuited.

5.3 Approximate Methods for Near Field Modeling

For validation and comparison with the proposed FDFD-method, two approximate techniques are used in the following. The schematic models of these techniques are depicted in Figs. 3.6b and 3.6c. A model of the same structure as the one simulated with the FDFD-method can be obtained by concatenation of a model for a radial line segment, e.g., in term of Y-parameters.

5.3.1 Coaxial-to-Radial Junction Model by Williamson

In [76], Williamson proposed an analytical model for radial line to coaxial line junctions with lossless and homogeneously filling) for application in an antenna context. This model has since been also applied for via modeling by several authors, e.g. in [63,83]. An equivalent circuit modeling the junction has been presented in [76] as well and is replicated inside the region that is marked with a dotted line in Fig. 3.6b.

Basic Formulation

In the following, the symmetric case is considered meaning the coaxial ports are identical. Then, with the port definitions given in Fig. 3.6b and the admittance matrix description of the radial line segment $\mathbf{Y}^{(R)}$ from (4.34), the admittance matrix for the junction can be written as

$$\mathbf{Y} = \begin{bmatrix} jB_a + Y_r & -Y_r & -Y_{1,2}^{(R)}/R \\ -Y_r & jB_a + Y_r & Y_{1,2}^{(R)}/R \\ -Y_{2,1}^{(R)}/R & Y_{2,1}^{(R)}/R & Y_{2,2}^{(R)} \end{bmatrix}, \quad (5.21)$$

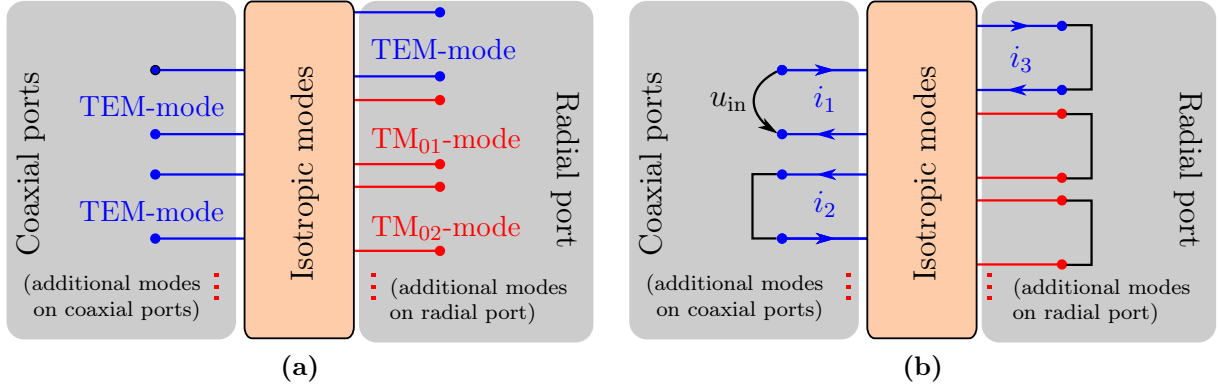


Figure 5.5: Interpretation of the the presented FDFD method in terms of mode termination: (a) All relevant modes which show no azimuthal variation. (b) Example for the interpretation of the implicitly executed evaluation: The modal currents are evaluated for excitation of one coaxial port and short-circuiting of all other ports.

where

$$Y_r = jB_b + \frac{jB_3 + Y_{1,1}^{(R)}}{R^2}. \quad (5.22)$$

The values of $B_a(= B_c)$, B_b , B_3 , and R are given in [76]. Note that [76, Eq. 28] gives R^2 , not R , and that the value of R is very close to 1 for many practical cases. Note also that, due to symmetry of the geometry and reciprocity, only 4 independent entries have to be computed for (5.21).

Adaptations for Comparison with the FDFD

The admittance matrix $Y^{(R)}$ is an analytical description of the radial line given in (4.34). For the following, comparison the complex silicon permittivity will be used with this model. Thereby, the silicon dioxide layers are replaced by silicon and the relevance of the layers for the physics that dominate the junction behavior is assumed to be low. By using this approximation, it is investigated if a homogeneous substrate can be used to model the layered substrate.

5.3.2 Quasi-static Near Field Modeling Using an Effective Admittance

The via-to-plane capacitance is a partial capacitance between a via barrel and one of the planes in a single cavity. The case with homogeneous filling can be evaluated using several methods, e.g. analytical solutions for the capacitances in multi-cavity PCBs [77, 81], or by using analytical descriptions of the coaxial to radial line junction [63, 76]. For the case without scattering from other vias and plane edges an analytic formula from [77] can be simplified to yield

$$C_{vp} = \frac{8\pi\epsilon}{t \ln\left(\frac{r_{\text{Antipad}}}{r_{\text{Barrel}}}\right)} \sum_{n=1,3,5,\dots} \frac{H_0^{(2)}(\theta_a) - H_0^{(2)}(\theta_b)}{k_n^2 H_0^{(2)}(\theta_b)}, \quad (5.23)$$

where $k_n = -\sqrt{\omega^2\mu\epsilon - (n\pi/t)^2}$, $\theta_b = k_n r_{\text{Barrel}}$, and $\theta_a = k_n r_{\text{Antipad}}$. The barrel and antipad radius are denoted by r_{Barrel} and r_{Antipad} , respectively. The thickness of the substrate is given by t . The negative sign is chosen for all k_n because only the fundamental parallel-plate mode is assumed to be able to propagate in the parallel-plate structure.

For the silicon interposer, a parallel and series connection of five elements as depicted in Fig. 5.6 is suggested to model the effective admittance. One capacitance is attributed to each of the silicon dioxide layers, the coaxial one around the via barrel $C_{\text{Ox,barrel}}$ and the one next to the plane metallizations $C_{\text{Ox,plate}}$. Capacitance C_{Substr} and conductance G_{Substr} in parallel are used to model the properties of the localized field parts inside the silicon layer. An overall admittance for the silicon substrate case is computed and related to effective resistance and conductance as

$$Y_{\text{eff}} = j\omega C_{\text{Antipad}} + Y_{\text{inner}} = j\omega C_{\text{eff}} + 1/R_{\text{eff}}, \quad (5.24)$$

where

$$\frac{1}{Y_{\text{inner}}} = \frac{1}{j\omega C_{\text{Ox,barrel}}} + \frac{1}{j\omega C_{\text{Substr}} + G_{\text{Substr}}} + \frac{1}{j\omega C_{\text{Ox,plate}}}. \quad (5.25)$$

The capacitance $C_{\text{Ox,plate}}$ can be estimated using a method similar to the one presented in [102, Appendix I]: From an extraction with a quasi-static 3D electromagnetic field solver [109] by simulating the structure with and without the oxide layer, it is estimated to range from 1 pF (50 μm silicon layer thickness) to 3 pF (100 μm silicon layer thickness) for the parameter values given in the caption of Fig. 5.6 and a silicon conductivity of up to 10 S/m.

To compute C_{Substr} , (5.23) is used with the real part of the considered silicon permittivity.

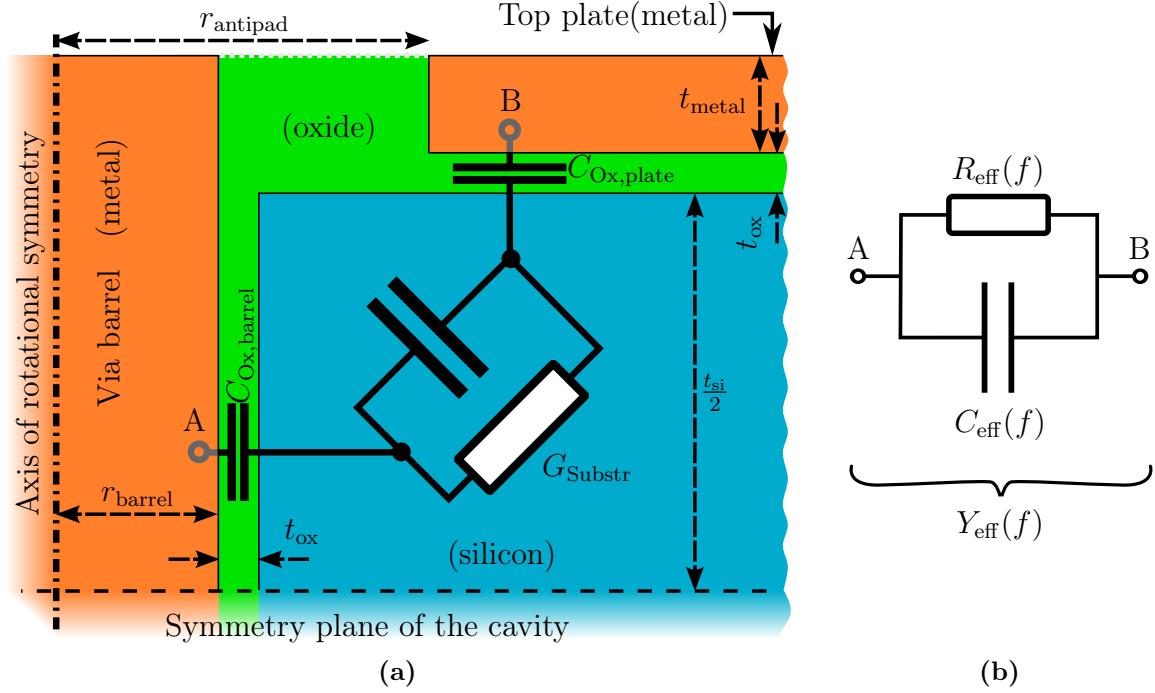


Figure 5.6: (a) Considered cross-section and (b) the corresponding equivalent circuit for modeling of the near-fields of the coaxially excited via with element values which are functions of the frequency. Typical dimensions are: via barrel radius $a = 15 \mu\text{m}$, antipad radius $b = 30 \mu\text{m}$, pitch $d_{\text{vias}} = 200 \mu\text{m}$, silicon substrate thickness $t_{\text{si}} = 100 \mu\text{m}$, plate thickness $t_{\text{metal}} = 5 \mu\text{m}$, and silicon dioxide thickness $t_{\text{ox}} = 1 \mu\text{m}$. Typical material properties are: $\epsilon_{\text{r,oxide}} = 4$ and $\epsilon_{\text{r,silicon}} = 11.9$.

To compute the conductance, the relation

$$C/G = \epsilon_{\text{silicon}}/\sigma_{\text{silicon}} \quad (5.26)$$

is applied, which relates the already computed capacitance to the parallel conductivity [110, Ch. 5-7]. Reference results are obtained with a quasi-static 3D electromagnetic field solver [109]. Using these results, the capacitance parts corresponding to the outer regions must be determined in separate simulations and subtracted from the complete admittance. Fig. 5.7 shows the results obtained for the case where a silicon conductivity is introduced. A good agreement with the reference results is obtained for the 1 S/m-case, a fair agreement for the 10 S/m-case. As will be seen in the overall results, this agreement is sufficient for the crosstalk analysis of many relevant cases.

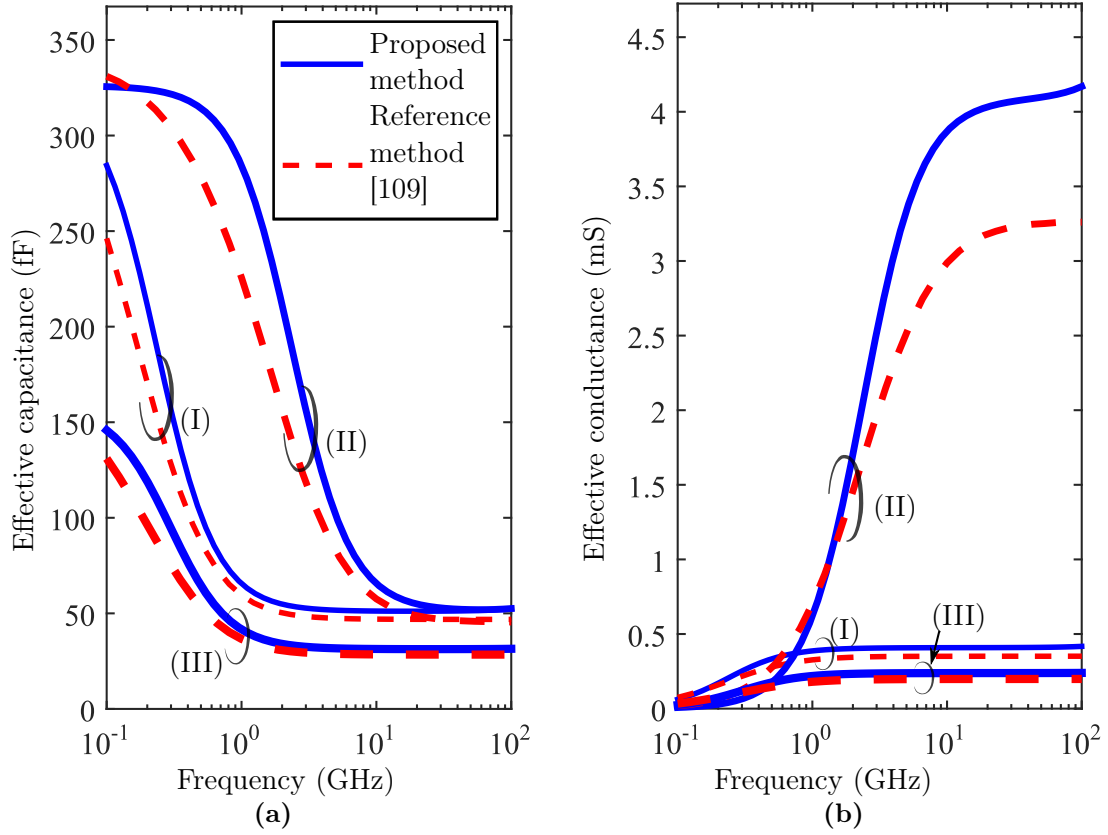


Figure 5.7: Validation of the proposed method for the computation of equivalent capacitance and conductance with three examples: (I) silicon thickness $100\text{ }\mu\text{m}$ and conductivity 1 S/m , (II) silicon thickness $100\text{ }\mu\text{m}$ and conductivity 10 S/m , (III) silicon thickness $50\text{ }\mu\text{m}$ and conductivity 1 S/m . All other parameter values are defined in the caption of Fig. 5.6.

5.4 Comparison and Validation

In the following, several comparisons of the proposed FDFD-method with FEM full-wave results and with results from the proposed approximate methods are performed for validation. These are carried out in a frequency range from 100 MHz to 100 GHz and for typical parameter values. In the frequency range from 100 GHz to 500 GHz which will also be considered in the application section, the silicon conductivity has a lower influence on the properties than at lower frequencies. Therefore, the validation focuses on the first frequency range in order to highlight the effects that occur due to the silicon conductivity at lower frequencies.

Most general-purpose full-wave solvers are restricted with respect to the shapes that wave ports can have, as they have to be planar in most case. The used FEM full-wave simulator

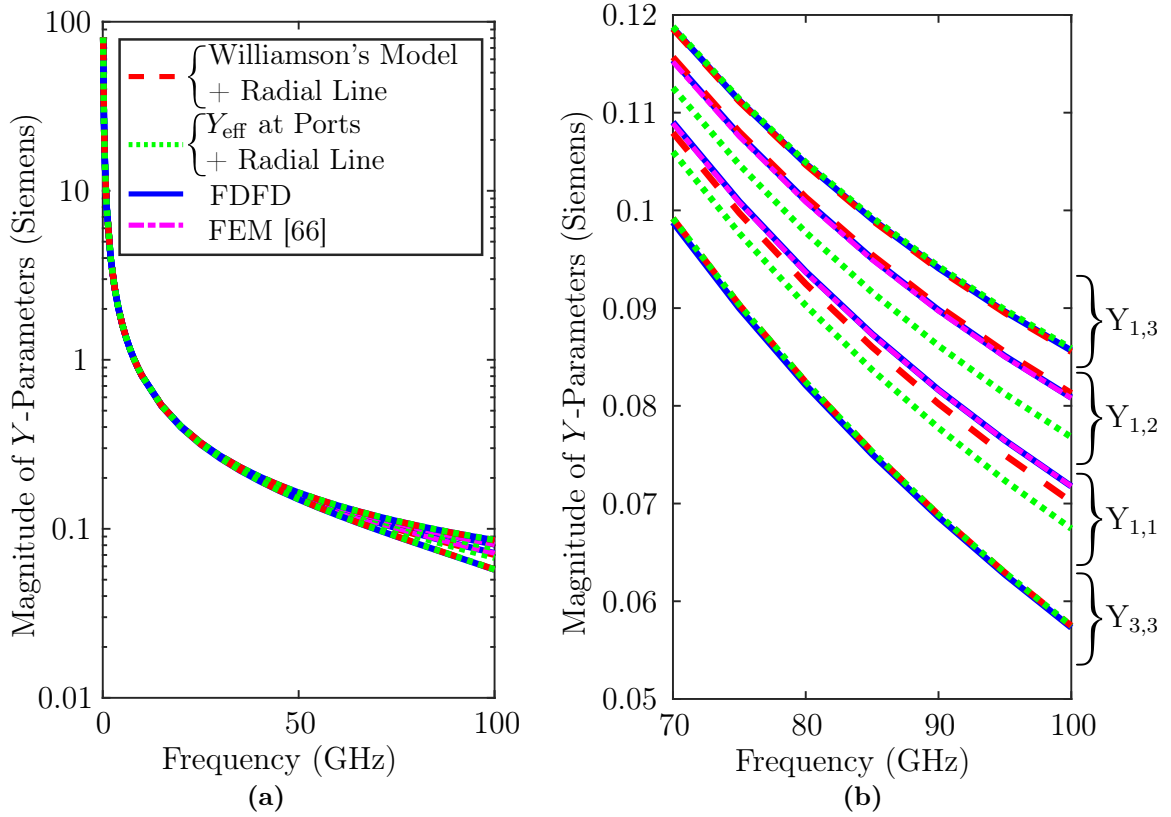


Figure 5.8: Validation results for barrel radius of $15\ \mu\text{m}$, antipad radius of $30\ \mu\text{m}$, silicon layer thickness of $50\ \mu\text{m}$, oxide layer thickness of $1\ \mu\text{m}$, radial waveguide radius of $100\ \mu\text{m}$, and a silicon conductivity of $10\ \text{S/m}$. The silicon permittivity is $11.9 \cdot \epsilon_0$ and the silicon dioxide permittivity is $4 \cdot \epsilon_0$. The reference plane is at the inner plane of the metallizations with the result that the coaxial antipad section is excluded. The legend refers to the models given in Fig. 3.6. (a) shows the complete frequency range, (b) the detail for the upper part of the frequency range with labeling of the parameters. Phases of all parameters are close to $\pm 90^\circ$. Results from FEM [66] are only available for $Y_{1,1}$, $Y_{1,2}$, $Y_{2,1}$, and $Y_{2,2}$. Figure and text adapted from [13].

[66] supports no radial ports. Therefore, the comparisons are carried out in terms of the coaxial via ports of which two are assigned at the top and the bottom of each via. This comparison is carried out with the different simulations to compare as follows: In the FDFD-method, the procedure presented before computes an admittance matrix with the first two indices corresponding to the top and bottom coaxial ports. The admittance matrix for the case the the radial line port is short-circuited (at some distance from the via barrel) is given by the upper left block $\mathbf{Y}_{[1,2],[1,2]}$. These admittance parameters can be compared to FEM simulations because a PEC boundary conditions can be applied on the radial line

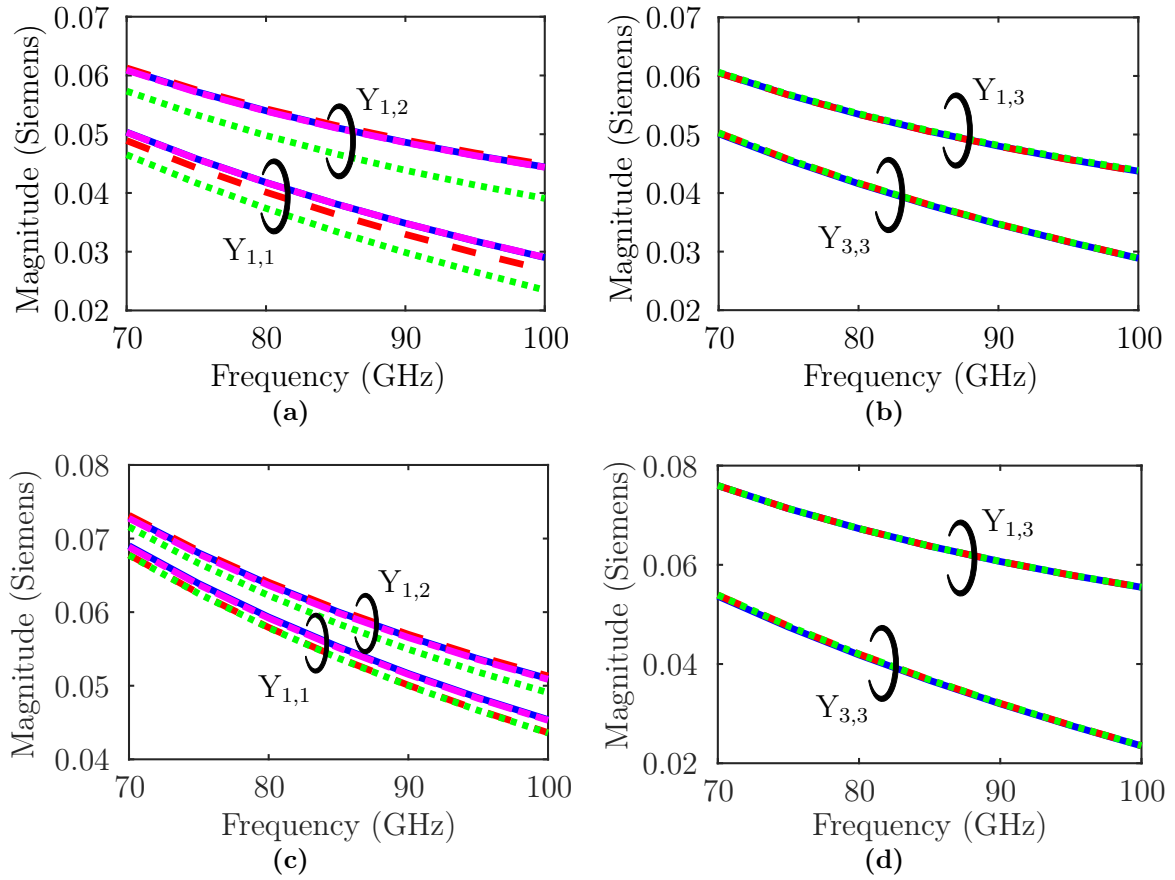


Figure 5.9: The configuration described in the caption of Fig. 5.8 applies, except for the following modifications: (a)–(b) The silicon layer thickness of $100\mu\text{m}$ is used. (c)–(d) The barrel radius and antipad radii are $5\mu\text{m}$ and $10\mu\text{m}$, respectively. Figure taken from [13].

port surface. Results for the other parameters cannot be compared with any FEM results but with result from the two approximate, analytical methods from Section 5.3.

In the following, the analytical description of a radial line segment with layered dielectric given in Section 4.7.2 is concatenated with the approximate near field models. The magnitudes of selected independent admittance parameters are shown in Figs. 5.8 and 5.9. At low frequencies, the structure is electrically short (partly due to the slow-wave effect) and all admittance parameters go to infinity. At higher frequencies, the structure is electrically longer and the effect of the localized near fields on the admittance parameters becomes more significant.

Several variations for parameters have been performed. Results for variations of the silicon layer thickness and of the barrel and antipad radii are shown in Fig. 5.9. With these and other variations including those of oxide thickness and silicon conductivity good agreement

is observed. Parameters $Y_{1,3}$ and $Y_{3,3}$ can only be compared with the approximate analytical methods and, again, a good agreement is observed. Parameters $Y_{1,1}$ and $Y_{1,2}$ can be compared for all mentioned methods and an excellent agreement of FDFD results with the FEM results is observed. Comparing the approximate analytical methods, the Williamson method, which ignores existence of the oxide layers, shows the better agreement with the reference results, especially for the higher frequencies. It is concluded that the FDFD method provides a high accuracy and, depending on the frequency range, the Williamson model can be used to obtain a good to fair accuracy.

5.4.1 Convergence Behavior and Conclusions

As has already been discussed, a high numerical efficiency is not required because in typical application scenarios of the near field model many identical vias of an array are simulated the near field needs to be computed only once. Most full-wave solvers could also compute this problem in acceptable times but lack the required radial port. The near field could only be obtained through a de-embedding procedure. In order to limit the computation time of the proposed FDFD method, the dependence of the accuracy of the results in terms of network parameters on the grid resolution are of interest. With increasing grid resolution, a convergence is expected. For a required accuracy of the network parameters, a necessary grid resolution can then be estimated and be used as the starting point for an iterative grid refinement. The expected convergence behavior can be observed in the example presented in Fig. 5.10: starting with a total number of 238 grid points of the primary grid, the grid resolution is increased up to 15232 grid points. Except for the self admittance parameter at the radial port $Y_{3,3}$, even the results for the lowest resolution are already close to those for the highest resolution. For the highest resolution with a total of 15232 grid primary points a computation time of approximately 0.55 s per frequency step has been measured. From experience, this is fast enough for most of the applications in the simulation of TSV arrays. Therefore, the FDFD-model is used exclusively in the following applications with the PBV.

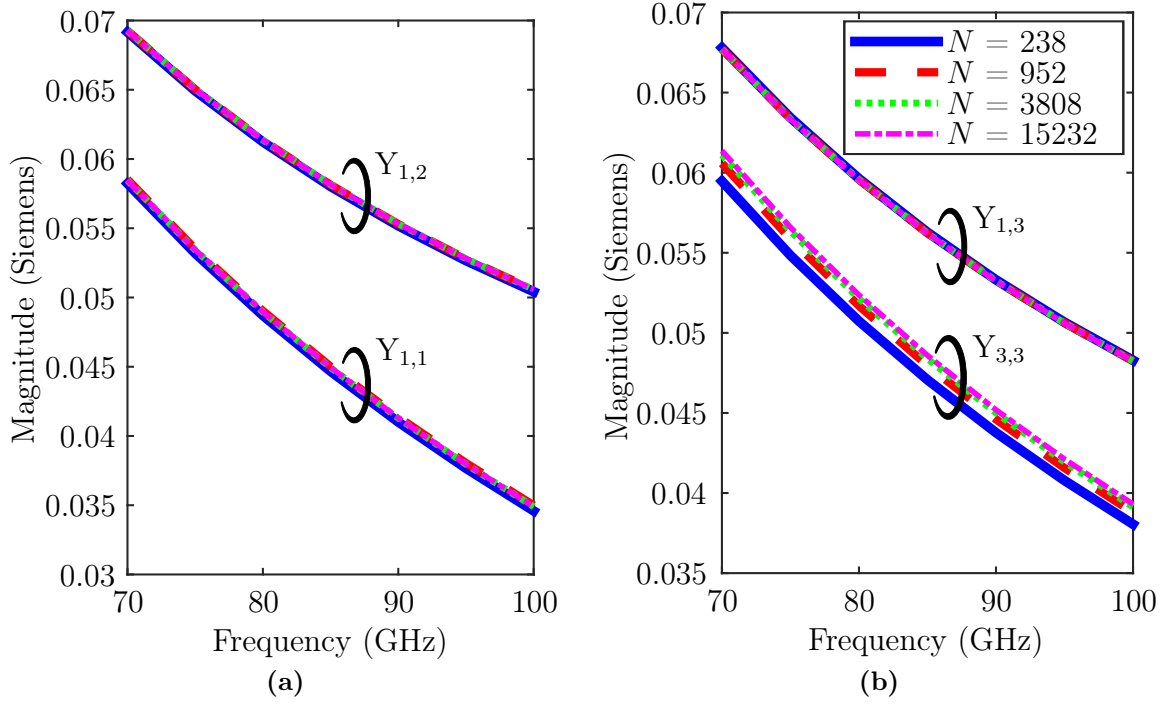


Figure 5.10: Analysis of convergence with increasing number of grid points: starting with a small number of grid points, e.g. only two grid points assigned to the oxide layers, the radial and axial number of grid points are doubled. The legend gives the total number N of primary grid points of the computational domain. The analysis uses a barrel radius of $15\text{ }\mu\text{m}$, antipad radius of $30\text{ }\mu\text{m}$, silicon layer thickness of $100\text{ }\mu\text{m}$, oxide layer thickness of $1\text{ }\mu\text{m}$, radial waveguide radius of $80\text{ }\mu\text{m}$, and a silicon conductivity of 10 S/m . Silicon permittivity is $11.9 \cdot \epsilon_0$ and silicon dioxide permittivity is $4 \cdot \epsilon_0$. Figure and text adapted from [13].

5.5 Application in Physics-Based Via Modeling

In this section, near field models are used in the PBV model in conjunction with the far field models presented in the previous chapter to obtain network parameter descriptions of silicon interposers. A description is thereby obtained for via links assigned to single vias and referenced to their coaxial ports. These ports are illustrated as A2 and B2 in Fig. 5.1.

Three different variants are considered for the PBV modeling and listed in Table 5.1. For the first variant, it is assumed that the near field model can be represented as in Fig. 3.6c, i.e., with only admittances which are parallel to each (coaxial) via port, and thus analogous to the Y_{eff} in Fig. 3.6c. Qualitatively, it can be expected that this is valid for low frequencies. From the FDFD-admittance matrix \mathbf{Y} , such an admittance Y_{ap} can be obtained. By identification of the entries $Y_{1,1} = Y_{\text{ap}} + Y_{1,1}^{(R)}$ and $Y_{1,2} = -Y_{1,1}^{(R)}$ one concludes

Variant	Description/Comment
1	Only parallel admittances Y_{ap} (cf. (5.27)) to model the near fields.
2	Segmentation of near fields as three-port at inner (barrel) radii.
3	As Variant 2, but with first anisotropic modes [56, 94].

Table 5.1: Physics-Based Via Model variants in Figs. 5.11 to 5.15. Table adapted from [13].

that

$$Y_{\text{ap}} = Y_{1,1} + Y_{1,2}. \quad (5.27)$$

The propagating field model uses only the isotropic mode for variants 1 and 2 and additionally the first anisotropic modes for variant 3. As it is discussed in Section 3.5.1 and validated in Section 6.2, anisotropic modes are short-circuited for the propagating field model. A radial line description as presented in (4.34) is used for de-embedding/extraction of a near field model from the FDFD results. This near field model is used in variants 2 and 3 for concatenation at the radial ports (ports C in Fig. 5.1). It has to be noted that a de-embedding is not strictly necessary as the radial ports of the CIM could also be adapted. Even if an FDFD domain size is chosen such that the corresponding CIM radial ports overlap, this would still be supported by the CIM method.

The geometry and results of the first application example are depicted in Fig. 5.11 in terms of magnitudes of scattering parameter results normalized to 50Ω . The structure has two signal and four ground vias. Due to the symmetry of the structure, only four of the overall 16 network parameters are of interest. As can be seen, the agreement of the proposed PBV methods show a good agreement with the FEM reference simulations [66]. FEM simulation have been carried out both with metal component of perfect conductivity and with metal component with the conductivity of aluminum of $\sigma = 3.4 \times 10^7 \text{ S/m}$. No significant differences can be observed between these two result sets. Larger deviations between the different PBV model variants can be observed only for variant 1 compared to the other variants. The inclusions of anisotropic modes has a small impact as is apparent from the good agreement of variants 1 and 2.

As has been discussed before, the consideration of complete plane metallizations is one of the limiting cases that enables an efficient physics-base modeling. In order to give in insight into the applicability range two cases with plane perforations have been simulated using FEM full-wave simulations and the results have been compared to the PBV results without plane perforations. The two cases of plane perforations are named “Mod.1” and “Mod.2” in Fig. 5.12 and can be described as follow: The first structure is named “Mod.1” and has comparatively large circular cutouts of only the top metallizations. The remainder of the structure (configuration of signal and ground vias) is the same as the as in Fig. 5.11. The

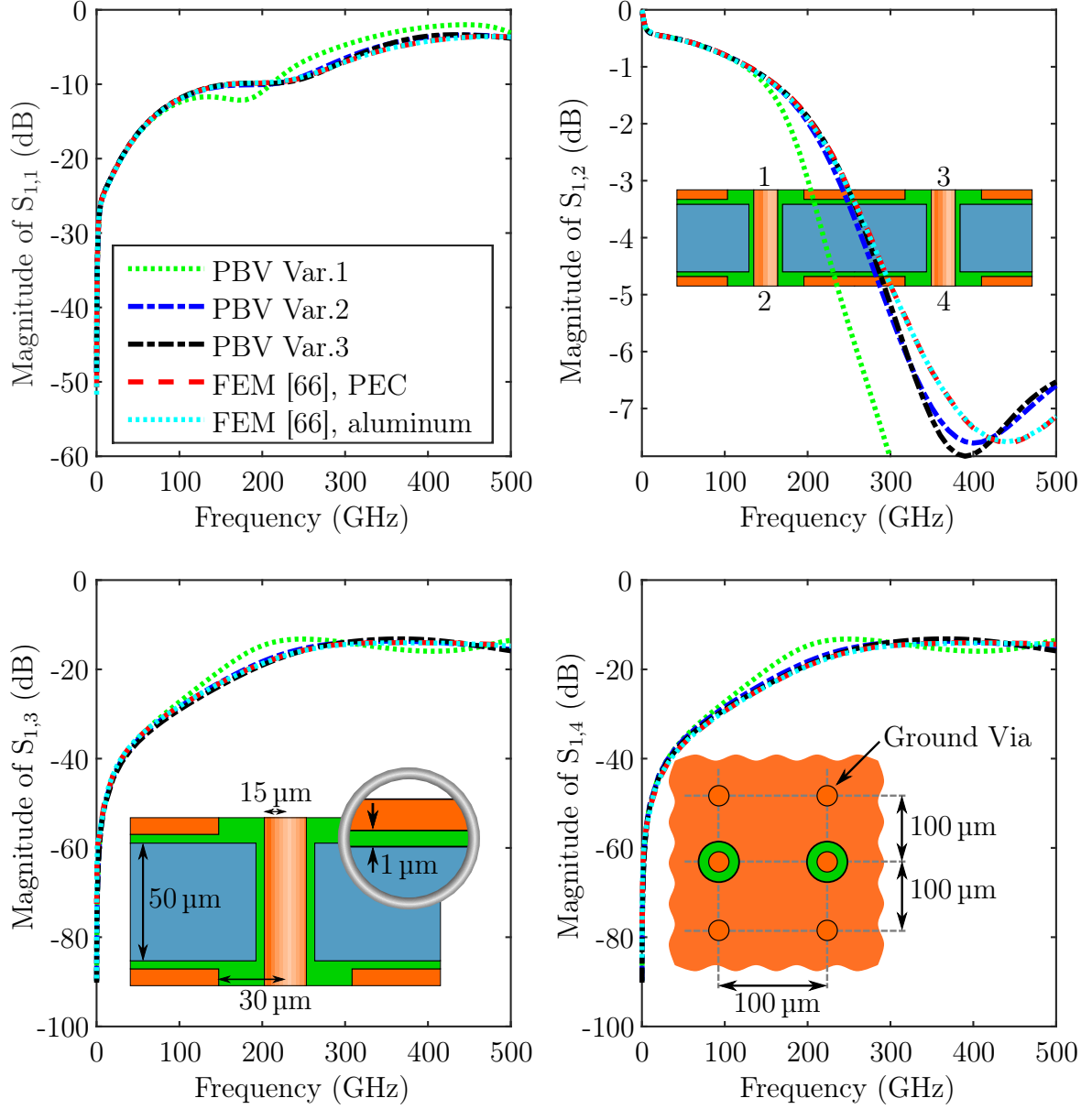


Figure 5.11: First application example with a pair of signal vias accompanied by four ground vias in an infinite parallel plate structure. In the reference FEM simulations both PEC and aluminum are considered as material for the via barrels and metallic plates. Dimensions are given in the insets, the silicon conductivity is 10 S/m . The silicon permittivity is $11.9 \cdot \epsilon_0$ and the silicon dioxide permittivity is $4 \cdot \epsilon_0$. A typical simulation time per frequency point for the FEM is 30 s; a typical time for the proposed method is 0.3 s. Figure taken and text adapted from [13].

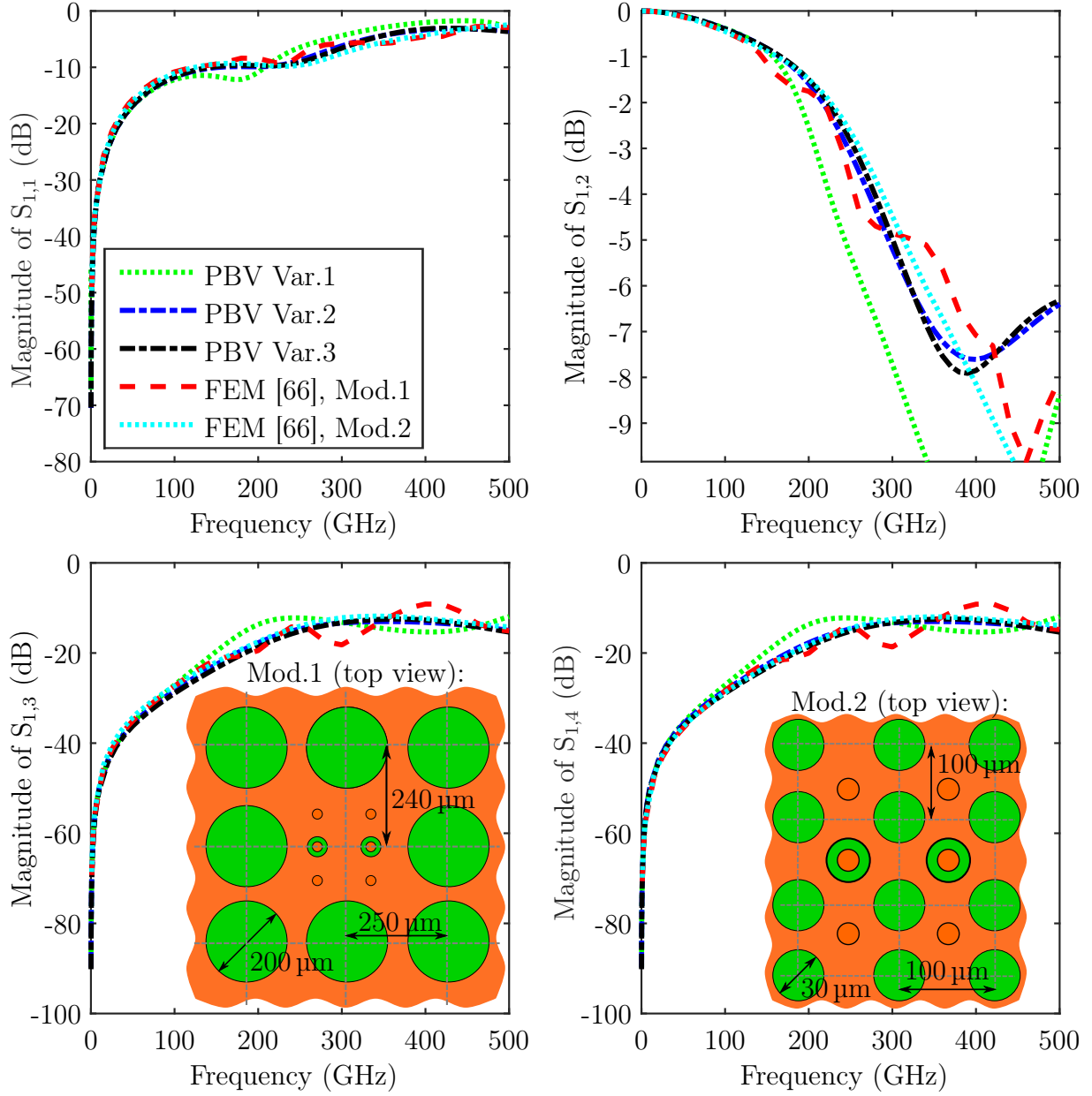


Figure 5.12: Second application example with a pair of signal vias accompanied by four ground vias as in Fig. 5.11 circular perforations. Via dimensions are the same as in Fig. 5.11, the silicon conductivity is 0 S/m, silicon permittivity is $11.9 \cdot \epsilon_0$ and silicon dioxide permittivity is $4 \cdot \epsilon_0$. The geometry of the plane perforations is given in the insets. Variant “Mod.1” has circular cutouts in the top plane, variant “Mod.2” has circular cutouts in both planes. Typical simulation times per frequency point for the FEM are 15 minutes (Mod.1) and 10 minutes (Mod.2); a typical time for the proposed method is 0.3 s. Figure and text adapted from [13].

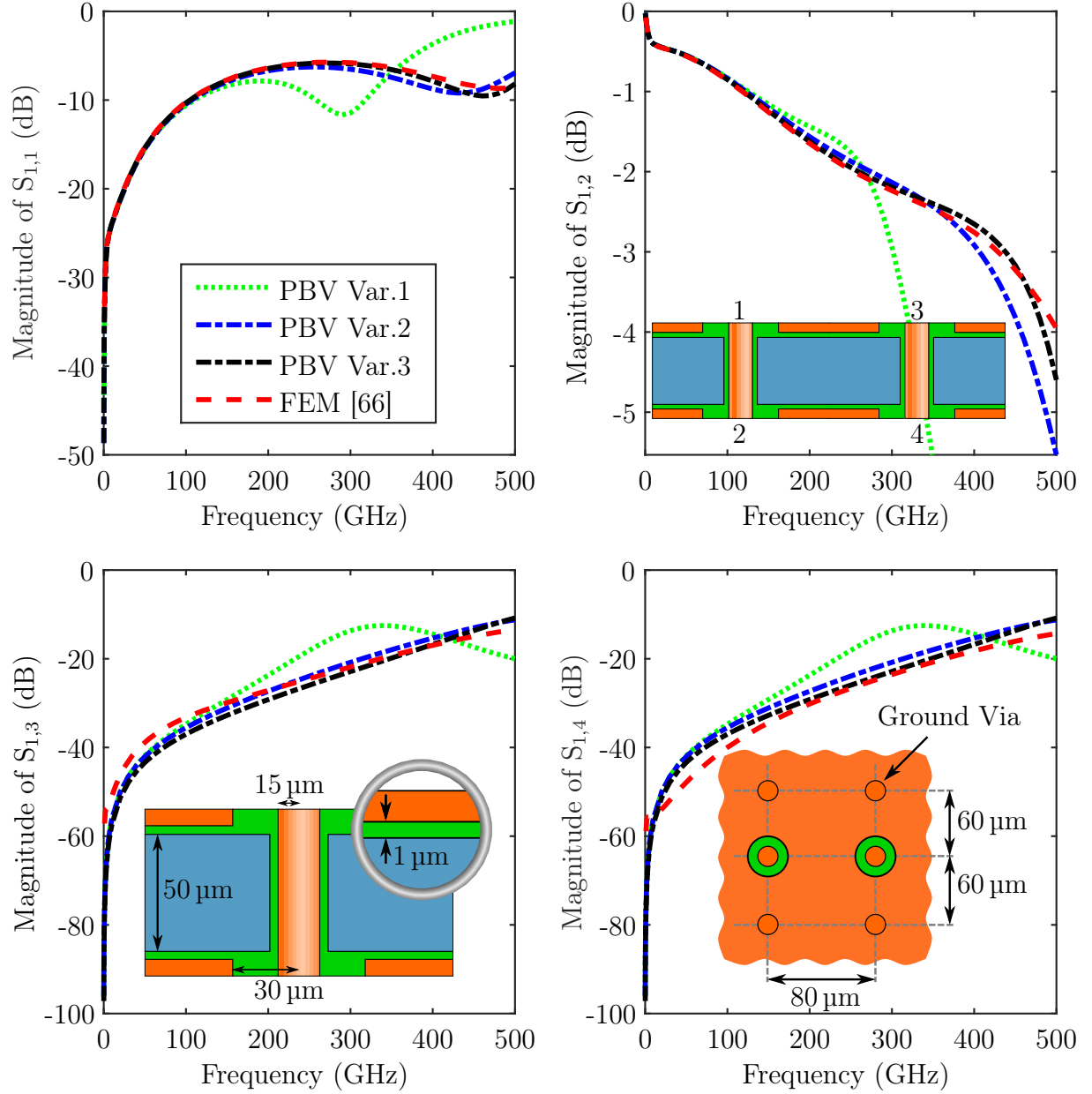


Figure 5.13: Third application example with a pair of signal vias accompanied by four ground vias. The difference of the configuration compared to Fig. 5.11 is the closer spacing of the vias. The silicon conductivity is 10 S/m, the silicon permittivity is $11.9 \cdot \epsilon_0$, and silicon dioxide permittivity is $4 \cdot \epsilon_0$. Figure and text taken from [13].

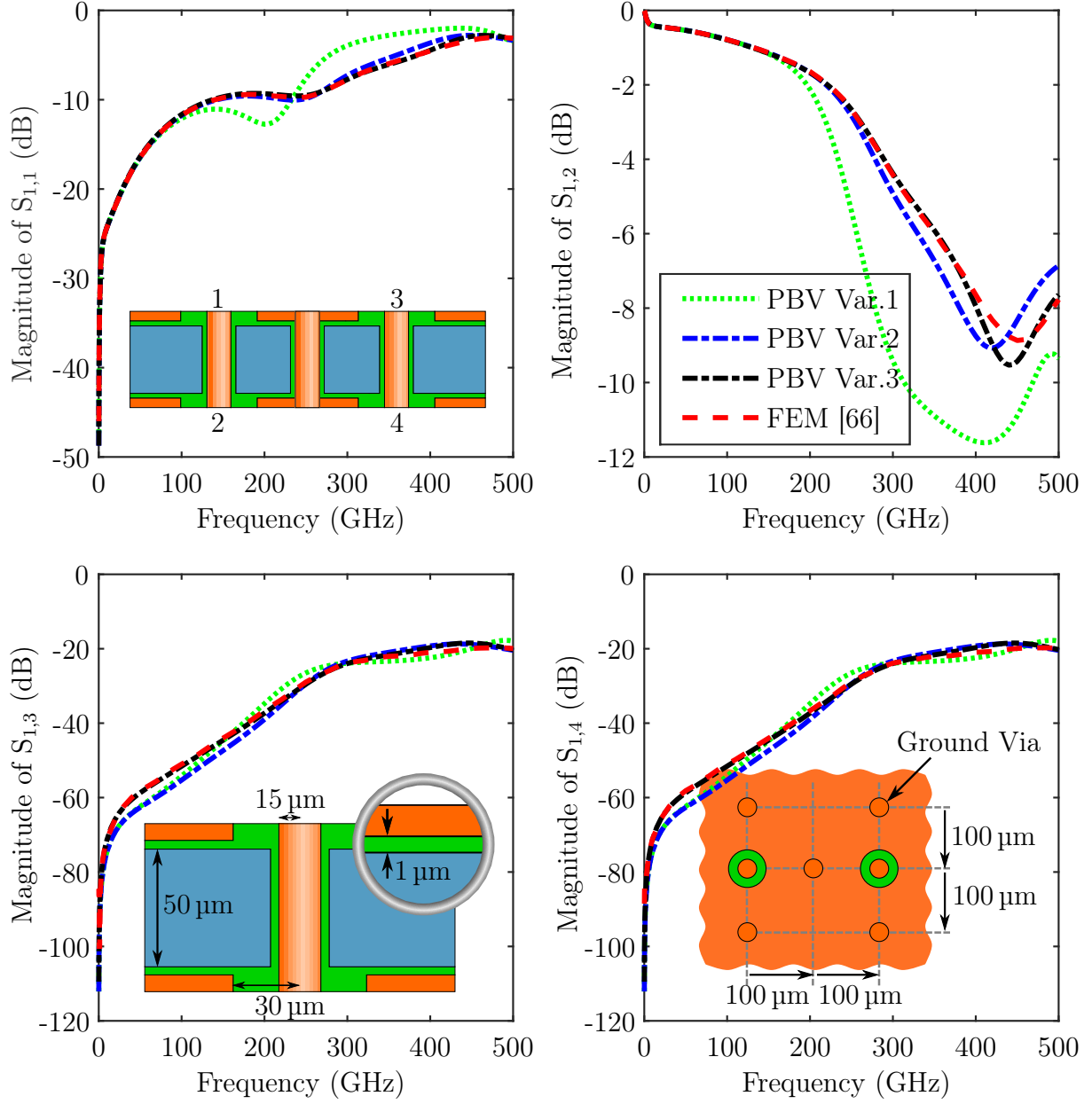


Figure 5.14: Fourth application example with an additional, central ground via compared to Fig. 5.11. Dimensions are given in the insets, the silicon conductivity is 10 S/m. Figure and text taken from [13].

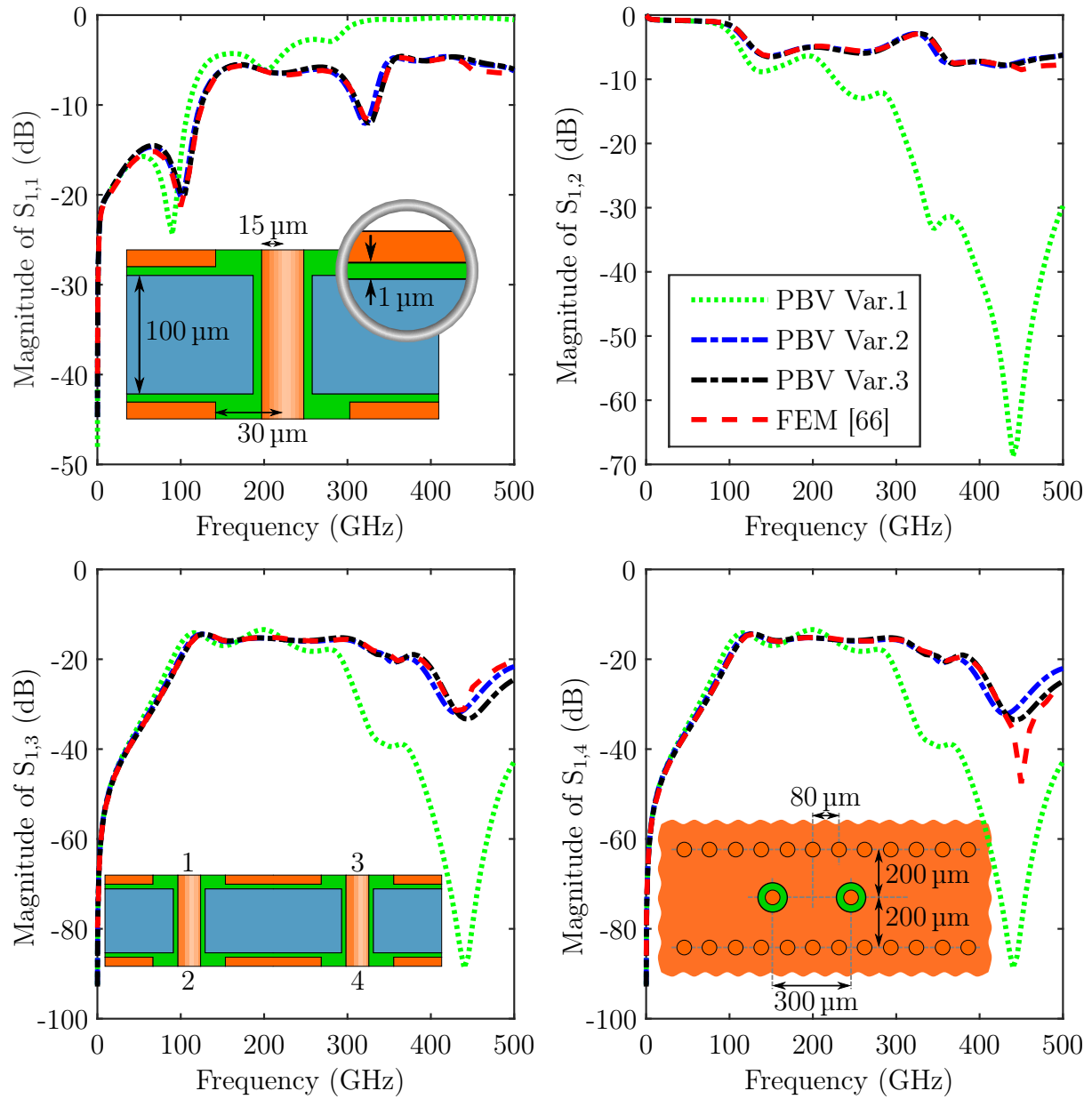


Figure 5.15: Fifth application example: two signal vias with ports at both ends and two rows of ground vias (via fences). Dimensions are given in the insets, the silicon conductivity is 10 S/m. Figure and text taken from [13].

second structure is named “Mod.2” and has comparatively small cutouts. These cutouts are around and between the vias (which again have the same configuration as in Fig. 5.11) and have sizes comparable to the via dimensions. In this case, the cutouts are applied to both the top and the bottom metallizations. Because models for the cutouts are not available for the PBV, they are not considered in it. The agreement of the results is still good up to 150 GHz for variant “Mod.1” and to about 400 GHz for variant “Mod.2”. In the FEM simulations empty air boxes with absorbing boundary conditions are attached to the areas of the perforated planes to model the environment. The influence in practical environments consisting of, e.g., redistribution layers of an interposer is thereby ignored.

A prerequisite for the applicability of the PBV model as presented in the previous chapter is the coupling of vias only through a propagating field. This condition is met if the via pitch is large enough in comparison to the distance at which a coupling through cut-off higher order parallel plate modes occurs. This distance in lateral directions is dependent on several parameters. It is, e.g., proportional to the height of the cavity between the plane metallizations. For the PCB application of the PBV, it has already been observed in [65] that an additional near-field coupling should be included in order to accurately model cases of very close via spacing. Using FEM full-wave results, it is investigated in the example shown in Fig. 5.13 which influence reduced distances between vias have. In comparison to the structure in Fig. 5.11 only the distances between signal vias and to ground vias are reduced, all other parameters are the same. It can be observed that there is still a good agreement with the reference full-wave results for the transmission $S_{1,1}$ and the reflection $S_{1,2}$. In contrast, the crosstalk parameters $S_{1,3}$ and $S_{1,4}$ show larger deviations. These deviations are most pronounced towards lower frequencies.

The next example is shown in Fig. 5.14 and allows to investigate the effect of an intermediate ground via between two signal vias. Variant 1 of the PBV model shows again the strongest deviations for frequencies above 150 GHz. Variant 2 also shows stronger deviations from the reference results Variant 3. Therefore, in this case, a clear advantage of including the first anisotropic modes in the far field model can be observed.

In the last example, which is shown in Fig. 5.15, a structure that has some similarity with a substrate integrated waveguide is considered. The structure consists of two signal vias and several ground vias constituting two ground via fences. Using the PVB in Variants 2 and 3, a good agreement can be observed up to about 400 GHz

In summary, it can be concluded that this section proves that with the proposed adaptation of the PBV, i.e., by using a local FDFD-based full-wave modeling and the CIM with wave number for the layered structure, an accurate modeling technique is available. The accuracy has been validated using several relevant example structure. The best accuracy

can be obtained by using the complete near field model which is obtained through a de-embedding procedure and by using also the first anisotropic mode in the CIM for the far field model.

5.6 Conclusions

An FDFD method has been presented for the near field modeling of TSV with the physics-based approach. Due to the compatible radial port definitions and its numerical efficiency it is well suited for the intended purpose. An FDFD method might also be a viable option for the computation of the coupling between vias through localized fields which is not covered by the PBV as presented in this thesis.

Chapter 6

Application to Large Scale Crosstalk Analysis of TSV Arrays

Up to this point, all relevant adaptations for the physics-based modeling of TSVs in silicon interposers have been discussed and validated for small structures. In the following, the PBV is also validated for mid-size TSV arrays and the mode terminations proposed in Section 3.5.1 are validated. Further, adaptations of the computational procedure are discussed that allow for a higher computational efficiency when computing the far field results. This enables the simulation of large TSV arrays and the investigation of all relevant interactions in terms of crosstalk. The definition of a power sum of uncorrelated crosstalk is motivated and subsequently used to investigate the crosstalk properties in larger via arrays. Finally, the effects of variations of several design parameters, such as silicon conductivity and pitch, on the defined total crosstalk are investigated. This enables an optimization of parameters within the bounds imposed by fabrication processes to reduce the crosstalk.

6.1 Adaptations and Optimizations for Large Scale Analysis

As discussed in Section 3.6.3, the CIM that is used for computation of the far field properties relates several modes on circular ports and single modes on linear ports. For the results in terms of scattering parameters that are referenced to the fundamental modes on coaxial via ports, the description in terms of the isotropic modes on radial¹ ports is required. The latter is concatenated with the near field models to obtain the desired result. It is obtained by enforcing specific boundary conditions on the anisotropic ports, i.e., these modes are terminated with impedances that correspond to these boundary conditions.

Conventionally, the network parameters are first computed for of all considered modes on

¹In the corresponding discussion in [14, Sec. II.C], it is erroneously referred to the coaxial ports instead of the radial ports.

all ports. The mode terminations are then enforced, e.g., by using sub-matrices of admittance or impedance parameter matrices to apply short circuit or open circuit terminations, respectively. The numerical efficiency of the computation of network parameters using the CIM can be improved by including port/mode terminations in the matrix setup and solution steps of CIM computation. For reduction of ground vias, this has already been presented, e.g., in [111]. In the following both short-circuit and open-circuit boundary conditions are included in the CIM solution step.

6.1.1 Derivation of Optimized Solution

The CIM as formulated and denoted in Appendix D is assumed with a matrix equation that relates vectors of modal voltages and currents \mathbf{V} and \mathbf{I} , respectively, by matrices \mathbf{U} and \mathbf{H} as

$$\mathbf{UV} = \mathbf{HI}. \quad (6.1)$$

The conventional evaluation then starts from the (parallel plate) admittance matrix given by $\mathbf{Y}_{pp} = \mathbf{H}^{-1}\mathbf{U}$ or the impedance matrix given by $\mathbf{Z}_{pp} = \mathbf{U}^{-1}\mathbf{H}$.

For the proposed approach, the CIM matrices \mathbf{U} and \mathbf{H} are ordered or set up with blocks which relate the modal voltages and currents of fundamental modes on signal vias (index f), open-circuited ports (index o), and short-circuited ports (index s). The assignment of modes to the last two categories will be discussed later in this section. The block-wise representation can be written as

$$\begin{bmatrix} \mathbf{U}_{ff} & \mathbf{U}_{fo} & \mathbf{U}_{fs} \\ \mathbf{U}_{of} & \mathbf{U}_{oo} & \mathbf{U}_{os} \\ \mathbf{U}_{sf} & \mathbf{U}_{so} & \mathbf{U}_{ss} \end{bmatrix} \begin{bmatrix} \mathbf{V}_f \\ \mathbf{V}_o \\ \mathbf{V}_s \end{bmatrix} = \begin{bmatrix} \mathbf{H}_{ff} & \mathbf{H}_{fo} & \mathbf{H}_{fs} \\ \mathbf{H}_{of} & \mathbf{H}_{oo} & \mathbf{H}_{os} \\ \mathbf{H}_{sf} & \mathbf{H}_{so} & \mathbf{H}_{ss} \end{bmatrix} \begin{bmatrix} \mathbf{I}_f \\ \mathbf{I}_o \\ \mathbf{I}_s \end{bmatrix}. \quad (6.2)$$

The two terminations $\mathbf{V}_s = \mathbf{0}$ and $\mathbf{I}_o = \mathbf{0}$ for short- and open-circuited port, respectively, are now enforced in (6.2). The second and third row of (6.2) then relate voltages \mathbf{V}_f and \mathbf{V}_o , and currents \mathbf{I}_f , and \mathbf{I}_s . Of these quantities, \mathbf{V}_o (modal voltages of open-circuited modes) and \mathbf{I}_s (modal currents of short-circuited modes) are not relevant for the subsequent computations and can therefore be eliminated. By permutation and insertion into the first row

$$\tilde{\mathbf{U}}\mathbf{V}_f = \tilde{\mathbf{H}}\mathbf{I}_f \quad (6.3a)$$

is obtained [14], where

$$\tilde{\mathbf{U}} = \mathbf{U}_{ff} - \mathbf{H}_{fs}\mathbf{A}^{-1}\mathbf{B} + \mathbf{U}_{fo}\mathbf{U}_{oo}^{-1}(\mathbf{H}_{os}\mathbf{A}^{-1}\mathbf{B} - \mathbf{U}_{of}), \quad (6.3b)$$

$$\tilde{\mathbf{H}} = \mathbf{H}_{ff} + \mathbf{H}_{fs}\mathbf{A}^{-1}\mathbf{C} - \mathbf{U}_{fo}\mathbf{U}_{oo}^{-1}(\mathbf{H}_{os}\mathbf{A}^{-1}\mathbf{C} + \mathbf{H}_{of}), \quad (6.3c)$$

with

$$\mathbf{A} = \mathbf{1}_{ss} - \mathbf{H}_{ss}^{-1}\mathbf{U}_{so}\mathbf{U}_{oo}^{-1}\mathbf{H}_{os}, \quad (6.3d)$$

$$\mathbf{B} = \mathbf{H}_{ss}^{-1}\mathbf{U}_{sf} - \mathbf{H}_{ss}^{-1}\mathbf{U}_{so}\mathbf{U}_{oo}^{-1}\mathbf{U}_{of}, \quad (6.3e)$$

$$\mathbf{C} = -\mathbf{H}_{ss}^{-1}\mathbf{H}_{sf} + \mathbf{H}_{ss}^{-1}\mathbf{U}_{so}\mathbf{U}_{oo}^{-1}\mathbf{H}_{of}, \quad (6.3f)$$

and the identity matrix $\mathbf{1}_{ss}$ of the size equal to the number of short-circuited modes. In (6.3b–f) several parts can be identified which appear repeatedly and should hence be computed only once to obtain a higher numerical efficiency. The parallel plate admittance and impedance in terms of the fundamental modes on circular ports are obtained as $\mathbf{Y}_{pp}^{(f)} = \tilde{\mathbf{H}}^{-1}\tilde{\mathbf{U}}$ and $\mathbf{Z}_{pp} = \tilde{\mathbf{U}}^{-1}\tilde{\mathbf{H}}$, respectively

6.1.2 Discussion of Savings

It should be emphasized that the method proposed above does not introduce any simplifying assumptions. Instead, it leads to a reduction in the number of required calculation steps by directly computing results for specific boundary conditions instead of computing results for arbitrary boundary conditions in an intermediate step.

Saving in Setup Step

Fewer elements have to be computed and stored in memory in the matrices $\tilde{\mathbf{U}}$ and $\tilde{\mathbf{H}}$ compared to the full/general CIM matrices \mathbf{U} and \mathbf{H} . Specifically, the elements in the sub-matrices/matrix blocks \mathbf{U}_{fs} , \mathbf{U}_{os} , \mathbf{U}_{ss} , \mathbf{H}_{fo} , \mathbf{H}_{oo} , and \mathbf{H}_{so} do not need to be computed. The improvement in efficiency of matrix setups is significant if one or more of the following is true:

- A large number of modes on circular ports is used to accurately model the anisotropy in radial wave propagation.
- The layout features many ground vias in comparison to the total number of vias. This can be the case, e.g., for substrate integrated waveguides in silicon interposers.

- There are many linear ports compared to the number of circular ports which are terminated with an open circuit. This can be, e.g., the case for evaluation at higher frequencies where a finer discretization of contours is needed.

The three conditions refer to three ratios which should be large in order to obtain a gain in efficiency. In the limit of all these ratios being large it can be seen that, at most, a reduction of memory and matrix setup time of 50 % is possible.

Saving in Solution Step

While for small arrays, the setup times typically dominate the overall computation time, the situation is different for large arrays where the solution step dominates. This can be attributed to the fact that the two parts scale differently. Further, small systems of equations can often be stored in the CPU cache memory which leads to faster computations for the same algorithmic efficiency. For large TSV arrays, the PBV computation time is dominated by the solution of the matrix equations for the computation of the parallel plate impedance/admittance. For the matrix equations in (6.1) and (6.3), the overall worst-case numerical complexity is $\mathcal{O}(n^3)$ [14]. For the conventional use of the CIM, $n = n_f + n_o + n_s$ where n_f , n_o , and n_s are the numbers of fundamental, open-circuited, and short-circuited ports, respectively. For the method described by (6.3), the numerical complexity is governed by the port type with the highest number of ports, i.e. in this case $n = \max\{n_f, n_o, n_s\}$. Consider, e.g., the case in which a large number of anisotropic modes on circular ports is used that gives a number of short-circuited ports that is larger than the number of open-circuited ports on the discretized plane contour. In this case, the number of open-circuited ports governs the n of the above numerical complexity.

6.2 Validation of the PBV Model for Mid-Scale TSV Arrays

In the following, several TSV arrays in metal-clad interposer of medium sizes are simulated. The simulations aim at the validation of the proposed PBV approaches by comparison with FEM full-wave simulation results [112]. The magnitudes of scattering parameters presented in the following show the crosstalk from one coaxial via port located on the top of the structure to ports of other vias on the bottom side, i.e. the far-end crosstalk (FEXT) is shown exclusively. The scattering parameters are normalized to $50\ \Omega$. The following investigations are limited to the FEXT because reflection and transmission have already been validated in Section 5.5 and far- and near-end crosstalk differ mainly in phase. The layout of the

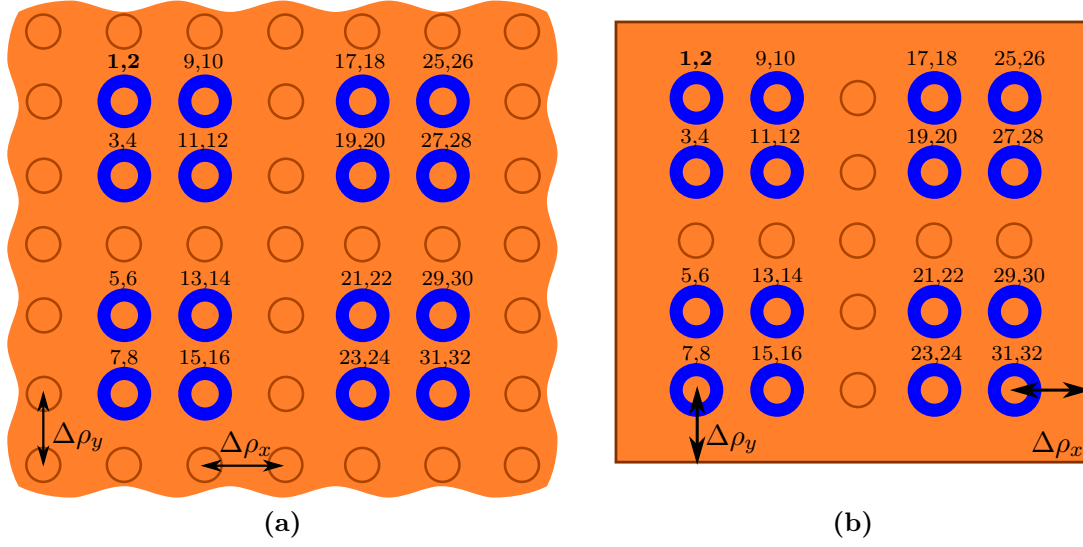


Figure 6.1: Validation structures with port numbering for the signal via ports. The first numbers above each via refers to for the (coaxial) top ports, the second number to the (coaxial) bottom port. Ground vias are shown as simple circles. The default pitch between all neighboring vias is $d_{\text{pitch}} = 200 \mu\text{m}$. (a) case with infinite planes (b) case with finite planes with, if not stated otherwise, $\Delta\rho_x = \Delta\rho_y = d_{\text{pitch}}$. Figure and text taken from [14].

considered structures including the assignment of signal and ground vias is illustrated in Fig. 6.1. Table 6.1 gives the the default parameter values. Further, the respective parameter variations are given in the figure captions.

The termination of the appropriate termination of the (azimuthally) anisotropic modes has been summarized in Sec. 3.9. It has been stated that the short-circuit should be the termination of choice for most practical cases. To gain more insight into the relevance of the type of mode termination, results for mode terminations with open circuits are also shown in several of the following cases.

The validation results are presented in Figures 6.2 through 6.4. These cover variations of the silicon conductivity, of the via pitch, and of the substrate metallization plane sizes. In general a good agreement of results can be observed in Figs. 6.2a and 6.2b. In some cases larger deviations are found at lower frequencies. There, a simple (inductive) behavior is expected [113]. Therefore, the variations of the reference results in these regions are unphysical.

As can be seen in the inset of Fig. 6.2a, below 600 MHz the reference simulation results show a more complex behavior than the PBV results. The latter are more reasonable since the crosstalk should show a simple inductive behavior at low frequency, cf. Appendix D.3.

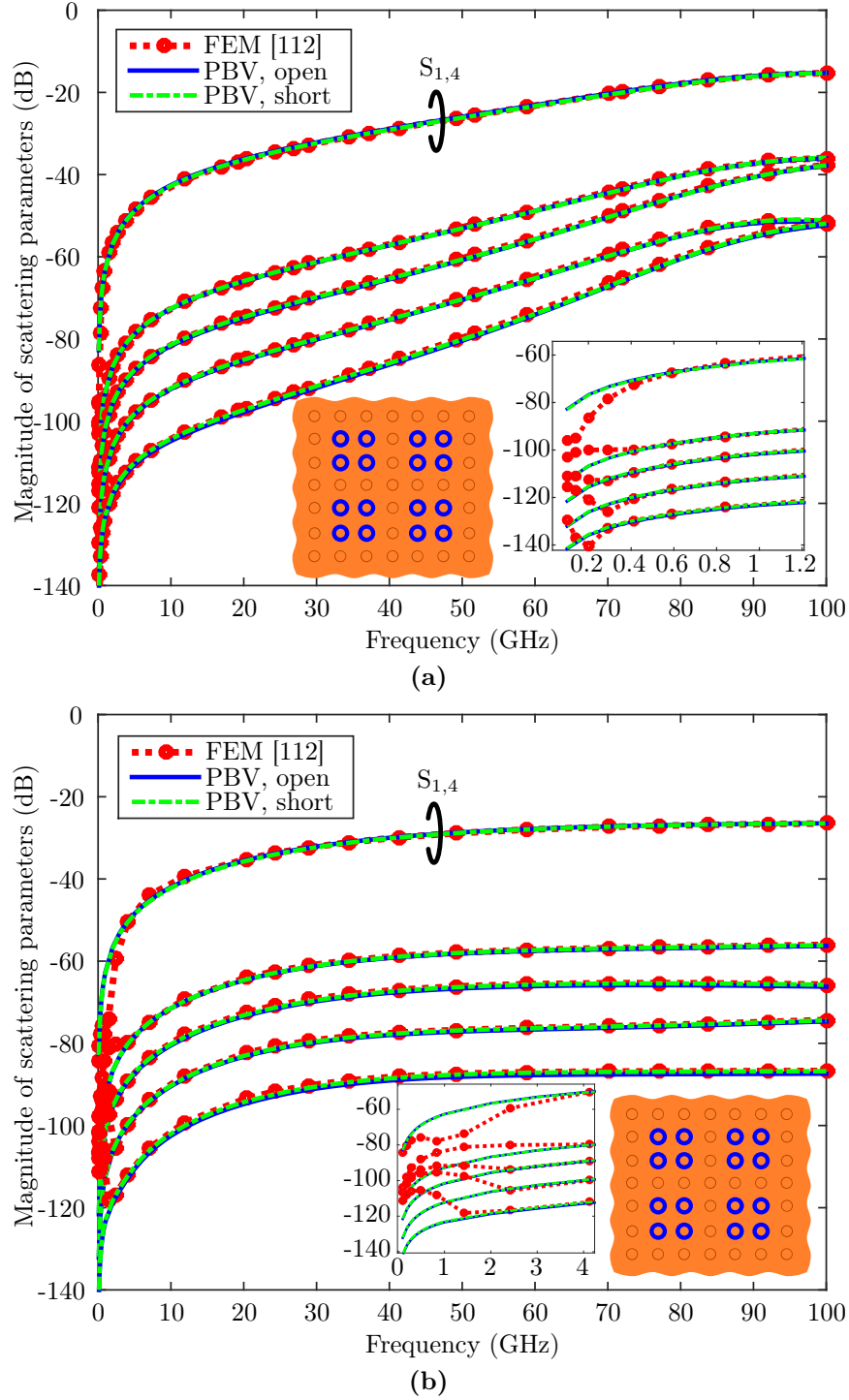


Figure 6.2: Far-end crosstalk from port 1 to ports 4, 6, 8, 22, and 32 (order of decreasing level at 50 GHz) for the layout in Fig. 6.1a with default parameter values and a pitch of 200 μm . Both PBV variations with either short-circuited or open-circuited ports of the anisotropic modes are shown. (a) With a silicon conductivity of 10 S/m. (b) With a silicon conductivity of 100 S/m. Figure and text adapted from [14].

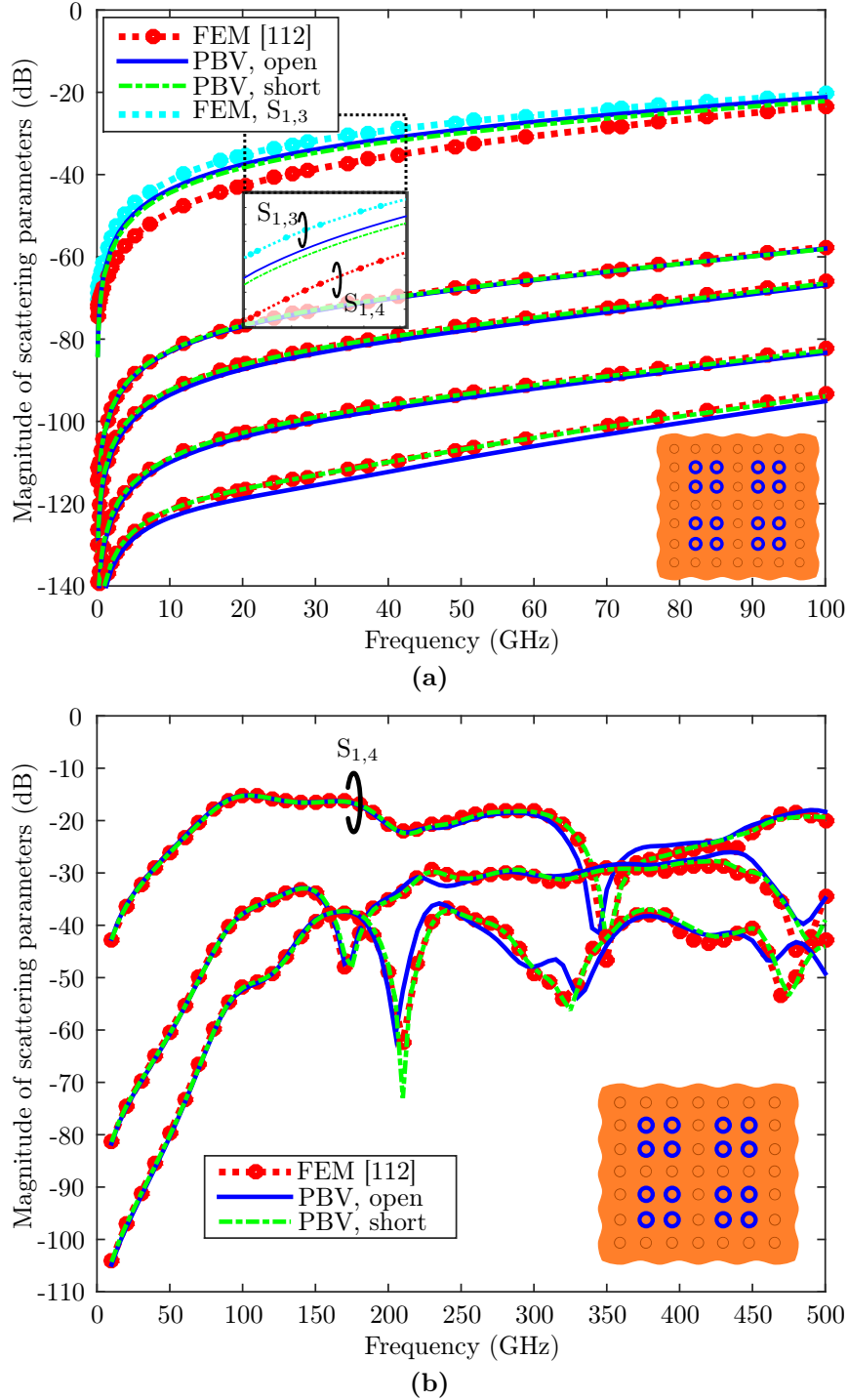


Figure 6.3: Far-end crosstalk for the layout in Fig. 6.1a with the following port ordering corresponding to decreasing levels at 50 GHz. (a) From port 1 to ports 3, 4, 6, 8, 22, and 32 with reduced pitch of 100 μm and silicon conductivity of 1 S/m. Inset: Detail of FEM reference results for $S_{1,3}$ and $S_{1,4}$ and the PBV results for both $S_{1,3}$ and $S_{1,4}$. (b) From port 1 to ports 4, 8, and 32 with default pitch and a silicon conductivity of 10 S/m. A maximum deviation of 4.8 dB and a mean deviation of 0.42 dB are obtained for $S_{1,4}$ with the PBV using short-circuit terminations. Figure and text adapted from [14].

Description	Name	Default Value
Radius of the via barrel	r_{via}	15 μm
Radius of the clearance/antipad	r_{antipad}	30 μm
Pitch	d_{pitch}	200 μm
Minimal distance between via antipads	d_{min}	$d_{\text{pitch}} - 2r_{\text{antipad}}$
Thickness of the oxide	t_{oxide}	1 μm
Thickness of the silicon	t_{silicon}	100 μm
Height of the cavity	t_{cavity}	$t_{\text{silicon}} + 2t_{\text{oxide}}$
Thickness of the plane metallizations	t_{metal}	5 μm
Relative permittivity of silicon	$\varepsilon_{\text{r,Si}}$	11.9
Relative permittivity of oxide (SiO_2)	$\varepsilon_{\text{r,oxide}}$	4

Table 6.1: Default Parameter Values for the Validation Setups. Table adapted from [14].

Above 5 GHz a maximum deviation of 0.28 dB and a mean deviation of 0.084 dB are obtained for $S_{1,4}$ with the PBV using short-circuit terminations.

In the inset of Fig. 6.2b it can be observed that below 4 GHz the reference simulation results show again unphysical behavior. Above 5 GHz a maximum deviation of 1.5 dB and a mean deviation of 0.24 dB are obtained for $S_{1,4}$ with the PBV using short-circuit terminations.

Good agreement with reference results is also obtained for most of the results from about 5 GHz to 100 GHz. The only major exceptions are those cases where a close spacing of vias in comparison to the cavity height is used. As discussed before, the PBV results are inaccurate in these cases because a near field coupling in addition to the coupling through parallel plate modes occurs. The existence of this mechanism can be concluded from the difference in near- and far-end crosstalk ($S_{1,3}$ and $S_{1,4}$, respectively) as observed in Fig. 6.3a. The relevant parameters that should be compared are the cavity height t_{cavity} and the minimal distance between vias d_{min} . In case of signal vias the latter is the minimal distance between the antipad regions. The order of the errors of the PBV that can be expected for different values of the ratio minimal distance to cavity height $d_{\text{min}}/t_{\text{cavity}}$ should be discussed here: For a ratio $d_{\text{min}}/t_{\text{cavity}} = 1$, a PBV error of about 0.5 dB and for a ratio $d_{\text{min}}/t_{\text{cavity}} = 0.5$ a PBV error of about 3 dB are obtained in Fig. 6.3a. For a minimal distance between antipads of 40 μm in Fig. 6.3a, a ratio of $d_{\text{min}}/t_{\text{cavity}} = 0.4$ results in an error of about 4.6 dB starting at a few GHz.

The investigation of higher frequencies in Fig. 6.3b shows very good agreement up to 200 GHz and good agreement up to 500 GHz. Also for the results with finite planes in Fig. 6.4, where both the PBV and the FEM simulation use open circuited boundaries at the plane edges, good agreement is obtained.

In conclusion, there is a good general agreement of the proposed PBV method with the

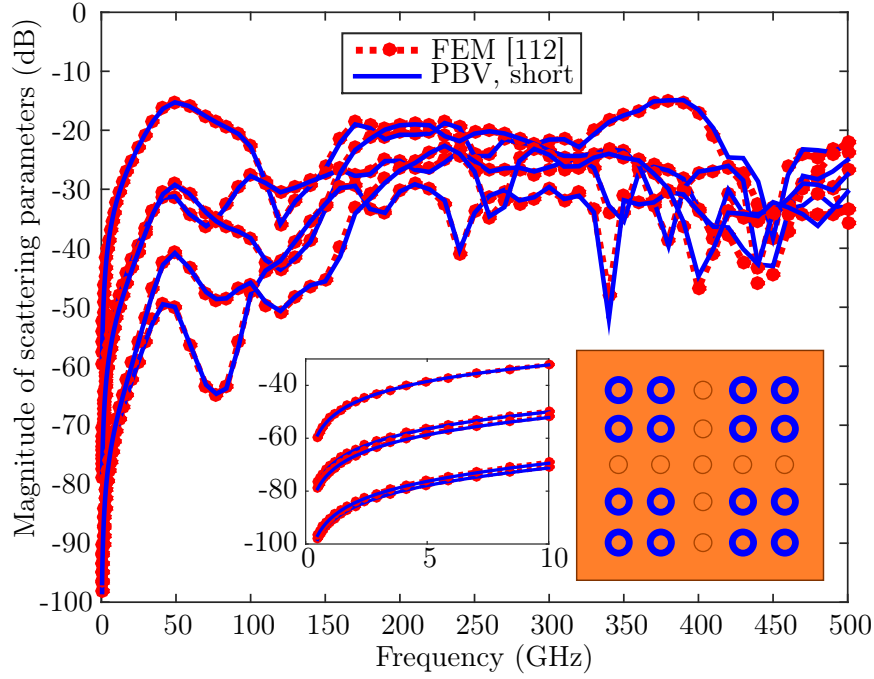


Figure 6.4: Far-end crosstalk from port 1 to ports 4, 8, 6, 32, and 22 (order of decreasing level at 50 GHz) for the layout in Fig. 6.1b with silicon conductivity of 10 S/m. Inset: For the case with finite planes a very good agreement with reference results can also be obtained for low frequencies. Figure taken and text adapted from [14].

FEM reference results in the results presented in Fig. 6.2a–6.4. In the cases of close spacing there are larger deviations with the FEXT being consistently overestimated.

6.2.1 Numerical Performance

The PBV simulations have been executed using implementations in MATLAB [114]. The computer system has an Intel Core i7-960 8-core 3.2 GHz CPU and 24 GB of RAM. For a TSV array that is significantly larger than the examples shown before, the magnitudes of scattering parameters are presented in Fig. 6.5. A 3×3 pattern is used with ground vias at two opposite corners and signal vias elsewhere. From this pattern, several arrays of different sizes are constructed and the admittance parameters are simulated with the isotropic and four anisotropic modes (modes with indices $0, \pm 1, \pm 2$, cf. Appendix D). The simulation times per frequency point are given in Table 6.2. On the used computer system, only the smaller arrays in Table 6.2 can be simulated due to limitations in RAM. For the FEM results in Table 6.2, both the simulation time for the “adaptive process” at the solution

frequency (iterative mesh refinement until a convergence measure is below a certain limit) and the per-frequency-point simulation time during the consecutive sweep are presented.

6.3 Time and Frequency Domain Superposition Techniques for Total Uncorrelated Crosstalk

In this section it is investigated if an upper bound to the total uncorrelated crosstalk can be computed for TSVs which are part of large arrays. It is important to quantify the crosstalk in via arrays, because it is known to contribute a substantial part to the overall crosstalk characteristics between channels of an interconnect regardless of whether each channel is assigned to a single via, i.e. using single-ended signaling, or to a pair of vias, i.e. using differential signaling. For a design that ensures signal integrity, the crosstalk a channel receives from all other channels must be quantified and the contributions must be superposed in an appropriate way. Further, if the characterization is carried out in frequency domain and the signal integrity characterization should be carried out for digital signals, several spectral contributions must be taken into account. In the following, a statistical superposition of crosstalk contributions in the frequency domain is proposed. It is computationally efficient and requires no conversion to the time domain. The result from the statistical superposition provides a measure of total crosstalk by assuming that the different crosstalk contributions from all channels are uncorrelated. For this type of crosstalk it can be demonstrated that an upper bound probably exists. This leads to the conclusion that, for very large TSV arrays, smaller arrays sizes can be determined that exhibit almost the same total crosstalk. Examples for sub-arrays that show approximately the same crosstalk as a larger full array are also given in this section.

The situation considered in this section is illustrated in the following: The vias in interposers are typically used in arrays of up to thousands. A small segment of such an array is

Array Size	PBV Model	FEM (sweep)
$8 \times 8 = 64$	0.3 s	7 min
$11 \times 11 = 121$	0.5 s	18 min
$36 \times 36 = 1296$	48 s	not available
$45 \times 45 = 2025$	140 s	not available
$63 \times 63 = 3969$	873 s	not available

Table 6.2: Approximate Simulation Times per Frequency Point. Table adapted from [14].

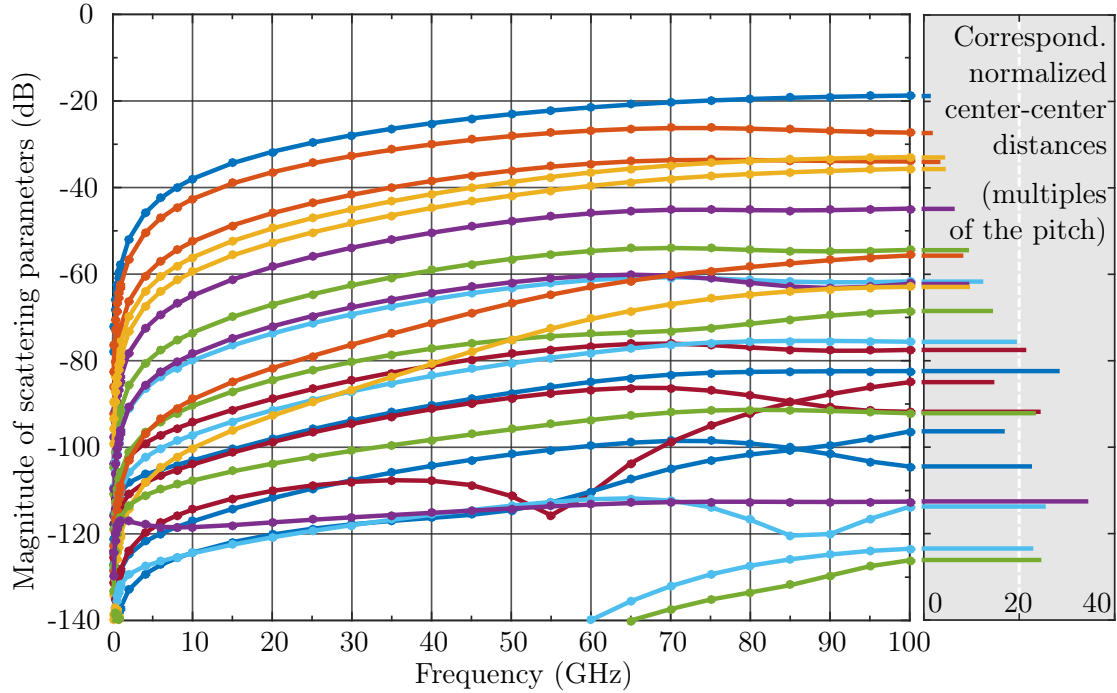


Figure 6.5: For an array with 36×36 (1296) vias, magnitudes of crosstalk (scattering parameters) from a port at the array corner to several far-end ports of the array and the corresponding normalized distances (multiples of pitch of the center to center distances of corresponding vias). The 3×3 pattern from which the array is created has ground vias at two opposite corners and signal vias elsewhere. Only values above -140 dB are shown. The average computation time per frequency step of the network parameters is 48s. Figure and text taken from [14].

drawn in Fig. 6.6. Consider digital signals as the one illustrated in Fig. 6.7a. In this case a simple train of pulses is used which could represent, e.g., a clock signal. For high data rates the spectral content of these digital signal includes high frequencies for which more often than not a stronger coupling occurs between vias and the corresponding channels than at low frequencies. In larger arrays, it might not be sufficient to consider only the crosstalk from directly neighboring vias and channels for the estimation of the overall crosstalk. Instead, it can be necessary to include also the crosstalk over large distances, i.e., from more distant vias. At the time these investigations are carried out, the typical array sizes which are of interest cannot be computed with FEM full-wave simulations on a personal computer. Therefore, the validated physics-based methods are exclusively applied in the following.

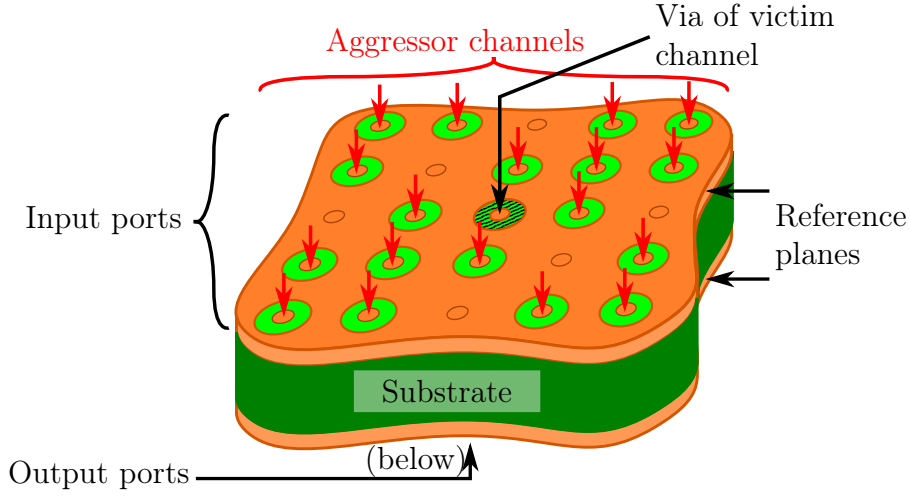


Figure 6.6: Considered type of through silicon via (TSV) structure with many parallel channels assigned to signal vias of a larger array. The investigated property is the total uncorrelated (far-end) crosstalk in large via arrays which is in the presented cases (mainly) due to parallel plate mode propagation. Figure and text taken from [11].

6.3.1 Computation of Total Uncorrelated Crosstalk

The starting point of signal integrity investigations can be the simulation of the structures of interest, here large TSV arrays. The large scale results are, e.g., obtained as network parameters. The individual contributions to crosstalk at individual frequencies can already be estimated from the scattering parameters which are normalized to a meaningful reference impedance (here 50Ω). The effective impact of crosstalk in digital system is typically evaluated in the time domain. An effective tool for this task is the eye diagram. An eye diagram provides a means of visualizing all relevant signal degradations such as effects of inter-symbol interference (ISI) and different transitions, and the remaining margin for a digital signal to be decoded correctly. A simplified eye diagram for the clock signal which mainly shows the effects rounded signal edges and of a superposed uncorrelated crosstalk is illustrated in Fig. 6.7b. In comparison to the input signal from Fig. 6.7a, the total uncorrelated crosstalk causes a widening of the lines in the eye diagram which is the same for all time instances.

The following investigations focus on the far-end crosstalk (FEXT). This situation is also visualized in Fig. 6.6. The FEXT is the crosstalk contributions on a victim channel (here assumed in the center of a large array) from all surrounding aggressor channels which only transmit signals in one direction, here from the top to the bottom ports.

The assumption of uncorrelated aggressor signals which allows for a computation of the total crosstalk still needs to be motivated. It can, e.g., be justified for cases where the

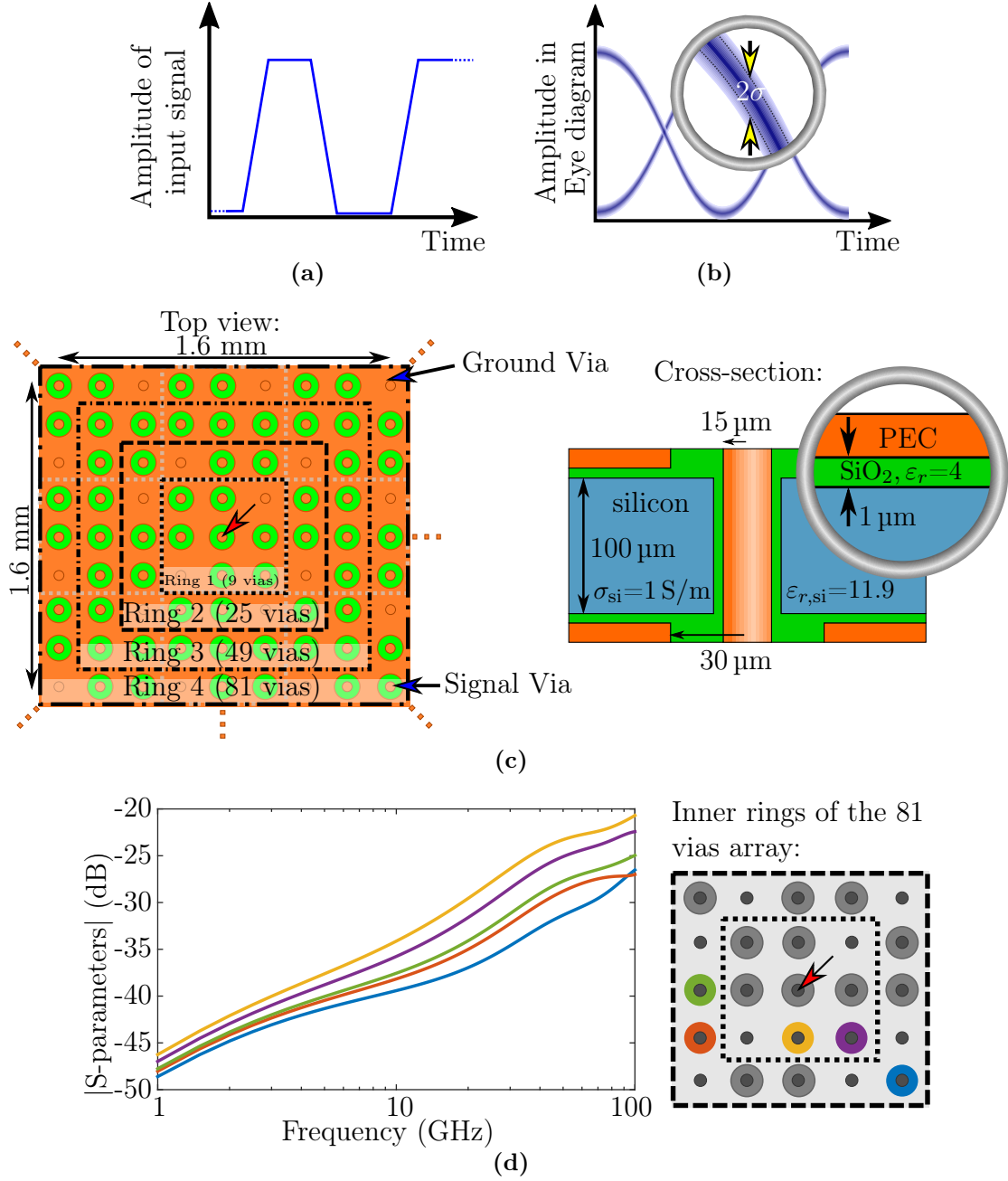


Figure 6.7: (a) Illustration of the type of trapezoidal, digital input signals that are considered. (b) The proposed crosstalk measure can be interpreted as a measure of the line widening in an eye diagram due to the uncorrelated crosstalk contributions. (c) Top and cross-sectional view of the considered TSV array. The via with the victim channel is in the center of any considered sub-array and marked with a red arrow. The planes extend infinitely, all ports are coaxial ports at the inner edges of the plane metallizations. The pitch is 200 μm . (d) Magnitudes of far-end crosstalk (FEXT) of several channels of the 9×9 (81 vias) array. The drawing to the right marks the locations of the victim channel/via using an arrow and the aggressor channels/vias using the corresponding line colors. Figures adapted and text taken from [11].

relative timings or assignments of channels are not yet determined as can be the case in early design phases. A worst-case scenario would be simulated by superposition in time domain of the maximum amplitudes of every crosstalk contribution but this could lead to too strict constraints. Therefore a “typical” total crosstalk as offered in the following will in many cases be preferred. The proposed measure might also be applicable in later design phases, e.g., if the channels are asynchronous.

Crosstalk Power Sum for Varied Array Size

In the following, the crosstalk is first considered for single frequencies. As an example, the scattering parameters in Fig. 6.7d illustrate the behavior from 1 GHz to 100 GHz for a setup depicted in Fig. 6.7c. At lower frequencies, the frequency-dependence is simple and almost linear (with dB magnitude scaling and logarithmic frequency scaling) but it becomes more complex with increasing frequency. For the investigation of the question which vias should be included, the behavior as a function of the distance from the victim via is of interest. The crosstalk level mainly decreases with increasing distance due to conduction losses, polarization losses of the materials, and due to the broadening of the cylindrical wave fronts. On the other hand, the number of aggressors within a circumference is proportional to the maximum distance that is considered [115]. With both these effects in mind, the question arises if the uncorrelated crosstalk of large arrays is bounded and how the dependence on the array size can be characterized.

The central limit theorem is applied in the following for the analysis and can be stated in the present context as follows: If a large number of contribution are added up, i.e. the superposition is linear, and all contributions are comparatively small, then the resulting probability function is approximately a normal distribution. This effect is qualitatively independent of the probability functions of the contributions. In the present context of crosstalk modeling, all contributions of inter-via crosstalk should be of similar orders of magnitude. This can be intuitively seen to apply for those aggressor vias which have the same distance from the victim via. The total uncorrelated crosstalk is known in the literature as the power sum of crosstalk (PSXT) [116, 117]. It can be formulated in terms of the scattering parameters for the (output) port of a victim via/channel with index i and for the (single) frequency with index k as

$$\text{PSXT}_{i,k} = \sqrt{\sum_{j=1; j \neq i}^{N_p} |\text{FEXT}_{i,j}(f_k)|^2} \quad (6.4)$$

where $\text{FEXT}_{i,j}$ is the far-end crosstalk (scattering parameter) from port j to port i . The

indices $j = 1, 2, \dots, i - 1, i + 1, \dots, N_p$ refer to selected ports, i.e., in the present case all far-end ports of the considered complete array (or sub-array), with respect to a considered port i of the victim channel except for the opposing port on the same via (which would refer to the transmission in the considered single-ended case). N_p is the highest index of the far-end ports.

As has been seen in the previous chapter, the far-end crosstalk differs from the near-end crosstalk mainly in phase and should therefore lead to magnitudes of crosstalk very similar to those presented in the following. As already discussed, there are exceptions to this. E.g., cases of very close spacing of vias where the physics-based modeling as presented in this thesis mostly leads to an underestimation of near end crosstalk and overestimation of far-end crosstalk.

An example how the total far-end crosstalk as defined in (6.4) evolves with the number of included vias is given in Fig. 6.8a. Different sub-arrays from the array in Fig. 6.7 are used and the simulation is repeated for all considered arrays sizes. It can be observed in Fig. 6.8a that at higher frequencies the PSXT increases monotonically with the array size. For lower frequencies, here below 50 GHz, the behavior is not monotonic but with a tendency of decreasing PSXT. It is important to note that not only signal vias but also ground vias are added to the array from one sub-array to the next larger one. The impact differs for different frequencies, i.e. the improved control of return currents due to attentional ground vias has a larger influence at lower frequencies and leads to the observed smaller PSXT for the larger arrays.

While the convergence can be observed in Fig. 6.8a, it is also interesting to examine the difference to a significantly larger array. Fig. 6.8b shows the deviations of the results for sub-arrays from those for the largest of all simulated arrays. The deviations (as defined in the caption of Fig. 6.8) for all frequencies are below 1 % if the array has 121 or more vias. In addition to the presented results, arrays have been simulated which have a lower silicon conductivity or a larger pitch. Either of these modifications leads to a slower development of the PSXT of the sub-array to the PSXT of the full array with increasing size but the general behavior is identical.

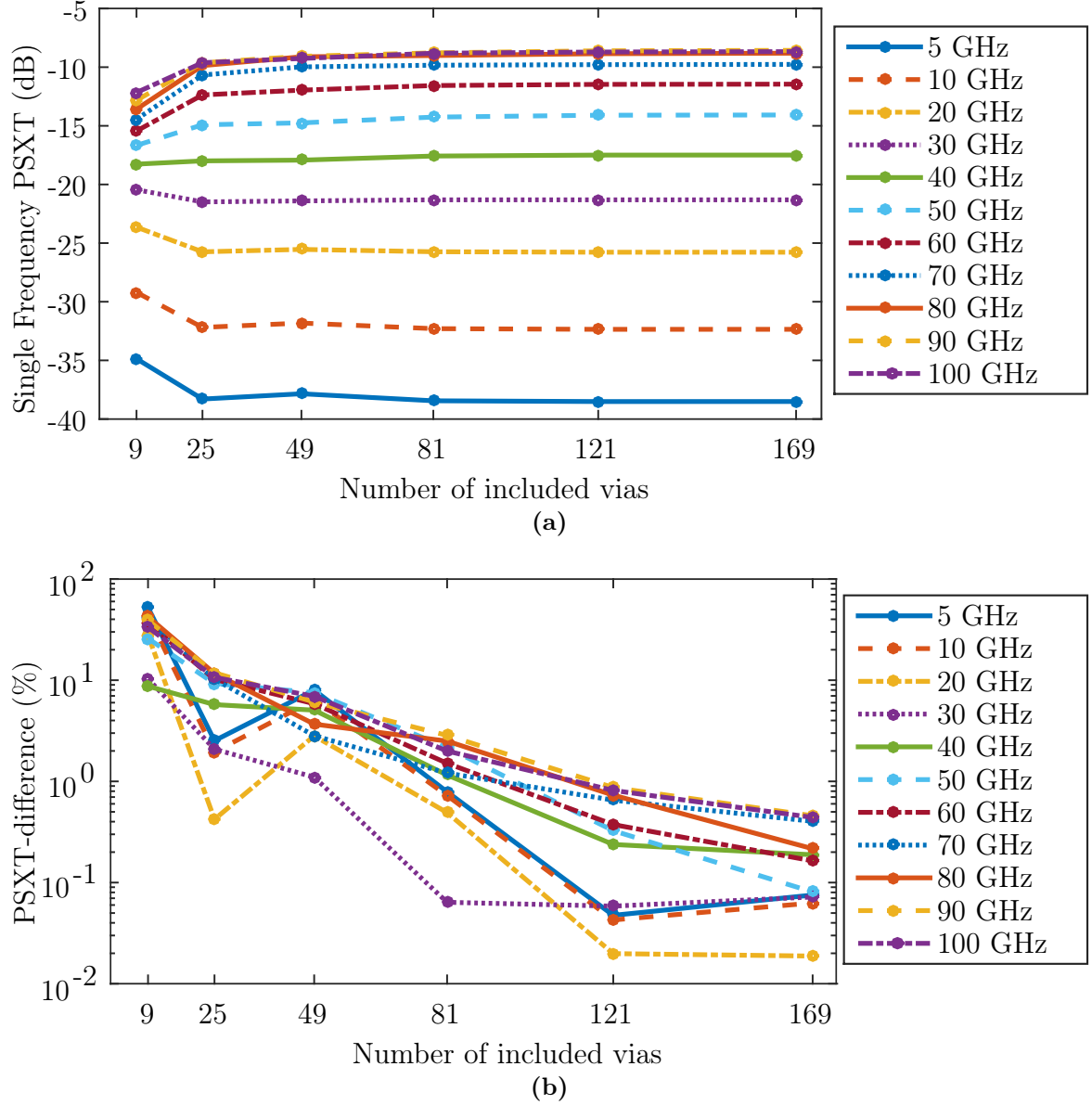


Figure 6.8: Comparison of power sum of crosstalk (PSXT) for different array sizes and thus different numbers of included crosstalk sources. (a) For the array given in Fig. 6.7(a), for several single frequencies as a function of several separately simulated sub-array sizes. (b) For the array given in Fig. 6.7(a), PSXT difference in percent for comparison of the sub-array results with results for a full $21 \times 21 = 441$ vias array defined as $\text{PSXT-difference} = |\text{PSXT}_{\text{subarray}} - \text{PSXT}_{\text{full}}| / |\text{PSXT}_{\text{full}}|$. Figure and text taken from [11].

Time Domain Approaches for Digital Signals

In the following, two statistical time domain approaches that are based on methods from [118–121] are briefly discussed and subsequently used to validate the proposed frequency domain approach. As the channels that are considered here are characterized in frequency domain by the PBV, the time domain signals have to be computed first. These are obtained using the channel properties in terms of complex scattering parameters of the crosstalk contributions, the complex spectra of the pulse trains or a pseudo random bit sequence (PRBS), a multiplication in frequency domain, and a Fourier transform to the time domain. Examples for the used spectra are depicted in Fig. 6.9a.

An example for a synthetic eye diagram based on the proposed approach is given in Fig. 6.9b and generated as follows: At any time instant the transmitted signal is computed (red solid line), here only for the transitions *high–low–high* and *low–high–low* (e.g. a clock signal). The crosstalk is characterized here independent of the time within the unit interval by the normal distribution with the standard deviation computed from the superposition in terms of power as in (6.4). The synthetic eye diagram can then be used to estimate quantities such as the vertical eye opening V_{eye} .

For the first time domain approach, the probability density functions (PDFs) of all time domain signals of crosstalk contributions are computed. These PDFs can be interpreted for each signal as giving the probabilities of a certain voltage levels to occur independent of the time instant. An input signal in time domain is illustrated together with a corresponding crosstalk signal in Fig. 6.10a. For signals composed of single frequencies, the PDFs can be directly given. Using the results from [122, Example 16.8], the PDF of a sine or cosine function $f(x) = a \sin(x)$ can be given analytically as

$$p(x) = \begin{cases} \frac{a}{\pi\sqrt{1-x^2}}, & \text{if } -1 < x < 1, \\ 0, & \text{otherwise,} \end{cases} \quad (6.5)$$

and is illustrated in Fig. 6.10b. The probability of a certain voltage range to occur is given by the integral of this density over the voltage range. The consideration of digital signals requires a numerical evaluation with discrete frequencies, time instances, and voltage levels. For the numerical application, a discretization needs to be used. This discretization can, e.g., be interpreted in one of two following ways: It can be interpreted as allowing only certain discrete voltage levels and using a probability mass (PMF) function as the one also shown in Fig. 6.10b and derived from the PDF. The discretization can also be interpreted as approximating the PDF with a PMF. In any case, the PMF can be computed, e.g., from the PDF by using intervals of equal sizes and assigning the integral of the PDF

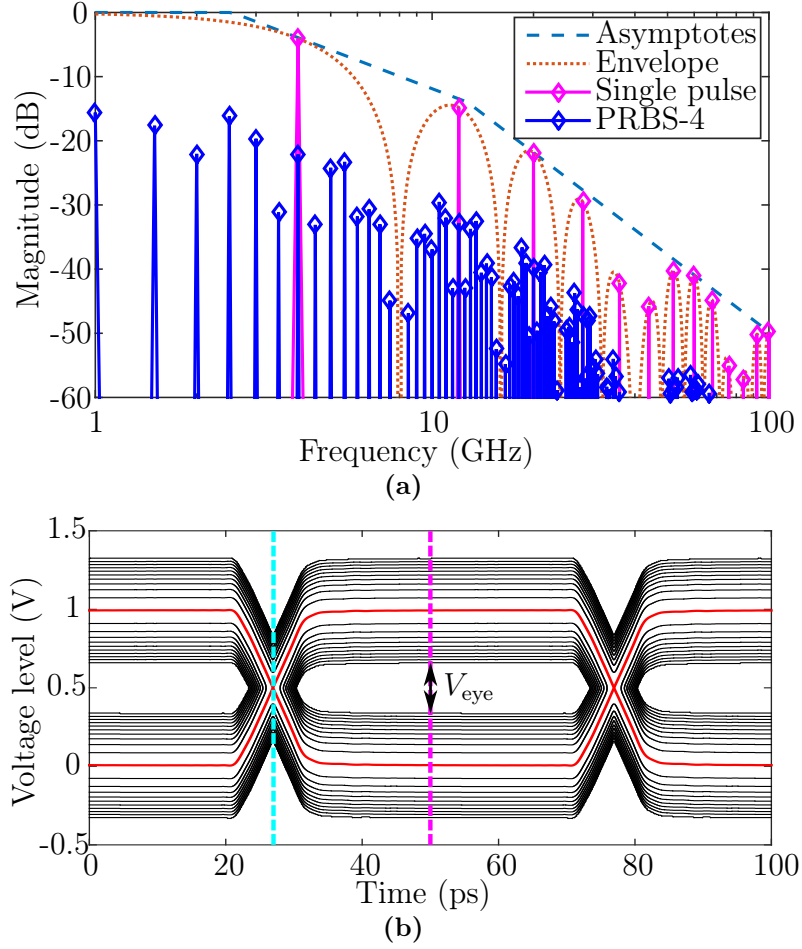


Figure 6.9: (a) Example for the line spectrum of a periodic single pulse and a pseudo-random bit sequence (PRBS) with the corresponding asymptotes and the envelope. (b) Eye diagram for a repeated single pulse (e.g. clock signal) in the form of contour lines (solid black lines) for the probabilities above and below the signal without crosstalk (solid red line). Statistically, no voltages from the innermost areas (eye opening) are observed during the time of 10^{12} pulses. Figures and text taken from [11].

over each interval to the center value of every interval. In the following these integrals are approximated by evaluating the PDF at the center values of the intervals and enforcing the sum of PMF values to equal 1. This implicitly amounts to application of a mid-point rule for the integrations over the intervals. A probability density corresponding to the crosstalk signal in Fig. 6.10a is depicted in Fig. 6.10c.

After obtaining the PDFs, the probability density of the superposition of all signals (as superposed in time domain) is given by the convolution of the individual PDFs. As predicted by the central limit theorem, for large numbers of superposed sources and relatively similar properties of the individual PDFs, the PDF that results from this convolution approaches

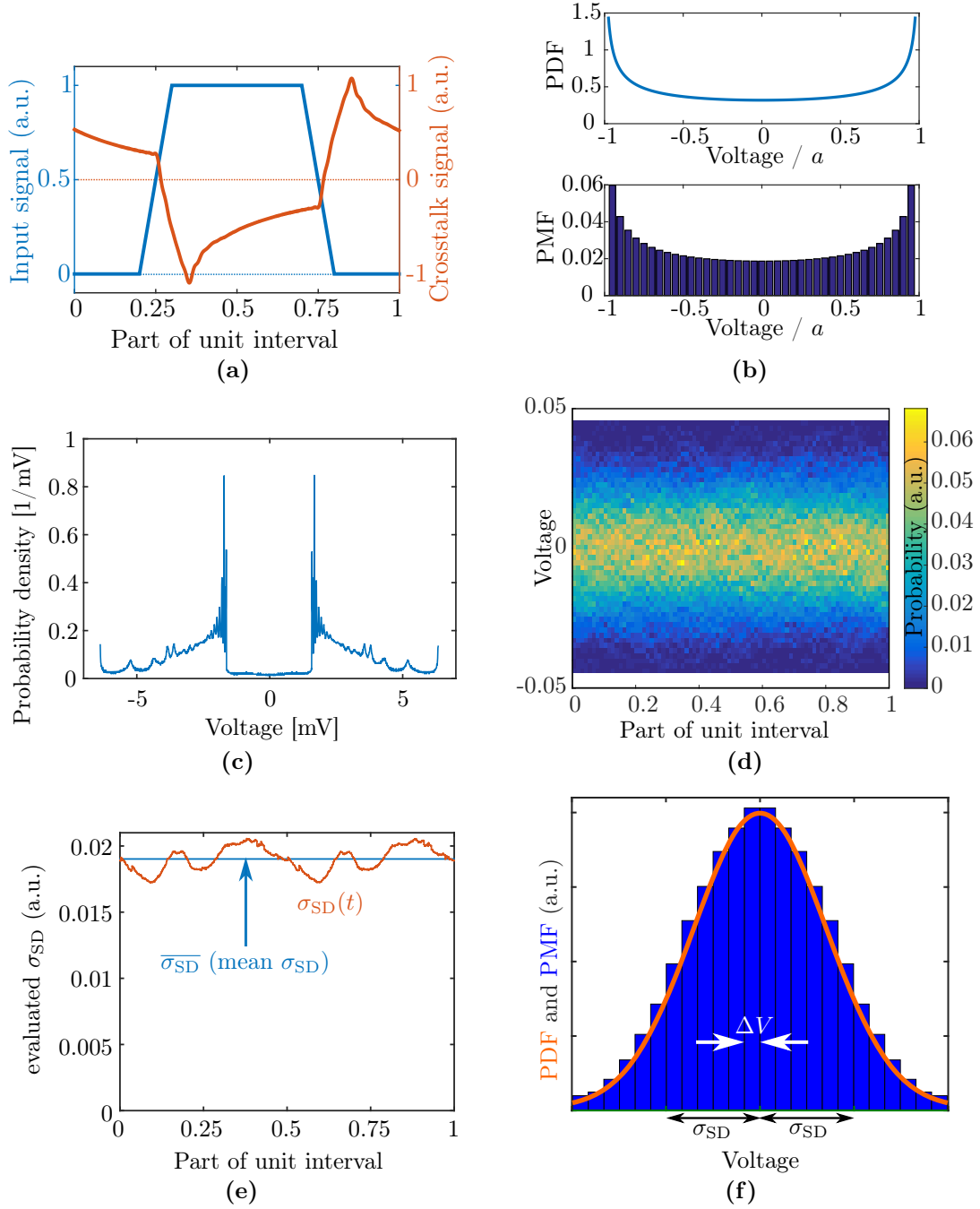


Figure 6.10: Illustration of the statistical evaluation techniques. *a.u.* means *arbitrary unit*. (a) Considered time domain input signal and example output signal. (b) PDF and PMF of a sine signal. (c) PDF of an example crosstalk signal. (d) 2D map of probabilities of voltage levels for a recording of a large number of time domain crosstalk signals. (e) Evaluation of the standard deviation for all times of the unit interval and its average. (f) Normal distributions approached by the PDFs at any time of the UI. Figures adapted from the corresponding presentation of [11].

a normal distribution. The most interesting characteristic of this normal distribution is the standard deviation as will be seen in the following. This is because an average close to zero is obtained if there is almost no DC coupling as in these structures. The results from this method are labeled as “PDF convolution” in the following validation section and Fig. 6.11a.

The second time domain approach can be interpreted as imitating the behavior of the traditional eye generation setup in which a pattern generator is used as a signal source and an oscilloscope superposes the time domain signal triggered/synchronized to a clock signal. Because only the crosstalk itself without the transmitted signal is investigated, no eye openings etc. can be observed but instead a probability of crosstalk levels at certain time instances. For the discrete time instances of the unit interval and discrete voltage levels, a 2D histogram as the one illustrated in Fig. 6.10d is obtained. For each time instance, a standard deviation can be computed which is depicted in Fig. 6.10e. With an increasing number of shifted crosstalk contributions the standard deviation at any time instant of the unit interval can be recorded and gives the graph $\sigma_{SD}(t)$ in the figure. The mean of the standard deviation $\overline{\sigma_{SD}}$ is assumed to be a good approximation of the value towards which the standard deviation for all samples converges if the averaging is performed over more samples. The results from this method (using the average of the standard deviations) are labeled as “time domain” in the following validation section and Fig. 6.11a.

For all time instances, the probability distributions are found to converge towards normal distributions. For these, both the PDF and the PMF are illustrated in Fig. 6.10f. The power of the crosstalk can therefore be characterized by a single quantity. In the following the standard deviation σ_{SD} is used for this purpose, i.e. the crosstalk measure in dBV for this case is given by $20 \cdot \log(\overline{\sigma_{SD}}/1 \text{ V})$.

Frequency Domain Approach for Digital Signals

By construction of the time domain signals, the phases of the spectral components of the crosstalk signals are taken into account. In the frequency domain approach it is assumed that this phase relation has no relevance for the superposition of uncorrelated signals and can therefore be ignored. The empirical justification of this assumption follows the following reasoning: consider the case in which all channels of the setup carry the same type of signal, i.e., the same discrete spectral contributions are relevant for all signals. This allows to determine the superposed spectral components first, i.e., for each spectral component the contributions from the individual channels are added up as powers as in (6.4). Next, the spectrum of total crosstalk is weighted with the spectrum of the signal which is identical for all channels considered here. This is possible because the phases of

both signals have been assumed to be uncorrelated, i.e., the phases due to the electrical lengths of the individual crosstalk paths are irrelevant.

This procedure of weighted superposition of powers has been proposed and named weighted power sum of crosstalk (WPSXT) in [11]. It can be summarized using the following formula as

$$\text{WPSXT}_i = \sqrt{\sum_{k=1}^{N_f} \left(\sum_{j=1; j \neq i}^{N_p} |\text{FEXT}_{i,j}(f_k)|^2 \right) \cdot |w(f_k)|^2}, \quad (6.6)$$

where the inner part in braces is the summation of power for a discrete frequency f_k as in (6.4). $j = 1, 2, \dots, i-1, i+1, \dots, N_p$ are the indices of the included ports corresponding to crosstalk onto channel i as in (6.4). The outer part is the weighting of the included, discrete frequencies with indices $k = 1, 2, \dots, N_f$ using the corresponding weights w .

When computing time domain crosstalk signals through multiplication of the spectrum of the input signal and transfer function in frequency domain, the complex two-sided spectra have to be used. Analogously, a two-sided spectrum has to be used in (6.6) for the scattering parameters $\text{FEXT}_{i,j}(f_k)$ and the weights $w(f_k)$ that characterize the digital signal spectrum. In comparison to the time domain signal computation, the phases of the spectrum can be neglected. The indices $k = 1, \dots, N_f$ refer to the components of the discrete spectrum of the signals and the $w(f_k)$ are computed by a discrete Fourier transform of the time domain signal with a normalized (e.g. 1 V) amplitude. From inspection of the crosstalk characteristics in Fig. 6.7d and the typical signal spectrum in Fig. 6.9a, a frequency range that dominates the overall properties in the examples investigated here can already be predicted: At low frequencies the crosstalk is comparatively low and at higher frequencies the contributions of power to the overall signal power are low. An intermediate frequency range should therefore dominate the overall crosstalk power.

Validation of the Frequency Domain Method

The proposed frequency domain approach which is summarized in (6.6) is validated in the following. The TSV array from Fig. 6.7a with 81 vias is investigated for (i) the pulse train (repeated single pulse that could represent a clock signal) and for (ii) two different pseudo random bit sequences (PRBS). The results are depicted in Fig. 6.11a. As can be seen, a good agreement is obtained for the proposed weighted PSXT from (6.6) and the two time domain approaches for the single pulse train. Only the time domain method which evaluates the results for a large number of time-shifted signals is used to also evaluate the total crosstalk for the sequences known as PRBS-4 and PRBS-5. A total crosstalk that is 2 dB to 3 dB lower than for the single pulse train results can be observed. An interpretation

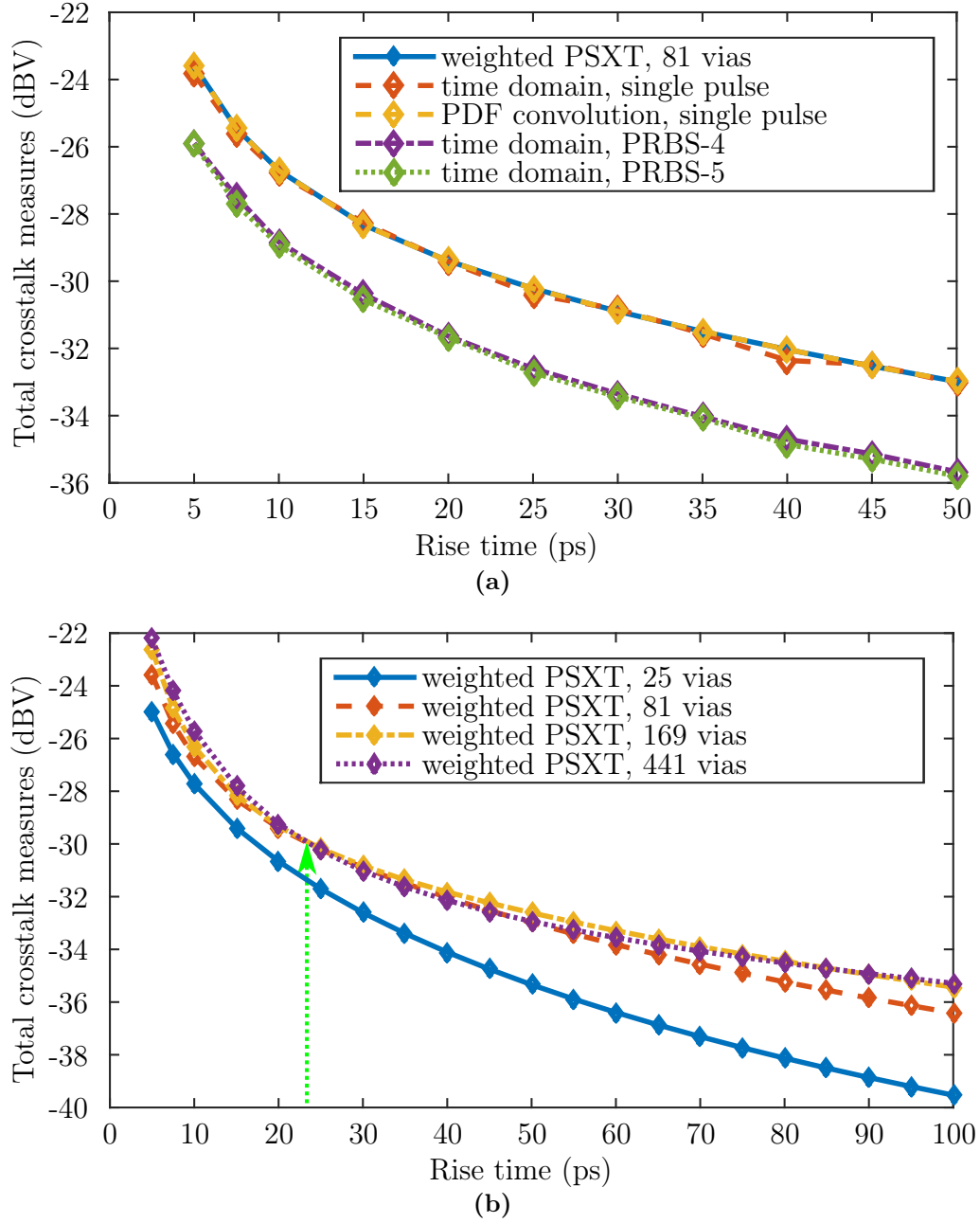


Figure 6.11: Validation and application of the frequency domain method. The signals on all channels have the same amplitude of 1 V. The crosstalk refers to the $\pm\sigma_{SD}$ -voltage levels of the corresponding probability distributions. (a) Comparison of the total crosstalk obtained with the discussed methods. The single pulses have a trapezoidal shape with a rise time from minimum to maximum value given on the x-axis of the plot and with respective widths at half maximum which are five times as large. (b) Comparison of weighted PSXT for different array sizes. Each data point results from a separate simulation with the specified array size instead of using the results for the sub-array from the simulation of the largest used array size. Figure and text taken from [11].

is feasible in frequency domain and in time domain: Qualitatively, the pseudo-random bit sequences have, for a given amplitude and the same rise times, a larger spectrum proportion at lower frequencies compared to the single pulse train. As the links under consideration have a low-pass behavior, the lower total crosstalk is therefore expected. Also, in time domain, the pseudo-random bit sequences have varying durations on the states of the lower or higher voltage level. The average number of transitions is half the number of transitions of the single pulse train. If intersymbol interference (ISI) of the crosstalk signal (per channel) is negligible, this corresponds to a 3 dB difference in the crosstalk power contributed. For the shorter rise time in Fig. 6.11a, the smaller difference in PSXT can be attributed to an ISI of the crosstalk signals.

Investigation of Sub-Array Approximation

Next, the results for the digital signals for different sub-array sizes can be compared; the results are presented in Fig. 6.11b. It can be seen that small sub-arrays, in the present case 25 vias, cannot represent the full array properties accurately in that the WPSXT is significantly different. The difference is larger for longer rise times which corresponds to lower frequency components. As has already been observed from the results shown in Fig. 6.8, the contributions from a smaller number of neighboring channels dominates the superposed crosstalk for lower frequencies. There are several intersections of the curves for different numbers of vias in Fig. 6.11b which indicates a non-monotonic convergence towards an upper limit. A convergence towards the upper limit can be observed in this example for all rise times but the intersections indicate different convergence behavior. This can again be attributed to the different convergence behavior of the spectral components that is already shown in Fig. 6.8 and the inclusion of not only additional aggressor channels but also additional ground vias.

Conclusions Regarding the WPSXT

The WPSXT proposed in this section has been shown to be a helpful and meaningful measure in evaluating a typical overall crosstalk if certain assumptions can be made. It is therefore more relevant for signal integrity analysis than single scattering parameter values, e.g., the crosstalk from the nearest channel. Therefore this measure is applied in the subsequent sections for all vias or larger arrays to give insight into the effects of variations of several relevant design parameters.

6.4 Total Uncorrelated Crosstalk in Large Arrays

In the following, several “crosstalk maps” [115] are presented that give an overview over the magnitudes of single and summed crosstalk terms at many locations on a TSV array. These maps use colored squares where the coordinate in the diagram refers to the location of a port and the corresponding via in the array. The color of each square corresponds to the level of a certain crosstalk measure, e.g. the magnitude of far-end crosstalk from a central via of the array. The rounded level value in dB is also printed on each square. These crosstalk maps are depicted in Figures 6.13, 6.14, and 6.15. The array for which all these maps are computed is based on a pattern of 3×3 vias. The vias at two opposite corners of this pattern are assigned as ground vias. By replicating this pattern 4 times along both coordinates, a total array size of 144 vias (112 signal vias and 32 ground vias) is obtained.

First, in Fig. 6.13a, the individual single-ended crosstalk terms (magnitudes of scattering parameters) of all vias in the array from a via at one of the central positions in the array are shown. Due to the symmetry, these are also the levels of (far-end) crosstalk at the via ports at these locations from the central via. As can be observed in Fig. 6.13a, the levels depend mainly on the distance between the vias and the number and locations of ground vias close to the locations of both the emitting and receiving via. In the next step, three vias near the array center are viewed as aggressor channels. In Fig. 6.13b these channels are marked with the letter “S”. Fig. 6.13b also shows the PSXT from these three channels at the other vias in the array. The level of this PSXT is then dependent on a larger number of different distances to aggressor vias and ground vias than the single crosstalk contribution in Fig. 6.13a. Next, the PSXT is computed for every via. Each single-ended channel that is attributed to a signal via is viewed as both an aggressor and victim of crosstalk. This is depicted in Fig. 6.13c. As can be seen, the PSXT is generally higher when vias have more signal vias and fewer ground vias close to them. The before crosstalk maps give an insight of an expected order of magnitude at the frequency of 50 GHz. In the next step, a weighting as in (6.6) is used to obtain the corresponding results for a digital signal which is a train of trapezoidal-shape pulses with 5 ps rise time and a full width at half maximum (FWHM) of 25 ps. The results for this WPSXT are depicted in Fig. 6.13d. The lowest crosstalk can be observed again at locations close to two ground vias. The highest crosstalk is observed at locations near the array rim. Except at positions near the array rim (here the two rows of vias closest to it) the PSXT and WPSXT is the same for the same positions in the 3×3 pattern. Results for the case with a finite size of the substrate and the plane metallizations are also considered and depicted in Fig. 6.14a. An influence of the finite metallizations, i.e. a relevant difference to the case with infinite planes, can only be observed at the two rows of vias nearest to the array rim. In the present example the vias in the upper right

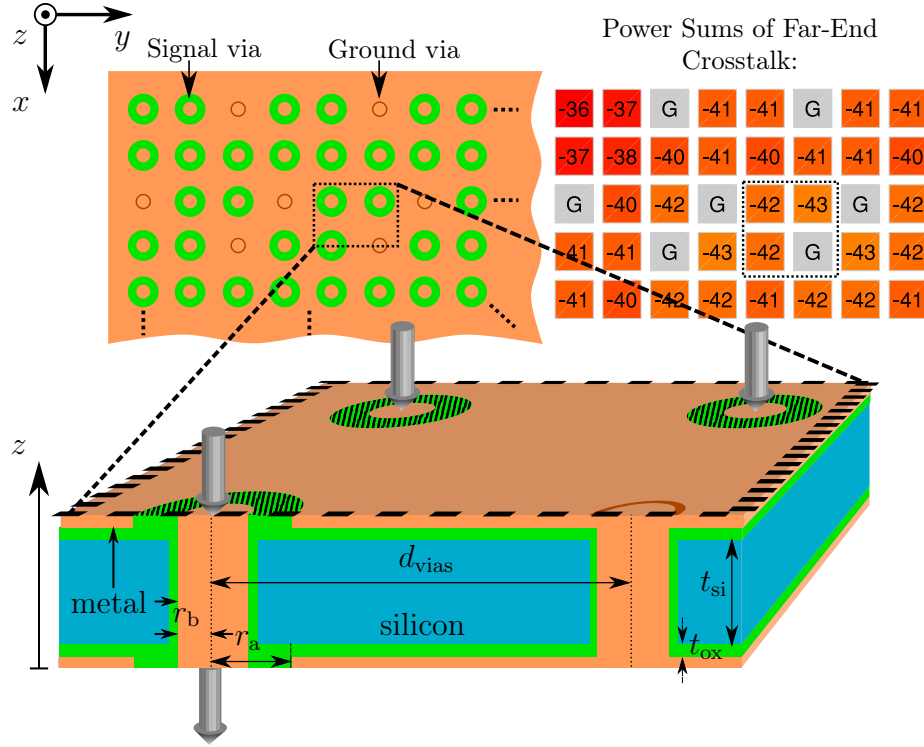


Figure 6.12: Silicon interposer structure consisting of a metal-clad substrate. The metal parts of cladding and via barrels are electrically isolated from the silicon substrate by silicon dioxide layers. The reference planes are at the outer planes of the metallizations. The top left part of the image shows a top view of the array, the right part shows corresponding levels of total far-end crosstalk on channels assigned to signal vias. Typical dimensions are: via barrel radius $r_b = 15 \mu\text{m}$, antipad radius $r_a = 30 \mu\text{m}$, pitch $d_{\text{vias}} = 200 \mu\text{m}$, silicon substrate thickness $t_{\text{si}} = 100 \mu\text{m}$, and silicon dioxide thickness $t_{\text{ox}} = 1 \mu\text{m}$. Figure and text taken from [14].

and lower left corner have the largest (average) distance to the ground vias and therefore show the highest PSXT levels.

Next, also an example for differential channels is investigated. These are obtained from the previously presented single-ended results by the methods discussed in Appendix G.3 and presented in Figs. 6.15a and 6.15b. As before, the single scattering parameters are mainly influenced (in magnitude) by the distance of the aggressor channels to the victim channels. For the WPSXT in 6.15b it can be observed that the levels of this differential crosstalk are between 13 dB and 25 dB lower than the corresponding single-ended results. The levels are between about -65 dB for those ports with more ground vias in close vicinity and about -55 dB for via pairs with another via pair close to them.

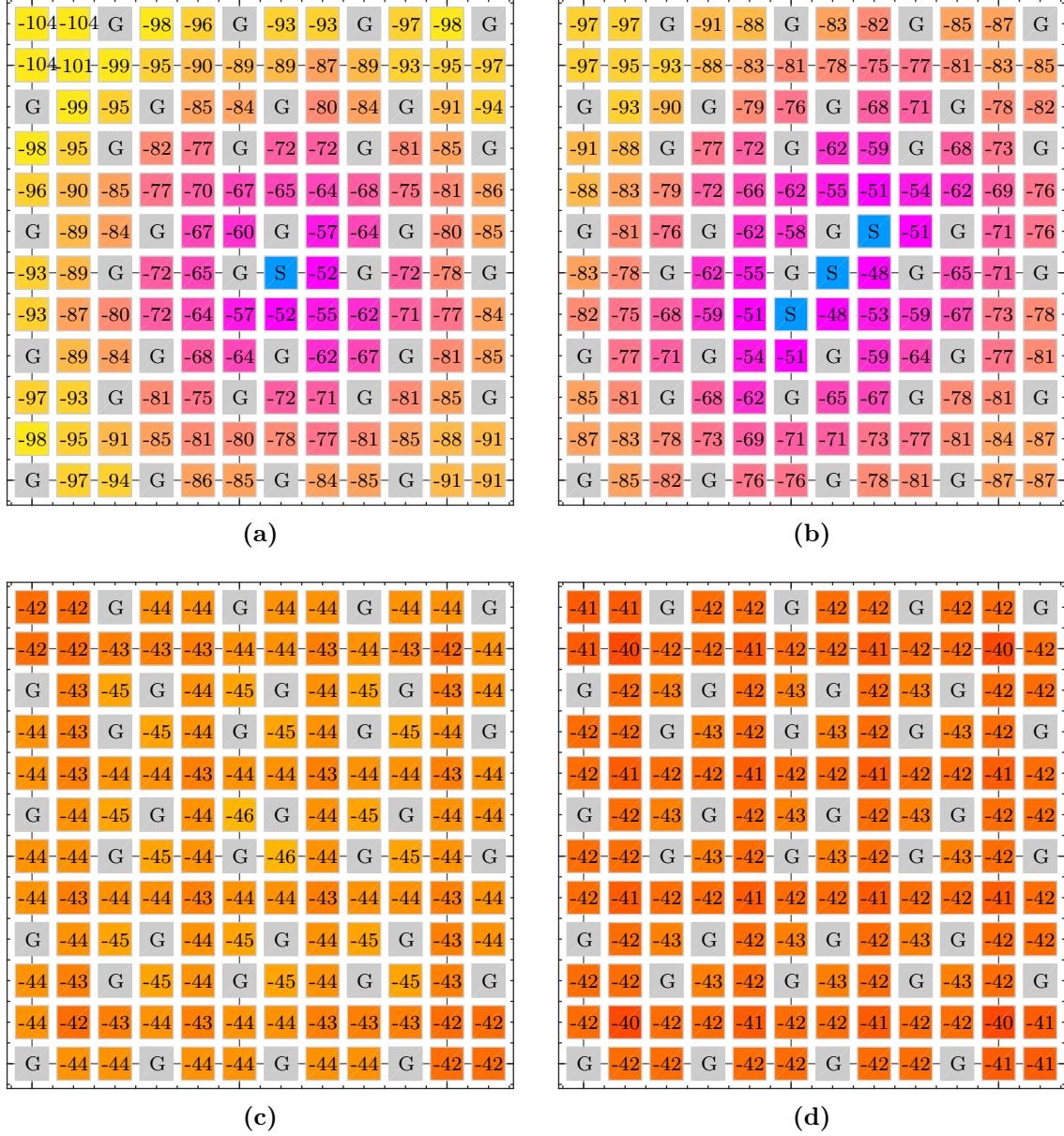


Figure 6.13: Crosstalk results for a setup with infinite planes, a pitch of 200 μm , an oxide thickness of 1 μm , a silicon layer thickness of 100 μm , and a silicon conductivity of 10 S/m. Ground Vias are marked with the letter “G”. Numbers indicate the respective levels in dB of far-end crosstalk. Different color maps are used for encoding the levels in order to magnify the difference within each map. (a) single-ended far-end crosstalk at 50 GHz to or from the channel assigned to the central via marked with the letter “S” (b) power summation of 3 aggressors which are each marked with the letter “S” (c) single-ended power sum of crosstalk (PSXT) at 50 GHz (d) total uncorrelated crosstalk (WPSXT) for the signal with 20 ps rise time and 100 ps FWHM. Figure and text taken from [14]. (continues in Fig. 6.14)

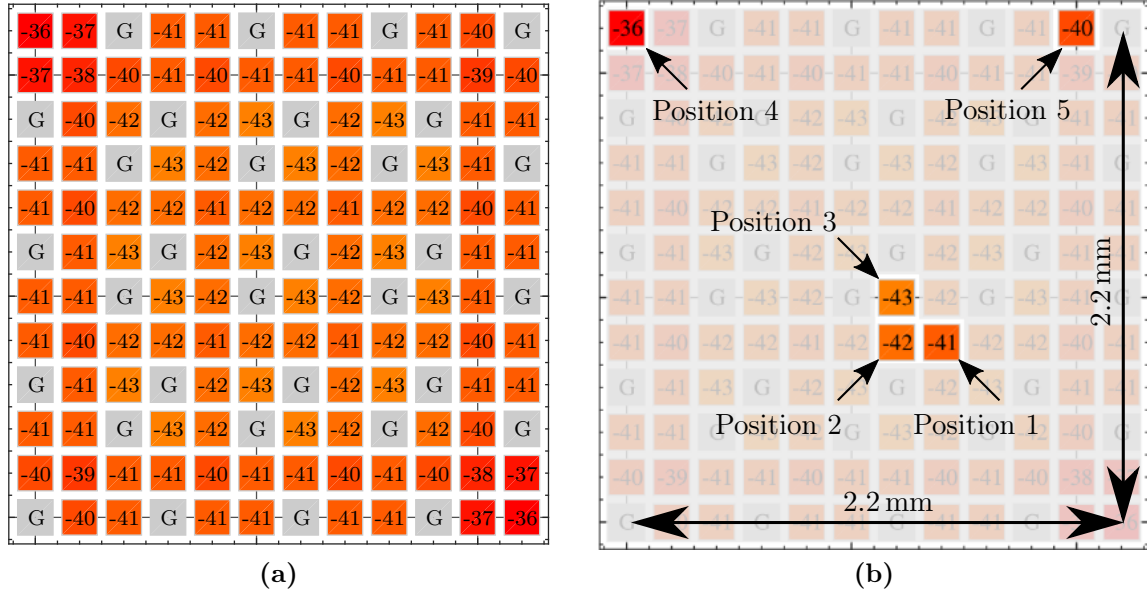


Figure 6.14: (continued from Fig. 6.13) (a) single-ended WPSXT as before but with finite planes with edges at 200 μm distance to array border (centers of outermost vias) (b) labeling of positions referred to in Fig. 6.16. Figure and text taken from [14].

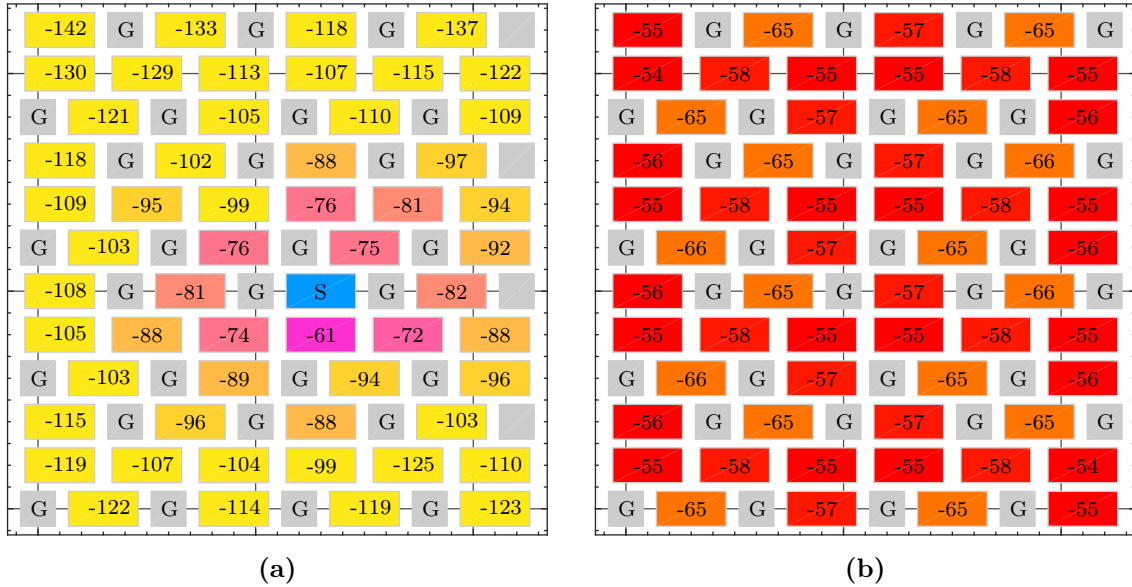


Figure 6.15: Setup as in Figs. 6.13/6.14 but single-ended channels combined to differential channels (a) far-end crosstalk in dB at 50 GHz between the differential channels created from pairs of adjacent vias to or from the central channel marked with the letter “S” (b) corresponding differential WPSXT for the signal with 20 ps rise time with finite planes with edges at 200 μm distance to array border. Figure and text taken from [14].

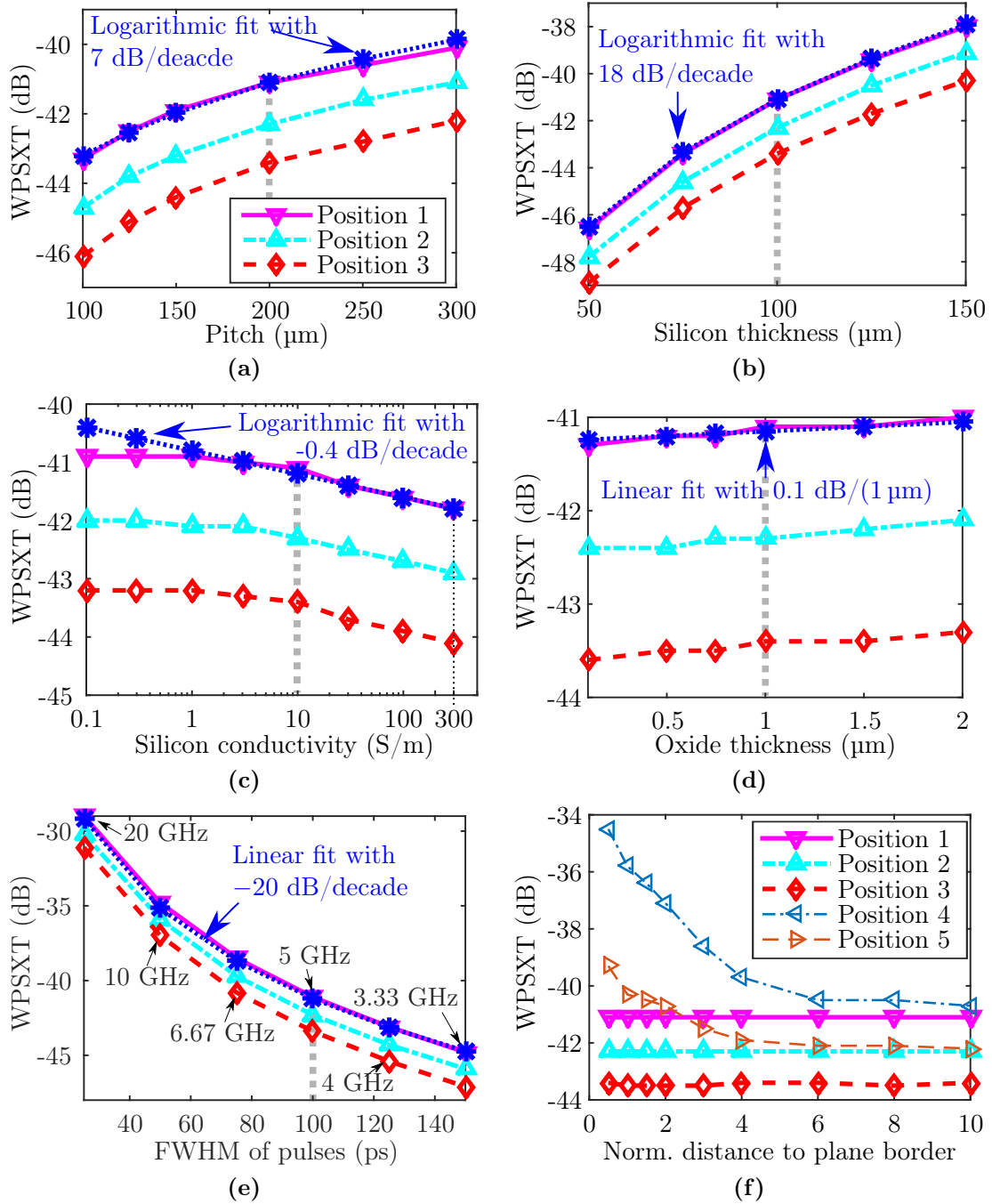


Figure 6.16: WPSXT as function of several varied parameters with the default parameter set being that of Fig. 6.13d. The default parameters are marked with gray vertical dashed lines. Except for the variation of signal and ground via assignment, the various lines give the values at the positions marked in Fig. 6.14f and the blue dashed lines give linear or logarithmic fits for position 1 where the highest crosstalk is observed. Parameter studies of (a) pitch, (b) silicon substrate thickness, (c) silicon conductivity, (d) oxide thickness, (e) pulse length, (f) distance of the plane border for the case of finite planes normalized to the pitch of 200 μm . (continued in Fig. 6.17) Figures adapted and text taken from [14].

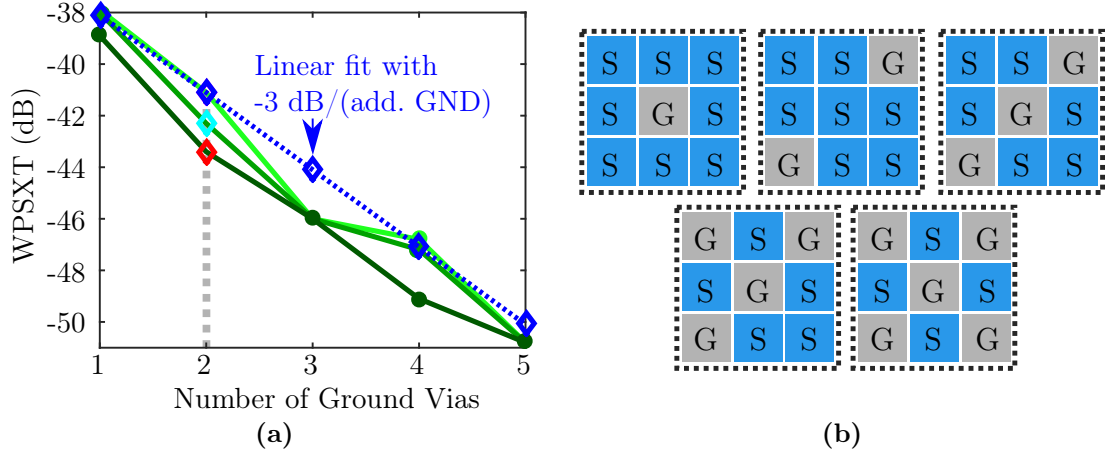


Figure 6.17: (continued from Fig. 6.16) (a) number of ground vias in the 3×3 pattern with (b) corresponding assignment variations. The lines in subfigure (a) are touching at several points because the symmetries of the used patterns lead to positions with almost identical total crosstalk. Figure and text taken from [14].

6.5 Analysis of Design Parameter Variation using WPSXT

The investigation of a fixed configuration in the previous section illustrated the relation of WPSXT and single crosstalk contributions. In the following, one out of several parameters is varied at a time and the WPSXT is evaluated. This is used to estimate dependencies on these parameters. The WPSXT is evaluated for three selected positions that are depicted in Fig. 6.14b. Position 1 is the position in the 3×3 pattern with the largest average distance to the ground vias. This results in a higher crosstalk than at other locations in the pattern except for locations near the array rim. As the highest WPSXT is consistently observed for position 1, the linear or logarithmic fits that are also shown are only given for this position.

In Fig. 6.16a, results for different value of the pitch are presented. In comparison to some of the other parameters, the influence is relatively high with a logarithmic fit of about 7 dB/decade. Smaller value of pitch lead to a better control of the return current which is established/accomplished by the ground vias. This effect compensates the effects due to narrower spacing of the vias and therefore smaller distances to other signal vias. The influence of the silicon substrate thickness is also relatively large, as can be observed in Fig. 6.16b. A logarithmic fit with about 18 dB/decade can be applied to this data. As the far-end crosstalk is investigated, it should again be mentioned that it is underestimated by the PBV for close spacing in comparison to the cavity height. The effect of a variation

in silicon conductivity is shown in Fig. 6.16c. It is found to be small with a logarithmic fit of about -0.4 dB/decade for the higher frequencies and almost constant values for low frequencies. The effect of the oxide thickness is also low with a linear fit of -0.4 dB/ μm that is shown in Fig. 6.16d. In the quasi-TEM frequency range, the oxide thickness has a small impact on the wave number and therefore on the crosstalk characteristics.

Next, the pulse train properties are varied with rise times between 5 ps and 30 ps and pulse lengths (FWHM) which are five times the respective rise time, i.e. with values between 25 ps and 150 ps. The corresponding results are presented in Fig. 6.16e. A dependence can be observed for which a logarithmic fit with -20 dB/decade can be applied. It is further of interest, which effect the finite-sized plane metallizations can have. The results for the considered positions and two additional positions at the array border are shown in Fig. 6.16f. The vias/channels at positions 1, 2, and 3 are hardly influenced by the variation of the normalized distance of the outermost vias of the array to the plane border (normalized to the array pitch). An influence for positions 4 and 5 can be observed for those cases where the plane border is closer than about 6 times the pitch. For a very close plane border, channel 4 shows one of the largest WPSXT values of the array.

Finally, the assignment of vias as signal or ground vias is also varied. The results for WPSXT at three unique positions are shown in Fig. 6.17a. The corresponding assignments in the 3×3 pattern are shown in Fig. 6.17b in which letters “S” mark the locations of signal vias and letters “G” mark the positions of ground vias. The number of ground vias is increased from one pattern to the next one. In the pattern the number of unique positions differs, e.g. in the case with three ground vias in the 3×3 pattern, every signal via has two other signal vias to two sides and two ground vias to the other two sides. The crosstalk is therefore only different at the unique positions if effects from the array border can be neglected. A fit is in this case determined for the highest unique value, i.e. it estimates the upper limit. Except for the value for 3 ground vias, a linear fit with -3 dB per added ground via describes the behavior quite well.

6.6 Summary and Conclusions

In this chapter, the PBV has been validated for medium sized arrays. The PBV proves to be a numerically efficient method enabling the simulation of large vias arrays not feasible with general-purpose 3D solvers. With the proposed modifications of the computation of the parallel plane impedance the efficiency can be further improved. The proposed crosstalk measure based on power sums for uncorrelated crosstalk provides a reduction to a single

figure of merit for every channel assigned to single vias or pairs thereof. This enables the investigation of the influence of several important design parameters. It could for example be observed that the influence of the silicon conductivity on the total uncorrelated crosstalk is relatively low whereas the influence of the value of the silicon layer thickness is large.

Chapter 7

Validation of Modeling Approaches

In this chapter, several correlations of modeling approaches and simulation results are presented. In the first part, the complementary modeling approach based on multi-conductor transmission line (MTL) theory is introduced. This approach and the PBV approach are compared for some simple structures and to FEM full-wave results for several stackups with TSV interposers. The latter enables a judgment of the applicability in a real-life environment.

In the second part of this chapter, measurement results are presented for several structures with TSVs. Because these structures must be tailored to the conditions imposed by the measurements, they include parts for which no electromagnetic models are available. Correlations are therefore only carried out with FEM full-wave simulation results.

7.1 Modeling Techniques for Wave Propagation Along the Via barrels

In this section, the complementary modeling approaches to the physics-based modeling are presented. These methods are based on the assumption that propagation occurs dominantly along the circular TSV conductors and can therefore be described by modes of the cross-section that are orthogonal to the TSV axes. As discussed before, these assumptions correspond to specific boundary conditions and excitations. In most practical cases (slow-wave and quasi-TEM regimes, as discussed in the following) this leads to a numerically efficient description as a multi-conductor transmission line. The following discussion starts with a brief look at the rigorous modeling which is only feasible for a TSV pair. The quasi-static modeling approaches which are still general enough for most practical applications and which can be used for the simulation of large arrays are introduced subsequently.

7.1.1 Rigorous Modeling of Two-Wire Lines Using the Multipole Expansion Method

One of the most rigorous and therefore most general methods of the modeling of wave propagation along the via barrels in the regard of the parameter range where it is applicable is the multi-pole expansion method (MEM) for through silicon via pairs that is presented in [25]. In the most general case, the modes that propagate along the pair of vias in the inhomogeneous structure (as the one illustrated in Fig. 7.1) are hybrid mode. This means that these modes have both electric and magnetic field components along the longitudinal direction, and therefore cannot be classified as either transverse electric, magnetic, or electromagnetic. The hybrid property is required because continuity of the tangential field components amounts to continuity of all four tangential field components (both longitudinal and azimuthal components of electric and magnetic field strength) at the Si-SiO₂-interfaces. The advantage of this method is its high accuracy. It can model the skin-effect mode in which a significant part of the conduction currents occurs in the silicon layer. For very high conductivities of the silicon and high frequencies, the field concentrates in the oxide layers. The skin-effect leads to fields of the propagation along each via barrel which are similar to those of a coaxial waveguide, i.e., a surface wave is guided along each Si-SiO₂-interface. In this case, the same numerical problems are expected as for the TRM for parallel plate waveguides, but these have not been further investigated in [25]. Because of the limitation to via pairs, this method is not applicable for via arrays in which there is typically a significant coupling to more than one neighboring via. The method can be use to validate the quasi-static models and to determine their validity range by comparing results for TSV pairs in silicon with, e.g., elevated conductivity levels.

7.1.2 Modeling Based on Quasi-Static Analysis

In many practical cases a quasi-static analysis is possible, namely for the cases where the relevant modes are either quasi-TEM modes or slow-wave modes. Even though it is based on the assumption that the modeled mode fields are transverse electromagnetic, it is found to be applicable for the quasi-TEM mode and for the slow-wave mode. This is because the longitudinal field components are also comparatively small in these modes. In case of the skin-effect mode, the longitudinal field components become significant and invalidates the assumption of an (almost) transverse electromagnetic field. As has already been seen during the discussion of the parallel plate modes, the silicon conductivity may at most have moderate values such that the skin-effect plays no role at any of the frequencies of interest.

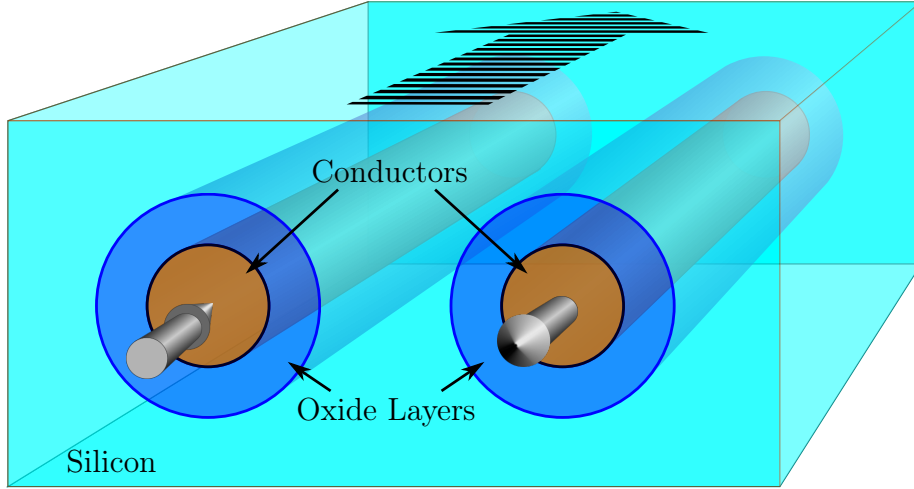


Figure 7.1: Illustration of the geometry of the two-wire line of oxide-coated parallel conductors in the silicon medium (not to scale, especially the thickness of the oxide layers is exaggerated). The arrow on the top illustrates the signal propagation direction. The arrow on the conductors mark directions of current flow.

The methods presented in the following have in common that for the multi-conductor modeling per-unit-length (PUL) parameters are computed of capacitance, conductance, inductance, and resistance (the latter only if conductor losses are included). Using the MTL theory, network parameters can be computed from these PUL parameters. In the conventional definition these are defined for terminals at both ends of the TSV conductors which refer to the same, single reference conductor. In order to make these results comparable to the physics based modeling (especially for the single-ended signaling where a significant number of ground vias is usually required) the assignment of several reference conductors is also discussed in sections 7.1.5 and E.7.3.

If two conductors carry currents of opposite directions, then, induction causes an accumulation of current and charge in the areas closest to the respective other conductor. If the conductors carry currents of equal direction, the accumulation occurs in the areas furthest from the respective other conductor. For the TEM mode it can be seen that the surface charge related to the transverse electric field and the surface current related to the transverse magnetic field must have an identical distribution. This is because the electric and magnetic field are related by the same intrinsic impedance everywhere inside the medium. The determination of one distribution is a dual problem to the determination of the other distribution which is discussed for the two-wire line in [98, Sec. 3.2.2.1] Current and charge density are functions of the position on the respective circumference. These function can be efficiently approximated by harmonics, i.e. orthogonal sinusoidal functions of the angle of the positions with respect to the center of the circular cross-section. This is performed

in the method presented in section 7.1.3. The method in Section 7.1.4 assumes uniform currents on each conductor circumference which is a sufficient approximation for most practical applications.

7.1.3 Per Unit Length Parameter Computation Based on a Fourier Method

The first quasi-static method is based on the Fourier expansion of charge densities. It is only discussed briefly here but in more detail in Appendix E.5 because it has not yet been published elsewhere. This method provides very accurate results in the cases where the quasi-static modeling is applicable, i.e. in cases where the silicon conductivity is comparatively low and the TSV metal conductivity is comparably high. The former enables an independent computation of the transverse electric and magnetic fields and the related per-unit-length admittance and impedance matrices. The latter allows to neglect the contributions to the effective properties from internal resistance and inductance of the metallic via barrels. The method is based on a Fourier expansion of the charge distributions on the TSV circumferences. With a sufficient number of Fourier coefficients, the effects of non-uniform charge distributions due to the proximity effect in cases with small via pitches (compared to the cross-sectional dimensions) can be accounted for with high accuracy. By allowing complex charges in the computation, the static analysis gives matrices for both an effective capacitance and (transverse) conductance.

7.1.4 Per Unit Length Parameter Computation Based on Thin-Wire Approximation

A method that introduces a further assumption regarding the geometry but leads to good accuracy for many practical cases [39] is the thin-wire approximation (TWA). The additional assumption of the thin-wire approximations is that the circular conductors of the multi-conductor transmission line are thin compared to all distances between conductors, which corresponds to a small radius for circular conductors. This approximation is also known as wide-separation approximation [98]. In the quasi-static analysis of this approach, the contour of each equipotential conductor has a uniform surface current and surface charge distribution whereas, as already discussed, it should be non-uniform due to the proximity effect. As shown in Appendix E.5.5, the Fourier method is equivalent to the thin-wire approximation for homogeneous dielectrics if only the 0th Fourier coefficient is used.

Homogeneous case

In case of a homogeneous substrate, the per-unit-length inductance terms can be obtained as [98]

$$\begin{aligned} l_{ii} &= \frac{\mu_0}{2\pi} \ln\left(\frac{d_{i0}}{r_{w0}}\right) \ln\left(\frac{d_{i0}}{r_{wi}}\right) = \frac{\mu_0}{2\pi} \ln\left(\frac{d_{i0}^2}{r_{w0}r_{wi}}\right) \\ &= \frac{\mu_0}{2\pi} (2 \ln d_{i0} - \ln r_{w0} - \ln r_{wi}) \end{aligned} \quad (7.1a)$$

and

$$\begin{aligned} l_{ij} &= \frac{\mu_0}{2\pi} \ln\left(\frac{d_{j0}}{d_{ij}}\right) \ln\left(\frac{d_{i0}}{r_{w0}}\right) = \frac{\mu_0}{2\pi} \ln\left(\frac{d_{j0}d_{i0}}{d_{ij}r_{w0}}\right) \\ &= \frac{\mu_0}{2\pi} (\ln d_{j0} + \ln d_{i0} - \ln d_{ij} - \ln r_{w0}) \end{aligned} \quad (i \neq j) \quad (7.1b)$$

where d_{ij} is the distance between conductors i and j , r_{wi} is the radius of conductor i , and indices 0 refer to the corresponding distances to and radii of the reference conductor. Which of the above representations is more suitable for the algorithmic implementation depends on the symmetries. If symmetries occur, the radii and several distances are the same. With the respective last line in (7.1a) and (7.1b), the logarithm should be evaluated only once for every unique value.

For the homogeneous case with a complex permittivity $\underline{\varepsilon} = \varepsilon + j\sigma/\omega$, the corresponding per-unit-length capacitance and conductance matrices are given by

$$\begin{aligned} \mathbf{C} + j\mathbf{G}/\omega &= \mu\underline{\varepsilon}\mathbf{L}^{-1} \\ &= \mu(\varepsilon + j\sigma/\omega)\mathbf{L}^{-1} \end{aligned} \quad (7.2a)$$

$$\mathbf{C} = \mu\varepsilon\mathbf{L}^{-1} \quad (7.2b)$$

$$\mathbf{G} = \mu\sigma\mathbf{L}^{-1} = \frac{\sigma}{\varepsilon}\mathbf{C} \quad (7.2c)$$

The per-unit-length impedance matrix, $\hat{\mathbf{Z}}$, and the per-unit-length admittance matrix, $\hat{\mathbf{Y}}$, are combined from \mathbf{R} , \mathbf{L} , \mathbf{G} , and \mathbf{C} as [98, Eq. 4.6]

$$\hat{\mathbf{Z}} = \mathbf{R} + j\omega\mathbf{L}, \quad (7.3a)$$

$$\hat{\mathbf{Y}} = \mathbf{G} + j\omega\mathbf{C}. \quad (7.3b)$$

In the following $\mathbf{R} = 0$ is assumed and only the external inductance is considered. As

proposed for TSV modeling in [39], internal inductance and resistance of the via barrels can be accounted for with an analytic relation that is further discussed in Appendix E.2.

Inhomogeneous case

As proposed in [39, Sec. III], the homogeneous case is extended to the inhomogeneous case with concentric dielectric layers that is depicted in Fig. 7.2. On the circumference of these layers, a uniform charge distribution follows from the assumption of uniform charge distribution on the conducting cylinders if they share the same axis. Only this case is considered in the following and it is also the most relevant one for practical applications. With uniform charge distributions, the capacitance contributions of the dielectric layers can be obtained from the (per-unit-length) coaxial capacitor formula given by [98, Eq. 3.58]

$$c = \frac{2\pi\varepsilon}{\ln(r_s/r_w)} \quad (7.4)$$

where r_s and r_w are the outer and inner radii of the coaxial structure, respectively, and ε is the permittivity of the dielectric layer.

The results for the coaxial layers have to be concatenated to every port of the admittance matrix from (7.3b) for the silicon region. This can be carried out, e.g., with the impedance parameters concatenation from Appendix G.2.4 with an impedance for the oxide layer using (7.4) concatenated to each terminal and the common reference conductor of the impedance matrix $\hat{\mathbf{Y}}^{-1}$ from (7.3b) for the silicon region. Alternatively, a concatenation using admittances from Appendix G.1.1 can be applied.

For the inductance, no modifications compared to the homogeneous case are required due to the MTL assumptions and exclusively non-magnetic materials.

7.1.5 Computation of Network Parameters from Per Unit Length Parameters

After the per-unit-length parameters have been computed, it is of interest to determine the network parameters of the structure with one multi-conductor port at the top of the interposer and one at the bottom. Each of these multi-conductor ports has N terminals if there are $N + 1$ conducting vias in the simulated structure. In general, several techniques are available for this task. Often, the excitations on terminals are explicitly or implicitly converted from terminal voltages and currents to modal voltages and currents. Examples for modes of multi-conductor lines are the even and odd mode of a symmetric three-conductor line. The transformation is achieved in general through a transformation matrix

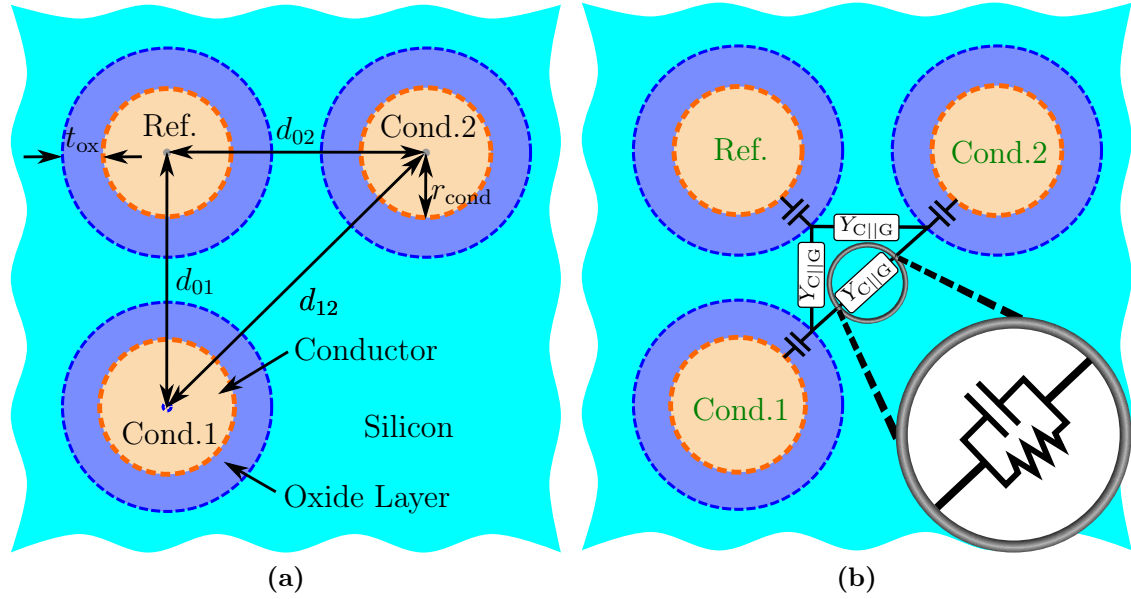


Figure 7.2: Definitions for TWA modeling: (a) Geometry of the cross-section (not to scale) (b) Corresponding equivalent circuit for the transverse admittance matrix.

which diagonalized the product of per-unit-length parameter matrices $\hat{\mathbf{Y}}\hat{\mathbf{Z}}$ [98, Sec. 4.4]. The methods based on diagonalization are not applicable if the medium is homogeneous in which case all modes have equal wave numbers. At the same time, a diagonalization is not required in case of a homogeneous medium [98, Sec. 4.41]. The medium is inhomogeneous for TSV applications and the above technique is applicable. A short discussion is given in Appendix E.7.1. For the comparisons in Appendix 7.2, an implementation based on the identities in [123] is used. In practice, TSVs are electrically short and therefore, lumped element representations as those discussed in Appendix E.7.2 can be used with good accuracy. The lumped element representation has the advantage of being applicable to both the homogeneous and inhomogeneous case. It can be accurate enough and lead to a higher numerical efficiency if large TSV arrays are simulated.

7.2 Comparison of Modeling Approaches

As pointed out before, there are several assumptions when applying one of the modeling approaches so far. Some of these assumptions are summarized in Fig. 7.4. If the assumptions are correct, certain boundary conditions, port definitions and simplifications regarding geometry and material properties are possible and efficient modeling techniques can be

used. The assumptions are also made to enable an independent modeling of different system levels. An example for these levels is illustrated in Fig. 7.3. It should be investigated here if assumptions regarding an independent modeling of a silicon interposer can be justified. In the following sections, simulation results for silicon interposer inside several different stack-up environments for frequencies up to 100 GHz are presented. These simulation are carried out in the following using FEM full-wave-, PBV-, and TWA-simulation. The comparison are referenced to well-defined coaxial ports in the FEM full-wave and PBV-simulations.

This section aims at showcasing to which extent the modeling approaches give similar or fundamentally different results. The investigation is limited here to single-ended scattering parameters at the respective ports, i.e. coaxial ports for the FEM and PBV and multi-conductor ports for the TWA. As both proposed modeling approaches are based on the concatenation of model parts, the applicability of the segmented analysis is thereby also assessed.

7.2.1 Modeling using FEM Full-Wave Simulations

The complete models that are considered in this section are shown in Fig. 7.5 and can only be simulated in all details by the reference simulations. These are again based on finite-element 3D full-wave simulations. The complete models include underfill areas with metallic bumps that connect the interposer to a PCB below. It includes also a redistribution layer near the top of the interposer and underfill areas on top of the interposer and below an IC connected to it. With one exception, the following investigations focus on the cases with metallizations at the outermost interfaces of the model. This way, coaxial ports can be used for an unambiguous definitions of the ports. Only in one case which is named “V5” and part of the investigations for which results are shown in Fig. 7.7, a multi-conductor/-terminal port is used. This type of port extends over the complete top and bottom surface of the structure and requires the definitions of a single reference conductor per port. In order to permit a comparisons with the cases of plane metallization further reference conductors should be defined; a post-processing step is required in this case.

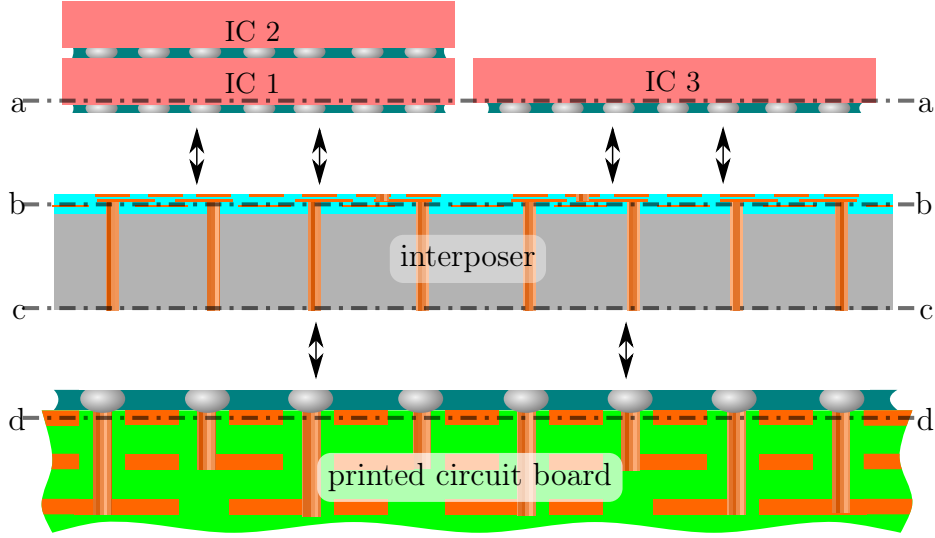


Figure 7.3: Interposer with an example for its electromagnetic environment: Below, it connects to a printed circuit board (PCB) through conducting bumps. Often, an underfill is used. High speed PCBs mostly feature plane metallizations. At the top of the interposer, redistribution layers constitute a (partially) conducting boundary. Through Silicon Vias (TSVs) can be part of an interposer or of integrated circuits (ICs) which are stacked on top of each other. The reference planes of the segmented modeling are defined at the positions marked with dash-dotted lines and letters a–d. Figure and text taken from [12].

7.2.2 Simulation of Several Stackups

The following analysis is based on the investigation of magnitudes of selected scattering parameters of silicon interposers which are embedded in several different stackups. The interposer properties are also varied. The varied interposer properties include the geometry of the redistribution layer (RDL) and the pitch of the 4×4 TSV array. The default configuration of the following investigations is given in Table 7.1 and further details are also mentioned in the captions of the figures with the respective simulation results.

Simulation of a Single and of Stacked Interposers

In the first part of the analysis, a single metal clad interposer, as well as stacks with 2 and 3 interposer are considered. Cross-sections of all 3 cases can be seen in Fig. 7.5a. In the stacks, the interposers are interconnects by conductive bumps. These have a radius of $13 \mu\text{m}$ radius and are embedded in a lossless dielectric with a relative permittivity of four. The separation of the neighboring metallizations is chosen as $20 \mu\text{m}$, the bumps are therefore oblate at the locations where they touch the TSVs. The structure with all details can be simulated in

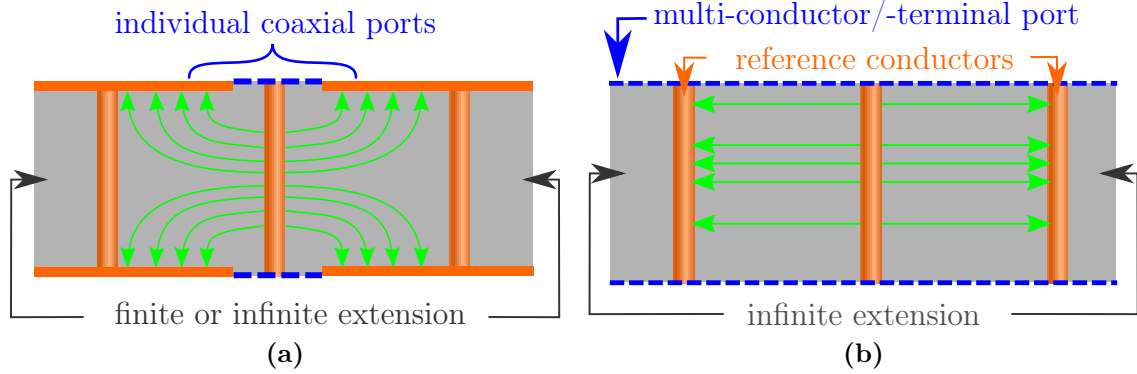


Figure 7.4: Illustration of the port definitions (blue dashed lines) and the electric near fields (green arrows). (a) For the physics-based via (PBV) modeling approach: On the top and bottom antipads of the signal vias, coaxial ports are defined. The outer vias connects the top and bottom metallizations and are referred to ground vias. (b) For the multi-conductor transmission line (MTL) theory based approach: On the same surface, several terminals and at least one reference conductor are defined. Figure taken from and text adapted from [12].

Parameter Description	Symbol	Default Value
Thickness of the silicon substrate	t	100 μm
Relative permittivity of silicon	$\epsilon_{r,\text{Si}}$	11.9
Thickness of the oxide	t_{oxide}	1 μm
Relative permittivity of the oxide (SiO_2)	$\epsilon_{r,\text{oxide}}$	4
Pitch of the TSVs	d_1	200 μm
Pitch of the RDL via barrels	d_2	100 μm
Radius of the interposer antipads	r_{antipad}	20 μm
Radius of the TSV barrels	r_{via}	10 μm

Table 7.1: Default Parameter Values for the Silicon Interposers. Table adapted from [12].

the FEM full-wave simulations, whereas some further simplifications are required for other the proposed methods. In both the PBV- and the TWA-method, the arrays of bumps (embedded in the underfill) are approximated as arrays of cylindrical barrels with radii equal to the TSV radius and the overall results are obtained by concatenation of the network parameter of the models, i.e., for the stack of three interposers, five models are concatenated. In the TWA-method, the planar metallizations are ignored. For an assumed propagation along a vertical signal path, the discontinuities along this path are constituted by both these metallizations and by the changes of permittivity of the dielectric medium. The former effect is therefore excluded whereas the latter effect is included. In the PBV model the short coaxial sections constituted by the antipad regions are neglected.

The magnitudes of the scattering parameters are given in Fig. 7.6. An additional FEM-

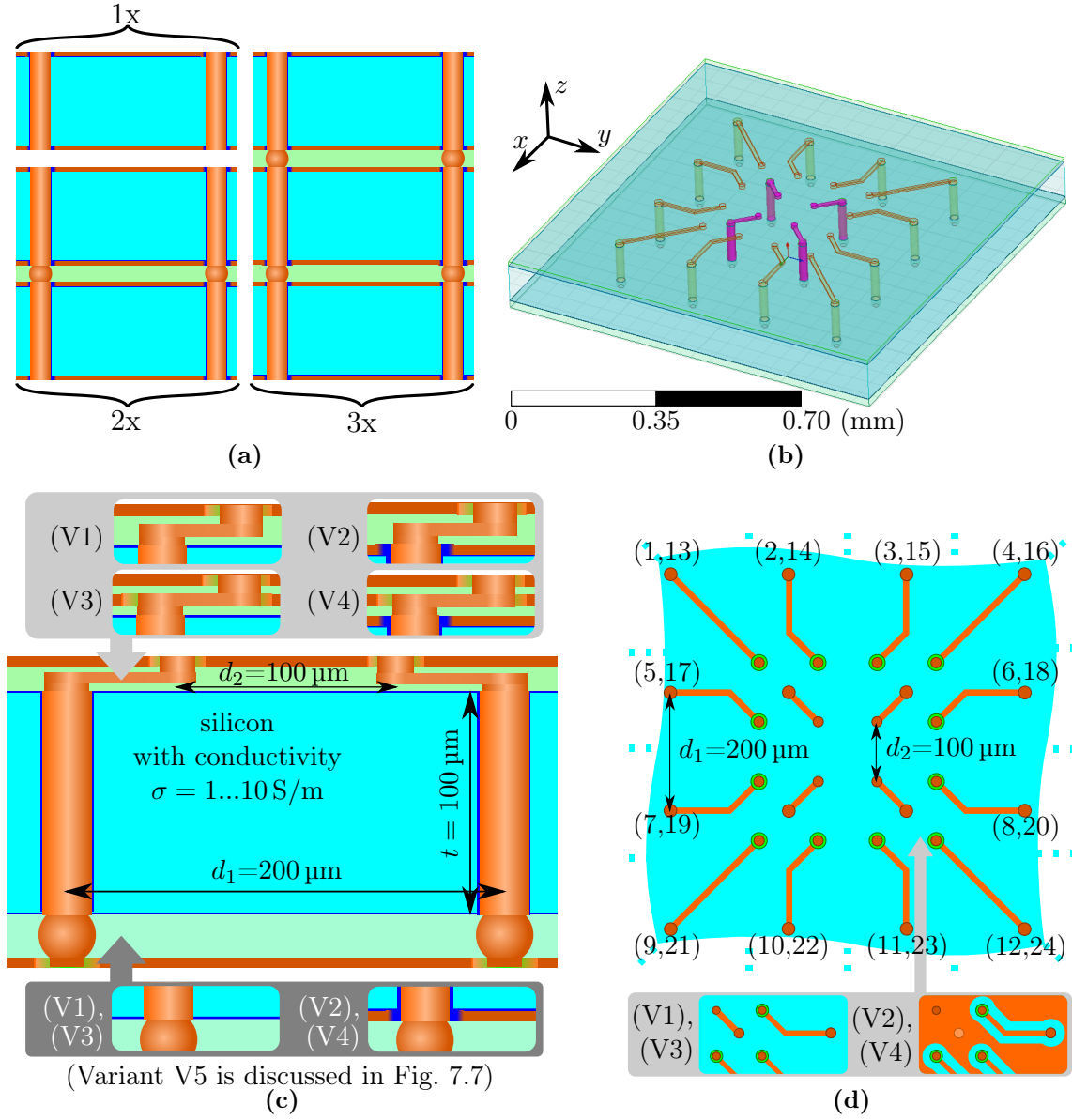


Figure 7.5: (a) Illustration of the single interposer with top and bottom metallizations, a stack of two interposers connected through PEC bumps and an underfill dielectric, and a stack of three interposers. (b) Perspective view of the structure used for the full-wave simulation in which the ground/reference conductors are highlighted. PMC boundary conditions are used to include the effect of reflections from the finite planes sizes ($2 \text{ mm} \times 2 \text{ mm}$ except for variation V5 in Fig. 7.7). (c) Cross-sectional view of a part of the stack-up with the considered variations of the redistribution layer and the interposer bottom metallization, and some of the default parameter values. The metal components are drawn in orange color. (d) Top view of the fan-out used in the redistribution layer (RDL) with the two used variations and with the port indices. The first number in the braces gives the index of the top port at the IC-plane, the second one the index of the bottom port at the PCB plane. The four inner vias of the 4×4 layout are assigned as ground vias/reference conductors. Figure and text taken/adapted from [12].

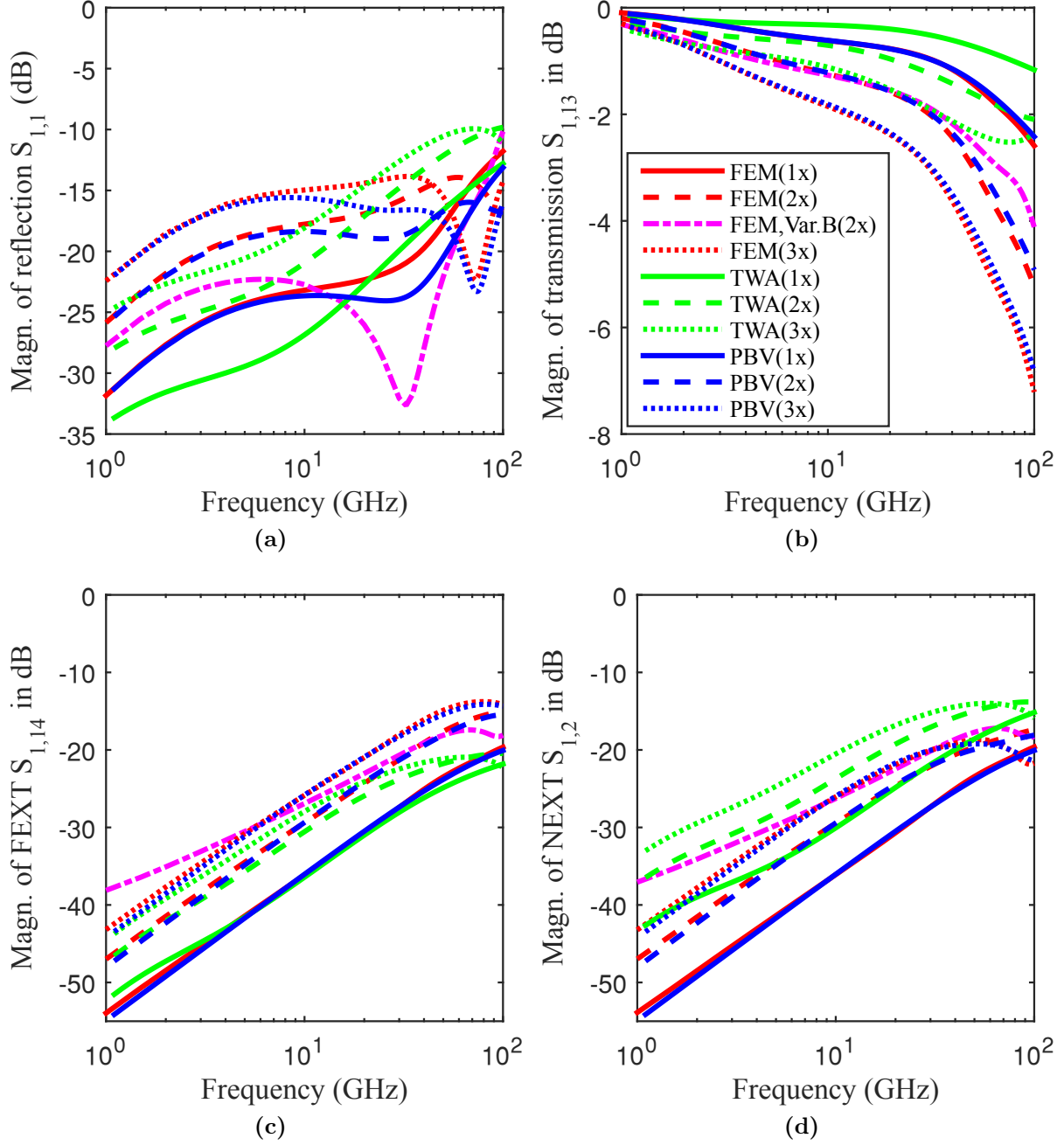


Figure 7.6: Magnitudes of selected scattering parameters (normalized to $50\ \Omega$) of the structures given in Fig. 7.5a. Further configuration can be found in Table 7.1, the silicon conductivity is 10 S/m . The PBV- and TWA-results for the different stacks are also given. In the legend, the number of stacked interposers is given in braces. Figure and text taken from [12].

result is given for the stack of two interposers: The structure is modified by replacing the topmost metallization of the lower interposer and the bottom metallization of the upper interposer with a dielectric layer with identical properties as the adjacent underfill area. This results in plane metallizations only at the outermost faces of the overall structure. This variation is named “FEM,Var.B(2x)” in Fig. 7.6. As can be expected due to very similar assumptions, the FEM and the PBV results show a good agreement for all shown scattering parameters. The TWA results show similar behavior with frequency but the following differences: Overall, there is mainly a higher transmission predicted by the TWA for all stackups. The far-end crosstalk computed by the TWA is very similar for low frequencies but significantly lower at higher frequencies. The near-end crosstalk computed by the TWA is significantly higher over the complete frequency range. The variation of the stack of two interposers named “FEM,Var.B(2x)” shows results that differ from both the PBV and the TWA results. Regarding the comparison of the results for different numbers of stacked interposer, the behavior is different for lower and higher frequencies. At low frequencies the crosstalk is proportional and the transmission is anti-proportional to the number of stacked interposer. At higher frequencies the behavior is more complex, e.g., the NEXT is lowest for the stack of three interposer at 100 GHz (FEM- and PBV-results).

Simulation of Interposers with Different Redistribution Layers and Adjacent Structures

In the following, the setups depicted in Figs. 7.5b–7.5d are considered. The setups are labeled as V1 to V4 and differ in the configuration of the boundaries at the top and at the bottom of the (single) interposer. Only the variations V2 and V4 have metallizations (reference planes) at the outermost faces of the interposer. Only the variations V3 and V4 have a metallic plane with cutouts in the same planes as the line patterns (fan-out). In the latter cases a structure similar to a (grounded) coplanar line is constituted. In the PBV- and the TWA-model several simplifications due to unavailability of the respective electromagnetic models for the fan-out pattern and the discontinuities to and from them are made. Only the models that have been explained before for the via arrays and arrays of bumps are concatenated. The default configuration from Table 7.1 applies again.

For the first configuration with the default pitch the magnitudes of scattering parameters are presented in Fig. 7.7. Results for the second configuration for which the pitch is reduced to 100 μm in the TSV array are shown in Fig. 7.8. Excluding the reflections, the general behavior with frequency is similar for all reconsidered variants. As can be seen for both cases, the results for variants V1 and V3 (both without interposer metallizations) are very similar. Except for the reflections, variants V2 and V4 (both with interposer metallizations)

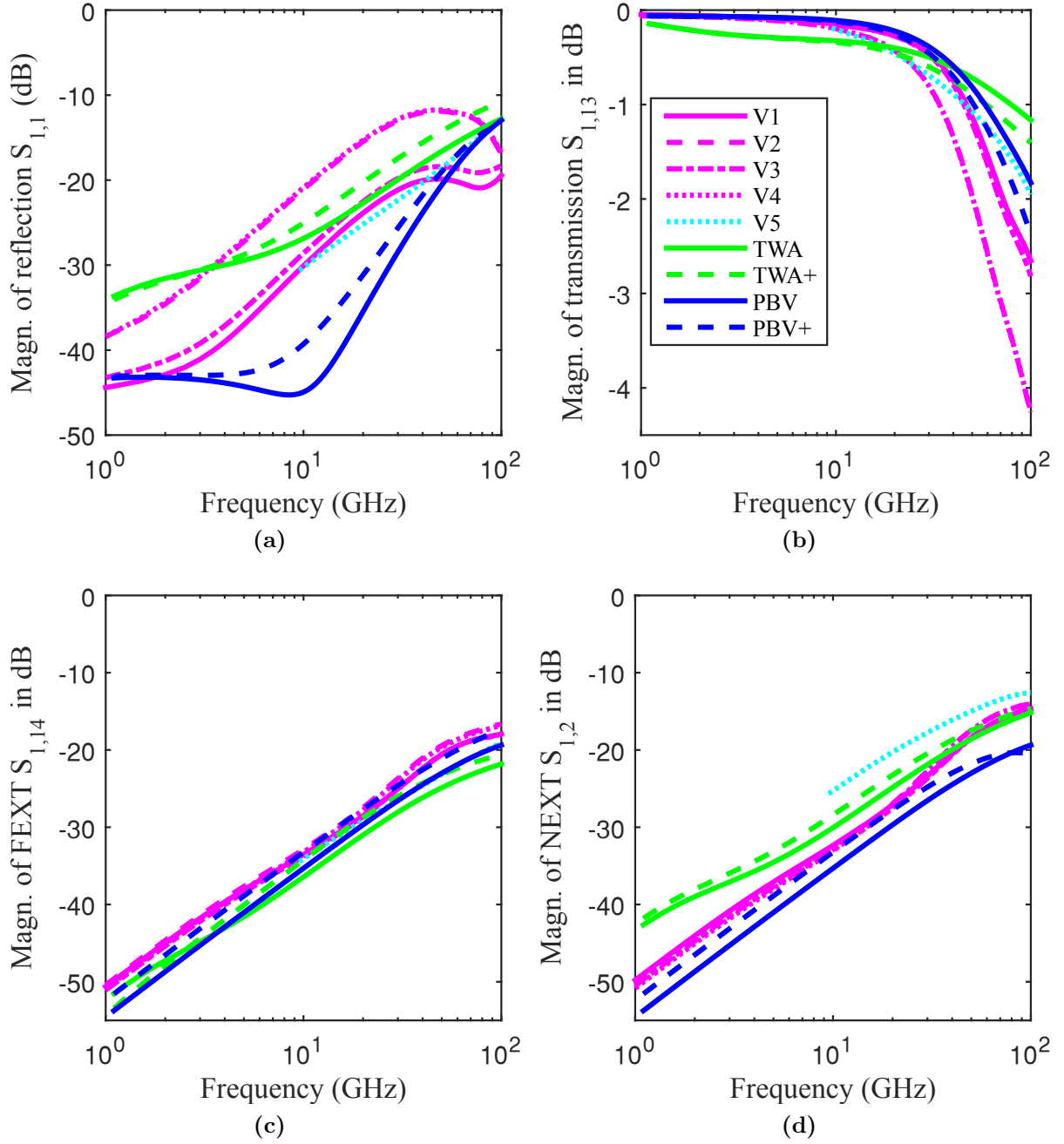


Figure 7.7: Scattering parameters (normalized to $50\ \Omega$) for comparison of variations of the stackup for 1 S/m silicon conductivity. Variant V5 is a full-wave simulation with FEM with a stackup identical to variant V1 for the inner parts but without the outermost metallizations, and with single multi-conductor/-terminals on top and bottom of the stackup. For V5, the simulation only converges down to about 10 GHz. In the legend, for PBV and TWA, the “+” refers to the case where simplified models for the adjacent structures are concatenated (with all metal planes as in variant V4). Figure and text taken from [12].

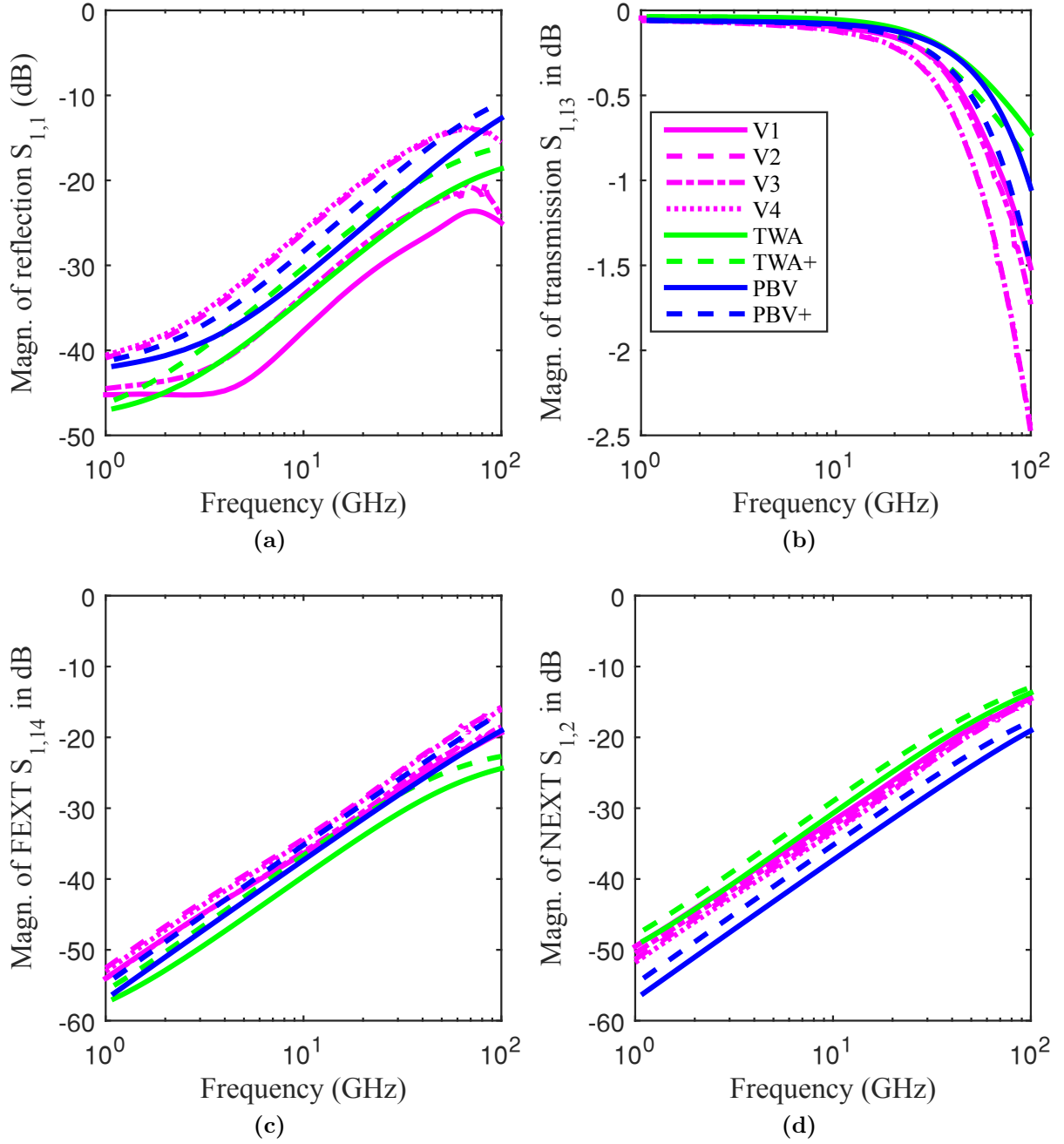


Figure 7.8: Scattering parameters (normalized to $50\ \Omega$) for comparison of variations of the stackup for 1 S/m silicon conductivity and a reduced pitch ($100\ \mu\text{m}$ in the interposer and $50\ \mu\text{m}$ in the RDL). Figure and text taken from [12].

also show very similar behavior. The PBV model which accounts for all arrays (“PBV+”) of the stackup shows a good agreements except for the reflection and for the near end crosstalk, especially for the case with the narrower spacing of the vias. The TWA model show larger average deviations from the FEM full-wave results for V1–V4. The FEXT is still adequately modeled over most of the frequency range. It is interesting to note that for the case of narrow spacing where the PBV underestimates the NEXT, the TWA overestimates it.

7.2.3 Conclusions Regarding Model Comparisons

It could be observed in the previous section, that up to 100 GHz, the considered stackups show qualitatively the same behavior. The link between top and bottom is almost transparent with high transmission and low reflection of the largest part of the frequency range. Furthermore, the crosstalk is inductively dominated in the via and bump arrays leading to a simple behavior over most the frequency range. The inductive coupling can be concluded from the phase and from the almost linear behavior in log-log scale which can be observed best at low frequencies. It could also be shown that the general behavior with frequency and the order of the results are in agreement with the FEM reference results. This is despite the fact that the underlying physics and boundary conditions are different for PBV and the MTL/TWA modeling. The fact that different boundary conditions lead to similar results puts into perspective the importance of exact modeling. Within certain limits that have not been determined in this thesis both modeling approaches therefore seem applicable for the simulation of practical TSV structures. This enables the analysis of large via arrays that cannot be (efficiently) simulated by general-purpose 3D full-wave solvers in the ways discussed in Sec. 6.5.

7.3 Correlation of Measurements and Full-Wave Simulations

Several test structures have been designed and measured at the Institute of Electromagnetic Theory (TET), Hamburg University of Technology, and at the Fraunhofer Institute for Reliability and Microintegration (IZM), Berlin. The structures have been fabricated at Fraunhofer IZM–ASSID (All-Silicon System Integration Dresden). The results from measurement of several of these structures are presented in this section together with several full-wave simulation results for correlation and thereby a partial validation of the general modeling assumptions. The fabricated structures are designed in such a manner that

they can be fabricated with the available processes and that they can be measured with the available techniques. They therefore include parts which cannot be modeled by the proposed approaches of this thesis. Hence, a validation is only carried out with full-wave simulations.

The remainder of this section is organized as follows: First, the justification, motivation, and aims of the TSV test structure designs are discussed. Then, the most relevant data for these structures is presented. Further, the measurement setups are shown. As the simulation setups are not fully analog to the measurement setups, their configurations also requires some discussion. Finally, several results are shown and interpreted in terms of applicability of signal links and in terms of agreement of measurement and simulation.

7.3.1 Motivation and Challenges

A major part of the project from which this thesis is reporting has been the electromagnetic characterizations by means of frequency domain measurements. Meaningful designs require a good knowledge of the marginal conditions, i.e., material properties, the stackup/buildup, via shape, allowed shapes of the planar metal structures etc. Especially the first two properties have not been known exactly at the beginning of this project. The materials are often only specified for a limited low frequency range or even only as a DC-value. Therefore, it has also been part of the project to characterize materials, especially the silicon substrate, over a large frequency range, i.e. up to 110 GHz [22, 23]. Stackup layer thicknesses and via shape are to some degree known from the fabrication process configuration. Values can be obtained from micrographs as the one shown in Fig. 7.9a, though there remains some uncertainty. It would be of advantage to design structures after all relevant process parameters have been determined. Unfortunately this second iteration could not be carried out within this project and constitutes a task for future research projects.

7.3.2 Designed and Fabricated Structures for TSV Characterization

Metal Geometries

Several TSV test structures were implemented both with and without metallizations at the top and bottom (only with neither or both) to investigate the influence and quantify the difference by measurements. A stacking of multiple chips could not be realized. Most of the implemented test structures consist of a transition from top to bottom and a connected transition back to the top side. Variations include the length of the lines at top and bottom

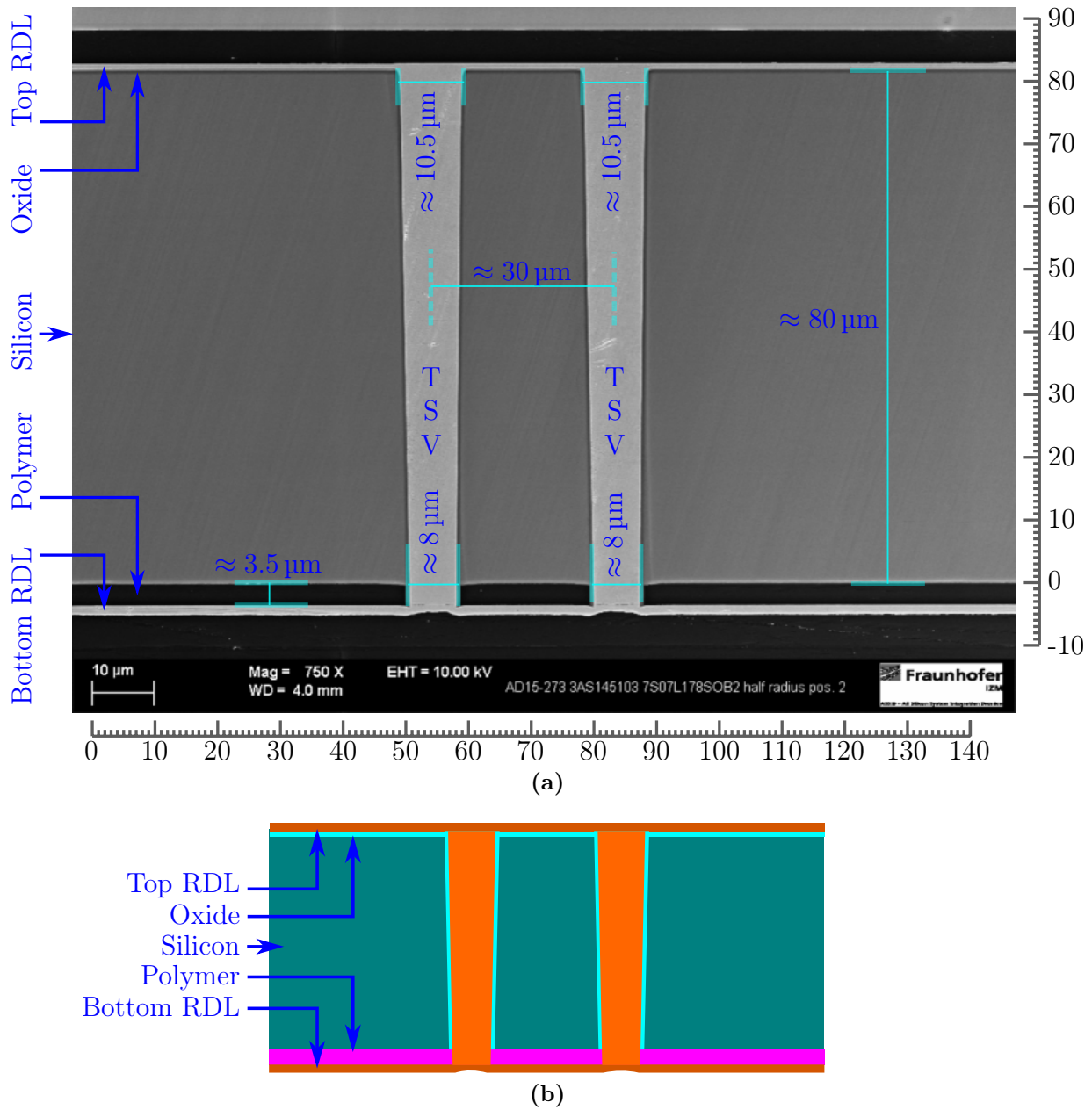


Figure 7.9: (a) Photo of the cross-section of the fabricated TSV-structures (microsection). All dimensions in μm . Photo courtesy of Fraunhofer Institute for Reliability and Microintegration (IZM), Berlin. (b) Schematic drawing (not to scale) showing the stackup configuration. Refer also to the description of measured structures in [23]. There, an oxide layer thickness of 500 nm and a 4.6 μm thick CVD polymer (WPR¹) are specified/used.

¹WPR is a trade name for photo-resists used by companies JSR Micro NV and DuPont, e.g., see [124, Table 15.7]

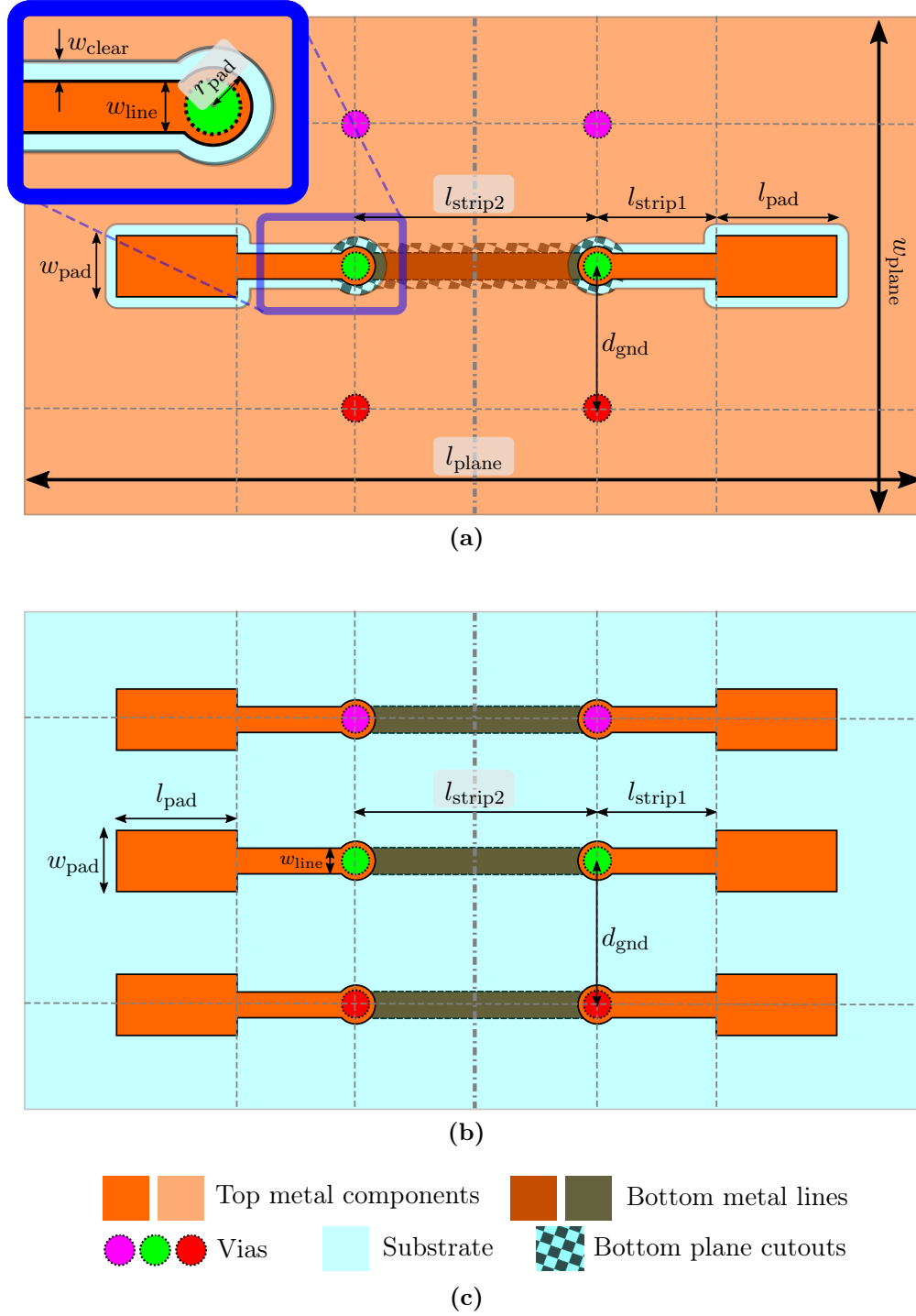


Figure 7.10: General layouts of the measured structures (a) with planes and (b) without planes and (c) the corresponding legend. Signal vias are shown in green. The ground vias are shown in purple and red. The number of ground vias is varied. Values of the parameters for the measured structures are given in Table H.1

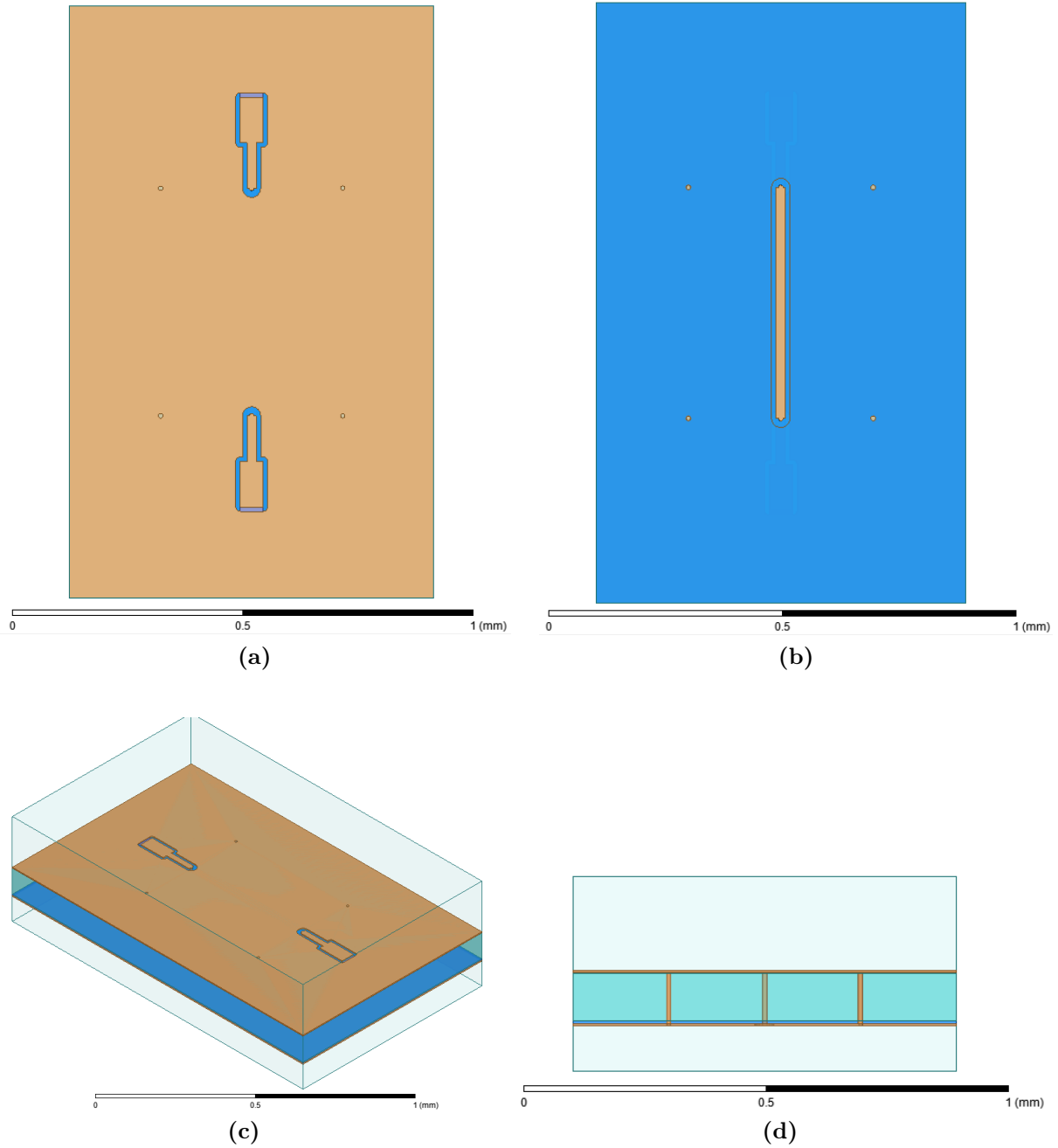


Figure 7.11: Views of one of the measured and simulated structures: (a) Top view (b) bottom view (c) perspective view (d) front view. The electrical connection is established by several coplanar lines in metallized areas on top and bottom of the silicon substrate connected by two via transitions. Each via transition consists of two to three vias of which the ones assigned as ground vias are connected to the metallizations. Lumped ports are used for the simulation of this type of test structure.

sides and (if present) the size of the plane metallizations. Schematic drawings of the two types of structures considered in the following are depicted in Fig. 7.10. For the structure with plane metallizations, several views in the modeler of the FEM software [66] are given in Fig. 7.11. The fabricated wafers have been cut into coupons for easier handling. Photos of such a coupon are presented in Fig. 7.12.

If plane metallizations are present, the lines on top and bottom sides behave similar to grounded coplanar lines. Without plane metallizations the GSG assignment of the three parallel strip conductors leads to coplanar mode fields. The same metal geometries are used for all stackups, some of which are presented in the following. As the properties of the involved materials were mostly unknown during the design phase, the designs were not optimized to specific characteristic impedances. Instead, the focus was on creating a large number of variations to choose from later.

Fabricated Stackups

The same structures have been fabricated with stackups that differ (apart from unknown differences due to fabrication tolerances) in the silicon properties and the used insulator at the via barrels and towards the top RDL. The variations that are considered in the following are listed in Table 7.2 with the assigned wafer-IDs. Fig. 7.9 shows the exemplary cross-sectional photo and the corresponding schematic drawing including the cross-section of two TSVs. The measurement results presented in the following have been selected by choosing structures with different technologies as long as the properties (i.e. mainly the losses due to the silicon substrate) permit a comparatively easy differentiation between good and insufficient calibrations. This excludes the low resistivity silicon substrate. The substrates with thermal oxide layers also show significantly lower losses than those with the SAVCD insulators. Therefore, of the fabricated stackup variations, only W23B, W21A, and W10A are selected for the correlation with FEM simulation results.

Wafer-ID	Silicon Substrate Properties	Insulator Properties
W23B	high resistivity ($\sigma \approx 1 \text{ S/m}$)	thermal oxide ($\varepsilon_r = 4$, $t \approx 200 \text{ nm}$)
W10A	standard resistivity	thermal oxide ($\varepsilon_r = 4$, $t \approx 200 \text{ nm}$)
W09	standard resistivity	thermal oxide ($\varepsilon_r = 4$, $t \approx 500 \text{ nm}$)

Table 7.2: Overview of all test wafer configurations which are considered in the following. Several additional test wafers with SACVD (sub-atmospheric chemical vapor deposition) oxide, with silicon substrates of lower conductivity, and with other oxide layer thicknesses have been fabricated by Fraunhofer IZM–ASSID (All-Silicon System Integration Dresden) but those are not considered in the following.

7.3.3 Measurement Setups

It has been the objective of the measurements to verify repeatability and ensure that the measurement process has minor influence. The electromagnetic environment may also influence the measured results. In Section 7.3.5 it is discussed how this has been considered in the full-wave simulations for correlation. Different setups have been used in order to increase the confidence in the results and in order to also include measurements up to 110 GHz which was not possible at the laboratory where the majority of the measurement work was carried out. The following sections give details about all measurement setups for which results are presented in the subsequent sections.

Measurements at the Institute of Electromagnetic Theory (TET), Hamburg University of Technology

The main setup of the measurements carried out at the Institute of Electromagnetic Theory (TET), Hamburg University of Technology is depicted in Fig. 7.13 and several details are listed in Table H.4. The mechanical part of the setup consists of a customized probing station. It has been customized by mounting micro-positioners with higher precision than the original positioners, replacing the metal chuck by one made of plastic material, and installation of a vacuum system. The electrical part consists of a vector network analyzer (VNA) connected to a personal computer from which the calibration measurements, error coefficient computation, and the effective measurements are controlled out using [125].

Measurements at the Fraunhofer Institute for Reliability and Microintegration (IZM), Berlin

The main setup of the measurements carried out at the Fraunhofer Institute for Reliability and Microintegration (IZM), Berlin is depicted in Fig. 7.14 and several details are listed in Table H.4. The mechanical part uses a custom probing station which also carries the frequency extension devices attached to the VNA. This station also features a vacuum system for suction towards the chuck. As this chuck is of metal, the measurements required a perforated plastic card of which the exact material properties are not known. The electrical part consists of a vector network analyzer with frequency extension devices which accomplish the up- and down-conversion in frequency of the applied and measured signal in order to extend the frequency range up to 110 GHz (if supported by the probe bandwidth). As listed in Table H.4, two types of micro-probes have been used, the ones also used in setups 1a/b which support frequencies up to 65 GHz and a second type that supports the

frequencies up to 110 GHz. Each micro-probe type is calibrated with the corresponding calibration substrate from the respective probe manufacturer.

7.3.4 Practical Challenges of the Measurement Execution

Several practical challenges occurred during the execution of the measurements which are mostly related to the proper mechanical and thereby electrical contacting of probing pads and areas with the micro-probes. With the first, mostly customized measurement setups (1a/b), it was difficult to implement a very high planarity/alignment such that the three probe tips of each micro-probes contact the test structure in a very similar way, i.e. with almost the same force on each probe tip, elastic deformation, and “skating” (forward movement) when lowering the micro-probes. Due to the elasticity the probes have some margin regarding the planarity but application of too much force to compensate for the limit planarity leads to the observed wear of the probe tips. With increasing number of contacts, it appeared to be more difficult to establish a reliable contact from which a probe tip wear is concluded. The reliable contact could only be verified indirectly. Probing problems have been approached as follows: During the calibration they were investigated by measuring a coplanar line on the calibration substrate and comparing with a larger number of measurements with different calibrations for this line. In case of too large deviations, the calibrations were discarded. Probing problems during the measurements were indicated by significant deviations from the results for similar structures and other unexpected behavior with frequency, e.g., fast variations of the magnitude where a smooth curve is expected. It proved to be helpful that the probing pads were all designed relatively long which enables a longer forward traveling of the micro-probe tips when contacting. However, of the variety of used probing pad sizes, the smallest ones with a width of 50 μm and a length of 100 μm have been found to be of sufficient size for reliable probing with all setups.

7.3.5 Measurement and Simulation Results

In the following, selected measurement results are presented. The parameter values (except for the stackup) of all presented structures are given in Table H.2 which refers to the definitions in Fig. 7.10a. All considered combinations of structures and wafer types are listed in Table H.3. In some cases two or three measurements of the same structure are available. As some of the repeated measurements differ in the corresponding setup, the confidence in the measurements is increased if the results show a good agreement.

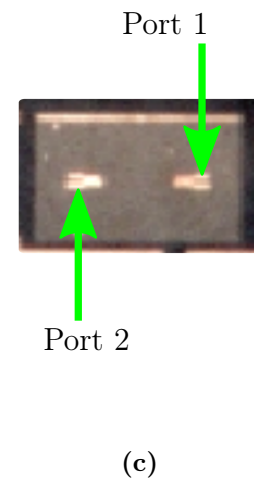
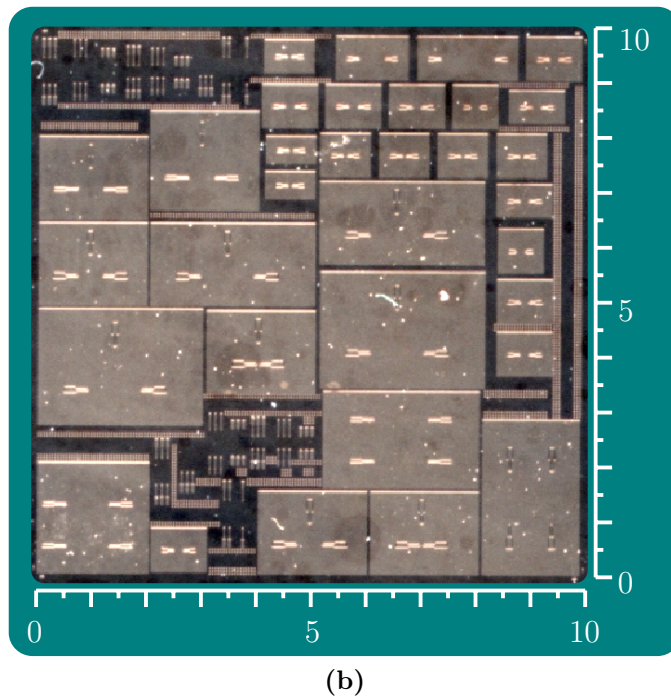
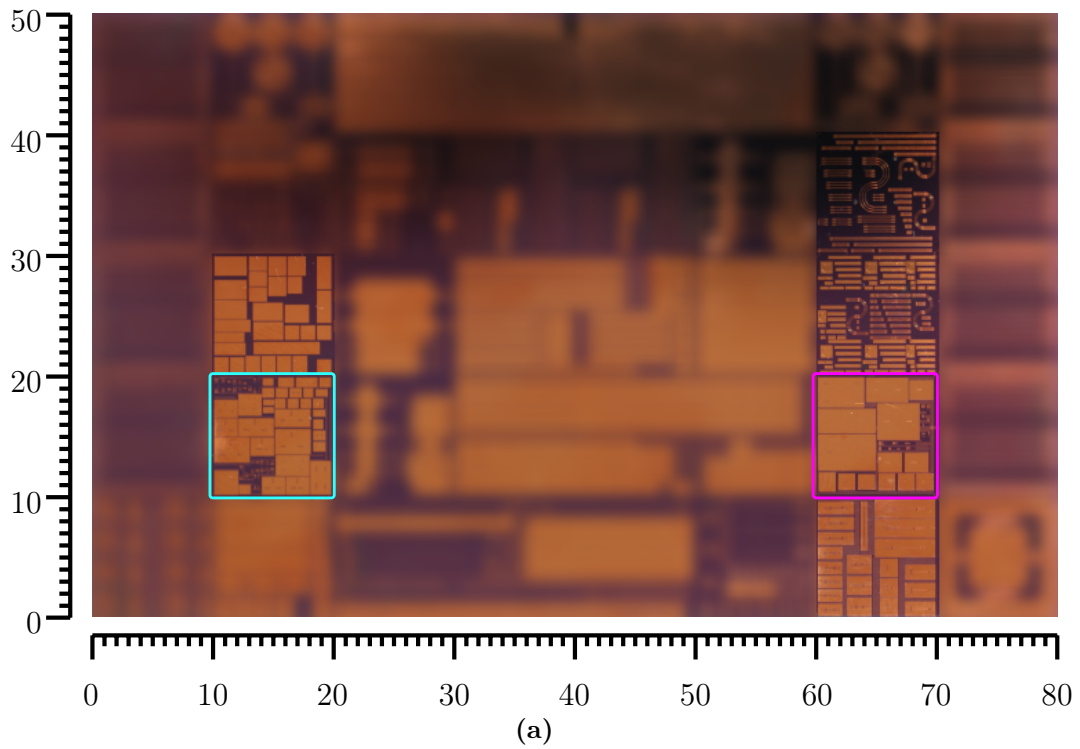


Figure 7.12: (a) Photograph of a coupon from one of the fabricated wafers (b) detailed view of the part with the DUTs of the following measurements (c) The two port measurements have port 1 at the respective higher coordinate as illustrated here. All scales/coordinates are in mm. Refer also to the drawing given in Figs. H.2 and H.3.

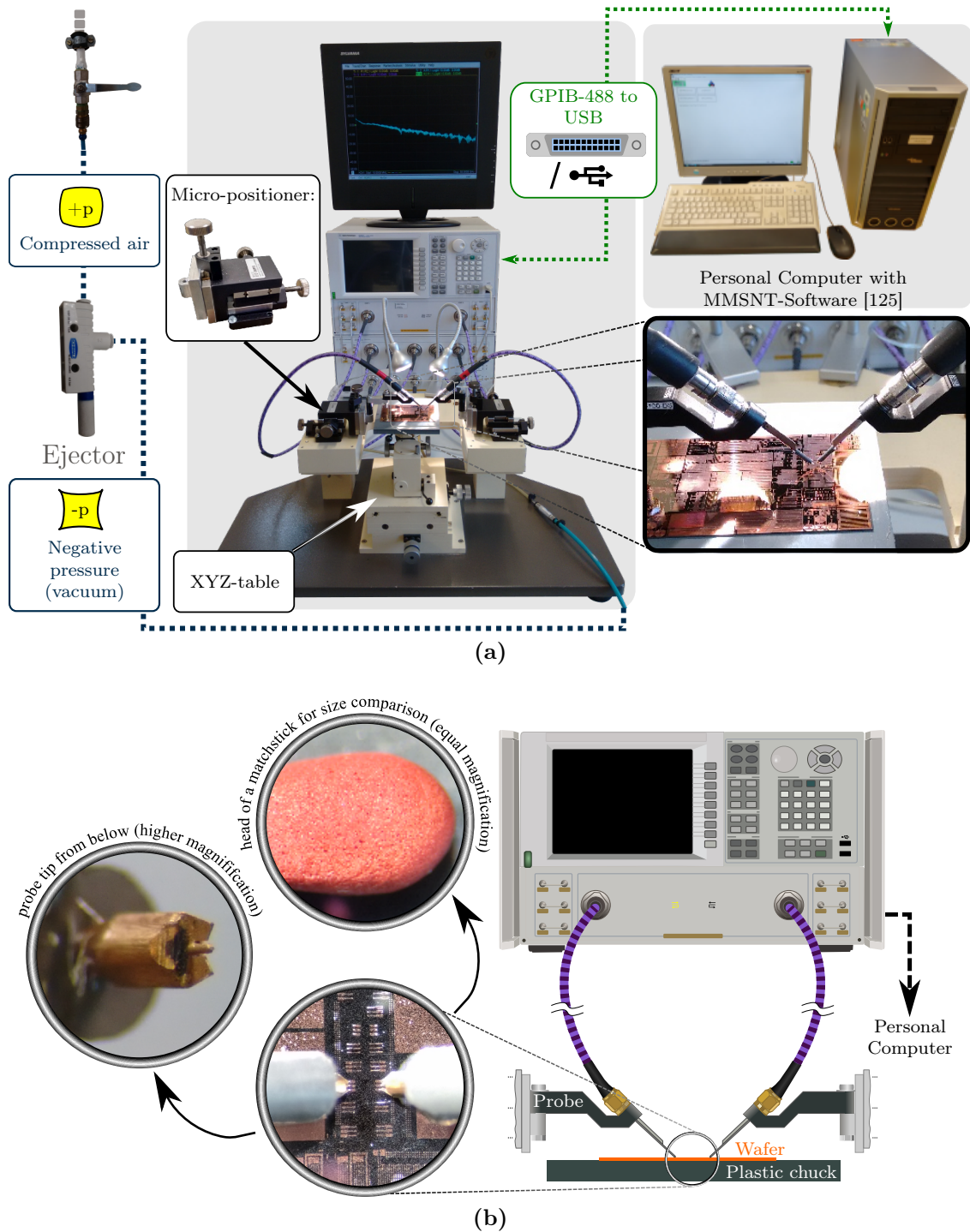


Figure 7.13: Measurement setup 1b (\rightarrow Table H.4): illustration of (a) the complete mechanical and electrical setup with all connections and (b) details of the setup 1b used for the electrical characterizations presented in this chapter.

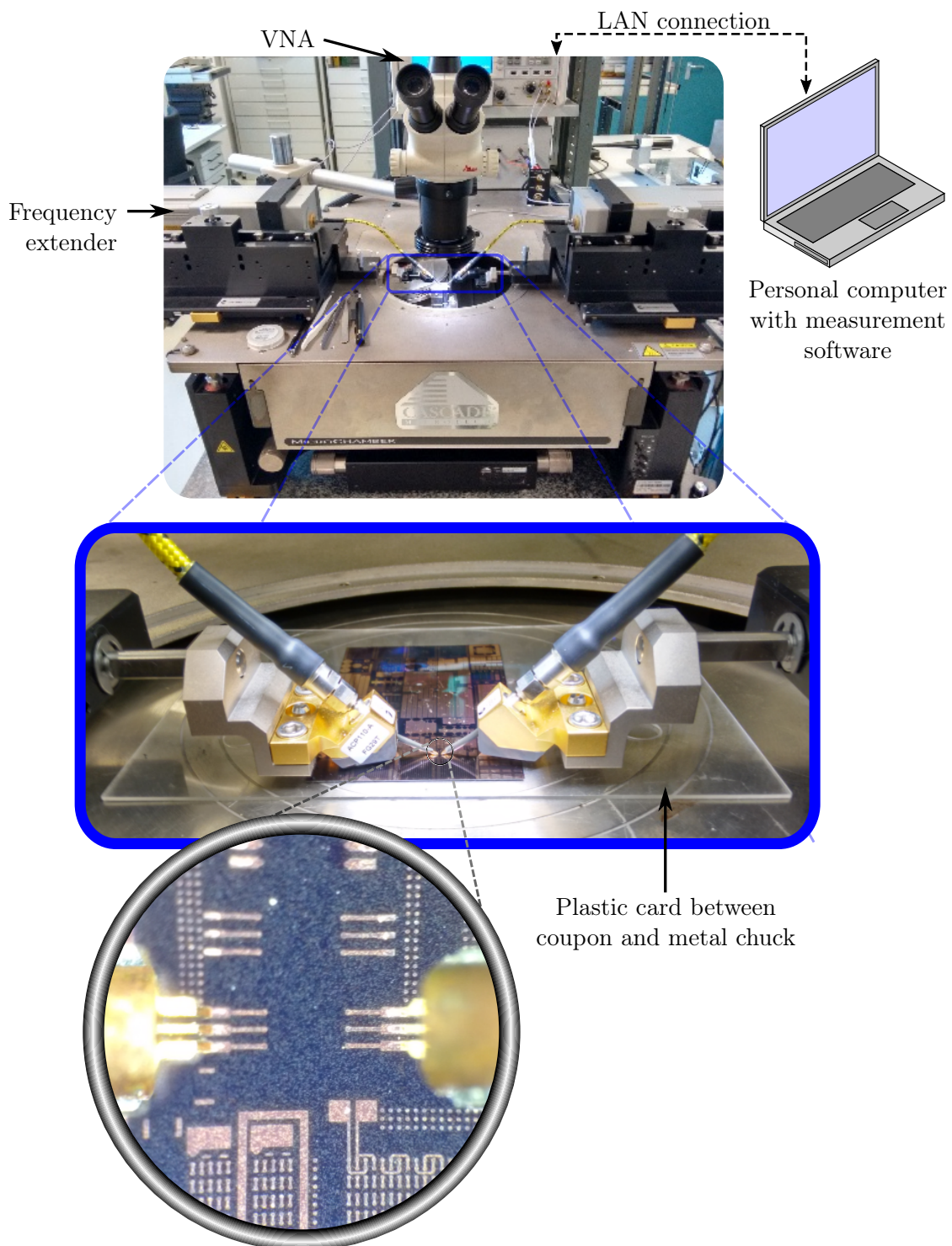


Figure 7.14: Illustration of measurement setup 2b (\rightarrow Table H.4).

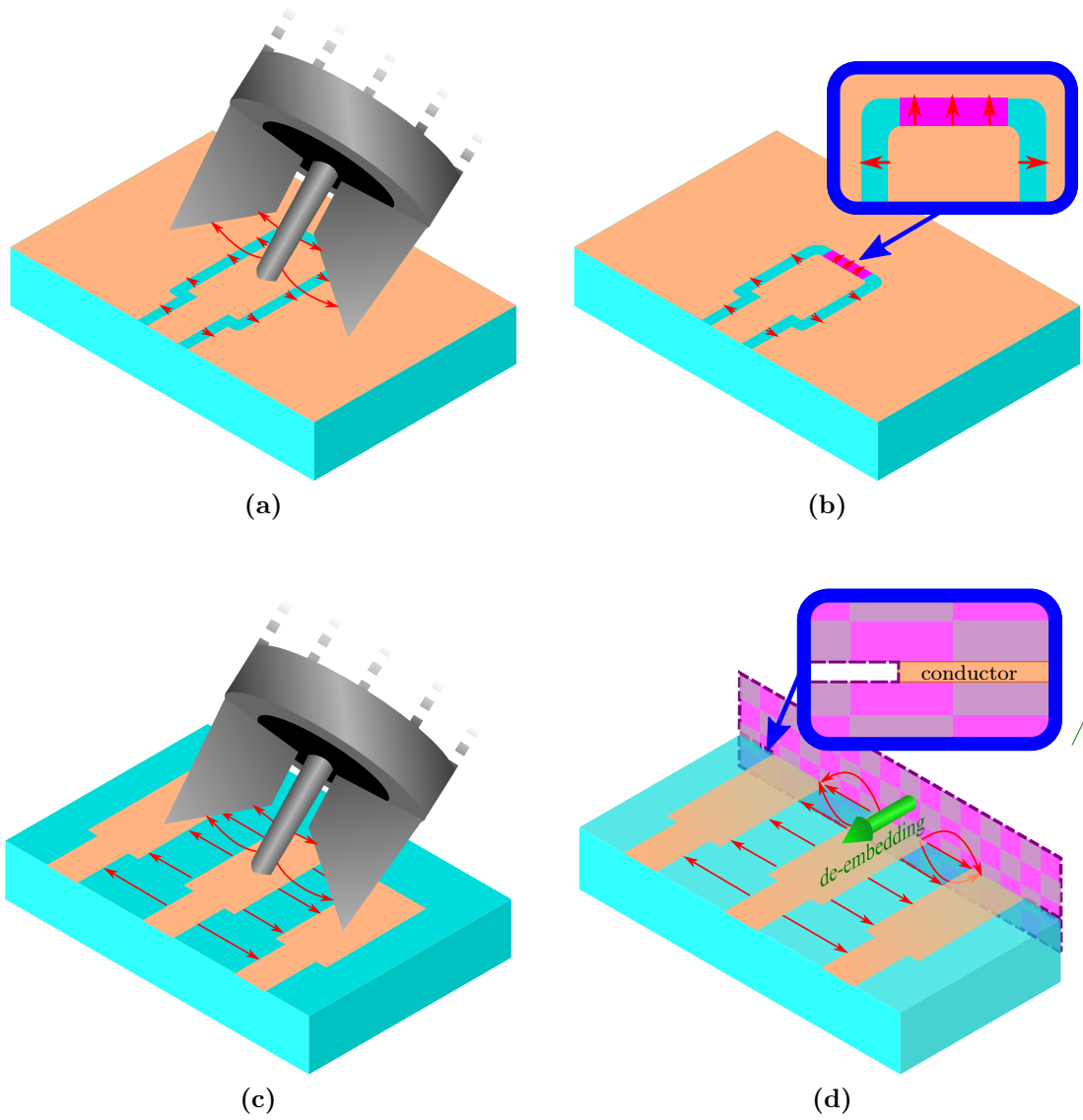


Figure 7.15: Comparison of the excitations in the real measurement and the approximations in the simulations. The illustrations show the field lines of the estimated electric field with red arrows. (a) Probing in the measurement in the case of plane metallizations and (b) corresponding signal launch of the simulation using a modified pad and a lumped port (marked with purple color). (c) Probing in the measurement in the case without plane metallizations and (d) corresponding excitation of the simulation using a wave port (marked with purple color and with checkerboard pattern) and de-embedding. Measurement drawings refer to the micro-probes used in measurement setups 1a/b and 2a but the probes used in setup 2b should show very similar behavior. Simulation drawings refer to the simulations for correlation carried out with [66]

Differentiation of the Used Parameter Values

For all measurements of this section, at least one simulation result set based on FEM full-wave simulations is given. As there is some uncertainty regarding the exact values of the layer thicknesses, some of these values have been varied in order to achieve a better agreement with the measurement results. A comparison of the *nominal values* that have been designed for, the *estimated values* that are based on the cross-sectional values, and the range of *simulated values* that has been used in order to fit simulation results to the measurement results are given in Table H.3. The focus of the fitting to the measurement results is to obtain both a similar general frequency behavior and the same orders of magnitude as the measurement results. The iterative fitting is based on educated guess rather than a complete investigation of the parameter space. The presented fit might therefore not be the optimal one within the realistic parameter ranges.

Modeling of the Signal Launch

An additional uncertainty is in effect due to the difficulty in appropriately modeling the signal launch. Firstly, the calibration for the (physical) measurement is expected to be slightly more inaccurate than for measurements on many other substrates, such as PCB laminates. This is mainly because the silicon substrate properties differ significantly from the properties of the calibration substrates which are typically ceramic materials. For the FEM simulations with [66], the optimal signal launch (exciting port with auxiliary structures) that corresponds to the micro-probe launch is also not obvious. A model for the micro-probe tip with a de-embedding to the probe tips might lead to a higher accuracy. Here, simpler excitations are used and explained in the following.

For structures of the type that is illustrated in Fig. 7.10a (with plane metallizations), a lumped port is placed between the outermost edge of the pad and the metallization. This excites the coplanar mode with good efficiency. In order to take into account the average probe position which is near the center of the pad, the pad is made slightly shorter (by about one third), such that the port coplanar mode field should be present at this position. The comparison of these signal launch setups of measurement and simulation is also illustrated in Figs. 7.15a and 7.15b, respectively.

For structures of the type illustrated in Fig. 7.10b (without plane metallizations), a waveguide port is used at the outermost ends of the pads. The waveguide port is assigned to an area above the bottom side metallization of the structure and shaped in a way that the port contour touches the outermost edges of the outer ground conductors. This way the coplanar mode of this structure is excited. Because the ground vias are at some dis-

tance plane from the probing position, the bottom metallization should have no significant influence on the mode field. A de-embedding is used to shift the reference plane half the length to the center of the probing pads. The comparison for this case is illustrated for measurement and simulation in Figs. 7.15c and 7.15d, respectively.

Modeling of the Electromagnetic Environment in the Simulation

The electromagnetic environment can in general not be ignored when carrying out measurements and corresponding simulations. For the measured structures this environment consists mainly of the neighboring structures on the silicon wafer coupon, the probe tips above the wafer coupon, and the plastic chuck or card (for the mounting) below the wafer coupon. The neighboring structures are ignored in the following simulations. The simulated area is equal to that of the plane metallizations if present and perfect magnetic conductor boundary conditions are used for the faces of the stackup between these planes. If no metallizations are present, a wave port is used. Therefore, the length of the simulated area is equal to the length of the structure and the width is chosen to be about 5 times the pitch. The presence of the probe tips is also neglected and signal launches are used as described before. The area above the wafer is extended with an air-box with absorbing boundary conditions except at the wave port areas. For the plastic mounting, a lossless dielectric with a relative permittivity of 4.3 is used with absorbing boundaries. From comparison with simulations where this is replaced by vacuum, it can be seen that the influence is small compared to the variation of uncertain parameter values.

Discussion of Correlation Between Measurement and Simulation Results

Figures 7.18–7.20 shows several measurement and simulation results. Due to the mentioned uncertainties, i.e. because the simulated structures could deviate in the relevant dimensions and material properties from the measured structures, some adaptations of dimensions and material properties have been tested by variation of several parameters within a plausible range. The electromagnetic environment has been taken into account in the manner discussed in the previous section.

The measurement results show several spikes that cannot be explained at this point and can most likely be attributed to the measurement devices. The measurements up to 50 GHz show spikes near 20 GHz in Fig. 7.20a ($S_{1,1}$) and in Fig. 7.18c ($S_{2,1}$). The measurements up to 65 GHz show spikes near 61 GHz in Fig. 7.16. While the overall behavior with frequency is the same for different measurements of the same structure, some larger deviations can also be observed.

It must be mentioned that no effort has been made during these measurements to investigate the effects due to depletion layers. As seen in section 2.5, this effect is relatively small and therefore out of the scope of the investigations presented here. For more rigorous investigations the power of the measurements could be calibrated and varied or the full-depletion case could be enforced by substrate biasing [126,127]. The latter requires an ohmic contact attached to the silicon layer.

Discussion of Test Structure Properties

Figures 7.16, 7.17, and 7.18 show structures on the same wafer, W23B. Due to the high resistivity, a good transmission is obtained, e.g., below 30 GHz the transmission is above -2 dB for all three structures. As seen for structures V10 and V13 with the low-loss silicon wafer W23B in Figs. 7.16 and 7.17, respectively, the planes introduce significant resonances which deteriorate the transmission at higher frequencies. Figures 7.19 and 7.20 show results for structure V13 on wafers with silicon of lower electrical resistivity. Except at the resonance frequencies of structure V13 on the high resistivity wafer W23B, the transmission is about one order of magnitude lower for these wafers of lower resistivity compared to the high resistivity wafer.

7.3.6 Summary and Conclusions Regarding Measurements

After a comprehensive discussion of the design of the test structures, the simulation setups, and the most relevant aspects of the configuration of the simulations, several results for measurements have been presented. It could be observed that despite several uncertainties regarding exact parameter values, overall, a good to fair agreement could be obtained in the reference simulations. Using silicon substrates of relatively high resistivity (here about 1 S/m), links can be established which should be transparent enough for the application in an interposer.

For future test structure designs and measurements, a vertical probing similar to the one presented in [128] could be evaluated. Implementation of stackups similar to the ones used in the model approach comparison of Section 7.2 could be implemented as physical test structures to further justify the assumptions made and validate the modeling approaches. The application of a substrate bias voltage could be used to further investigate the depletion layer influence.

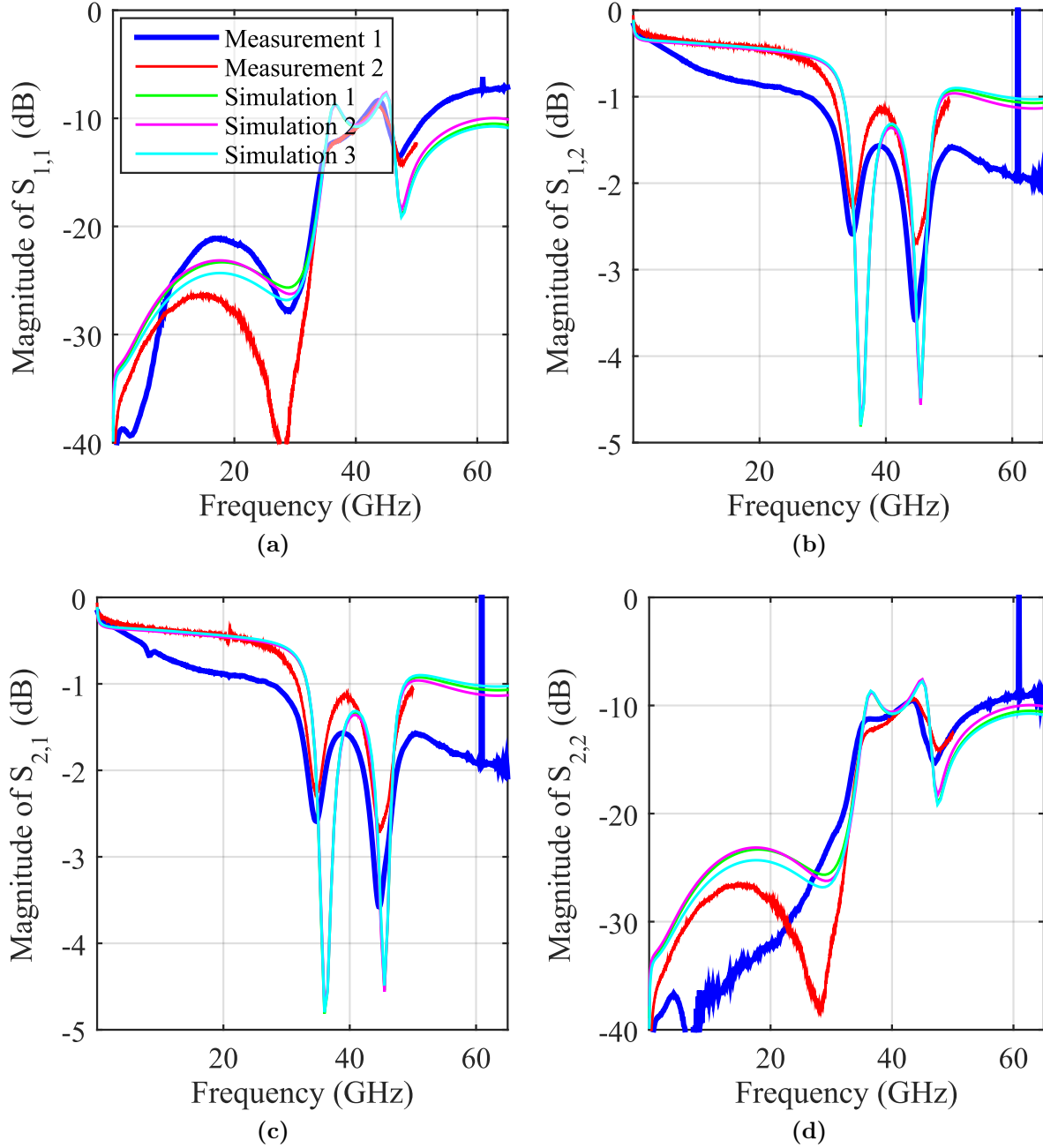


Figure 7.16: Measurement and simulation results for structure V10 (\rightarrow Fig. 7.10a, Table H.1) on wafer W23B (\rightarrow Fig. 7.2). Measurement 1 uses setup 1b, Measurement 2 uses setup 1a (\rightarrow Table H.4). All simulations use a silicon conductivity of 1 S/m, a silicon layer thickness of 80 μm , and a thickness of the WPR layer of 3.5 μm . The thickness of the oxide layer is 200 nm in Simulation 1, 150 nm in Simulation 2, and 250 nm in Simulation 3.

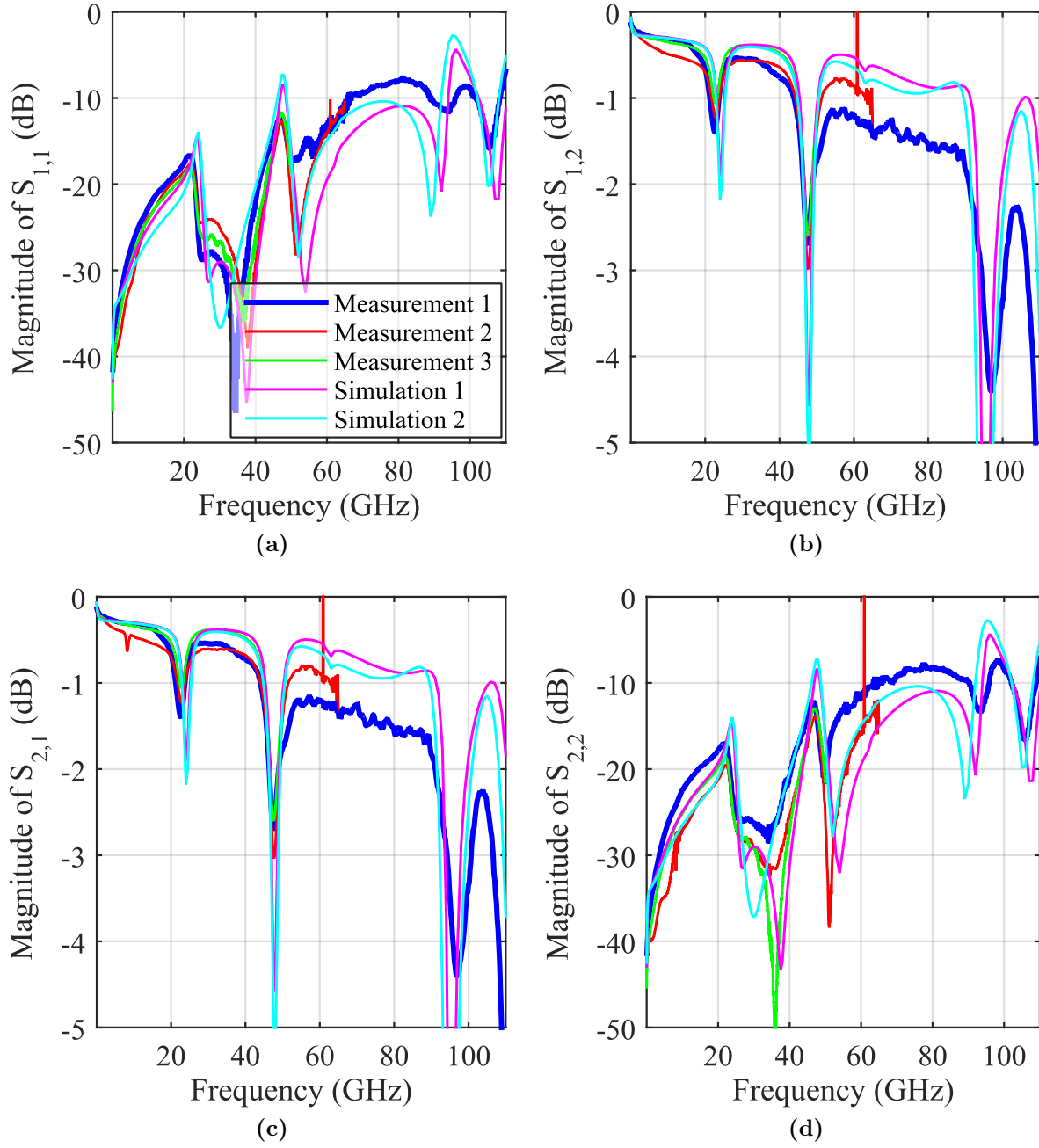


Figure 7.17: Measurement and simulation results for structure V13 (\rightarrow Fig. 7.10a, Table H.1) on wafer W23B (\rightarrow Fig. 7.2). Measurement 1 uses setup 2b, Measurement 2 uses setup 2a, and Measurement 3 uses setup 1b (\rightarrow Table H.4). All simulations use a silicon conductivity of 1 S/m and a silicon dioxide layer thickness of 500 nm. Simulation 1 uses a thickness of the WPR layer of 3.5 μm and a thickness of the silicon layer of 80 μm . Simulation 2 uses a thickness of the WPR layer of 4.5 μm and a thickness of the silicon layer of 100 μm .

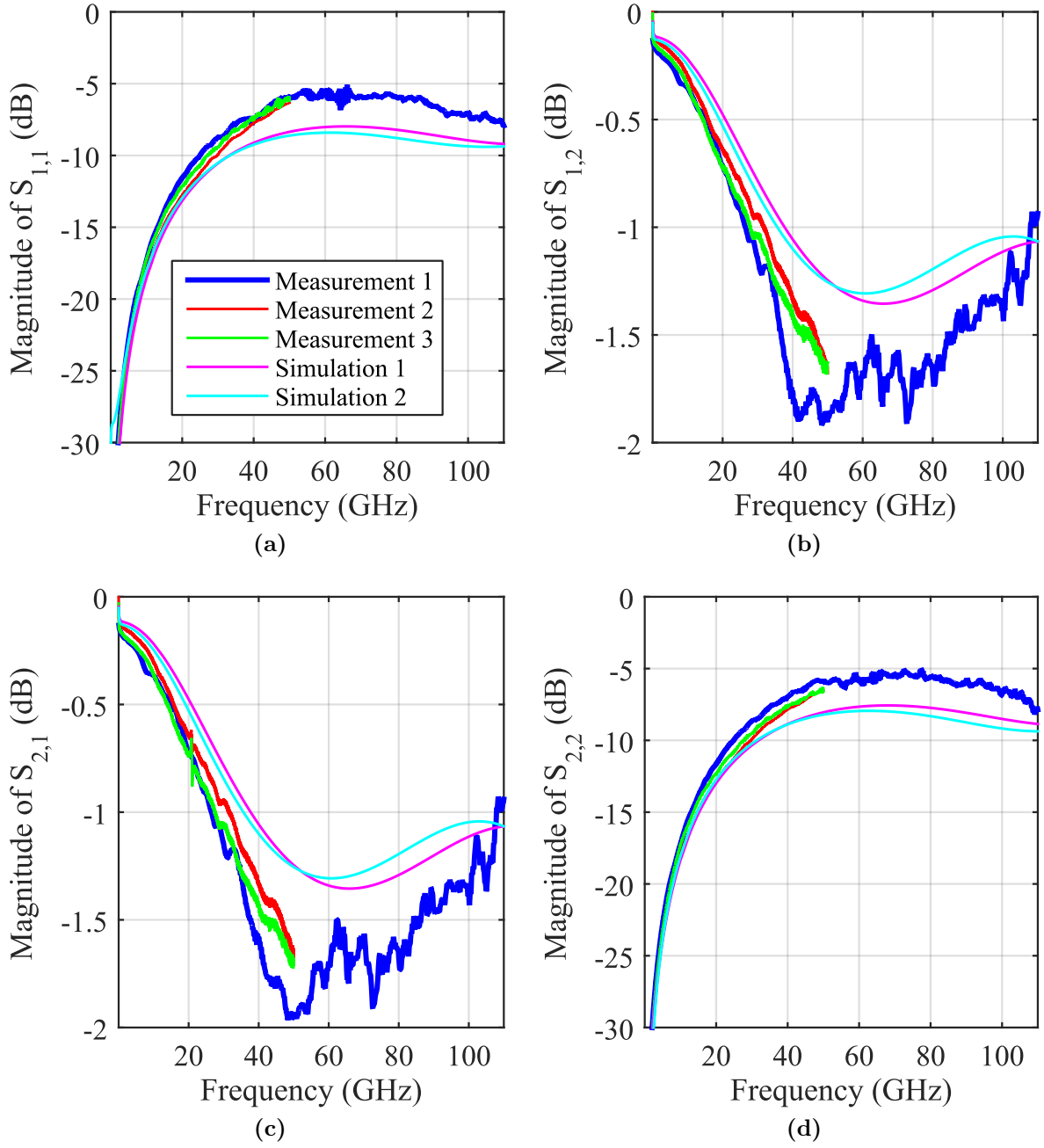


Figure 7.18: Measurement and simulation results for structure V5 (\rightarrow Fig. 7.10a, Table H.1) on wafer W23B (\rightarrow Fig. 7.2). Measurement 1 uses setup 2b, Measurements 2 and 3 use setup 1b (\rightarrow Table H.4). All simulations use a silicon conductivity of 1 S/m and a silicon dioxide layer thickness of 500 nm. Simulation 1 uses a thickness of the WPR layer of 3.5 μm and a thickness of the silicon layer of 80 μm . Simulation 2 uses a thickness of the WPR layer of 4.5 μm and a thickness of the silicon layer of 100 μm .

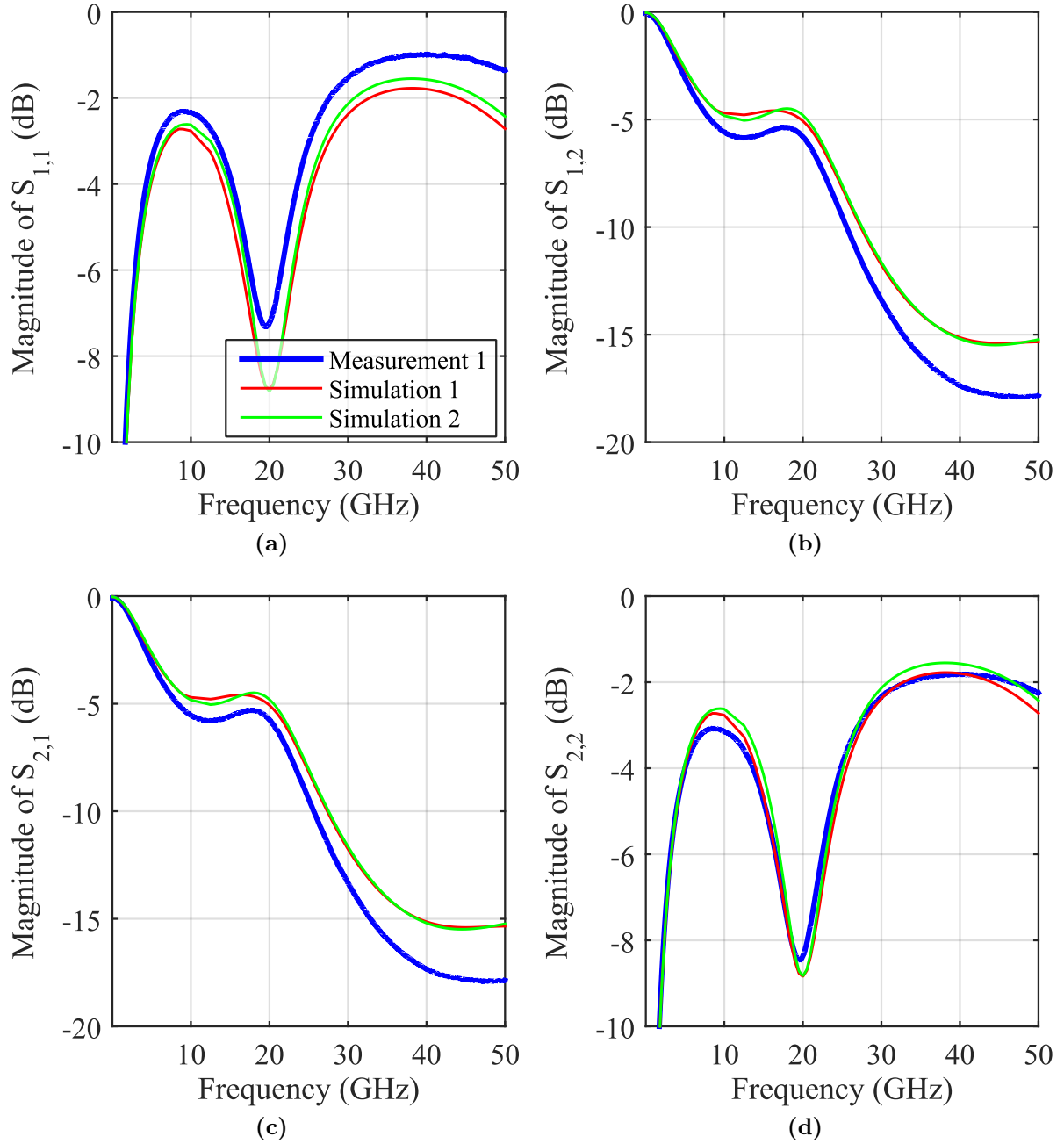


Figure 7.19: Measurement and simulation results for structure V13 (\rightarrow Fig. 7.10a, Table H.1) on wafer W09 (\rightarrow Fig. 7.2). Measurement 1 uses setup 1a (\rightarrow Table H.4). All simulations use a thickness of the WPR layer of $4.5\text{ }\mu\text{m}$, a thickness of the silicon layer of $100\text{ }\mu\text{m}$, and a silicon dioxide layer thickness of 500 nm . Simulation 1 uses a silicon conductivity of $2 \times 10^3\text{ S/m}$ and Simulation 2 uses a silicon conductivity of $1 \times 10^5\text{ S/m}$.

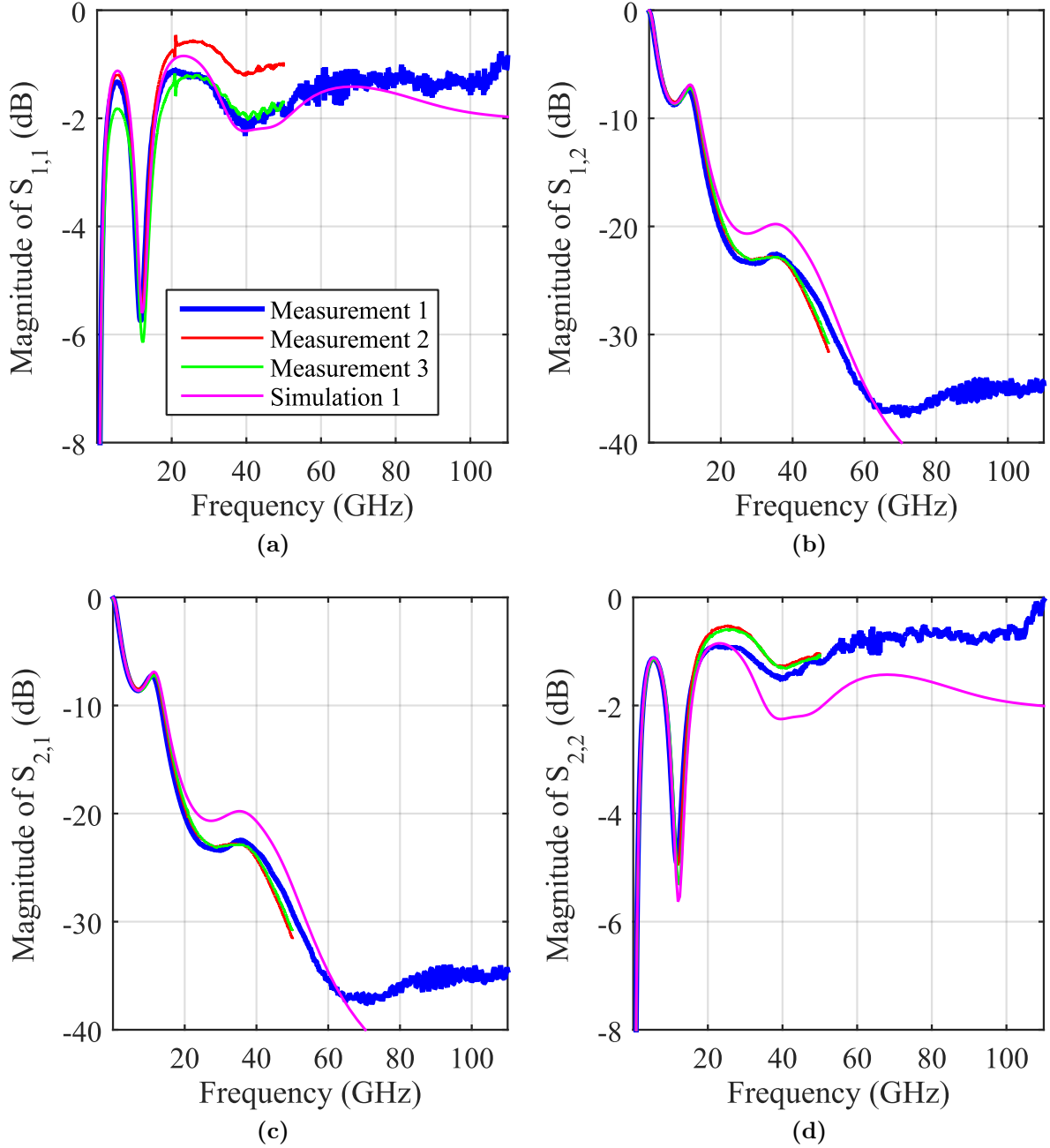


Figure 7.20: Measurement and simulation results for structure V13 (\rightarrow Fig. 7.10a, Table H.1) on wafer W10A (\rightarrow Fig. 7.2). Measurement 1 uses setup 2b, Measurements 2 and 3 use setup 1b (\rightarrow Table H.4). Simulation 1 uses a silicon conductivity of 2×10^3 S/m, a thickness of the WPR layer of $4.5 \mu\text{m}$, a thickness of the silicon layer of $100 \mu\text{m}$, and a silicon dioxide layer thickness of 180 nm .

Chapter 8

Conclusion and Outlook

This thesis has presented contributions to the electromagnetic modeling of through silicon vias (TSVs) for application in silicon interposers. It has been shown that by adaptations of both the near field and the far field parts of the model, a physics-based via model that was originally conceived for vias in multilayer printed circuit boards achieves a very good accuracy up to several hundreds of Gigahertz in a large parameter range. In addition, the already high numerical efficiency of the method could be increased further.

The method has proven itself to be applicable even with metals of lower conductivity such as aluminum and with incomplete metallizations. Major limitations have only been found in cases with very narrow spacing of the TSVs. The relevant dimensions have been determined to be the minimal distances between antipad clearances and the cavity height. For the near field modeling, a finite-difference frequency-domain method has been developed and shown to lead to results of high accuracy. The rotational symmetry that is exploited during the computation of the near field leads to a high numerical efficiency. It is therefore the recommended method for near field computation at all frequencies.

The overall reduced computational effort of the modeling has enabled the analysis of the crosstalk of large via arrays. The power sum of total uncorrelated crosstalk has been justified as a parameter for the efficient estimation of effective crosstalk levels in first design phases of large TSV arrays. The summation in terms of power has been extended to periodic digital signals and enables the reduction to a single figure of merit for each via to quantify a typical crosstalk value. Overall, the presented methods constitute a numerically very efficient procedure for the analysis and design of large and therefore realistic arrays.

Complementary modeling approaches have been motivated, discussed and correlated with the PBM models for the modeling of TSVs in several stackup environments. Even though an influence of the stackup environments could be observed, it has been found that the general frequency behavior and the orders of magnitude of transmission and crosstalk are similar. In the last part of this thesis, measurement and FEM full-wave simulation results have been

correlated for several structures that aim to characterize electromagnetic characterization of TSVs. A good agreement could be observed which validates the applicability of both the FEM-simulations and the FEM-models.

In future research on the modeling of TSVs, the PBV model could be extended in order to achieve an even large parameter range where it is applicable. Especially a model for the near field coupling between TSVs is of interest. At several hundreds of Gigahertz, it might also be required to take into account other effects that have been neglected so far such as the surface roughness of conductors. Regarding the simulation of interposers with partial metallizations, criteria could be developed to decide which of the modeling approaches, the physics-based model or the multi-conductor model, is better suited for an interposer inside a specific electromagnetic environment. The measurements have shown that a good transmission over TSV transitions is possible if silicon substrates of high resistivity are used. Therefore, the application of an interposer in a demonstrator for signal transmission at several tens of gigabit could be feasible.

Appendix A

Numerical Methods

A.1 Root Search Techniques for the Complex Domain

The analytical methods for the determination of the wave number of modes in several guiding structures presented in this thesis can be formulated as the mathematical problem of finding locations with function values of zero in the complex plane of a single valued complex function. The chosen methods to solve this task are typically a tradeoff between several factors such as the generality of application, the overall numerical efficiency, and the ease of implementation.

First in this chapter, the Newton-Method and related techniques are discussed. These method are based on a good initial guess of the root value and under certain conditions enable an iterative approximation towards the true value. As the functions encountered with the presented waveguide problems have an infinite number of complex roots and guessing the initial values that lead to a converging series of iterations towards the desired root is difficult, additional techniques are in many cases helpful. The argument principle method for the generation of these start values from the evaluation of contours of areas in the complex domain is therefore also presented in this chapter.

A.1.1 Newton's Method

Starting from a initial value $x^{(0)}$ the iteration formula is given by [129, Sec. 9.4.1]

$$x^{(k+1)} = x^{(k)} - \frac{f(x^{(k)})}{f'(x^{(k)})} \quad (\text{A.1})$$

where $f'(x)$ is the first derivative with respect to the variable x for which the condition $f'(x^{(k)}) \neq 0$ for any k must hold.

$f'(x)$ is either computed numerically or analytically. If $f(x)$ is a real function, the numerical computation can use finite differences. The choice of interval has to consider the numerical effects that arise from the finite computational accuracy of the computer system. If $f(x)$ is a complex function, the numerical computation can be based on the numerical evaluation of a contour integral that is given in [101, Eq. 9]. Often, analytical derivative can be computed. For the TRM, this is discussed in Sec. B.4.

A.1.2 Halley's method

Analog to the Newton's Method, an iterative approach can be formulated that also uses the second derivative $f''(x)$ and is known as Halley's Method:

$$x^{(k+1)} = x^{(k)} - \frac{2f(x^{(k)})f'(x^{(k)})}{2(f'(x^{(k)}))^2 - f(x^{(k)})f''(x^{(k)})} \quad (\text{A.2})$$

For the cost of computing the second derivative, a cubic convergence (instead of a quadratic convergence with Newton's Method) is achieved [130].

A.1.3 Argument Principle Method

Theory and application of the Argument Principle Method (APM) are given in great detail in [101]. For the sake of completeness the most important parts of the theory are replicated here. The Argument Principle Method is based on the generalized argument principle theorem which can be formulated as [101]

$$\sigma_P = \frac{1}{j2\pi} \oint_C x^P \frac{f'(x)}{f(x)} dx = \sum_{i=1}^n \zeta_i^P \quad (\text{A.3})$$

where $f(x)$ is an analytic/holomorphic complex function inside the complex domain of and on the simple and closed contour C and $f'(x)$ is its derivative. Further, no zeros of the function $f(x)$ may be located on the contour. These conditions are met for all considered problems if the integration paths are appropriately chosen. ζ_i^P is the i th of the n roots of the function inside contour C raised to the P th power. σ_P is then the result of the summation for each value of $P = \{0, 1, 2, \dots\}$. For $P = 0$ (A.3) gives the number of complex roots inside the region bounded by the contour C . For $P > 0$ it gives summations from which coefficients of a polynomial with the same roots as the investigated function can be computed [101, Sec. III].

In many cases the derivative $f'(x)$ can be given analytically. In the transverse resonance

method for arbitrary numbers of layers a recursive formula can be given in order to compute the first derivatives of the function that involves matrix multiplications. If the derivative $f'(x)$ cannot be given analytically, the (complex) derivative can be obtained numerically through Cauchy's theorem that is given by [101]

$$f'(x_0) = \left. \frac{\partial f(x)}{\partial x} \right|_{x=x_0} = \frac{1}{j2\pi} \oint_D \frac{f(x)}{(x-x_0)^2} dx. \quad (\text{A.4})$$

D is a simple, e.g., circular contour around the point x_0 . Further $f(x)$ is analytic/holomorphic on and inside the contour D .

Unless an interpolation procedure is used (e.g. the Lagrangian Interpolation [129, Sec. 7.3.2]), to improve the accuracy and robustness of the computation of the derivative by finite differences, the application of finite differences leads to the numerical problems discussed in A.1.1. In contrast to finite differences, the contour integral in (A.4) facilitates the implementation of a robust method. This is because the numerical integration can be carried out with a fine discretization of the contour. A good approximation of the derivative can be assumed if derivatives computed with sufficiently different discretizations show a good agreement, i.e., a convergence is observed.

A.2 Numerical Integration using Gauss Quadrature

The Gauss Quadrature is a method for the numerical integration of functions that, under certain conditions, leads to optimal results for many practical functions that feature a certain degree of smoothness. The method is optimal in the sense that, if the the points of function evaluation can be chosen, the numerical error is minimized with this method. In the following, only the Gauss-Legendre Quadrature is considered which is based on Legendre polynomials [129, Sec. 7.3.3.3]: Conventionally, the interval is normalized to $[-1, 1]$ which can be achieved for an original interval $[a, b]$ through the following mapping function [129, Sec. 7.3.3.3]

$$f(x) = 2 \frac{x-a}{b-a} - 1 = \frac{2x-a-b}{b-a} \quad (\text{A.5})$$

Selected values for Gauss-Legendre abscissae and weights can be found in Table A.1. In order to increase the numerical efficiency and achieve a better control of the numerical error of the integration, a Gauss-Kronrod integration can also be used [101, Sec. III.A].

n=2	{	Abscissa ≥ 0	Weight
		0.57735026918963	1.00000000000000
n=3	{	Abscissa ≥ 0	Weight
		0	0.88888888888889
		0.77459666924148	0.55555555555555
n=4	{	Abscissa ≥ 0	Weight
		0.33998104358486	0.65214515486255
		0.86113631159405	0.34785484513745
n=5	{	Abscissa ≥ 0	Weight
		0	0.56888888888889
		0.53846931010568	0.47862867049937
		0.90617984593866	0.23692688505619
n=6	{	Abscissa ≥ 0	Weight
		0.23861918608320	0.46791393457269
		0.66120938646626	0.36076157304814
		0.93246951420315	0.17132449237917
n=7	{	Abscissa ≥ 0	Weight
		0	0.41795918367347
		0.40584515137740	0.38183005050512
		0.74153118559939	0.27970539148928
		0.94910791234276	0.12948496616887
n=8	{	Abscissa ≥ 0	Weight
		0.18343464249565	0.36268378337836
		0.52553240991633	0.31370664587789
		0.79666647741363	0.22238103445337
		0.96028985649754	0.10122853629038
n=9	{	Abscissa ≥ 0	Weight
		0	0.33023935500126
		0.32425342340381	0.31234707704000
		0.61337143270059	0.26061069640294
		0.83603110732664	0.18064816069486
		0.96816023950763	0.08127438836157

Table A.1: Gauss abscissae and weights for numbers of integration points n in range $2 \leq n \leq 9$. Tabulated are only abscissae ≥ 0 ; for every abscissa > 0 there exists also an abscissa with the respective negative value and the same weight.

Appendix B

Parallel-Plate Waveguides

B.1 Parallel Plate Waveguide With Homogeneous, Isotropic, Lossless Dielectric and Perfect Conductor Plates

The parallel plate waveguide with homogeneous, isotropic, lossless dielectric and perfect conductor plates supports a TEM mode and depending on the geometry, materials and frequency of operation several TE- and TM-modes. This structure lends itself to an intuitive understanding because waves are reflected at the conducting planes without phase change.

B.2 Characteristic Equation for a Single Intermediate Layer

For a single intermediate layer i (e.g. for application with the dielectric slab waveguide) the resulting characteristic equation can be arranged as

$$\left(\frac{\gamma_{x,l}}{\varepsilon_l^*} + \frac{\gamma_{x,u}}{\varepsilon_u^*} \right) \cos(k_{x,i} t_i) + \left(\frac{\varepsilon_i^*}{k_{x,i}} \frac{\gamma_{x,l}}{\varepsilon_l^*} \frac{\gamma_{x,u}}{\varepsilon_u^*} - \frac{k_{x,i}}{\varepsilon_i^*} \right) \sin(k_{x,i} t_i) = 0 \quad (\text{B.1})$$

or as

$$\frac{\gamma_{x,l}}{\varepsilon_l^*} + \frac{\gamma_{x,u}}{\varepsilon_u^*} + \left(\frac{\varepsilon_i^*}{k_{x,i}} \frac{\gamma_{x,l}}{\varepsilon_l^*} \frac{\gamma_{x,u}}{\varepsilon_u^*} - \frac{k_{x,i}}{\varepsilon_i^*} \right) \tan(k_{x,i} t_i) = 0 \quad (\text{B.2})$$

Symmetric Case

If the structure is also the symmetric, two cases can be distinguished, namely the even and odd symmetry cases. In case of odd symmetry, which is the case for the lowest order TM-mode, the electric field component that is parallel to the plane interfaces follows a sine function and is zero in the center of the dielectric slab. If the lower half of the structure is considered, then it follows from the first row of (4.25) and by application of (4.24) that

$$\begin{aligned} E(t_N/2, y)_{z,N} = 0 &= \cos(k_{x,i}t_i/2)E(0, y)_{z,1} + j\frac{k_{x,i}}{\omega\varepsilon_i^*}\sin(k_{x,i}t_i/2)H(0, y)_{x,1} \\ &= E(0, y)_{z,1} + j\frac{k_{x,i}}{\omega\varepsilon_i^*}\tan(k_{x,i}t_i/2)\frac{\omega\varepsilon_l^*}{-j\gamma_{x,l}}E(0, y)_{z,1} \end{aligned} \quad (\text{B.3})$$

and

$$0 = 1 - \frac{k_{x,i}}{\varepsilon_i^*} \frac{\varepsilon_l^*}{\gamma_{x,l}} \tan(k_{x,i}t_i/2) \quad (\text{B.4})$$

$$\frac{\gamma_{x,l}}{k_{x,i}} = \frac{\varepsilon_l^*}{\varepsilon_i^*} \tan(k_{x,i}t_i/2) \quad (\text{B.5})$$

B.3 Application to Radial Waveguides

As can be seen from the derivation in [96, Sec. 5-5] for two layers, the wave numbers of the TM_{0n} radial waveguide modes are equal to those of the TM_0 parallel plate waveguide modes with the same layering. As discussed in [96, Sec. 5-5] this is expected because the radial waves become similar to plane waves at large distances. In the following, the characteristic equations for computation of wave numbers of a PEC-bounded radial waveguide with an arbitrary number of layers is derived. It is shown that the characteristic equation is identical to the corresponding plane wave and independent from azimuthal variations.

B.3.1 Derivation of the General Transfer Matrix

The (scalar) Helmholtz equation for the cylindrical coordinate system is given by [96, Eq. 5-1]

$$\frac{1}{\rho} \frac{\partial}{\partial \rho} \left(\rho \frac{\partial \psi}{\partial \rho} \right) + \frac{1}{\rho^2} \frac{\partial^2 \psi}{\partial \phi^2} + \frac{\partial^2 \psi}{\partial z^2} + k^2 \psi = 0. \quad (\text{B.6})$$

As discussed in [96, Sec. 5-1], for a separation of variables, solutions of the form

$$\psi = R(\rho) \Phi(\phi) Z(z) \quad (\text{B.7})$$

are assumed and the separated equations are given by [96, Eq. 5-7]

$$\rho \frac{d}{d\rho} \left(\rho \frac{dR}{d\rho} \right) + [(k_\rho \rho)^2 - n^2]R = 0, \quad (\text{B.8a})$$

$$\frac{d^2\Phi}{d\phi^2} + n^2\Phi = 0, \quad (\text{B.8b})$$

$$\frac{d^2Z}{dk_z^2} + k_z^2Z = 0. \quad (\text{B.8c})$$

for which the following separation parameter condition holds:

$$k_\rho^2 + k_z^2 = k^2. \quad (\text{B.9})$$

It should be noted that (B.9) is completely analogous to the separation parameter condition for the plane wave solutions.

It follows that the Φ - and Z -functions are harmonic functions which are notated as in [96, Sec. 5-1] as $h(n\phi)$ and $h(k_z z)$, respectively. As noted in [96, Sec. 5-1], the functions $h(n\phi)$ are either $\sin(n\phi)$ or $\cos(n\phi)$ with integer n in order to have non single-valued ψ . They can further be represented by complex exponentials $e^{jn\phi}$ and $e^{-jn\phi}$ which is advantageous in many analytic derivations. This form is, e.g., used in the CIM with anisotropic ports. Each term can (by itself) be interpreted as describing a modulated phase along the azimuthal coordinate. A single term could in fact be used to describe azimuthally “circulating” waves. Here, we are interested in the radially propagating waves which are standing waves with respect to the azimuthal directions. Therefore the harmonic representations $\sin(n\phi)$ or $\cos(n\phi)$ are more descriptive.

The R -functions are solutions to Bessel’s differential equation. Different solution sets are possible; any two functions chosen from the following set are linearly independent solutions and thus an applicable solution set:

$$\{J_n(k_\rho \rho), Y_n(k_\rho \rho), H_n^{(1)}(k_\rho \rho), H_n^{(2)}(k_\rho \rho)\} \quad (\text{B.10})$$

where $J_n(k_\rho \rho)$ and $Y_n(k_\rho \rho)$ are the Bessel functions of first and second kind, respectively, and order n , and $H_n^{(1)}(k_\rho \rho)$ and $H_n^{(2)}(k_\rho \rho)$ are the Hankel functions of first and second kind, respectively, and order n .

For the radial waveguides with equiphase surfaces that are cylinders the following wave functions are used [96, Sec. 5-3]

$$\psi = h(k_z z)h(n\phi) \left\{ \begin{array}{l} H_n^{(1)}(k_\rho \rho) \\ H_n^{(2)}(k_\rho \rho) \end{array} \right\}. \quad (\text{B.11})$$

For TM-waves between two PEC-planes at z -coordinates 0 and a , the following wave

function satisfies the boundary conditions [96, Eq. 5-33]

$$\psi_{m,n}^{(TM)} = \cos\left(\frac{m\pi}{a}z\right) \cos(n\phi) \begin{Bmatrix} H_n^{(1)}(k_\rho\rho) \\ H_n^{(2)}(k_\rho\rho) \end{Bmatrix}, \quad (\text{B.12})$$

where m and n are integers equal to or larger than 0 and

$$k_\rho = \sqrt{k^2 - \left(\frac{m\pi}{a}\right)^2}. \quad (\text{B.13})$$

The electric and magnetic field for this mode that is TM to z are given by [96, Eq. 5-18]

$$E_\rho = \frac{1}{\hat{y}} \frac{\partial^2 \psi}{\partial \rho \partial z}, \quad (\text{B.14a})$$

$$E_\phi = \frac{1}{\hat{\rho}} \frac{\partial^2 \psi}{\partial \phi \partial z}, \quad (\text{B.14b})$$

$$E_z = \frac{1}{\hat{y}} \left(\frac{\partial^2}{\partial z^2} + k^2 \right) \psi, \quad (\text{B.14c})$$

and

$$H_\rho = \frac{1}{\rho} \frac{\partial \psi}{\partial \phi}, \quad (\text{B.15a})$$

$$H_\phi = -\frac{\partial \psi}{\partial \rho}, \quad (\text{B.15b})$$

$$H_z = 0, \quad (\text{B.15c})$$

where

$$\hat{y} = \hat{\sigma}(f) + j\omega\hat{\varepsilon}(f) = j\omega\varepsilon^* \quad (\text{B.16})$$

which has the dimensions of an admittance per unit length [96, Eq. 1-47].

Derivation Using Exponential Functions for z -Dependence

For the layered radial waveguide, the wave functions for the diverging wave with cosinusoidal azimuthal dependence in the i th layer that extends from 0 to d_i in its local coordinate system can be given with exponential functions for the z -dependence as

$$\psi_i = C_i e^{\pm k_{z,i}z} \cos(n\phi) H_n^{(2)}(k_\rho\rho) \quad (\text{B.17})$$

where

$$k_\rho^2 + k_{z,i}^2 = k_i^2 = \omega\varepsilon_i\mu_i \quad (\text{B.18})$$

and n is an integer equal to or larger than 0.

The continuity of the tangential fields at the layer interfaces needs to be enforced. There-

fore, the electric and magnetic fields at the two interfaces of each layer are related. For $n = 0$, these field components are H_ϕ and E_ρ , of $n > 0$, there are additional field components H_ρ and E_ϕ . The former case is considered first, the latter case is discussed in Appendix B.3.3.

The wave function ψ_i can be written as

$$\psi_i = C_i R(\rho) \Phi(\phi) Z(z) \quad (\text{B.19})$$

where

$$Z(z) = \tilde{A}e^{-jk_{z,i}z} + \tilde{B}e^{jk_{z,i}z} \quad (\text{B.20a})$$

$$\Phi(\phi) = \cos(n\phi) \quad (\text{B.20b})$$

$$R(\rho) = H_n^{(2)}(k_\rho \rho) \quad (\text{B.20c})$$

Then, using (B.14a), the electric field component is given by

$$\begin{aligned} E_\rho &= \frac{1}{\hat{y}} \frac{\partial^2 \psi}{\partial \rho \partial z} = \frac{1}{\hat{y}} C_i \Phi(\phi) \frac{\partial R(\rho)}{\partial \rho} \frac{\partial Z(z)}{\partial z} \\ &= \frac{1}{\hat{y}} C_i \Phi(\phi) \frac{\partial R(\rho)}{\partial \rho} \frac{\partial}{\partial z} \left(\tilde{A}e^{-jk_{z,i}z} + \tilde{B}e^{jk_{z,i}z} \right) \\ &= \frac{-jk_{z,i}}{\hat{y}} (Ae^{-jk_{z,i}z} - Be^{jk_{z,i}z}) \end{aligned} \quad (\text{B.21})$$

and using (B.15a) the magnetic field component is given by

$$\begin{aligned} H_\phi &= -\frac{\partial \psi}{\partial \rho} = -C_i \Phi(\phi) \frac{\partial R(\rho)}{\partial \rho} Z(z) \\ &= -C_i \Phi(\phi) \frac{\partial R(\rho)}{\partial \rho} \left(\tilde{A}e^{-jk_{z,i}z} + \tilde{B}e^{jk_{z,i}z} \right) \\ &= -(Ae^{-jk_{z,i}z} + Be^{jk_{z,i}z}) \end{aligned} \quad (\text{B.22})$$

where A and B include the azimuthal and radial dependencies which the electric and magnetic field components E_ρ and H_ϕ share. At the origin of the local coordinates with $z = 0$, the evaluation of (B.21) and (B.22) can be expressed as

$$-E_\rho(0) \frac{\hat{y}}{jk_{z,i}} = (A - B) \quad (\text{B.23a})$$

$$-H_\phi(0) = (A + B) \quad (\text{B.23b})$$

From the sum and the difference of (B.23a) and (B.23b) it follows that

$$A = -\frac{1}{2} \left(\frac{\hat{y}}{jk_{z,i}} E_\rho(0) + H_\phi(0) \right) \quad (\text{B.24a})$$

$$B = \frac{1}{2} \left(-H_\phi(0) + \frac{\hat{y}}{jk_{z,i}} E_\rho(0) \right) \quad (\text{B.24b})$$

Insertion of (B.24) into the general expressions for the electric field (B.21) gives

$$\begin{aligned} E_\rho &= \frac{-jk_{z,i}}{\hat{y}} \left(-\frac{1}{2} \left(\frac{\hat{y}}{jk_{z,i}} E_\rho(0) + H_\phi(0) \right) \right) e^{-jk_{z,i}z} - \frac{1}{2} \left(-H_\phi(0) + \frac{\hat{y}}{jk_{z,i}} E_\rho(0) \right) e^{+jk_{z,i}z} \\ &= \frac{1}{2} (e^{-jk_{z,i}z} + e^{+jk_{z,i}z}) E_\rho(0) + \frac{-jk_{z,i}}{\hat{y}} \frac{1}{2} (e^{+jk_{z,i}z} - e^{-jk_{z,i}z}) H_\phi(0) \\ &= \cos(k_{z,i}z) E_\rho(0) + \frac{-jk_{z,i}}{\hat{y}} j \sin(k_{z,i}z) H_\phi(0) \\ &= \cos(k_{z,i}z) E_\rho(0) + \frac{k_{z,i}}{\hat{y}} \sin(k_{z,i}z) H_\phi(0) \end{aligned} \quad (\text{B.25})$$

and for the magnetic field, the insertion into (B.22) gives

$$\begin{aligned} H_\phi &= - \left(-\frac{1}{2} \left(\frac{\hat{y}}{jk_{z,i}} E_\rho(0) + H_\phi(0) \right) \right) e^{-jk_{z,i}z} - \frac{1}{2} \left(-H_\phi(0) + \frac{\hat{y}}{jk_{z,i}} E_\rho(0) \right) e^{+jk_{z,i}z} \\ &= \frac{1}{2} \frac{\hat{y}}{jk_{z,i}} (e^{-jk_{z,i}z} - e^{+jk_{z,i}z}) E_\rho(0) + \frac{1}{2} (e^{-jk_{z,i}z} + e^{+jk_{z,i}z}) H_\phi(0) \\ &= \frac{\hat{y}}{jk_{z,i}} (-j) \sin(k_{z,i}z) E_\rho(0) + \cos(k_{z,i}z) H_\phi(0) \\ &= -\frac{\hat{y}}{k_{z,i}} \sin(k_{z,i}z) E_\rho(0) + \cos(k_{z,i}z) H_\phi(0) \end{aligned} \quad (\text{B.26})$$

Combining (B.25) and (B.26) in matrix notation for the evaluation of the field at the upper end of the layer $z = d_i$, one obtains

$$\begin{bmatrix} E_\rho(d_i) \\ H_\phi(d_i) \end{bmatrix} = \begin{bmatrix} \cos(k_{z,i}d_i) & \frac{k_{z,i}}{\hat{y}} \sin(k_{z,i}d_i) \\ -\frac{\hat{y}}{k_{z,i}} \sin(k_{z,i}d_i) & \cos(k_{z,i}d_i) \end{bmatrix} \begin{bmatrix} E_\rho(0) \\ H_\phi(0) \end{bmatrix} \quad (\text{B.27})$$

which in the written out form using (B.16) is given by

$$\begin{bmatrix} E_\rho(d_i) \\ H_\phi(d_i) \end{bmatrix} = \begin{bmatrix} \cos(k_{z,i}d_i) & \frac{k_{z,i}}{j\omega\epsilon_i^*} \sin(k_{z,i}d_i) \\ \frac{\omega\epsilon_i^*}{jk_{z,i}} \sin(k_{z,i}d_i) & \cos(k_{z,i}d_i) \end{bmatrix} \begin{bmatrix} E_\rho(0) \\ H_\phi(0) \end{bmatrix} \quad (\text{B.28})$$

which is in agreement with [99, Eq. 2.3.111]. Using (B.16) and (B.67) one can obtain the

identity $k_{z,i}/\hat{y} = -j\eta_i$ which allows to express (B.27) as

$$\begin{bmatrix} E_\rho(d_i) \\ H_\phi(d_i) \end{bmatrix} = \begin{bmatrix} \cos(k_{z,i}d_i) & -j\eta_i \sin(k_{z,i}d_i) \\ -j \sin(k_{z,i}d_i)/\eta_i & \cos(k_{z,i}d_i) \end{bmatrix} \begin{bmatrix} E_\rho(0) \\ H_\phi(0) \end{bmatrix} \quad (\text{B.29})$$

Derivation Using Sinusoidal Function for z -Dependence

Analogous to the derivation which use the exponential functions we wave function is given in this case as

$$\psi_i = C_i \cos(k_{z,i}z) \cos(n\phi) H_n^{(2)}(k_\rho \rho) \quad (\text{B.30})$$

where again

$$k_\rho^2 + k_{z,i}^2 = k_i^2 = \omega \varepsilon_i \mu_i \quad (\text{B.31})$$

and n is an integer equal to or larger than 0.

The ψ_i can be in this case written as

$$\psi_i = C_i R(\rho) \Phi(\phi) Z(z) \quad (\text{B.32})$$

where

$$Z(z) = \cos(k_{z,i}z) \quad (\text{B.33a})$$

$$\Phi(\phi) = \cos(n\phi) \quad (\text{B.33b})$$

$$R(\rho) = H_n^{(2)}(k_\rho \rho) \quad (\text{B.33c})$$

Then

$$\begin{aligned} E_\rho &= \frac{1}{\hat{y}} \frac{\partial^2 \psi}{\partial \rho \partial z} = \frac{1}{\hat{y}} C_i \Phi(\phi) \frac{\partial R(\rho)}{\partial \rho} \frac{\partial Z(z)}{\partial z} \\ &= -\frac{1}{\hat{y}} C_i \Phi(\phi) \frac{\partial R(\rho)}{\partial \rho} \sin(k_{z,i}z) k_{z,i} \end{aligned} \quad (\text{B.34})$$

and

$$\begin{aligned} H_\phi &= -\frac{\partial \psi}{\partial \rho} = -C_i \Phi(\phi) \frac{\partial R(\rho)}{\partial \rho} Z(z) \\ &= -C_i \Phi(\phi) \frac{\partial R(\rho)}{\partial \rho} \cos(k_{z,i}z) \end{aligned} \quad (\text{B.35})$$

Also the following relations between the $Z(z)$ and $\frac{\partial Z(z)}{\partial z}$ referenced to the beginning of the respective layer at $z_{0,i}$ can be established using the well-known addition theorems for

harmonic functions

$$\cos(k_{z,i}z) = \cos(k_{z,i}(z - z_{0,i})) \cos(k_{z,i}z_{0,i}) - \sin(k_{z,i}(z - z_{0,i})) \sin(k_{z,i}z_{0,i}), \quad (\text{B.36})$$

$$\sin(k_{z,i}z) = \sin(k_{z,i}(z - z_{0,i})) \cos(k_{z,i}z_{0,i}) + \cos(k_{z,i}(z - z_{0,i})) \sin(k_{z,i}z_{0,i}). \quad (\text{B.37})$$

Then for the electric field

$$\begin{aligned} E_\rho(z) &= -\frac{1}{\hat{y}} C_i \Phi(\phi) \frac{\partial R(\rho)}{\partial \rho} \sin(k_{z,i}z) k_{z,i} \\ &= -\frac{1}{\hat{y}} C_i \Phi(\phi) \frac{\partial R(\rho)}{\partial \rho} k_{z,i} (\sin(k_{z,i}(z - z_{0,i})) \cos(k_{z,i}z_{0,i}) + \cos(k_{z,i}(z - z_{0,i})) \sin(k_{z,i}z_{0,i})) \\ &= \sin(k_{z,i}(z - z_{0,i})) \left(-\frac{1}{\hat{y}} C_i \Phi(\phi) \frac{\partial R(\rho)}{\partial \rho} \cos(k_{z,i}z_{0,i}) k_{z,i} \right) \\ &\quad + \cos(k_{z,i}(z - z_{0,i})) \left(-\frac{1}{\hat{y}} C_i \Phi(\phi) \frac{\partial R(\rho)}{\partial \rho} \sin(k_{z,i}z_{0,i}) k_{z,i} \right) \\ &= \sin(k_{z,i}(z - z_{0,i})) \frac{k_{z,i}}{\hat{y}} H_\phi(z_{0,i}) + \cos(k_{z,i}(z - z_{0,i})) E_\rho(z_{0,i}) \end{aligned}$$

Analogously for the magnetic field

$$\begin{aligned} H_\phi(z) &= -C_i \Phi(\phi) \frac{\partial R(\rho)}{\partial \rho} \cos(k_{z,i}z) \\ &= -C_i \Phi(\phi) \frac{\partial R(\rho)}{\partial \rho} (\cos(k_{z,i}(z - z_{0,i})) \cos(k_{z,i}z_{0,i}) - \sin(k_{z,i}(z - z_{0,i})) \sin(k_{z,i}z_{0,i})) \\ &= \cos(k_{z,i}(z - z_{0,i})) \left(-C_i \Phi(\phi) \frac{\partial R(\rho)}{\partial \rho} \cos(k_{z,i}z_{0,i}) \right) \\ &\quad + \sin(k_{z,i}(z - z_{0,i})) \left(C_i \Phi(\phi) \frac{\partial R(\rho)}{\partial \rho} \sin(k_{z,i}z_{0,i}) \right) \\ &= \cos(k_{z,i}(z - z_{0,i})) H_\phi(z_{0,i}) + \sin(k_{z,i}(z - z_{0,i})) \left(-\frac{\hat{y}}{k_{z,i}} E_\rho(z_{0,i}) \right) \end{aligned}$$

Combined in matrix notation this can be written as

$$\begin{bmatrix} E_\rho(z) \\ H_\phi(z) \end{bmatrix} = \begin{bmatrix} \cos(k_{z,i}(z - z_{0,i})) & \frac{k_{z,i}}{\hat{y}} \sin(k_{z,i}(z - z_{0,i})) \\ -\frac{\hat{y}}{k_{z,i}} \sin(k_{z,i}(z - z_{0,i})) & \cos(k_{z,i}(z - z_{0,i})) \end{bmatrix} \begin{bmatrix} E_\rho(z_{0,i}) \\ H_\phi(z_{0,i}) \end{bmatrix} \quad (\text{B.38})$$

which in the written out form using (B.16) is given by

$$\begin{bmatrix} E_\rho(z) \\ H_\phi(z) \end{bmatrix} = \begin{bmatrix} \cos(k_{z,i}(z - z_{0,i})) & \frac{k_{z,i}}{j\omega\epsilon_i^*} \sin(k_{z,i}(z - z_{0,i})) \\ \frac{\omega\epsilon_i^*}{jk_{z,i}} \sin(k_{z,i}(z - z_{0,i})) & \cos(k_{z,i}(z - z_{0,i})) \end{bmatrix} \begin{bmatrix} E_\rho(z_{0,i}) \\ H_\phi(z_{0,i}) \end{bmatrix} \quad (\text{B.39})$$

The relation between the lower and upper end of the layer is established by inserting

$z = z_{0,i} + d_i$ to obtain

$$\begin{bmatrix} E_\rho(z_{0,i} + d_i) \\ H_\phi(z_{0,i} + d_i) \end{bmatrix} = \begin{bmatrix} \cos(k_{z,i}d_i) & \frac{k_{z,i}}{j\omega\varepsilon_i^*} \sin(k_{z,i}d_i) \\ \frac{\omega\varepsilon_i^*}{jk_{z,i}} \sin(k_{z,i}d_i) & \cos(k_{z,i}d_i) \end{bmatrix} \begin{bmatrix} E_\rho(z_{0,i}) \\ H_\phi(z_{0,i}) \end{bmatrix} \quad (\text{B.40})$$

which is also in agreement with [99, Eq. 2.3.111].

Definitions of Transverse Impedances

Transverse impedances can also be defined to establish a characteristic equation. By division of the first row by the second row of (B.40) and using upper indices (l) and (u) to mark evaluation of the fields and impedances the lower and upper end, respectively, of the layer one obtains

$$\begin{aligned} \frac{E_\rho^{(u)}}{H_\phi^{(u)}} = \eta_{\text{transv.}}^{(u)}(z) &= \frac{\cos(k_{z,i}d_i)E_\rho^{(l)} + \frac{k_{z,i}}{\hat{y}} \sin(k_{z,i}d_i)H_\phi^{(l)}}{-\frac{\hat{y}}{k_{z,i}} \sin(k_{z,i}d_i)E_\rho^{(l)} + \cos(k_{z,i}d_i)H_\phi^{(l)}} \\ &= \frac{\eta_{\text{transv.}}^{(l)} + \frac{k_{z,i}}{\hat{y}} \tan(k_{z,i}d_i)}{-\frac{\hat{y}}{k_{z,i}} \tan(k_{z,i}d_i)\eta_{\text{transv.}}^{(l)} + 1} = \frac{\eta_{\text{transv.}}^{(l)} + j\eta_i \tan(k_{z,i}d_i)}{\frac{j}{\eta_i} \tan(k_{z,i}d_i)\eta_{\text{transv.}}^{(l)} + 1} \\ &= \eta_i \frac{\eta_{\text{transv.}}^{(l)} + j\eta_i \tan(k_{z,i}d_i)}{\eta_i + j\eta_{\text{transv.}}^{(l)} \tan(k_{z,i}d_i)}, \end{aligned} \quad (\text{B.41})$$

where $E_\rho^{(l)}/H_\phi^{(l)} = \eta_{\text{transv.}}^{(l)}$ and $k_{z,i}/\hat{y} = j\eta_i$ have been defined in the first and the second step, respectively, of the manipulation in (B.41). With the last manipulation of (B.41) the well-known form of the impedance transformation formula is obtained.

B.3.2 Characteristic Equation for Two Layers

The two interfaces at positions $z_{e,i}$ and $z_{0,i}$ are then related as

$$\begin{pmatrix} E_\rho(z_{e,i}) \\ H_\phi(z_{e,i}) \end{pmatrix} = \begin{pmatrix} \cos(\theta_i) & \frac{k_{z,i}}{\hat{y}} \sin(\theta_i) \\ -\frac{\hat{y}}{k_{z,i}} \sin(\theta_i) & \cos(\theta_i) \end{pmatrix} \begin{pmatrix} E_\rho(z_{0,i}) \\ H_\phi(z_{0,i}) \end{pmatrix} \quad (\text{B.42})$$

where $\theta_i = k_{z,i}(z_{e,i} - z_{0,i}) = k_{z,i}d_i$.

For the two-layer guide one obtains

$$E_\rho(z_{e,2}) = 0 = \begin{pmatrix} \cos(\theta_2) & \frac{k_{z,2}}{\hat{y}_2} \sin(\theta_2) \end{pmatrix} \begin{pmatrix} \frac{k_{z,1}}{\hat{y}_1} \sin(\theta_1) \\ \cos(\theta_1) \end{pmatrix} H_\phi(z_{0,1}). \quad (\text{B.43})$$

As in general $H_\phi(z_{0,1}) \neq 0$, (B.43) leads to the condition

$$\frac{k_{z,2}}{\hat{y}_2} \tan(\theta_2) = -\frac{k_{z,1}}{\hat{y}_1} \tan(\theta_1) \quad (\text{B.44})$$

which is equivalent to [96, Eq. 5-63].

B.3.3 Adaptations for Modes with Azimuthal Variations

For $n > 0$, the procedure is the same as for E_ρ and H_ϕ . For the other components one obtains

$$\begin{aligned} E_\phi &= \frac{1}{\hat{y}\rho} \frac{\partial^2 \psi}{\partial \phi \partial z} = \frac{1}{\hat{y}\rho} C_i R(\rho) \frac{\partial \Phi(\phi)}{\partial \phi} \frac{\partial Z(z)}{\partial z} \\ &= -\frac{1}{\hat{y}\rho} C_i R(\rho) \frac{\partial \Phi(\phi)}{\partial \phi} \sin(k_{z,i} z) k_{z,i} \end{aligned} \quad (\text{B.45})$$

and

$$\begin{aligned} H_\rho &= \frac{1}{\rho} \frac{\partial \psi}{\partial \phi} = \frac{1}{\rho} C_i R(\rho) \frac{\partial \Phi(\phi)}{\partial \phi} Z(z) \\ &= \frac{1}{\rho} C_i R(\rho) \frac{\partial \Phi(\phi)}{\partial \phi} \cos(k_{z,i} z). \end{aligned} \quad (\text{B.46})$$

It can be observed that, except for a different sign, the ratio of E_ϕ to H_ρ is the same as the ratio E_ρ and H_ϕ . Therefore, the transfer matrix for these field components can be derived in an analogous way and can be written as

$$\begin{pmatrix} -E_\phi(z_{e,i}) \\ H_\rho(z_{e,i}) \end{pmatrix} = \begin{pmatrix} \cos(\theta_i) & \frac{k_{z,i}}{\hat{y}} \sin(\theta_i) \\ -\frac{\hat{y}}{k_{z,i}} \sin(\theta_i) & \cos(\theta_i) \end{pmatrix} \begin{pmatrix} -E_\phi(z_{0,i}) \\ H_\rho(z_{0,i}) \end{pmatrix} \quad (\text{B.47})$$

where (as before) $\theta_i = k_{z,i}(z_{e,i} - z_{0,i}) = k_{z,i}d_i$. From comparison with (B.42), it can be concluded that the matrices express the same conditions. The difference in sign of the electric field in (B.47) leads (by construction of the wave solution) to an orientation of the transverse component of the wave vector which is the same as in (B.42).

For mode order index $n = 0$ and with PEC boundary conditions at the outermost layer interfaces it is thereby shown that the same transfer matrix can be used for the determination of the wave numbers of the radial waveguides. The following cases can be shown in an analogous way:

- Cases with $n > 0$ and with the complementary sinusoidal azimuthal dependence.
- Non-PEC boundary conditions with decaying fields away from the waveguide analog to the method in Section 4.3.3.

B.3.4 Approximate Solution for a PEC-bounded Single Layer

For the single layer it follows that

$$k_\rho = k_i = \omega \sqrt{\varepsilon_i \mu_i} \quad (\text{B.48})$$

If a loss tangent $\tan \delta$ of the dielectric medium is defined by $\varepsilon_i = \varepsilon_0 \varepsilon_{r,i} (1 - j \tan \delta)$, then for small loss tangents, using the series expansion of the square root, the wave number can be given as

$$\begin{aligned} k_\rho &= \omega \sqrt{\varepsilon_0 \varepsilon_{r,i} (1 - j \tan \delta) \mu_i} \\ &\approx \omega \sqrt{\varepsilon_0 \varepsilon_{r,i} \mu_i} \left(1 - j \frac{\tan \delta}{2} \right). \end{aligned} \quad (\text{B.49})$$

This is the same result for the attenuation due to dielectric loss (in an unlayered medium) as the one derived through considerations of power in [91, Eq. A2.8].

B.4 Analytical Derivatives for the TRM

The numerical efficiency and robustness can be improved by making use of analytical derivatives of the function of which the roots need to be determined when using one of the root-search techniques that involve derivatives of the characteristic function. Consider the following form of the transfer matrix for layer i

$$\mathbf{T}_i = \begin{pmatrix} \cos(\theta_i) & -j \varepsilon_{r,i} \sin(\theta_i) / k_i \\ -j k_i \sin(\theta_i) / \varepsilon_{r,i} & \cos(\theta_i) \end{pmatrix} \quad (\text{B.50})$$

where $\varepsilon_{r,i} = \varepsilon_i / \varepsilon_0$ is equal to the (complex) relative permittivity, $k_i = \pm \sqrt{k_{0,i}^2 - k_z^2}$, and $\theta_i = k_i t_i$. Note that the sign chosen for the k_i of the intermediate layers is irrelevant. This is because $\cos(k_i t_i)$, $\sin(k_i t_i) / k_i$, and $k_i \sin(k_i t_i)$ are all even functions for their complex argument k_i (see also Appendix F.2) and therefore invariant to its sign.

The transfer function for two consecutive layer i and j is given by the matrix product

$$\mathbf{T}_{\{i,j\}} = \mathbf{T}_i \mathbf{T}_j \quad (\text{B.51})$$

and for all N layers analogously by

$$\mathbf{T} = \mathbf{T}_{\{1,2,\dots,N\}} = \prod_{i=1}^N \mathbf{T}_i = \begin{pmatrix} T_{1,1} & T_{1,2} \\ T_{2,1} & T_{2,2} \end{pmatrix}, \quad (\text{B.52})$$

where the product is defined recursively by

$$\prod_{i=1}^n \mathbf{T}_i = \left(\prod_{i=1}^{n-1} \mathbf{T}_i \right) \mathbf{T}_n. \quad (\text{B.53})$$

The characteristic function $f(k_z)$ for the general case (arbitrary non-magnetic materials at outermost layers) is then given by

$$f(k_z) = -jk_s T_{1,1}/\varepsilon_{r,s} - jk_c T_{2,2}/\varepsilon_{r,c} - T_{2,1} + k_s k_c T_{1,2}/(\varepsilon_{r,s} \varepsilon_{r,c}), \quad (\text{B.54})$$

where for the space below the first layer (“substrate”) $k_s = \pm \sqrt{k_z^2 - k_{0,s}^2}$ and $\varepsilon_{r,s} = \varepsilon_s/\varepsilon_0$. For the space above the uppermost layer (“cladding”) $k_c = \pm \sqrt{k_z^2 - k_{0,c}^2}$ and $\varepsilon_{r,c} = \varepsilon_c/\varepsilon_0$. In both cases the sign for the wavenumber has to be chosen such that the real part is positive which corresponds to a wave that decays in the transverse direction(s) away from the waveguide.

B.4.1 First Derivative of the Transfer Matrix

The first derivative of the transfer matrix of layer i with respect to the longitudinal wave number k_x can be given as

$$\begin{aligned} \frac{\partial \mathbf{T}_i}{\partial k_x} &= \frac{\partial}{\partial k_x} \begin{bmatrix} \cos(\theta_i) & -j \sin(\theta_i) k_i / (\omega \varepsilon_n^*) \\ -j \omega \varepsilon_n^* \sin(\theta_i) / k_i & \cos(\theta_i) \end{bmatrix} \\ &= \begin{bmatrix} -\sin(\theta_i) \theta'_i & -j(k_i \cos(\theta_i) \theta'_i + k'_i \sin(\theta_i)) / (\omega \varepsilon_n^*) \\ -j \omega \varepsilon_n^* (k_i \cos(\theta_i) \theta'_i - k'_i \sin(\theta_i)) / k_i^2 & -\sin(\theta_i) \theta'_i \end{bmatrix} \end{aligned} \quad (\text{B.55})$$

where $\theta'_i = k'_i t_i$ and $k'_i = -k_x (k_{0,i}^2 - k_x^2)^{-1/2}$.

The first derivative of the transfer matrix for two consecutive layer i and j is given by the sum of matrix products involving the transfer matrices and their derivatives:

$$\frac{\partial \mathbf{T}_{\{i,j\}}}{\partial k_x} = \frac{\partial (\mathbf{T}_i \mathbf{T}_j)}{\partial k_x} = \frac{\partial \mathbf{T}_i}{\partial k_x} \mathbf{T}_j + \mathbf{T}_i \frac{\partial \mathbf{T}_j}{\partial k_x} \quad (\text{B.56})$$

The first derivative of the overall transfer matrix for all N layers can be formulated in a recursive way as

$$\mathbf{T}' = \frac{\partial \mathbf{T}_{\{1,2,\dots,N\}}}{\partial k_x} = \begin{pmatrix} T'_{1,1} & T'_{1,2} \\ T'_{2,1} & T'_{2,2} \end{pmatrix} \quad (\text{B.57})$$

$$\frac{\partial \mathbf{T}_{\{1,2,\dots,n\}}}{\partial k_x} = \frac{\partial \mathbf{T}_{\{1,2,\dots,n-1\}}}{\partial k_x} \mathbf{T}_n + \mathbf{T}_{\{1,2,\dots,n-1\}} \frac{\partial \mathbf{T}_n}{\partial k_x} \quad (\text{B.58})$$

B.4.2 First Derivative of the Characteristic Function

The derivative of the characteristic function is given by differentiation of (4.26) as

$$\begin{aligned} \frac{\partial F(k_z)}{\partial k_x} &= \frac{\partial}{\partial k_x} \left(jT_{1,1} \frac{\gamma_{z,l}}{\omega \varepsilon_l^*} - T_{2,1} \frac{\gamma_{z,l}}{\omega \varepsilon_l^*} \frac{\gamma_{z,u}}{\omega \varepsilon_u^*} + jT_{2,2} \frac{\gamma_{z,u}}{\omega \varepsilon_u^*} + T_{1,2} \right) \\ &= \frac{j}{\omega \varepsilon_l^*} (T'_{1,1} \gamma_{z,l} + T_{1,1} \gamma'_{z,l}) + \frac{j}{\omega \varepsilon_u^*} (T'_{2,2} \gamma_{z,u} + T_{2,2} \gamma'_{z,u}) + T'_{1,2} \\ &\quad - \frac{1}{\omega^2 \varepsilon_l^* \varepsilon_u^*} (T'_{2,1} \gamma_{z,l} \gamma_{z,u} + T_{2,1} \gamma'_{z,l} \gamma_{z,u} + T_{2,1} \gamma_{z,l} \gamma'_{z,u}) \end{aligned} \quad (\text{B.59})$$

where $\gamma'_{z,u} = \pm k_x (\omega^2 \mu \varepsilon_u^* - k_x^2)^{-1/2}$ and $\gamma'_{z,l} = \pm k_x (\omega^2 \mu \varepsilon_l^* - k_x^2)^{-1/2}$. Again, the signs have to be chosen such that the real parts of both $\gamma'_{z,u}$ and $\gamma'_{z,l}$ are positive.

B.5 Characteristic Impedance and Wave Impedances of Parallel Plate Waveguides

B.5.1 Impedances of the Homogeneously Filled Waveguide

Consider a parallel plate waveguide with perfectly conducting plates, width w and plate separation d . The homogeneous filling has a permittivity ε and a permeability μ_0 . The characteristic impedance can be expressed as a function of the per-unit-length capacitance and inductance which are easily derived as

$$L' = \varepsilon w / d, \quad (\text{B.60})$$

$$C' = \mu_0 d / w. \quad (\text{B.61})$$

The characteristic impedance of the (fundamental) TEM mode is then given as

$$Z_0 = \sqrt{\frac{L'}{C'}} = \sqrt{\frac{\varepsilon w / d}{\mu_0 d / w}} = \eta \frac{w}{d}. \quad (\text{B.62})$$

Equation (B.62) can be applied, e.g., when using the characteristic impedance Z_0 from port solutions of FEM full-wave simulations or the network parameter of a transmission line segment to determine the wave impedance η of the material.

B.5.2 Impedances of the Layered Waveguide

For the i th layer of the multilayer waveguide, a TM-wave exists for which the longitudinal impedance can be related to the longitudinal wave number as

$$\eta_{\text{TM}_x} = \frac{k_x}{\omega \varepsilon_i}. \quad (\text{B.63})$$

I.e., the wave impedance is related to the permittivity of the respective layer, but the longitudinal wave number is the same for all layers and is determined with one of the methods discussed before.

Next, the characteristic impedance of the layered waveguide is considered for the case where it can be related to capacitances and inductances. For the silicon structures that are of interest in this thesis this has been found to be applicable for the slow-wave and quasi-TEM regimes where the (effective) wave number has been with good accuracy approximated as

$$k_x = \omega \sqrt{L' C'} = \omega \sqrt{\mu_0 \varepsilon_{\text{eff}}^*} \quad (\text{B.64})$$

where

$$\varepsilon_{\text{eff}}^* = \frac{\sum_{i=1}^n t_i}{\sum_{i=1}^n \frac{t_i}{\varepsilon_i^*}} \quad (\text{B.65})$$

In (B.64), $C' = \varepsilon_{\text{eff}}^* w/d$ has in general assumed to be complex.

Using L' which is identical to the empty guide and C' for the characteristic impedances, one obtains

$$Z_0 = \sqrt{\frac{L'}{C'}} = \sqrt{\frac{\varepsilon_{\text{eff}}^* w/d}{\mu_0 d/w}} = \eta_{\text{eff}} \frac{w}{d}. \quad (\text{B.66})$$

In the last step of (B.66) an effective wave impedance η_{eff} is defined that is analog to the one of the homogeneously filled guide and is related to the characteristic impedance by only geometrical parameters. It is different in that it cannot in general relate the transverse electric and magnetic field components of the mode. For the effective wave impedance, also (B.63) can be used together with (B.64) as

$$\eta_{\text{eff}} = \frac{k_x}{\omega \varepsilon_{\text{eff}}^*} = \frac{\omega \sqrt{\mu_0 \varepsilon_{\text{eff}}^*}}{\omega \varepsilon_{\text{eff}}^*} = \frac{\omega \mu_0}{\omega \sqrt{\mu_0 \varepsilon_{\text{eff}}^*}} = \frac{\omega \mu_0}{k_x}. \quad (\text{B.67})$$

From the last result in (B.67) it can be seen that with these assumptions, the TM- and TE-mode impedances coincide.

Note that these results are equivalent to those used in other publications. For the modeling

of the multi-conductor lines in [25], a characteristic impedance

$$Z_c = \frac{1}{\sqrt{\varepsilon_{\text{eff}}} c_0 C_0} \quad (\text{B.68})$$

is used where c_0 is the speed of light, C_0 is the capacitance of the structure with all dielectrics replaced by vacuum, and

$$\varepsilon_{\text{eff}} = \left(\frac{k_z c_0}{\omega} \right)^2. \quad (\text{B.69})$$

This formulation can be traced back to [131–133]. It should be noted that, while [132] relates the characteristic impedance to the (real) phase velocity, it is related to the complex propagation constant by [131]. Applicability of the latter is assumed with the above formulas.

Appendix C

Computation of Waveguides Based on Cylindrical Wave Functions

The electromagnetic theory of many of the structures considered in this work is based on cylindrical wave functions. Structures and components which fall in this category are

- Coaxial waveguides with homogeneous filling for coaxial apertures of the via antipads in metal-clad interposers.
- Coaxial waveguides with inhomogeneous filling for coaxial TSVs.
- Radial waveguides with inhomogeneous filling for metal-clad silicon interposer.

C.1 Computation of Wave Numbers of Propagation in Coaxial TSVs

The section presents a matrix method for the computation of the wave number of the fundamental mode of propagation along a radial layered coaxial waveguide from [10]. This modeling is applicable for concentric coaxial TSV for which a PEC boundary is an appropriate approximation for the inner and outer conductor. In contrast to lumped element models, the method is also applicable with layers of elevated conductivity which are larger (in the transvers direction) than the skin depth. For the case where a layering with silicon and silicon dioxide is used the physical phenomena of quasi TEM, slow-wave and skin-effect propagation are again observed.

C.1.1 Adaptation of a Matrix Method for Radially Layered Coaxial TSVs

The coaxial structure as depicted in Fig. C.1 is considered which consists of a concentric coaxial waveguide with inner and outer radii r_i and r_N , respectively, and (in general) N layers of the radially layered filling. The n th layer is characterized by an outer radius of r_n , a relative permittivity ε_n , and a conductivity σ_n . The matrix method that is presented in the following adapts theory of the radially layered dielectric structure [134, 135]. To account for the losses in comparison to the mostly discussed lossless structures, the adaptation consists in the use of a complex permittivity. Similar to the formulation in the transverse resonance method (TRM), a characteristic function is derived for the which the (in general complex) roots correspond to the modal wave numbers.

The radial variations of the modal fields are efficiently described by using Bessel functions. The modes of lowest order of the TM- and TE-type are modes without angular/azimuthal variation of the fields. In comparison to the higher order modes, a smaller number of field components is necessary for the description. In the following, the notation from [134] is adopted and the main findings for the fundamental TM-mode in the purely dielectric structure are reproduced. Subsequently the adaptations for the modeling of the coaxial waveguide are discussed.

The general solution of the wave equation for each layer is given by a (weighted) superposition of Bessel functions to describe the radial dependence and a harmonic function to describe the azimuthal variation:

$$E_z = [AJ_l(k_i\rho) + BY_l(k_i\rho)] \cos(l\theta + \Phi) \quad (\text{C.1a})$$

$$H_z = [CJ_l(k_i\rho) + DY_l(k_i\rho)] \cos(l\theta + \Phi) \quad (\text{C.1b})$$

where $J_l(x)$ and $Y_l(x)$ are Bessel functions of the first and the second kind, respectively, of order l and argument x , and primed cylinder functions $J'_l(x)$ and $Y'_l(x)$ which in the following denote the derivative with respect to the respective argument x . ρ is the (transverse) radial coordinate and k_i the radial component of the wave number in the i -th layer. The transverse propagation constants (radial components) for non-magnetic materials are given by ¹

$$k_i = \sqrt{k_0^2 \varepsilon_{r,i} - k_z^2}, \quad (\text{C.2})$$

where k_0 is the free space wave number. k_z is the yet unknown wave number of guided wave propagation that is determined by the presented method. The complex relative permittivity

¹The negative of the root in (C.2) also fulfills the separation parameter condition. The principal square root has been used to compute the example presented in the following. It is not proven in this thesis that this applies to the general case.

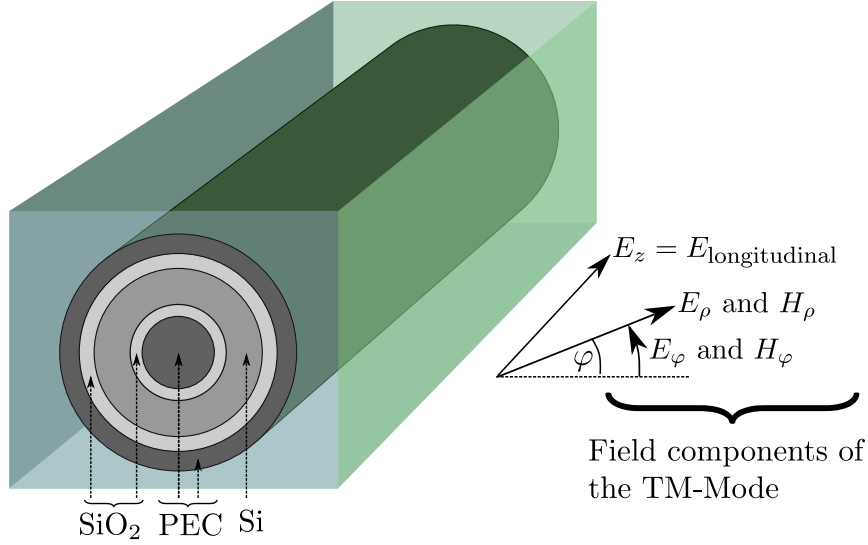


Figure C.1: Structure of the coaxial waveguide embedded in a dielectric (silicon) substrate. For the transverse magnetic modes of this waveguide the field components are given. Figure and text taken from [10].

of the i th layer is

$$\underline{\varepsilon}_{r,i} = \varepsilon_{r,i} - j(\sigma_i/\varepsilon_0\omega), \quad (\text{C.3})$$

where $\varepsilon_{r,i}$ is the real part of the relative permittivity of the material in the i th layer, σ_i is the material conductivity, ε_0 is the free space permittivity, and ω is the angular frequency.

The cosine terms in (C.1) describe an azimuthal dependence which is only relevant for the higher order modes. These are hybrid in that they have both electric and magnetic field components in propagation direction. For the fundamental TM-mode that is of interest here the H_z component and the azimuthal dependence $\cos(l\theta + \Phi)$ can be dropped.

The derivation starts by enforcing the continuity of the tangential field components E_z , E_θ , H_z , and H_θ at the interfaces of each pair of adjacent layers. This gives a 2×2 matrix that relates the coefficients of the Bessel functions, A and B , as

$$\mathbf{M}_2 \begin{bmatrix} A_2 \\ B_2 \end{bmatrix} = \mathbf{M}_1 \begin{bmatrix} A_1 \\ B_1 \end{bmatrix}. \quad (\text{C.4})$$

In order to simplify the notation, the two adjacent layer are indexed with 1 for inner one and 2 for the outer one of the two layers. The reduced matrix for the TM-case is given by (with index i is either 1 or 2):

$$\mathbf{M}_i(\rho_n) = \begin{bmatrix} J_l(k_i\rho_n) & Y_l(k_i\rho_n) \\ \frac{\omega\varepsilon_i J'_l(k_i\rho_n)}{k_z k_i} & \frac{\omega\varepsilon_i Y'_l(k_i\rho_n)}{k_z k_i} \end{bmatrix}, \quad (\text{C.5})$$

where $\varepsilon_i = \varepsilon_{0\varepsilon_{r,i}}$ and ρ_n is the radius of the interfaces.

In order to perform a concatenation for the description in (C.4), a transfer matrix is derived as

$$\begin{bmatrix} A_2 \\ B_2 \end{bmatrix} = \underbrace{(\mathbf{M}_2(\rho_n))^{-1} \cdot \mathbf{M}_1(\rho_n)}_{\mathbf{M}_{1,2}} \begin{bmatrix} A_1 \\ B_1 \end{bmatrix}, \quad (\text{C.6})$$

for which the elements are given as

$$\mathbf{M}_{1,2} = \frac{\pi k_2 \rho_n}{2} \begin{bmatrix} m_a & m_b \\ m_c & m_d \end{bmatrix}, \quad (\text{C.7a})$$

where

$$m_a = J_l(k_1 \rho_n) Y'_l(k_2 \rho_n) - \frac{k_2 \varepsilon_1}{k_1 \varepsilon_2} J'_l(k_1 \rho_n) Y_l(k_2 \rho_n), \quad (\text{C.7b})$$

$$m_b = Y_l(k_1 \rho_n) Y'_l(k_2 \rho_n) - \frac{k_2 \varepsilon_1}{k_1 \varepsilon_2} Y'_l(k_1 \rho_n) Y_l(k_2 \rho_n), \quad (\text{C.7c})$$

$$m_c = \frac{k_2 \varepsilon_1}{k_1 \varepsilon_2} J'_l(k_1 \rho_n) J_l(k_2 \rho_n) - J_l(k_1 \rho_n) J'_l(k_2 \rho_n), \quad (\text{C.7d})$$

$$m_d = \frac{k_2 \varepsilon_1}{k_1 \varepsilon_2} Y'_l(k_1 \rho_n) J_l(k_2 \rho_n) - Y_l(k_1 \rho_n) J'_l(k_2 \rho_n). \quad (\text{C.7e})$$

The coefficients for the outermost layers are then related by

$$\begin{aligned} \begin{bmatrix} A_N \\ B_N \end{bmatrix} &= \mathbf{M}_{N-1,N} \begin{bmatrix} A_{N-1} \\ B_{N-1} \end{bmatrix} \\ &= \underbrace{\mathbf{M}_{N-1,N} \mathbf{M}_{N-2,N-1} \dots \mathbf{M}_{2,3} \mathbf{M}_{1,2}}_{\begin{bmatrix} M_{11} & M_{12} \\ M_{21} & M_{22} \end{bmatrix}} \begin{bmatrix} A_1 \\ B_1 \end{bmatrix}, \end{aligned} \quad (\text{C.8})$$

where index 1 refers now to the innermost dielectric layer and index N for the outermost one. Compared to the theory for the Bragg fiber from [134], the boundary conditions are different and therefore need to be adapted as follows. The PEC boundaries require the tangential electrical field components E_z and E_ρ to disappear at the surfaces of the inner and outer conductor, i.e. at $\rho = r_0$ and $\rho = r_N$. This can be fulfilled by coefficients for the Bessel functions in the inner- and outermost layers

$$A_{1,N} = Y_l(k_{1,N} r_{0,N}), \quad (\text{C.9a})$$

$$B_{1,N} = -J_l(k_{1,N} r_{0,N}) \quad (\text{C.9b})$$

where r_0 is the radius of the inner conductor, r_N is the inner radius of the outer conduc-

tor, and $k_{1,N}$ are the transverse wave numbers (radial components) of the innermost and outermost layer, respectively.

An equation system can then be written as

$$\begin{bmatrix} Y_l(k_N r_N) \\ -J_l(k_N r_N) \end{bmatrix} = \begin{bmatrix} M_{11} & M_{12} \\ M_{21} & M_{22} \end{bmatrix} \begin{bmatrix} Y_l(k_1 r_0) \\ -J_l(k_1 r_0) \end{bmatrix} \quad (\text{C.10})$$

After multiplication of the first row of (C.10) with $-J_l(k_N r_N)$ and the second row with $Y_l(k_N r_N)$, the rows can be equated to obtain ²

$$\begin{aligned} 0 = & J_l(k_N r_N) [M_{11} Y_l(k_1 r_0) - M_{12} J_l(k_1 r_0)] \\ & + Y_l(k_N r_N) [Y_l(k_1 r_0) M_{21} - M_{22} J_l(k_1 r_0)] \end{aligned} \quad (\text{C.11})$$

C.1.2 Quasi-static First Order Approximation

As is in the case of planar layering, a quasi-static approximation should be applicable if the transverse dimensions are electrically small and the skin effect is not significant such that the products of transverse wave numbers and layer thicknesses are small. For the coaxially layered case with silicon and silicon dioxide layers, the structure is depicted in Fig. C.2a and the equivalent circuit is depicted in Fig. C.2b. The per unit length admittance of this coaxial structures is computed using the series connection of parallel capacitances and conductances for every layer as

$$Y'_{\text{Total}} = \frac{j\omega 2\pi}{\sum_{n=1}^N (\ln(r_n) - \ln(r_{n-1})) / (\varepsilon_0 \varepsilon_{r,n})}. \quad (\text{C.12})$$

Using (C.12), the wave number of guided wave propagation is obtained as

$$k_z = k_0 \varepsilon_{r,\text{eff}} = k_0 Y'_{\text{Total}} / (j\omega C'_0) \quad (\text{C.13})$$

where C'_0 is the per unit length capacitance of the empty coaxial guide with the same dimensions.

²In contrast to the system of nonlinear equations from [10], the formulation can therefore also be cast into this scalar equation which is easier to solve.

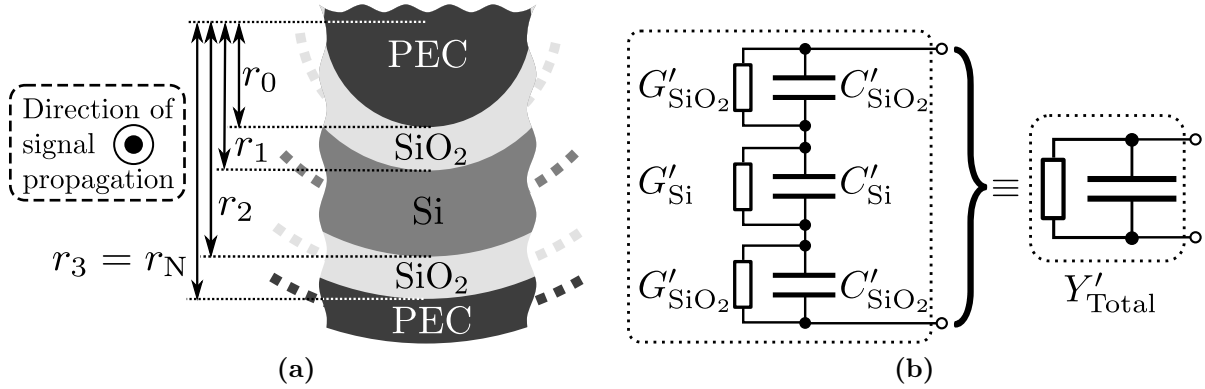


Figure C.2: (a) Detail view of the considered structure for the case of three layers with a configuration consisting of a silicon layer enclosed by silicon oxide layers. (b) Equivalent circuit for the fundamental mode used in the approximate analysis. When neglecting losses in the silicon dioxide the corresponding resistors can be omitted. For the silicon layer, the resistor does not play a role in the quasi TEM regime. Text taken and figure adapted from [10].

C.1.3 Application to Coaxial TSV Structures

In the following, several example results from [10] are presented with a comparison of wave number results obtained from the two proposed methods, the exact matrix method and the approximation from (C.13), and 2D FEM results from [112].

Numerical Implementation and Efficiency

As start values for the root search of the matrix method, the approximate values from (C.13) are used. The numerical techniques based on the APM as discussed in Appendix A.1.3 would also be applicable. An analytical derivative analog to the one for the planar layering presented in Section B.4 could also be derived.

Using the FEM simulation, approximately 1 s to 2 s are needed for the FEM simulation on a personal computer with 3.2 GHz CPU. The proposed methods are implemented in MATLAB and run on the same computer. For the proposed matrix method, two domains must be differentiated. In regions near and inside the skin-effect mode domain, the approximate method described above is neither valid nor does it provide reliable start values for a root search based on the Newton Method. Therefore, a domain subdivision method has been implemented which evaluated the sign changes of real and imaginary part on the contour and estimates the positions of roots from this. While this method has been successfully applied, the methods such as the APM are recommended for future investigations because they are based on more rigorous and well-studied techniques. Using the outline domain

subdivision, a computation time below 1 s is measured if reasonable sub-domain resolutions are determined in advance. In contrast, a good convergence is observed with the Newton root search that starts at the approximate values if inside the quasi-TEM and slow-wave regimes. A fast and reliable convergence then leads to computation times below around 25 ms for the matrix method. If occurrence of the skin-effect mode can be ruled out, the proposed approximate can be solely used and computes each wave number in less than 1 ms. For the structures and frequencies investigated in the following a fair agreement with the other methods is observed up to conductivities of the silicon of about 500 S/m.

Discussion of Example Results

The computed results are presented in Figs. C.3 through C.6. The results in Figs. C.3 and C.4 show the behavior that is expected from the results for the planar layers: At low frequencies a slow-wave propagation occurs with relatively low attenuation because most of the electrical field is concentrated inside the oxide layer. Due to strong interfacial polarizations, the phase velocity is lower than in a waveguide with either silicon or silicon dioxide [38]. Towards higher frequencies, a transition occurs towards the quasi-TEM mode where the phase velocity is between the values for the involved dielectrics and the attenuation also increases. A good agreement of all methods is observed except for the phase velocity inside the transition region. Fig. C.5 shows the transition from the slow-wave regime towards the skin-effect regime. It can be seen that the matrix method also shows a good agreement with reference results while the effects are not represented/modeled by the approximate method, especially regarding the attenuation. Further results are given in the form of a frequency-resistivity-chart in Fig. C.6 for the phase velocity normalized to the free-space phase velocity.

C.2 TM_{0n} -Modes of the Radial Waveguide

The TM_{0n} -modes play an important role for the description of radial wave propagation in planar circuits described in this thesis. They are supported by a parallel pair of conducting planes. In this section the network parameters for the the ideal (lossless and homogeneously filled) radial waveguide for one of these modes are derived. Radial ports are defined on surfaces that are the lateral faces of a circular cylinder. The two radial ports are located at an (inner) radius r_a and an (outer) radius r_b .

The electric and magnetic fields in the waveguide can be derived from a scalar mode

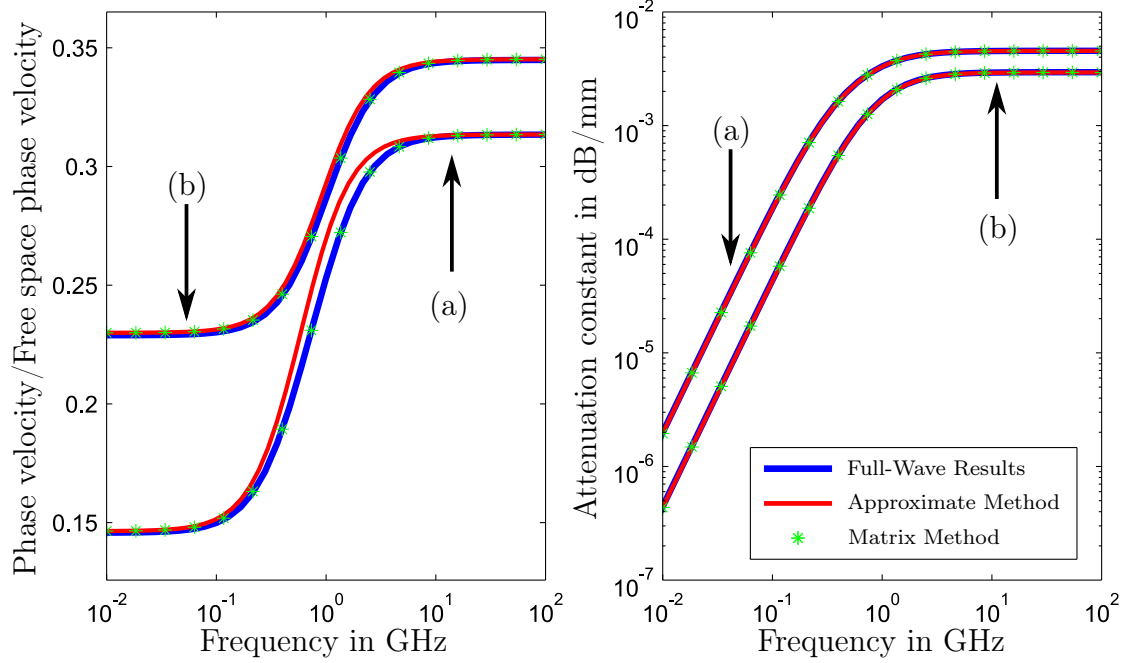


Figure C.3: Correlation results for a structure with an inner conductor of radius $5\text{ }\mu\text{m}$, an outer conductor of radius $10\text{ }\mu\text{m}$ and a silicon dioxide layer thickness of (a) $0.2\text{ }\mu\text{m}$ and (b) $0.5\text{ }\mu\text{m}$, respectively. The silicon conductivity is 1 S/m ($100\text{ }\Omega\text{ cm}$). Figure and text taken from [10].

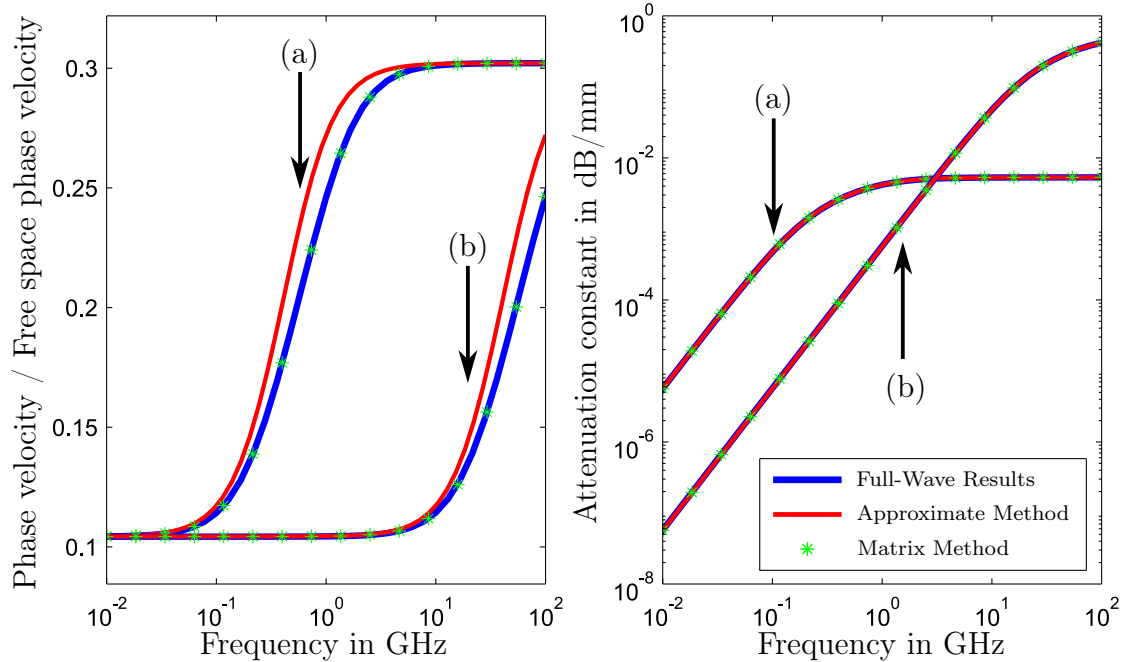


Figure C.4: Correlation results for a structure with an inner conductor of radius $10\text{ }\mu\text{m}$, an outer conductor of radius $110\text{ }\mu\text{m}$, and a silicon dioxide layer thickness of $1\text{ }\mu\text{m}$. The silicon conductivity is (a) 1 S/m and (b) 100 S/m , respectively. Figure and text taken from [10].

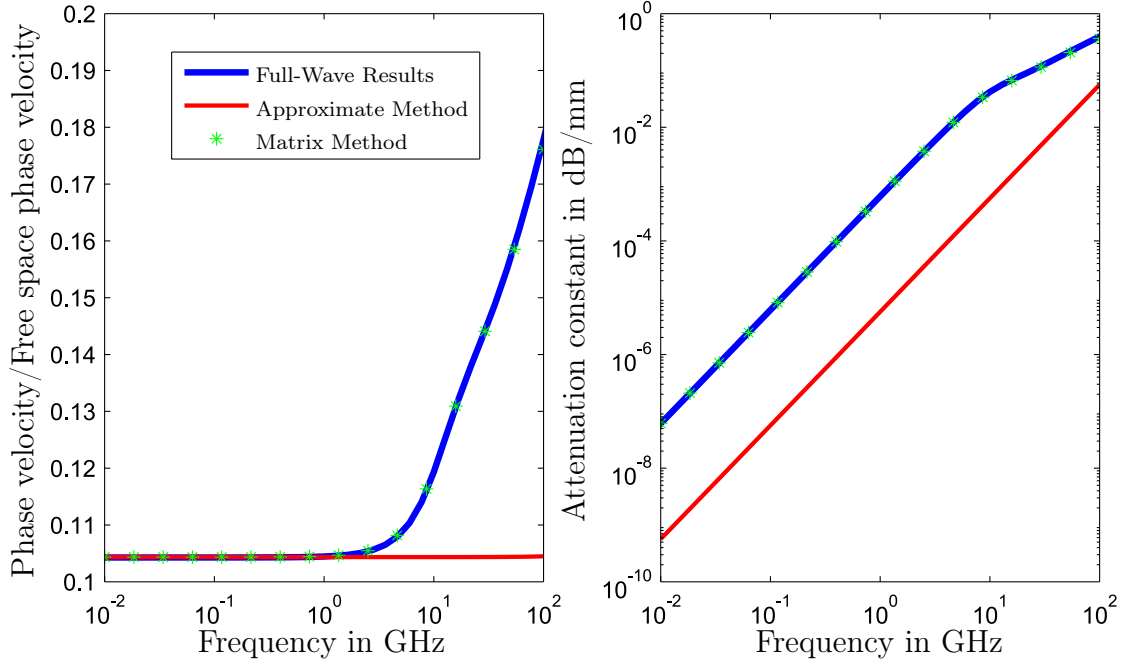


Figure C.5: Correlation results for a structure with an inner conductor of radius 10 μm , an outer conductor of radius 110 μm , and a silicon dioxide layer thickness of 1 μm . The silicon conductivity is 10^4 S/m ($10^{-2} \Omega \text{ cm}$). Figure and text taken from [10].

function [96, Sec. 5-3]

$$\Psi_{0n}^{\text{TM}} = \cos(n\phi) \begin{Bmatrix} H_n^{(1)}(k\rho) \\ H_n^{(2)}(k\rho) \end{Bmatrix}, \quad (\text{C.14})$$

where $k = k_\rho$ and $n = 0, 1, 2, \dots$.

For the complete set of modes, also the following scalar mode function must be considered [96, Sec. 5-3]

$$\Psi_{0n}^{\text{TM}} = \sin(n\phi) \begin{Bmatrix} H_n^{(1)}(k\rho) \\ H_n^{(2)}(k\rho) \end{Bmatrix}. \quad (\text{C.15})$$

From (C.14), the following electric field components are derived:

$$E_\rho = 0 \quad (\text{C.16})$$

$$E_\phi = 0 \quad (\text{C.17})$$

$$E_z = \frac{1}{j\omega\varepsilon} \left(\frac{\partial^2}{\partial z^2} + k^2 \right) \Psi_{0n}^{\text{TM}} = \frac{k^2}{j\omega\varepsilon} \cos(n\phi) \begin{Bmatrix} H_n^{(1)}(k\rho) \\ H_n^{(2)}(k\rho) \end{Bmatrix} \quad (\text{C.18})$$

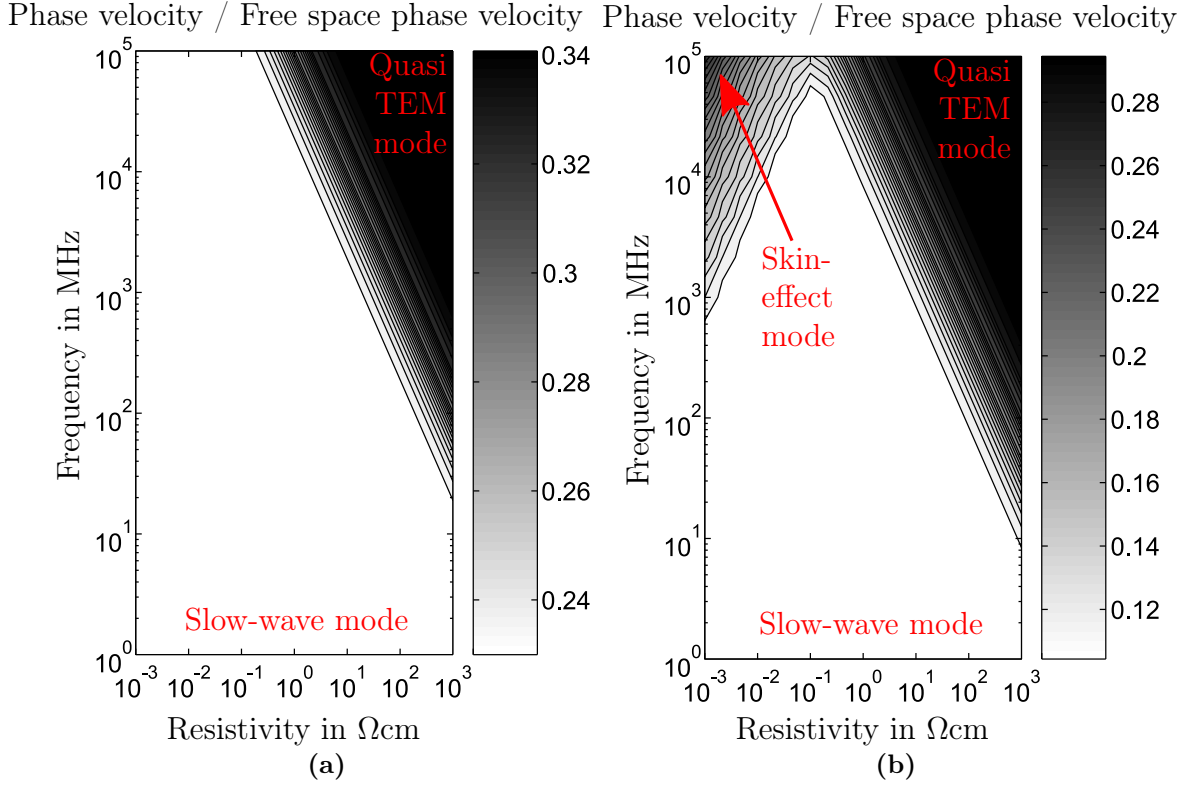


Figure C.6: Normalized phase velocity plotted in resistivity-frequency charts for the structures with (a) an inner conductor of radius $5\text{ }\mu\text{m}$, an outer conductor of radius $10\text{ }\mu\text{m}$ and a silicon dioxide layer thickness of $0.5\text{ }\mu\text{m}$. (b) with an inner conductor of radius $10\text{ }\mu\text{m}$, an outer conductor of radius $110\text{ }\mu\text{m}$ and a silicon dioxide layer thickness of $1\text{ }\mu\text{m}$. The scaling was chosen as to facilitate comparison with results in [8] and [104]. To compute the charts 304 parameter sets were evaluated. Absence of skin-effect mode in (a) allows for fast conversion from approximate values resulting in a total simulation time of only $\approx 7.5\text{ s}$. Text taken and figures adapted from [10].

The magnetic field components are given by

$$H_\rho = \frac{1}{\rho} \frac{\partial \Psi_{0n}^{\text{TM}}}{\partial \Phi} = -\frac{1}{\rho} n \sin(n\phi) \begin{Bmatrix} H_n^{(1)}(k\rho) \\ H_n^{(2)}(k\rho) \end{Bmatrix} \quad (\text{C.19})$$

$$H_\phi = -\frac{\partial \Psi_{0n}^{\text{TM}}}{\partial \rho} = -\cos(n\phi) k \begin{Bmatrix} H_n'^{(1)}(k\rho) \\ H_n'^{(2)}(k\rho) \end{Bmatrix} \quad (\text{C.20})$$

$$H_z = 0 \quad (\text{C.21})$$

In (C.20), $H_n'^{(1)}$ and $H_n'^{(2)}$ are the derivatives with respect the complete argument of the Hankel functions of first and second kind, respectively, and order n . Relations for Bessel function derivatives can be found in Appendix F.3.

If port 1 is the inner port, then the admittance $Y_{1,1}$ can be obtained by enforcing $V_2 = 0$ (short-circuit of the outer port) and relating modal voltage and current at the inner port. The condition of the voltage being zero at the outer port is enforced by setting the overall field equal to zero

$$E_z^{(0n)}(\rho = r_b) = \frac{k^2}{j\omega\varepsilon} \cos(n\phi) (A \cdot H_n^{(1)}(kr_b) + B \cdot H_n^{(2)}(kr_b)) = 0, \quad (\text{C.22})$$

where A and B are yet unknown constants. This can be solved for a relation between A and B :

$$A = -B \cdot \frac{H_n^{(2)}(kr_b)}{H_n^{(1)}(kr_b)} \quad (\text{C.23})$$

For $Y_{1,1}$ the magnetic field has to be integrated along the azimuthal circumference of port 1 and the electric field along the vertical cross-section to obtain

$$\begin{aligned} Y_{1,1} &= \left. \frac{2\pi r_a H_\phi(r_a)}{h E_z^{(0n)}(r_a)} \right|_{E_z(r_b)=0} \\ &= \frac{2\pi r_a}{h} \cdot \frac{j\omega\varepsilon}{k} \cdot \frac{A H_n'^{(1)}(kr_a) + B H_n'^{(2)}(kr_a)}{A H_n^{(1)}(kr_a) + B H_n^{(2)}(kr_a)} \\ &= \frac{2\pi r_a}{h} \cdot \frac{j\omega\varepsilon}{k} \cdot \frac{-H_n^{(2)}(kr_b) H_n'^{(1)}(kr_a) + H_n^{(1)}(kr_b) H_n'^{(2)}(kr_a)}{-H_n^{(2)}(kr_b) H_n^{(1)}(kr_a) + H_n^{(1)}(kr_b) H_n^{(2)}(kr_a)}. \end{aligned} \quad (\text{C.24})$$

See Section B.3 for a discussion of the wave numbers of these TM-modes.

Appendix D

The Contour Integral Method for Planar Circuits

In this chapter, the theory of the Contour Integral Method (CIM) is discussed. First, the original formulation and the main results of the adaptation to circular ports are presented. This discussion assumes a parallel plate structure with homogeneous substrate. Then, the adaptations for layered substrates are discussed. Finally, some guidance is provided for the practical implementation of efficient CIM algorithms.

D.1 Theoretical Foundations of the Contour Integral Method

The CIM is a numerical technique for computation of electromagnetic properties of 2D planar structures by means of a contour integral formulation. The method can hence be classified as a boundary element method (BEM). The planar circuit is regarded as an N -port circuit with modal voltages and currents along the contours which are integral quantities of associated tangential electric and magnetic fields at the contours. In the original formulation of the CIM for arbitrary shapes, all inner and outer 1D contours of the computational domain are discretized and constant electric and magnetic field are assumed on the ports assigned to the segments of the discretized contour. Using a sufficiently fine discretization of the boundary (e.g. 10 segments per wavelength for relatively simple shapes), the method has been shown to produce good results with reduced numerical effort when compared to methods with volume or surface discretization. The corresponding 3D geometry of a linear port is a square-shaped area with metallizations at the top and bottom contour lines. The basis functions on the linear segments are pulse basis functions and the matching point is chosen at the center of each segment.

Later, the CIM has been extended to circular ports. The corresponding 3D geometry of a circular port is shaped as the lateral surface of a circular cylinder. This 3D counterpart of

this port type is therefore not planar. Instead of a point matching, a Galerkin matching is carried out with the functions of a Fourier expansion defined on each port. The finite number of Fourier functions determines the accuracy related to the circular ports whereas the accuracy related to the linear port is influenced by both the port size and the type of numerical integration used for evaluation of fields on it.

The voltages and currents at all ports are related through a linear system of equations for all ports on the contour. With the characterization in terms of the ports, no assumption is yet made regarding circuits connected to these ports except that the discretization is fine enough to represent the field with the required accuracy. The characterization in terms of network parameters can therefore be used in segmentation approaches to compute the properties of parts of circuits independently and concatenate them subsequently. Ports can also be located at positions of the boundary of the computational domain which correspond to a boundary in the modeled physical structure. These ports may, e.g., represent open circuited contours, a discontinuity due to the finite plane which reflects the cylindrical waves that propagate between the parallel plates. The effect of real contours is modeled by terminations of the corresponding ports.

General Form of the CIM

In the following, modal voltages and currents on linear and circular ports are related by matrices \mathbf{U} and \mathbf{H} in the general form

$$\mathbf{U}\mathbf{V} = \mathbf{H}\mathbf{I}. \quad (\text{D.1})$$

The description in (D.1) can be used to compute more explicit descriptions in form of the so-called parallel-plate impedance matrix as

$$\mathbf{Z} = \mathbf{U}^{-1}\mathbf{H} \quad (\text{D.2a})$$

or in form of the corresponding parallel-plate admittance matrix as

$$\mathbf{Y} = \mathbf{H}^{-1}\mathbf{U}. \quad (\text{D.2b})$$

As shown in Section 6.1, it can be numerically beneficial to incorporate fixed port terminations into the solution step instead of terminating the network parameter after the computation as in (D.2).

Indices	Equations in the references	Equations in this chapter
ll	[91, Eqs. 3.3, 3.4]	(D.5)
lc	[93, Eqs. 4.19, 4.20]	(D.7)
la	[93, Eqs. 4.48, 4.49]	(D.14)
cl	[93, Eqs. 4.21, 4.22]	(D.8)
cc	[93, Eqs. 4.11, 4.12]	(D.6)
ca, ac, aa	[56, Eqs. 4.44, 4.45]	(D.12), (D.13)
al	[93, Eqs. 4.50, 4.51]	(D.15)

Table D.1: Indices of the U- and H-matrix parts as organized in (D.4) with the original references and the equations numbers used within this chapter.

Structure of the CIM matrices with All Port Types

For the modal voltages and currents in (D.1), the following differentiation and ordering can be used

$$\mathbf{V} = \begin{pmatrix} \mathbf{V}_l \\ \mathbf{V}_c \\ \mathbf{V}_a \end{pmatrix}, \quad (\text{D.3a})$$

$$\mathbf{I} = \begin{pmatrix} \mathbf{I}_l \\ \mathbf{I}_c \\ \mathbf{I}_a \end{pmatrix}, \quad (\text{D.3b})$$

where indices l correspond to the single modes on line ports, indices c to the isotropic modes on circular ports, and indices a to the anisotropic modes on circular ports.¹ The \mathbf{U} -matrix and the \mathbf{H} -matrix are accordingly organized blockwise as follows

$$\mathbf{U} = \begin{pmatrix} \mathbf{U}^{(ll)} & \mathbf{U}^{(lc)} & \mathbf{U}^{(la)} \\ \mathbf{U}^{(cl)} & \mathbf{U}^{(cc)} & \mathbf{U}^{(ca)} \\ \mathbf{U}^{(al)} & \mathbf{U}^{(ac)} & \mathbf{U}^{(aa)} \end{pmatrix}, \quad (\text{D.4a})$$

$$\mathbf{H} = \begin{pmatrix} \mathbf{H}^{(ll)} & \mathbf{H}^{(lc)} & \mathbf{H}^{(la)} \\ \mathbf{H}^{(cl)} & \mathbf{H}^{(cc)} & \mathbf{H}^{(ca)} \\ \mathbf{H}^{(al)} & \mathbf{H}^{(ac)} & \mathbf{H}^{(aa)} \end{pmatrix}, \quad (\text{D.4b})$$

These parts are given in the following and the overview is provided in Table D.1.

¹For comparison with the reference: In [93], isotropic and anisotropic circular modes are not distinguished with this kind of index. Instead, indices p are used for all modes on circular ports and indices q are used for the linear ports.

D.1.1 Original Formulation for Line Ports

The original formulation of the CIM includes only line ports. Using a notation that is close to the one from [93] the entries of the matrices $\mathbf{U}^{(ll)}$ and $\mathbf{H}^{(ll)}$ are given in [91] as²

$$U_{op}^{(ll)} = \delta_{op} - \frac{k}{2j} \int_{W_p} \langle \hat{\mathbf{R}}, \hat{\mathbf{n}}' \rangle H_1^{(2)}(k\rho_{op}) ds_p, \quad (\text{D.5a})$$

and

$$H_{op}^{(ll)} = \begin{cases} \frac{\omega\mu d}{2W_p} \int_{W_p} H_0^{(2)}(k\rho_{op}) ds_p & \text{for } o \neq p, \\ \frac{\omega\mu d}{2} \left[1 - \frac{2j}{\pi} \left(\ln \left(\frac{kW_o}{4} \right) - 1 + \gamma \right) \right] & \text{for } o = p, \end{cases} \quad (\text{D.5b})$$

Refer to Fig. D.1 for parts of the following notation. δ_{op} is the Kronecker delta (equal to 1 for $o = p$ and 0 else). W_p is the width of the p th port. k is the wave number of propagation in the parallel plate structure. $\rho_{op} = \|\mathbf{r}_o - \mathbf{r}_p\|_2$ is the distance between locations on ports o and p : For the observation port with index o , this location of the observation point is typically chosen at the geometrical center of the port. For the source point with index p , this location corresponds to the points along the port contour that are used for the numerical integration along the source port. $\hat{\mathbf{R}} = (\mathbf{r}_o - \mathbf{r}_p)/\rho_{op}$ is the source–observation point unit vector. $\hat{\mathbf{n}}'$ is the normal vector at the source boundary port. As depicted in Fig. D.1, it points outward for the outer contour C that is discretized with linear segments and towards the center of the inner circular contour C' . μ is the permeability of the dielectric. $\omega = 2\pi f$ is the angular frequency. d is the plate separation which is equal to the thickness of the dielectric. γ is the Euler-Mascheroni constant ($\gamma \approx 0.577215665$).

D.1.2 Extensions to Isotropic Modes on Circular Ports

An extension of the CIM is presented in [92, 93] which introduces analytical solutions for the integral over circular ports. By using the extended model the numerical effort can be reduced, especially if only the fundamental isotropic mode needs to be considered.

²The formulation in [93] for (D.5b) differs by a factor of $1/2$ from the one in [91] because the port currents are defined differently.

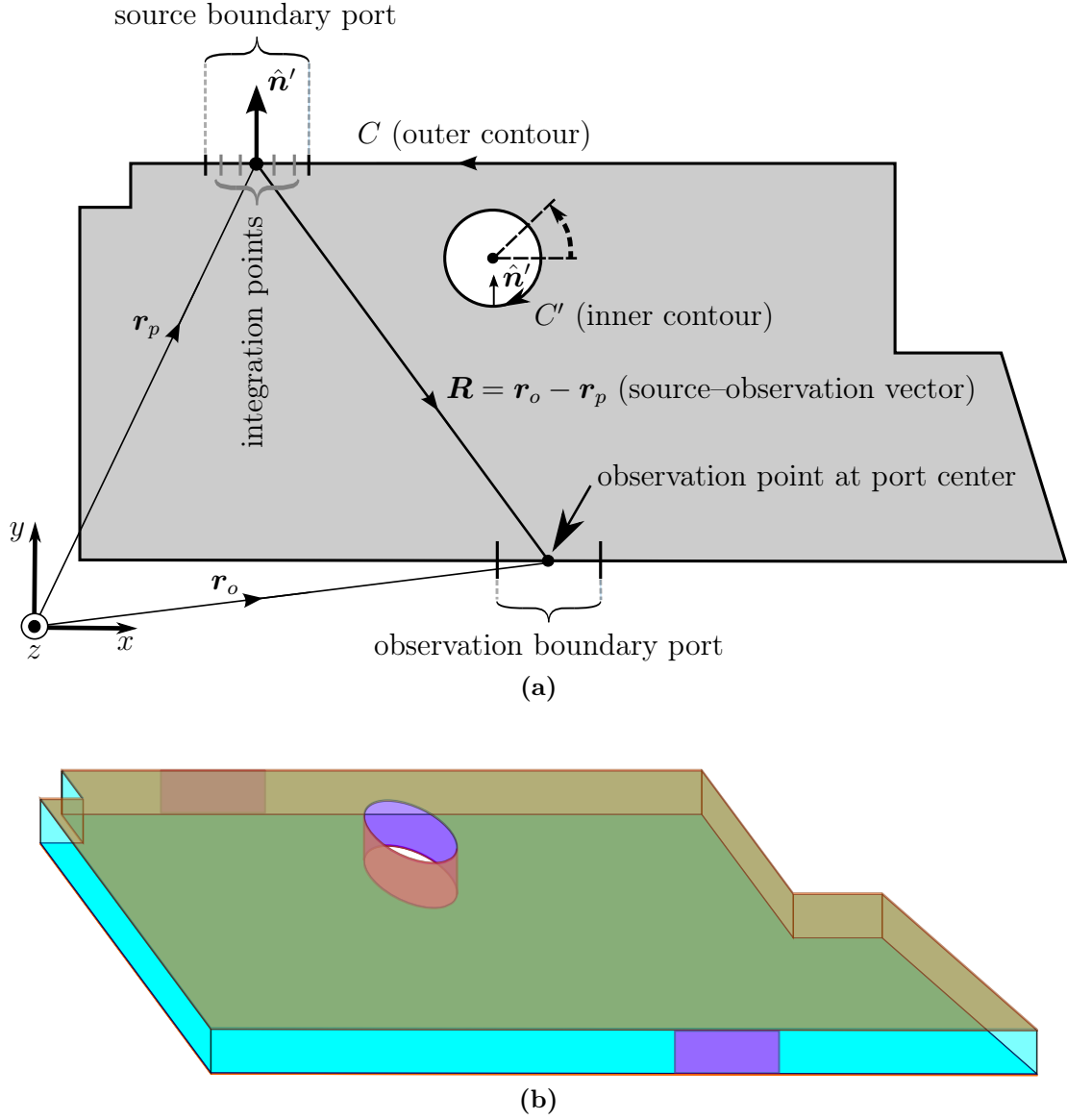


Figure D.1: (a) Port and vector definitions for the CIM with finite planes: All the contours and the tangential vector are assumed to be oriented in counterclockwise direction for outer contours and clockwise for inner countours (cutouts). The normal vector on segments are assumed to points outwards from the planes in both cases. The source-observation vector \mathbf{R} points from the source boundary point center to the center of the observation boundary port. Figure adapted from [93, Fig. 3.1]. (b) Illustration of the corresponding 3D structure.

Only Circular Ports

In many of the applications of the CIM in this thesis, the case of infinite planes is considered which is equivalent to radiation from the boundary without reflected waves or very large planes from which no significant signal is effectively scattered back because a strong attenuation of propagation in the horizontal plane occurs. The wave propagating in the parallel plate structure is in this case only scattered at the vias. Therefore only the radial ports at which the via near field models are concatenated are required.

If only the fundamental, isotropic mode is considered on circular ports, then the entries of $\mathbf{U}^{(cc)}$ and $\mathbf{H}^{(cc)}$ are given by [92]:

$$U_{oo}^{(cc)} = \frac{k\pi a_p}{j} \begin{cases} J_0(ka_p)H_1^{(2)}(ka_p) & (o = p), \\ J_0(ka_o)J_1(ka_p)H_0^{(2)}(k\rho_{op}) & (o \neq p), \end{cases} \quad (\text{D.6a})$$

$$H_{oo}^{(cc)} = \frac{k\eta d}{2} \begin{cases} J_0(ka_p)H_0^{(2)}(ka_p) & (o = p), \\ J_0(ka_o)J_0(ka_p)H_0^{(2)}(k\rho_{op}) & (o \neq p), \end{cases} \quad (\text{D.6b})$$

where k is again the wave number of propagation in horizontal directions in the parallel-plate structure. η is the wave impedance of this wave propagation which is further discussed in Appendix D.2. d is the plate separation which is equal to the thickness of the dielectric filling. a_o and a_p are the radii of circular ports o and p , respectively. ρ_{op} is the distance between the centers of the circular ports o and p .

Both Linear and Circular Ports

For circular ports as source ports and line ports as observation ports, the matrix entries are given by [92, Eq. 42]

$$U_{op}^{(lc)} = \frac{k\pi a_p}{j} \cdot J_1(ka_p)H_0^{(2)}(k\rho_{op}), \quad (\text{D.7a})$$

$$U_{op}^{(lc)} = \frac{k\eta d}{2} \cdot J_0(ka_p)H_0^{(2)}(k\rho_{op}). \quad (\text{D.7b})$$

For line ports as source ports and circular ports as observation ports, the matrix entries are given by [92, Eq. 42]

$$U_{op}^{(cl)} = -\frac{k}{2j} \cdot J_0(ka_o) \cdot \int_{W_p} \langle \hat{\mathbf{R}}, \hat{\mathbf{n}}' \rangle H_1^{(2)}(k\rho_{op}) \, ds', \quad (\text{D.8a})$$

$$H_{op}^{(cl)} = \frac{k\eta d}{2} \cdot J_0(ka_o) \cdot \frac{1}{W_p} \int_{W_p} H_0^{(2)}(k\rho_{op}) \, ds'. \quad (\text{D.8b})$$

D.1.3 Extensions to Anisotropic Modes on Circular Ports

Port Definitions for Anisotropic Modes

Meaningful port definitions for anisotropic modes on circular ports are required. In [56, Eq. 4.23], these are given as

$$E_z(\mathbf{r}) = \sum_{n=-\infty}^{\infty} \tilde{E}_n \exp(jn\phi) \quad (\text{D.9a})$$

$$H_\phi(\mathbf{r}) = \sum_{n=-\infty}^{\infty} \tilde{H}_n \exp(jn\phi) \quad (\text{D.9b})$$

where ϕ is the azimuthal angle along the circular port circumference and the Fourier coefficients \tilde{E}_n and \tilde{H}_n are given by [56, Eq. 4.24]

$$\tilde{E}_n = \frac{1}{2\pi} \sum_{n=-\infty}^{\infty} E_z(\mathbf{r}) \exp(-jn\phi) d\phi \quad (\text{D.10a})$$

$$\tilde{H}_n = \frac{1}{2\pi} \sum_{n=-\infty}^{\infty} H_\phi(\mathbf{r}) \exp(-jn\phi) d\phi \quad (\text{D.10b})$$

As noted in [56, Sec. 4.4], in order to keep consistency with the isotropic mode definitions, the following modal voltages and currents are defined

$$V_n = \tilde{E}_n d \quad (\text{D.11a})$$

$$I_n = \tilde{H}_n 2\pi a \quad (\text{D.11b})$$

where d and a are the port height and radius, respectively, of the circular port.

Relations Between Modes on Circular Ports

In order to simplify the notation, a specific ordering of modes is chosen. In the following ordering all entries with one combination of the two mode indices are assembled in one block. If modes in the ranges $-M, \dots, M$ and $-N, \dots, N$ are used with $M = N$ the organizations of the blocks for the relation between all modes on circular ports except for those between the isotropic modes can be given for the \mathbf{U} -matrix as

$$\mathbf{U}^{(ca)} = [\mathbf{U}^{(0,-N)} \quad \mathbf{U}^{(0,-N+1)} \quad \dots \quad \mathbf{U}^{(0,-1)} \quad \mathbf{U}^{(0,+1)} \quad \dots \quad \mathbf{U}^{(0,+N)}] \quad (\text{D.12a})$$

$$\mathbf{U}^{(ac)} = \begin{bmatrix} \mathbf{U}^{(-M,0)} \\ \mathbf{U}^{(-M+1,0)} \\ \vdots \\ \mathbf{U}^{(-1,0)} \\ \mathbf{U}^{(+1,0)} \\ \vdots \\ \mathbf{U}^{(+M,0)} \end{bmatrix} \quad (\text{D.12b})$$

$$\mathbf{U}^{(aa)} = \begin{bmatrix} \mathbf{U}^{(-M,-N)} & \mathbf{U}^{(-M,-N+1)} & \dots & \mathbf{U}^{(-M,-1)} & \mathbf{U}^{(-M,+1)} & \dots & \mathbf{U}^{(-M,+N)} \\ \mathbf{U}^{(-M+1,-N)} & \mathbf{U}^{(-M+1,-N+1)} & \dots & \mathbf{U}^{(-M+1,-1)} & \mathbf{U}^{(-M+1,+1)} & \dots & \mathbf{U}^{(-M+1,+N)} \\ \vdots & \vdots & \ddots & \vdots & \vdots & \ddots & \vdots \\ \mathbf{U}^{(-1,-N)} & \mathbf{U}^{(-1,-N+1)} & \dots & \mathbf{U}^{(-1,-1)} & \mathbf{U}^{(-1,+1)} & \dots & \mathbf{U}^{(-1,+N)} \\ \mathbf{U}^{(+1,-N)} & \mathbf{U}^{(+1,-N+1)} & \dots & \mathbf{U}^{(+1,-1)} & \mathbf{U}^{(+1,+1)} & \dots & \mathbf{U}^{(+1,+N)} \\ \vdots & \vdots & \ddots & \vdots & \vdots & \ddots & \vdots \\ \mathbf{U}^{(+M,-N)} & \mathbf{U}^{(+M,-N+1)} & \dots & \mathbf{U}^{(+M,-1)} & \mathbf{U}^{(+M,+1)} & \dots & \mathbf{U}^{(+M,+N)} \end{bmatrix} \quad (\text{D.12c})$$

The organization of the \mathbf{H} -matrix is correspondingly. With the definitions in (D.11), the entire of the blocks of the \mathbf{U} -matrix and \mathbf{H} -matrix for the interaction between anisotropic modes on circular ports and between the isotropic and anisotropic modes can be given as [56, Eqs. 4.44–4.45], [93, Eq. 17a]³

$$U_{o,p}^{(m,n)} = -\frac{k\pi a_p}{j} \cdot J_m(ka_o) \cdot \begin{cases} J'_m(ka_p) H_{m-n}^{(2)}(k\rho_{o,p}) \exp(-j(m-n)\phi_{o,p}) & (o \neq p), \\ H_m^{(2)}(ka_o) & (m=n) \wedge (o=p), \\ 0 & \text{else,} \end{cases} \quad (\text{D.13a})$$

$$H_{o,p}^{(m,n)} = \frac{k\eta d}{2} \cdot J_m(ka_o) \cdot \begin{cases} J_m(ka_p) H_{m-n}^{(2)}(k\rho_{op}) \exp(-j(m-n)\phi_{o,p}) & (o \neq p), \\ H_m^{(2)}(ka_o) & (m=n) \wedge (o=p), \\ 0 & \text{else.} \end{cases} \quad (\text{D.13b})$$

The primes in (D.13a) denote the derivative of the respective Bessel and Hankel functions with respect to their complete argument. $\phi_{o,p}$ is the angle between the vector from observation point to source point and the positive x-axis, cf. [56, Figs. 4.2, A.2]

³In [56, Eq. 4.44], the first minus sign is incorrectly missing, while it is present in [93, Eq. 17a]

Relations Between Modes on Circular Ports and Linear Ports

As given in [56, Eqs. 4.48–4.51]

$$\mathbf{U}^{(la)} = [\mathbf{U}^{(-N)} \quad \mathbf{U}^{(-N+1)} \quad \dots \quad \mathbf{U}^{(-1)} \quad \mathbf{U}^{(+1)} \quad \dots \quad \mathbf{U}^{(+N)}] \quad (\text{D.14a})$$

$$U_{o,p}^{(n)} = -\frac{k\pi a_p}{j} \cdot J'_n(ka_p) H_n^{(2)}(k\rho_{op}) \exp(-jn(\phi_{o,p} + \pi)) \quad (\text{D.14b})$$

$$H_{o,p}^{(n)} = \frac{k\eta d}{2} \cdot J_n(ka_p) H_n^{(2)}(k\rho_{op}) \exp(-jn(\phi_{o,p} + \pi)) \quad (\text{D.14c})$$

$$\mathbf{U}^{(al)} = \begin{bmatrix} \mathbf{U}^{(-M)} \\ \mathbf{U}^{(-M+1)} \\ \vdots \\ \mathbf{U}^{(-1)} \\ \mathbf{U}^{(+1)} \\ \vdots \\ \mathbf{U}^{(+M)} \end{bmatrix} \quad (\text{D.15a})$$

$$U_{o,p}^{(m)} = -\frac{k}{2j} \cdot J_m(ka_o) \int_{W_p} \langle \hat{\mathbf{R}}, \hat{\mathbf{n}}' \rangle H_m^{(2)}(k\rho_{o,p}) \exp(-jm\phi_{o,p}) \, ds' \quad (\text{D.15b})$$

$$H_{o,p}^{(m)} = \frac{k\eta d}{2} \cdot J_m(ka_o) \cdot \frac{1}{W_p} \int_{W_p} H_m^{(2)}(k\rho_{o,p}) \exp(-jm\phi_{o,p}) \, ds' \quad (\text{D.15c})$$

For $n = m = 0$ and using (F.6), these equations reduce to the interaction between line ports and the isotropic mode on circular ports given in [92, Eqs. 42c–d], [56, Eqs. 4.19–4.22]⁴.

D.2 Adaptation to Layered Substrates

As can be seen in (D.5), the entries of the matrices \mathbf{U} and \mathbf{H} are functions of the wave number k and the permeability μ . This is because of the assumption that the transverse wave numbers are small in which case (B.67) holds. The required adaptation to layered substrates for (D.5) consists therefore only in the use of the wave number of the layered structure, computed either from the TRM as in Section 4.3.2 or using the approximate formula as in Section 4.3.4. In the remaining entries for matrices \mathbf{U} and \mathbf{H} of Sections D.1.2–D.1.3, the

⁴In [56, Eqs. 4.19–4.22] the arguments of the Hankel functions should read “ $k\rho_{i,j}$ ” and in [56, Eqs. 4.21–4.22] the upper index should be “ pq ” instead of “ qp ”.

formulation uses an impedance η . With the assumption of small transverse wave numbers, as discussed in Section B.5.2, one can use the approximation from (B.67) as

$$\omega\mu = k\eta \quad (\text{D.16})$$

which is also the assumption of the CIM. One can therefore replace the product $k\eta$ by the product $\omega\mu$ in the entries of the \mathbf{H} -matrices or use the effective impedance defined in (B.67). It must be noted that with or without this replacement, the CIM with the proposed adaptation is only valid for cases where the assumption of small transverse wave numbers is correct.

D.3 Radial Waveguide Example for Low Frequencies

As a reference for the expected behavior at low frequencies, example results for the parallel plate impedance for a structure with two ports computed with the radial waveguide method [136, 137] and the corresponding scattering parameters are shown in Fig. D.2. For the scattering parameters which are defined for top and bottom ports, the expansion in (3.1) is used but the near field model is neglected. As can be seen from the linear behavior (in the log-log scale) over most of the frequency range in Fig. D.2a, a simple inductive behavior is obtained. Scattering parameters for crosstalk ($S_{1,2}$ and $S_{1,4}$) in Fig. D.2b likewise show a dominantly linear behavior.

D.4 Practical Application of the CIM

D.4.1 Suggestions for Efficient Implementation

This section presents some suggestions regarding the efficient implementation of the CIM. First, the matrix setup is considered which benefits from parallel computation and from saving re-computations. Secondly, the solution steps is studied which benefits from the use of adapted numerical solvers and from the incorporation of boundary conditions into the solution process.

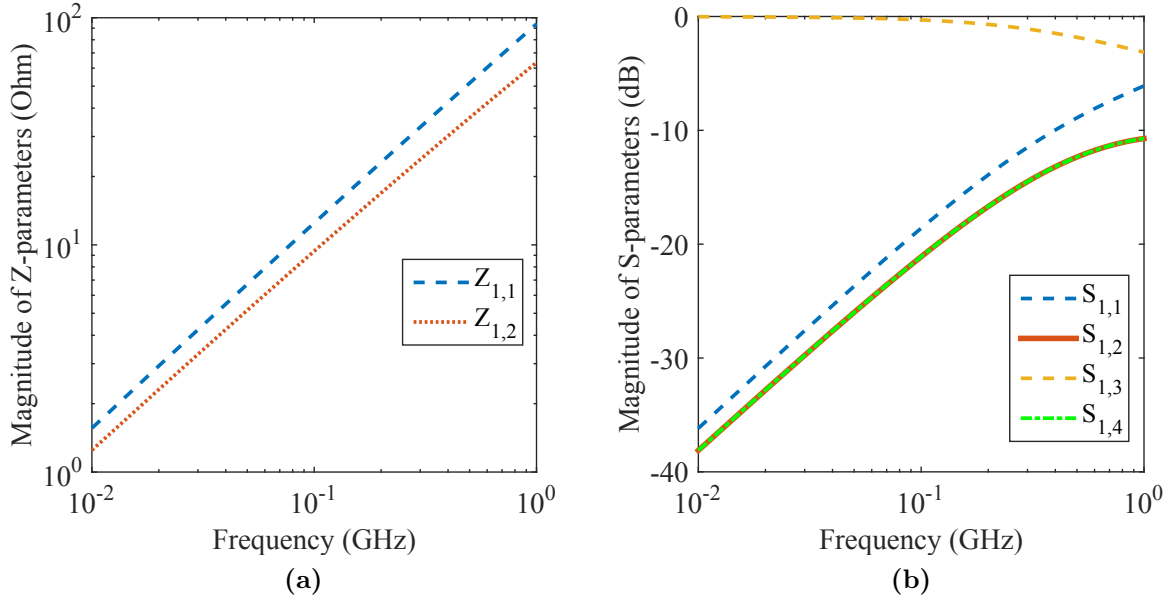


Figure D.2: (a) Parallel plate impedance parameters and (b) corresponding magnitudes of scattering parameters normalized to $50\ \Omega$. The following configuration is used: a relative permeability of 1, a relative permittivity of 11.9, a plate separation of $100\ \mu\text{m}$, a port radius of $20\ \mu\text{m}$, and a port distance of $200\ \mu\text{m}$.

Matrix Setup

For the computation of the matrix entries, the following aspects could be considered. In many cases, the optimizations aim at reducing the number of evaluation of Bessel functions which represents a part that is relatively costly with regard to the numerical complexity.

- Note that for the case for the interaction between linear segments, if these segments stem from a discretization of straight contour lines, $\langle \hat{\mathbf{R}}, \hat{\mathbf{n}}' \rangle$ is zero for many terms and the evaluation of the remainder of terms such as (D.5a) is not necessary.
- It can be seen that the entries of the \mathbf{U} -matrix have expressions with Bessel functions which are the derivative of the corresponding entry of the \mathbf{H} -matrix. Using the relation given in (F.5), only one additional evaluation of a Bessel function is therefore necessary if the \mathbf{U} -matrix entry has already been computed.
- If many or all port radii are equal, the computation of the corresponding Bessel functions which have a product of the wave number with the port radius as their argument should be precomputed.

- The distances ρ_{op} are invariant for an interchange of the indices o and p . The corresponding Bessel functions therefore have to be evaluated only once for each (un-ordered) pair of indices.

Solution Step

- From the structure of the problem one can see that it is possible to directly solve for a single column of the admittance or impedance matrix. In this case, only one column of either the \mathbf{U} -matrix or the \mathbf{H} -matrix needs to be stored in memory. Due to the symmetry of admittance and impedance matrices, this is equal to the solution for a single row with the same index.
- As mentioned in [56, Sec. 7], solvers that are adapted to the structure of the equation could be used. In regular via arrays there can be many symmetries, i.e., many distances and angles can be equal and the involved matrices then have a Toeplitz form.
- As discussed in Section 6.1, the boundary conditions can be incorporated into the solution steps to save both memory and computation time.

D.4.2 Principal Steps of the CIM Application

In the following, the principal steps of the practical application of the CIM are summarized:

- If present, arbitrarily shaped contours are discretized into linear segments. A sufficiently fine discretization that leads to a desired accuracy will in general be frequency-dependent as the tangential electric and magnetic fields are assumed to be constant on each segment. With the analytical formulations presented in this chapter the discretization of inner circular ports is not required.
- The accuracy is also influenced by the type of numerical integration that is used. The mid-point rule is the most simple integration that can be chosen and leads to a good accuracy in most cases [56, p. 24].
- If circular ports are used, the number of modes to use on each circular contour has to be chosen. A sufficiently large number will in general be frequency-dependent. The

relevance of the higher order anisotropic modes increases with narrow spacings of circular contours and with small distances to the linear segments.

- The matrices \mathbf{U} and \mathbf{H} are set up that constitute linear systems of equations.
- The effective solution step is carried out by computing the impedance or admittance parameters using, e.g., (D.2a), (D.2b), or (6.3).
- In subsequent steps, boundary conditions can be applied on further ports which are not connected to other network by applying the appropriate terminating impedances.
- Voltage and current excitations can be used to compute the voltages or currents on all ports. Using the relations from [56, Eq. 3.23], the fields can be computed for any point inside the 2D circuit.

Appendix E

Derivations for Multiconductor Transmission Line Models

E.1 Two-Conductor Transmission Lines

E.1.1 Network Parameters

The general frequency domain solution for a two-conductor transmission line section which extends along the x -coordinate in terms of voltages and currents of the forward and backward propagation waves, both with a wave number k_x , is given by

$$V(x) = V^{(+)}e^{-jk_x x} + V^{(-)}e^{jk_x x}, \quad (\text{E.1})$$

$$I(x) = \frac{V^{(+)}}{Z_0}e^{-jk_x x} - \frac{V^{(-)}}{Z_0}e^{jk_x x}, \quad (\text{E.2})$$

where upper indices (+) and (−) refer to the forward and backward propagation wave, respectively, and Z_0 is the characteristic impedance of the transmission line. The impedance matrix for a transmission line segment of length l and a wave number of propagation along the x -direction k_x is then given by

$$\begin{pmatrix} V_1 \\ V_2 \end{pmatrix} = Z_0 \underbrace{\begin{pmatrix} \coth(jk_x l) & 1/\sinh(jk_x l) \\ 1/\sinh(jk_x l) & \coth(jk_x l) \end{pmatrix}}_{Z^{(\text{tl})}} \begin{pmatrix} I_1 \\ I_2 \end{pmatrix} \quad (\text{E.3})$$

and the admittance matrix is given by

$$\begin{pmatrix} I_1 \\ I_2 \end{pmatrix} = \frac{1}{Z_0} \underbrace{\begin{pmatrix} \coth(jk_x l) & -1/\sinh(jk_x l) \\ -1/\sinh(jk_x l) & \coth(jk_x l) \end{pmatrix}}_{Y^{(\text{tl})}} \begin{pmatrix} V_1 \\ V_2 \end{pmatrix} \quad (\text{E.4})$$

E.1.2 Determination of Wave Number From Network Parameters

Direct Method

From the two-port network parameters of a uniform transmission line section, one can obtain expressions which are only functions of its geometrical length and the guided wave number. For impedance and admittance parameters, these are for example given by

$$\frac{Y_{1,1}^{(\text{tl})}}{Y_{1,2}^{(\text{tl})}} = -\frac{Z_{1,1}^{(\text{tl})}}{Z_{1,2}^{(\text{tl})}} = \coth(jk_x l) \sinh(jk_x l) = \cosh(jk_x l) \quad (\text{E.5})$$

The phase- and attenuation-information of the guided wave number is contained in

$$\text{arcosh}\left(\frac{Y_{1,1}^{(\text{tl})}}{Y_{1,2}^{(\text{tl})}}\right) = \text{arcosh}\left(-\frac{Z_{1,1}^{(\text{tl})}}{Z_{1,2}^{(\text{tl})}}\right) = jk_x l = j(\beta - j\alpha)l \stackrel{\text{def.}}{=} j\theta + \alpha l \quad (\text{E.6})$$

where θ is the phase difference as determined from the two-port parameters. The above entries of the admittance and impedance matrices are in general complex. The periodicity of the fields in space is reflected in the periodicity of the hyperbolic functions and equivalent representations based on trigonometric functions. The former are periodic with respect to the imaginary part of their argument, the latter with respect to the real part. In all cases the true phase difference θ_{true} between the fields at the two ports is mapped to an interval of size 2π or smaller. The true phase difference θ_{true} is sometimes also referred to as the electrical length of a structure. As an example, the branch cut of the inverse hyperbolic cosine function arcosh^{-1} is usually chosen along the negative real axis. The phases are therefore mapped to the interval $(-\pi, +\pi)$ whereas the true phase is

$$\theta_{\text{true}} = \theta + n \cdot 2\pi \quad (n \in \mathbb{Z}) \quad (\text{E.7})$$

with the unknown integer n . In the most general case, i.e. if no assumptions about the structure can be made, the actual phase cannot be determined. In practical cases though, one can usually assume that the structure is electrically short at low frequencies. For decreasing frequency the phase constant β and the phases θ_{true} hence approach 0. If the phase constant also increases monotonically with frequency, the correct phase can be computed by a method often referred to as unwrapping. Even if the monotonicity exists theoretically for the investigated structures, simulation inaccuracies sometimes lead to phase fluctuations that break the monotonicity and thereby complicate the phase unwrapping. Because of the discussed difficulties, the following approaches can be favorable.

Using De-Embedding with Identical Line Properties

The network parameters of a short waveguide section can be obtained by simulation of at least two waveguides which differ by a length that is known (or estimated) to be electrically shorter than the phase value at which the wrap-around occurs. This is achieved through a de-embedding step with the two network parameter sets. The most general de-embedding in the sense that all coupling terms are included can be found as de-segmentation for Z-matrices in [95, 138] and for S-parameters in [139]. A summary of these techniques is given in [140, Ch. 3]. After computing the network parameters of the de-embedded transmission line segment (E.6) can be used without unwrapping of the phase.

Using De-Embedding with Differing Line Properties

More general methods can be found in the literature which are based on theory from multi-line calibration techniques. E.g., in [141], a method for determination of the propagation constant using two (uncalibrated) measurements of two waveguides is presented. The method is based on the extraction of the matrix of a de-embedded waveguide segment of which the eigenvalues can be related to the propagation constant.

E.2 Internal Impedance of Circular Cylindrical Conductors

E.2.1 Exact Solution for Single Circular Cylindrical Conductor

For a circular cylindrical conductor of radius r , the per-unit-length internal impedance given in [98, Eq. 3.196] can be written as

$$\hat{z}_{\text{int}} = \frac{j}{\sqrt{2\pi r \sigma \delta_s}} \frac{\text{ber}(q) + j \text{bei}(q)}{\text{ber}'(q) + j \text{bei}'(q)} \quad (\text{E.8})$$

where $\text{ber}(x)$ and $\text{bei}(x)$ are the real and imaginary part, respectively, of the Bessel function of the first kind of a complex argument [98, p. 165]. The prime denotes the derivative with respect to the complete argument and $q = \sqrt{2}r/\delta_s$. The skin depth is given by

$$\delta_s = \sqrt{\frac{2}{\omega \sigma \mu}} = \frac{1}{\sqrt{\pi f \sigma \mu}} \quad (\text{E.9})$$

Using the relations

$$\text{ber}(x) + j \text{bei}(x) = I_0(\sqrt{j}x), \quad (\text{E.10a})$$

$$\frac{d(\text{ber}(x) + j \text{bei}(x))}{dx} = \frac{dI_0(\sqrt{j}x)}{dx}, \quad (\text{E.10b})$$

$$\text{ber}'(x) + j \text{bei}'(x) = \sqrt{j}I_1(\sqrt{j}x),$$

where I_0 and I_1 are the modified Bessel functions of the first kind and order 0 and 1, respectively, the impedance in (E.8) can be rewritten as

$$\begin{aligned} \hat{z}_{\text{int}} &= \frac{j}{\sqrt{2\pi r \sigma \delta_s}} \frac{I_0(\sqrt{j}\sqrt{2r}/\delta_s)}{\sqrt{j}I_1(\sqrt{j}\sqrt{2r}/\delta_s)} = \frac{\sqrt{j}}{\sqrt{2\pi r \sigma}} \sqrt{\frac{\omega \sigma \mu}{2}} \frac{I_0(\sqrt{j}\sqrt{2r}\sqrt{\omega \sigma \mu/2})}{I_1(\sqrt{j}\sqrt{2r}\sqrt{\omega \sigma \mu/2})} \\ &= \frac{\sqrt{j\omega \mu/\sigma}}{2\pi r} \frac{I_0(r\sqrt{j\omega \sigma \mu})}{I_1(r\sqrt{j\omega \sigma \mu})}. \end{aligned} \quad (\text{E.11})$$

The latter formulation is used in [39, Eq. 11] and in [142, Eq. 9]¹.

E.2.2 Approximate Solutions for Single Circular Cylindrical Conductor

As discussed in [98, Sec. 3.6.2.2], there is a transition region from weak to strong skin effect occurring around $r = \delta_s$. The following approximations lead to a high accuracy only far away from this transition region. The per-unit-length resistance and inductance can be given as [98, Eq. 3.202]

$$r = \begin{cases} \frac{1}{\sigma \pi r^2} & (r < 2\delta_s), \\ \frac{1}{2\pi r \sigma \delta_s} & (r > 2\delta_s), \end{cases} \quad (\text{E.12a})$$

$$l_{\text{int}} = \begin{cases} \frac{\mu_0}{8\pi} & (r < 2\delta_s), \\ \frac{\mu}{4\pi r \delta_s} & (r > 2\delta_s). \end{cases} \quad (\text{E.12b})$$

¹with two presumably typographical errors

E.2.3 Incorporation of Internal Parts Into Resistivity and Inductance Matrices

The overall inductance is given by [98, Eq. 3.13]

$$\mathbf{L} = r_0 \begin{pmatrix} l_{11} & l_{12} & \cdots & l_{1n} \\ l_{21} & l_{22} & \cdots & l_{2n} \\ \vdots & \vdots & \ddots & \vdots \\ l_{n1} & l_{n2} & \cdots & l_{nn} \end{pmatrix} + \begin{pmatrix} l_{\text{int},1} & 0 & \cdots & 0 \\ 0 & l_{\text{int},2} & \cdots & 0 \\ \vdots & \vdots & \ddots & \vdots \\ 0 & 0 & \cdots & l_{\text{int},n} \end{pmatrix} \quad (\text{E.13})$$

The overall resistance matrix is given by

$$\mathbf{R} = r_0 \underbrace{\begin{pmatrix} 1 & 1 & \cdots & 1 \\ 1 & 1 & \cdots & 1 \\ \vdots & \vdots & \ddots & \vdots \\ 1 & 1 & \cdots & 1 \end{pmatrix}}_{\mathbf{J}_n} + \begin{pmatrix} r_1 & 0 & \cdots & 0 \\ 0 & r_2 & \cdots & 0 \\ \vdots & \vdots & \ddots & \vdots \\ 0 & 0 & \cdots & r_n \end{pmatrix}, \quad (\text{E.14})$$

where r_0 is the internal resistance of the reference conductor and r_i is the internal resistance of the i th conductor.

If all internal resistances are equal, i.e. if $r = r_0 = r_1 = r_2 = \cdots = r_n$, then (E.14) reduces to

$$\mathbf{R} = r(\mathbf{J}_n + \mathbf{1}_n). \quad (\text{E.15})$$

E.3 Complex Analytical Capacitance and Effective Permittivity of Two Circular TSVs

This case is approximated using the exact solution for the symmetric case of two circular conductors of equal radius in a homogeneous medium and the exact solution for the coaxial capacitor. A separation as wide as in the wide separation approximation is not required because the non-uniformity of charge along the conductor and dielectric interface circumferences is better approximated. It represents a good approximation if the oxide layers are thin and if the dielectric contrast of the involved materials is not too large. The per-unit-length capacitance is given by

$$C'_{\text{total}} = \left(\frac{2}{C_{\text{ox}}} + \frac{1}{C_{\text{si}}} \right)^{-1} = \frac{\pi \varepsilon_{\text{eff}}}{\cosh^{-1} \left(\frac{d}{2a_i} \right)} = \left(\frac{\cosh^{-1} \left(\frac{d}{2a_o} \right)}{\pi \varepsilon_{\text{si}}} + 2 \frac{\ln \left(\frac{a_o}{a_i} \right)}{2\pi \varepsilon_{\text{ox}}} \right)^{-1}. \quad (\text{E.16})$$

The effective permittivity is then given by

$$\underline{\varepsilon}_{\text{eff}} = \frac{\cosh^{-1}\left(\frac{d}{2a_i}\right)}{\cosh^{-1}\left(\frac{d}{2a_o}\right)/\underline{\varepsilon}_{\text{si}} + \ln\left(\frac{a_o}{a_i}\right)/\varepsilon_{\text{ox}}}. \quad (\text{E.17})$$

Using $\cosh^{-1}(x) = \ln(x + \sqrt{x^2 - 1})$ this can after a few manipulations also be written in the form given in [24]

$$\underline{\varepsilon}_{\text{eff}} = \frac{\cosh^{-1}\left(\frac{d}{2a_i}\right)}{\ln\left(\frac{d/2 + \sqrt{(d/2)^2 - a_o^2}}{a_i}\right) + \frac{\underline{\varepsilon}_{\text{si}} - \varepsilon_{\text{ox}}}{\varepsilon_{\text{ox}}} \ln\left(\frac{a_o}{a_i}\right)}. \quad (\text{E.18})$$

E.4 Exact Capacitance for Two Circular Conductors in Homogeneous Medium

The exact analytical solution for the per-unit-length capacitance of two cylindrical conductors of circular cross-section in homogeneous medium can serve as a reference for the methods described in the previous section. As derived in [98, Eq. 3.48]

$$c = \frac{\pi \varepsilon}{\cosh^{-1}\left(\frac{s^2 - r_{w1}^2 - r_{w2}^2}{2r_{w1}r_{w2}}\right)}, \quad (\text{E.19})$$

where ε is the permittivity of the infinitely extending medium in which the conductors are embedeed, s is the center-to-center distance of the conductors (distance between the axes), and r_{w1} and r_{w2} are their radii. Further, \cosh^{-1} is the inverse hyperbolic cosine that can also be expressed with the natural logarithm as [98, Eq. 3.47]

$$\cosh^{-1} x = \ln\left(x + \sqrt{x^2 - 1}\right). \quad (\text{E.20})$$

E.5 Fourier Method for Exact Capacitance Calculation

The following sections (E.5.1–E.5.3) present a Fourier method developed by Xioamin Duan (received through personal communication during the year 2015) based on previous work for the modeling of the DC-resistance of printed circuit board power planes published in [143]. In the subsequent section (E.5.5), some further derivations by the author of this thesis concerning this method are provided.

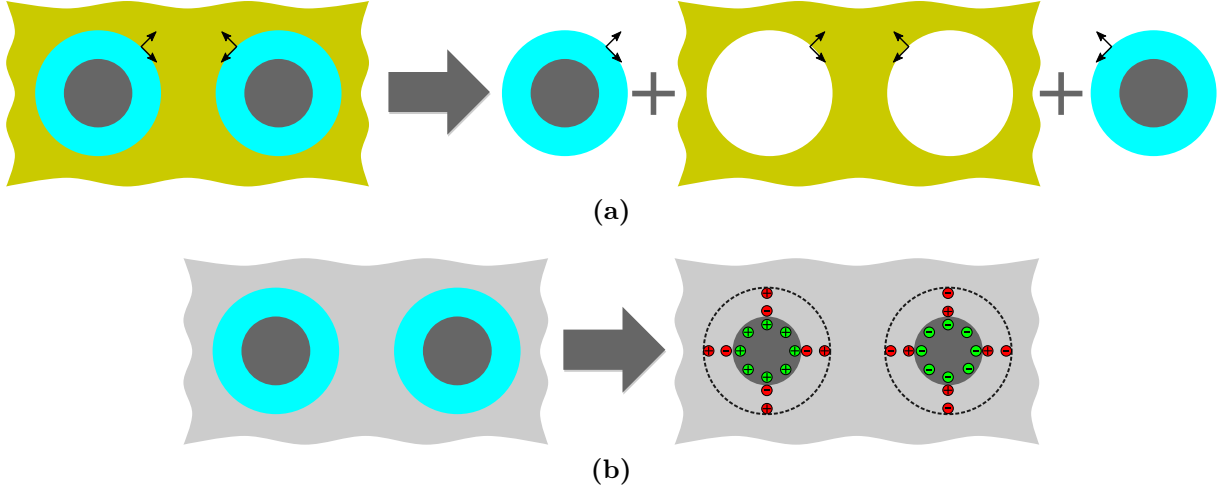


Figure E.1: Illustrations for the comparison of two approaches for modeling the inhomogeneous substrates: (a) Domain decomposition approach in which homogeneous regions are computed individually and related by enforcing continuity of tangential field components. (b) Equivalent surface charge approach in which the dielectric is replaced with an equivalent configuration in a homogeneous medium with bound surface charges at the positions of the original dielectric interfaces and at the interfaces between dielectrics and conductors. The distributed surfaces charges are illustrated as discrete charges in red and green.

The presented method uses a decomposition of the inhomogeneous substrate material domain into homogeneous subdomains. An alternative approach would be the use of equivalent surface charges, which is, e.g., used in [98, Sec. 3.2.4.1]. Both perspectives and approaches are illustrated and shortly discussed in Fig. E.1.

E.5.1 Basic Formulation of the Quasi-Static Analysis

In absence of charges in a closed 2D-region, the contour integral from [144, Eq. 8.7] reduces to [143, Eq. 1]

$$\varphi(\mathbf{r}) = \frac{1}{\pi} \oint_C \left[\frac{\partial \ln |\mathbf{r} - \mathbf{r}'|}{\partial \hat{\mathbf{n}}} \varphi(\mathbf{r}') - \ln |\mathbf{r} - \mathbf{r}'| \frac{\partial \varphi(\mathbf{r}')}{\partial \hat{\mathbf{n}}} \right] ds' \quad (\text{E.21})$$

The integral gives the electric potential φ at any location \mathbf{r} as a function of the potential of all locations on all contours. The normal vectors on the contour point towards the centers of the respective circular contour on which the normal vector is evaluated.

The following relation can be applied analogously to [143, Eq. 2] by using (F.2):

$$\frac{\partial \varphi(\mathbf{r}')}{\partial \hat{\mathbf{n}}} \stackrel{(\text{F.2})}{=} \langle \nabla \varphi(\mathbf{r}'), \hat{\mathbf{n}} \rangle = \langle -\nabla \mathbf{E}(\mathbf{r}'), \hat{\mathbf{n}} \rangle = \frac{\langle -\nabla \mathbf{D}(\mathbf{r}'), \hat{\mathbf{n}} \rangle}{\varepsilon} = \frac{\lambda(\mathbf{r}')}{\varepsilon}. \quad (\text{E.22})$$

The last identity is due to the direction of the normal vector described before. Here, $\lambda(\mathbf{r}')$ is the surface charge density at location \mathbf{r}' and ε is the permittivity in the considered (homogeneous) region. As given in [143, Eq. 3]

$$\frac{\partial \ln |\mathbf{r} - \mathbf{r}'|}{\partial \hat{\mathbf{n}}} = \frac{\partial \ln |\mathbf{r} - \mathbf{r}'|}{\partial |\mathbf{r} - \mathbf{r}'|} \cdot \frac{\partial |\mathbf{r} - \mathbf{r}'|}{\partial \hat{\mathbf{n}}} \stackrel{(F.2)}{=} \frac{1}{|\mathbf{r} - \mathbf{r}'|} \cdot \langle \nabla |\mathbf{r} - \mathbf{r}'|, \hat{\mathbf{n}} \rangle = \frac{\langle \hat{\boldsymbol{\rho}}, \hat{\mathbf{n}} \rangle}{|\mathbf{r} - \mathbf{r}'|}, \quad (\text{E.23})$$

where $\hat{\boldsymbol{\rho}}$ is the normalized vector from the location of the observation point to the source point, i.e. from the location at \mathbf{r} to \mathbf{r}' . By inserting (E.22) and (E.23) into (E.21), one obtains analogously to [143, Eq. 4]

$$\varphi(\mathbf{r}) = \frac{1}{\pi} \oint_C \left[\frac{\langle \hat{\boldsymbol{\rho}}, \hat{\mathbf{n}} \rangle}{|\mathbf{r} - \mathbf{r}'|} \varphi(\mathbf{r}') - \ln |\mathbf{r} - \mathbf{r}'| \frac{\lambda(\mathbf{r}')}{\varepsilon} \right] ds'. \quad (\text{E.24})$$

Based on (E.24), a contour integral with cylindrical expansion is presented in [143]. The entries of the linear system of equations for this method can be used after replacement of every occurrence of the product κd by the complex permittivity ε . The results of this replacement step are given in Tables E.1 and E.2 with the used coefficient tabulated in Table E.3.

E.5.2 Solution Inside the Silicon Region

In the silicon region, the potentials and surface charge densities are related as

$$\begin{pmatrix} U_{11} & U_{12} \\ U_{21} & U_{22} \end{pmatrix} \begin{pmatrix} \varphi_{\text{si}}^0 \\ \varphi_{\text{si}}^m \end{pmatrix} = \begin{pmatrix} H_{11} & H_{12} \\ H_{21} & H_{22} \end{pmatrix} \begin{pmatrix} \sigma_{\text{si}}^0 \\ \sigma_{\text{si}}^m \end{pmatrix}, \quad (\text{E.25})$$

where upper index 0 corresponds to the fundamental and isotropic mode of the Fourier expansion, and the upper index m corresponds to the vector of anisotropic modes with their even and odd parts. The expansion can be performed either in terms of exponential or trigonometric functions. Both are in general complex and both permit a representation of complex charge distributions which is required to compute capacitance and conductivity as real and imaginary parts, respectively, of a complex capacitance.

Table E.1: Matrix entries for \mathbf{U}_{pp} from [143]. Definition and reference values for b_{mn} are given in table E.3. Further, $s_n(\phi_{ij}) = \sin(n\phi_{ij})$ and $c_n(\phi_{ij}) = \cos(n\phi_{ij})$.

		$n=0$	n , even part	n , odd part
$m=0$	$i = j$	1	0	0
	$i \neq j$	0	$-(a_j/\rho_{ij})^n c_n(\phi_{ij})$	$-(a_j/\rho_{ij})^n s_n(\phi_{ij})$
m , even part	$i = j$	0	δ_{mn}	0
	$i \neq j$	0	$-\frac{(-a_i)^m a_j^n b_{mn} c_{m+n}(\phi_{ij})}{\rho_{ij}^{m+n}}$	$-\frac{(-a_i)^m a_j^n b_{mn} s_{m+n}(\phi_{ij})}{\rho_{ij}^{m+n}}$
m , odd part	$i = j$	0	0	δ_{mn}
	$i \neq j$	0	$-\frac{(-a_i)^m a_j^n b_{mn} s_{m+n}(\phi_{ij})}{\rho_{ij}^{m+n}}$	$\frac{(-a_i)^m a_j^n b_{mn} c_{m+n}(\phi_{ij})}{\rho_{ij}^{m+n}}$

Table E.2: Matrix entries for \mathbf{H}_{pp} from [143] after replacement $\kappa d \rightarrow \varepsilon$. Definition and reference values for b_{mn} are given in table E.3. Further, $s_n(\phi_{ij}) = \sin(n\phi_{ij})$ and $c_n(\phi_{ij}) = \cos(n\phi_{ij})$.

		$n=0$	n , even part	n , odd part
$m=0$	$i = j$	$-\frac{\ln a_i}{2\pi\varepsilon} = -\frac{\ln a_j}{2\pi\varepsilon}$	0	0
	$i \neq j$	$-\frac{\ln \rho_{ij}}{2\pi\varepsilon}$	$\left(\frac{a_j}{\rho_{ij}}\right)^n \cdot \frac{c_n(\phi_{ij})}{2n\pi\varepsilon}$	$\left(\frac{a_j}{\rho_{ij}}\right)^n \cdot \frac{s_n(\phi_{ij})}{2n\pi\varepsilon}$
m , even part	$i = j$	0	$\frac{\delta_{mn}}{2m\pi\varepsilon}$	0
	$i \neq j$	$\left(\frac{-a_i}{\rho_{ij}}\right)^m \cdot \frac{c_m(\phi_{ij})}{2m\pi\varepsilon} \dagger^1$	$\frac{(-a_i)^m a_j^n b_{mn} c_{m+n}(\phi_{ij})}{\rho_{ij}^{m+n} 2n\pi\varepsilon}$	$\frac{(-a_i)^m a_j^n b_{mn} s_{m+n}(\phi_{ij})}{\rho_{ij}^{m+n} 2n\pi\varepsilon}$
m , odd part	$i = j$	0	0	$\frac{\delta_{mn}}{2m\pi\varepsilon}$
	$i \neq j$	$\left(\frac{-a_i}{\rho_{ij}}\right)^m \cdot \frac{s_m(\phi_{ij})}{2m\pi\varepsilon} \dagger^1$	$\frac{(-a_i)^m a_j^n b_{mn} s_{m+n}(\phi_{ij})}{\rho_{ij}^{m+n} 2n\pi\varepsilon} \dagger^2$	$-\frac{(-a_i)^m a_j^n b_{mn} c_{m+n}(\phi_{ij})}{\rho_{ij}^{m+n} 2n\pi\varepsilon}$

^{†1}In [143, Table II], c_m and s_m are erroneously typeset as c_n and s_n , respectively, in these formulas.

^{†2}In [143, Table II], the κ to replace is erroneously typeset as k in this formula.

Multipole Expansion in the Oxide Areas

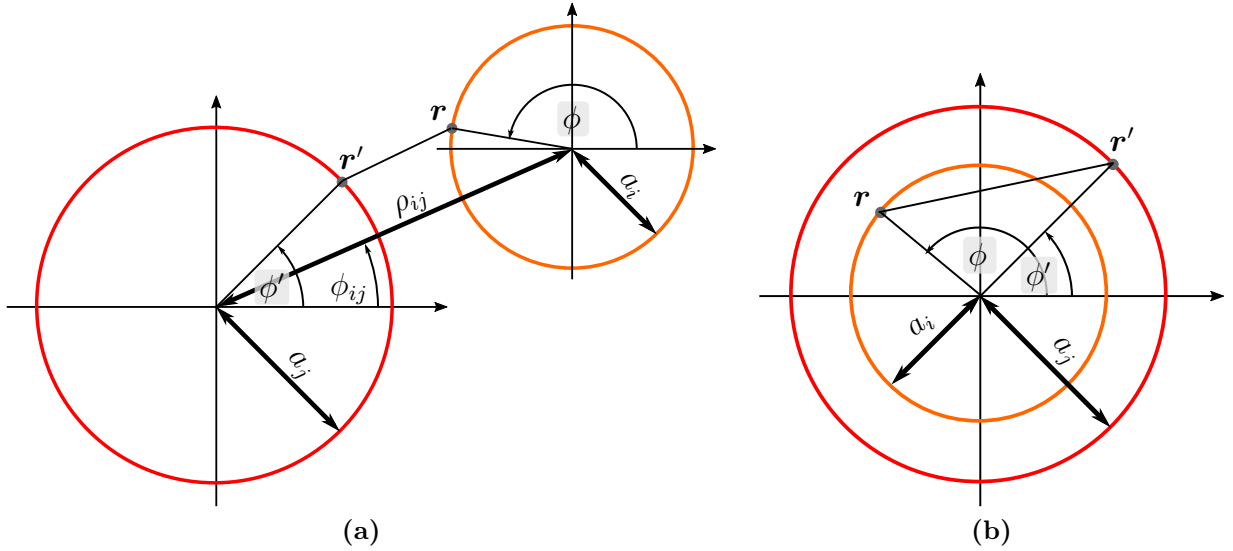
The integral equation is given by

$$\begin{aligned}
 \varphi(\mathbf{r}) &= \frac{1}{\pi} \sum_{j=1,2} \oint_{C_j} \frac{\partial \ln |\mathbf{r} - \mathbf{r}'|}{\mathbf{n}} \varphi(\mathbf{r}') d\mathbf{s}' - \frac{1}{\pi\varepsilon} \sum_{j=1,2} \oint_{C_j} \ln |\mathbf{r} - \mathbf{r}'| \lambda(\mathbf{r}') d\mathbf{s}' \\
 &= \frac{1}{\pi} \sum_{j=1,2} \int_0^{2\pi} \frac{\partial \ln |\mathbf{r} - \mathbf{r}'|}{\mathbf{n}} \varphi(\mathbf{r}') a_j d\phi - \frac{1}{\pi\varepsilon} \sum_{j=1,2} \int_0^{2\pi} \ln |\mathbf{r} - \mathbf{r}'| \lambda(\mathbf{r}') a_j d\phi
 \end{aligned} \tag{E.26}$$

Table E.3: Table with values for b_{mn} for $m \leq 5$ and $n \leq 5$ used in Tables E.1 and E.2

	n=1	n=2	n=3	n=4	n=5
m=1	1	2	3	4	5
m=2	1	3	6	10	15
m=3	1	4	10	20	35
m=4	1	5	15	35	70
m=5	1	6	21	56	126

Based on the recursive formula from [143, Table II]:
 $b_{mn} = \frac{1}{m} \sum_{k=1}^m (kn - m + k) b_{(m-k)n}$ with $b_{0n} = 1$


Figure E.2: Geometry definitions for the used multipole expansions. (a) General case (b) Concentric case.

The Fourier coefficients of the expansion are defined as

$$\varphi(\mathbf{r}') = \sum_{n=-\infty}^{+\infty} \tilde{\varphi}_n e^{jn\phi} \quad (\text{E.27a})$$

$$\tilde{\varphi}_n = \frac{1}{2\pi} \int_0^{2\pi} \varphi(\mathbf{r}') e^{-jn\phi} d\phi \quad (\text{E.27b})$$

for the potential and for the surface charge density λ and the per-unit-length surface charge

density σ (with a radius a of the respective circular contour) as

$$\lambda_i(\mathbf{r}') = \sum_{n=-\infty}^{+\infty} \tilde{\lambda}_{n,i} e^{jn\phi} \quad (\text{E.28a})$$

$$\tilde{\lambda}_{n,i} = \frac{1}{2\pi} \int_0^{2\pi} \lambda_i(\mathbf{r}') e^{-jn\phi} d\phi \quad (\text{E.28b})$$

$$\tilde{\sigma}_{n,i} = 2\pi a_i \tilde{\lambda}_{n,i} \quad (\text{E.28c})$$

Multipole expansions are used to split up the functional dependence into parts of products some of which only depend on the distances and some of which only depend on the relative angles. Again, (E.24) holds and the following multipole expansions for the cases where $|\mathbf{r}| < |\mathbf{r}'|$ or $|\mathbf{r}| = |\mathbf{r}'|$ are applied

$$\ln |\mathbf{r} - \mathbf{r}'| = \ln |\mathbf{r}'| - \sum_{n \in A} \frac{1}{2|n|} e^{jn(\phi' - \phi)} \quad (|\mathbf{r}| = |\mathbf{r}'|) \quad (\text{E.29a})$$

$$\frac{\partial \ln |\mathbf{r} - \mathbf{r}'|}{\partial \mathbf{n}} = -\frac{1}{2|\mathbf{r}'|} \quad (|\mathbf{r}| = |\mathbf{r}'|) \quad (\text{E.29b})$$

$$\ln |\mathbf{r} - \mathbf{r}'| = \ln |\mathbf{r}'| - \sum_{n \in A} \frac{1}{2|n|} \left(\frac{|\mathbf{r}|}{|\mathbf{r}'|} \right)^{|n|} e^{jn(\phi - \phi')} \quad (|\mathbf{r}| < |\mathbf{r}'|) \quad (\text{E.29c})$$

$$\frac{\partial \ln |\mathbf{r} - \mathbf{r}'|}{\partial \mathbf{n}} = \frac{1}{|\mathbf{r}'|} + \frac{1}{|\mathbf{r}'|} \sum_{n \in A} \frac{1}{2} \left(\frac{|\mathbf{r}|}{|\mathbf{r}'|} \right)^{|n|} e^{jn(\phi - \phi')} \quad (|\mathbf{r}| < |\mathbf{r}'|) \quad (\text{E.29d})$$

where the sums are performed over the set A of integer indices defined as $A = \mathbb{Z} \setminus \{0\} = \{-\infty, \dots, -1, 1, \dots, \infty\}$. Using (E.29a) through (E.29d) with (E.26), the integral equation for the inner contour can be given as a function of the expansion coefficients for potential and charge at the radii a_1 and a_2 as

$$\begin{aligned} \varphi_1(\mathbf{r}) = & -\frac{1}{\pi} \int_0^{2\pi} \left(\frac{1}{2a_1} \right) e^{-jn\phi} \varphi_1(\mathbf{r}) a_1 d\phi \\ & + \frac{1}{\pi} \int_0^{2\pi} \left(\frac{1}{a_2} + \frac{1}{a_2} \sum_{n \in A} \frac{1}{2} \left(\frac{a_1}{a_2} \right)^{|n|} e^{-jn\phi'} e^{-jn\phi} \right) \varphi_2(\mathbf{r}) a_2 d\phi \\ & - \frac{1}{\varepsilon\pi} \int_0^{2\pi} \left(\ln a_1 - \sum_{n \in A} \frac{1}{2|n|} e^{jn\phi'} e^{-jn\phi} \right) \lambda_1(\mathbf{r}) a_1 d\phi \\ & - \frac{1}{\varepsilon\pi} \int_0^{2\pi} \left(\ln a_2 - \sum_{n \in A} \frac{1}{2|n|} \left(\frac{a_1}{a_2} \right)^{|n|} e^{jn\phi'} e^{-jn\phi} \right) \lambda_2(\mathbf{r}) a_2 d\phi \end{aligned} \quad (\text{E.30})$$

Using now the the definitions of the Fourier coefficient in (E.27) and (E.28), and their

orthogonality, one obtains

$$\begin{aligned}\varphi_1(\mathbf{r}) = & -\tilde{\varphi}_{1,0} + 2\tilde{\varphi}_{2,0} + \sum_{n \in A} \left(\frac{a_1}{a_2}\right)^{|n|} e^{-jn\phi} \tilde{\varphi}_{2,n} \\ & - \frac{1}{\varepsilon\pi} \ln a_1 \tilde{\sigma}_{1,0} + \frac{1}{\varepsilon\pi} \sum_{n \in A} \frac{1}{2|n|} e^{-jn\phi} \tilde{\sigma}_{1,n} \\ & - \frac{1}{\varepsilon\pi} \ln a_2 \tilde{\sigma}_{2,0} + \frac{1}{\varepsilon\pi} \sum_{n \in A} \frac{1}{2|n|} \left(\frac{a_1}{a_2}\right)^{|n|} e^{-jn\phi} \tilde{\sigma}_{2,n}\end{aligned}\quad (\text{E.31})$$

Application of the testing function leads to a system of equations which is decoupled with respect to the mode order. These equations are given as

$$\tilde{\varphi}_{1,0} = -\tilde{\varphi}_{1,0} + 2\tilde{\varphi}_{2,0} - \frac{1}{\varepsilon\pi} \ln a_1 \tilde{\sigma}_{1,0} - \frac{1}{\varepsilon\pi} \ln a_2 \tilde{\sigma}_{2,0} \quad (n = 0) \quad (\text{E.32})$$

$$\tilde{\varphi}_{1,n} = \left(\frac{a_1}{a_2}\right)^{|n|} \tilde{\varphi}_{2,n} + \frac{1}{\varepsilon\pi} \frac{1}{2|n|} \tilde{\sigma}_{1,n} + \frac{1}{\varepsilon\pi} \frac{1}{2|n|} \left(\frac{a_1}{a_2}\right)^{|n|} \tilde{\sigma}_{2,n} \quad (n \neq 0) \quad (\text{E.33})$$

Analogously, for the outer contour the following two expansion are used

$$\ln |\mathbf{r} - \mathbf{r}'| = \ln |\mathbf{r}| - \sum_{n \in A} \frac{1}{2|n|} \left(\frac{|\mathbf{r}'|}{|\mathbf{r}|}\right)^{|n|} e^{jn(\phi' - \phi)} \quad (|\mathbf{r}| > |\mathbf{r}'|) \quad (\text{E.34a})$$

$$\frac{\partial \ln |\mathbf{r} - \mathbf{r}'|}{\partial \mathbf{n}} = \frac{1}{|\mathbf{r}'|} \sum_{n \in A} \frac{1}{2} \left(\frac{|\mathbf{r}'|}{|\mathbf{r}|}\right)^{|n|} e^{jn(\phi' - \phi)} \quad (|\mathbf{r}| > |\mathbf{r}'|) \quad (\text{E.34b})$$

Using (E.29a), (E.29b), (E.34a), and (E.34b) with (E.26) one finds for the outer contour

$$\begin{aligned}\varphi_2(\mathbf{r}) = & -\frac{1}{\pi} \int_0^{2\pi} \left(\frac{1}{2a_2}\right) e^{-jn\phi} \varphi_2(\mathbf{r}) a_2 d\phi \\ & + \frac{1}{\pi} \int_0^{2\pi} \frac{1}{a_1} \sum_{n \in A} \frac{1}{2} \left(\frac{a_1}{a_2}\right)^{|n|} e^{-jn\phi'} e^{-jn\phi} \varphi_1(\mathbf{r}) a_1 d\phi \\ & - \frac{1}{\varepsilon\pi} \int_0^{2\pi} \left(\ln a_2 - \sum_{n \in A} \frac{1}{2|n|} e^{jn\phi'} e^{-jn\phi} \right) \lambda_2(\mathbf{r}) a_2 d\phi \\ & - \frac{1}{\varepsilon\pi} \int_0^{2\pi} \left(\ln a_2 - \sum_{n \in A} \frac{1}{2|n|} \left(\frac{a_1}{a_2}\right)^{|n|} e^{jn\phi'} e^{-jn\phi} \right) \lambda_1(\mathbf{r}) a_1 d\phi\end{aligned}\quad (\text{E.35})$$

and

$$\begin{aligned}
 \varphi_2(\mathbf{r}) = & -\tilde{\varphi}_{2,0} + \sum_{n \in A} \left(\frac{a_1}{a_2} \right)^{|n|} e^{-jn\phi} \tilde{\varphi}_{1,n} \\
 & - \frac{1}{\varepsilon\pi} \ln a_2 \tilde{\sigma}_{2,0} + \frac{1}{\varepsilon\pi} \sum_{n \in A} \frac{1}{2|n|} e^{-jn\phi} \tilde{\sigma}_{2,n} \\
 & - \frac{1}{\varepsilon\pi} \ln a_2 \tilde{\sigma}_{1,0} + \frac{1}{\varepsilon\pi} \sum_{n \in A} \frac{1}{2|n|} \left(\frac{a_1}{a_2} \right)^{|n|} e^{-jn\phi} \tilde{\sigma}_{1,n}
 \end{aligned} \tag{E.36}$$

Proceeding for the outer contour as for the inner contour one obtains

$$\tilde{\varphi}_{2,0} = -\tilde{\varphi}_{2,0} - \frac{1}{\varepsilon\pi} \ln a_2 \tilde{\sigma}_{2,0} - \frac{1}{\varepsilon\pi} \ln a_2 \tilde{\sigma}_{1,0} \quad (n = 0) \tag{E.37}$$

$$\tilde{\varphi}_{2,n} = \left(\frac{a_1}{a_2} \right)^{|n|} \tilde{\varphi}_{1,n} + \frac{1}{\varepsilon\pi} \frac{1}{2|n|} \tilde{\sigma}_{2,n} + \frac{1}{\varepsilon\pi} \frac{1}{2|n|} \left(\frac{a_1}{a_2} \right)^{|n|} \tilde{\sigma}_{1,n} \quad (n \neq 0) \tag{E.38}$$

The difference of (E.32) and (E.37) can be rearranged to

$$\tilde{\varphi}_{1,0} - \tilde{\varphi}_{2,0} = -\frac{1}{2\varepsilon\pi} (\ln a_1 \tilde{\sigma}_{1,0} + \ln a_2 \tilde{\sigma}_{1,0} + 2 \ln a_2 \tilde{\sigma}_{2,0}) \tag{E.39}$$

A constant potential on the inner contour is enforced by setting to zero all potential coefficients with indices different from 0. In term of even and odd coefficients the relation is given by

$$\begin{Bmatrix} \tilde{\varphi}_{2,m}^e \\ \tilde{\varphi}_{2,m}^o \end{Bmatrix} = \frac{1}{2\pi\varepsilon m} \frac{1 - \left(\frac{a_1}{a_2} \right)^{2m}}{1 + \left(\frac{a_1}{a_2} \right)^{2m}} \begin{Bmatrix} \tilde{\sigma}_{2,m}^e \\ \tilde{\sigma}_{2,m}^o \end{Bmatrix} \tag{E.40}$$

The coefficients of potential which are hereby determined are similar to terminating impedances of modes of a network.

E.5.3 Assembly of the Descriptions for Oxide and Silicon Areas

In each oxide region, the relation for all anisotropic modes ($m > 0$) can be given as

$$\varphi_{\text{ox}}^m = \mathbf{Q} \boldsymbol{\sigma}_{\text{ox}}^m. \tag{E.41}$$

Assuming a block-wise ordering with blocks for all anisotropic modes for one oxide region, this has a form

$$\begin{pmatrix} \varphi_{\text{ox}}^{(1)} \\ \varphi_{\text{ox}}^{(2)} \\ \vdots \\ \varphi_{\text{ox}}^{(N)} \end{pmatrix} = \begin{pmatrix} \mathbf{Q}^{(1)} & 0 & \cdots & 0 \\ 0 & \mathbf{Q}^{(2)} & \cdots & 0 \\ \vdots & \vdots & \ddots & \vdots \\ 0 & 0 & \cdots & \mathbf{Q}^{(n)} \end{pmatrix} \begin{pmatrix} \sigma_{\text{ox}}^{(1)} \\ \sigma_{\text{ox}}^{(2)} \\ \vdots \\ \sigma_{\text{ox}}^{(N)} \end{pmatrix}. \quad (\text{E.42})$$

The entries of each $\mathbf{Q}^{(k)}$ are given from (E.40) by

$$Q_{m,n}^{(k)} = \begin{cases} \frac{1}{2\pi\epsilon m} \cdot \frac{1 - (a_{k,\text{inner}}/a_{k,\text{outer}})^{2m}}{1 + (a_{k,\text{inner}}/a_{k,\text{outer}})^{2m}} & (m = n) \\ 0 & (m \neq n) \end{cases} \quad (\text{E.43})$$

The relation for the isotropic mode can be obtained from (E.39) with $\tilde{\sigma}_{2,0} = -\tilde{\sigma}_{1,0}$ (as justified in the following discussion) as

$$\sigma_{\text{cond}}^0 = \varphi_{\text{ox}}^0 - \mathbf{R}\sigma_{\text{ox}}^0 \quad (\text{E.44})$$

with the entries of \mathbf{R} given by

$$R_{i,j} = \begin{cases} \frac{1}{2\pi\epsilon} \cdot \ln\left(\frac{a_{i,\text{outer}}}{a_{i,\text{inner}}}\right) & (i = j) \\ 0 & (i \neq j) \end{cases} \quad (\text{E.45})$$

At the oxide-silicon interface, both the potential and the normal component of the electric flux density must be continuous. The latter is equivalent to the equality (with adapted signs) of the surface charge densities of the respective regions. The surface charge densities at the silicon region contours are equal in magnitude and opposite in sign to the corresponding surface charge densities at the outer oxide layer circumferences.

$$\sigma_{\text{si}}^m = -\sigma_{\text{ox}}^m \quad (m \in \mathbb{Z} \setminus 0) \quad (\text{E.46a})$$

$$\sigma_{\text{si}}^0 = -\sigma_{\text{ox}}^0 \quad (\text{E.46b})$$

This is equivalent to the continuity of dielectric displacement (flux) across the dielectric-dielectric interfaces. The condition is true for all coefficients of the expansion.

For the isotropic mode of the expansion (0-index coefficients), the surface charge densities of the oxide are also equal in magnitude and opposite in sign to the corresponding surface charge densities on the corresponding conductors.

$$\sigma_{\text{ox}}^0 = -\sigma_{\text{cond}}^0 \quad (\text{E.47})$$

Note that this charge density is already related to the free charge on the conductor not to

the total charge density. Combining (E.46b) and (E.47) gives

$$\sigma_{\text{si}}^0 = \sigma_{\text{cond}}^0. \quad (\text{E.48})$$

Further the continuity of the potentials at the interfaces is expressed as

$$\varphi_{\text{si}}^m = \varphi_{\text{ox}}^m \quad (m \in \mathbb{Z} \setminus 0) \quad (\text{E.49a})$$

$$\varphi_{\text{si}}^0 = \varphi_{\text{ox}}^0 \quad (\text{E.49b})$$

Using the previously derived relations, one can now establish the following relations for potential and charge of the anisotropic modes on the silicon interfaces

$$\varphi_{\text{si}}^m \stackrel{(\text{E.49a})}{=} \varphi_{\text{ox}}^m \stackrel{(\text{E.41})}{=} Q \sigma_{\text{ox}}^m \stackrel{(\text{E.46a})}{=} -Q \sigma_{\text{si}}^m \quad (\text{E.50})$$

The equation system in (E.25) can be solved for the potentials as

$$\begin{pmatrix} \varphi_{\text{si}}^0 \\ \varphi_{\text{si}}^m \end{pmatrix} = U^{-1} H \begin{pmatrix} \sigma_{\text{si}}^0 \\ \sigma_{\text{si}}^m \end{pmatrix} = \begin{pmatrix} P_{11} & P_{12} \\ P_{21} & P_{22} \end{pmatrix} \begin{pmatrix} \sigma_{\text{si}}^0 \\ \sigma_{\text{si}}^m \end{pmatrix} \quad (\text{E.51})$$

Using the second row of the equation system in (E.51) with (E.50), the following relation can be established

$$\varphi_{\text{si}}^m = P_{21} \sigma_{\text{si}}^0 + P_{22} \sigma_{\text{si}}^m \stackrel{(\text{E.50})}{=} -Q \sigma_{\text{si}}^m \quad (\text{E.52})$$

Rearranging to this for σ_{si}^m gives

$$\sigma_{\text{si}}^m = -(P_{22} + Q)^{-1} P_{21} \sigma_{\text{si}}^0 \quad (\text{E.53})$$

Using the first row of the equation system in (E.51) with (E.53) gives

$$\varphi_{\text{si}}^0 = P_{11} \sigma_{\text{si}}^0 + P_{12} \sigma_{\text{si}}^m \stackrel{(\text{E.53})}{=} (P_{11} - P_{12} (P_{22} + Q)^{-1} P_{21}) \sigma_{\text{si}}^0 \quad (\text{E.54})$$

Then

$$\begin{aligned} \varphi_{\text{conductor}}^0 &\stackrel{(\text{E.44})}{=} \varphi_{\text{ox}}^0 - R \sigma_{\text{ox}}^0 \\ &\stackrel{(\text{E.49b}, \text{E.46b})}{=} \varphi_{\text{si}}^0 + R \sigma_{\text{si}}^0 \\ &\stackrel{(\text{E.54}, \text{E.48})}{=} (P_{11} - P_{12} (P_{22} + Q)^{-1} P_{21} + R) \sigma_{\text{cond}}^0 \end{aligned} \quad (\text{E.55})$$

The generalized capacitance matrix is then obtained after the computation of an inverse as

$$C = [P_{11} - P_{12} (P_{22} + Q)^{-1} P_{21} + R]^{-1}. \quad (\text{E.56})$$

E.5.4 Inclusion of Complex Permittivities

The capacitance matrix given in (E.56) has real entries if only real permittivities are assumed for all involved materials. If complex permittivities are used for any of the materials, the surface charges of this method and the capacitance matrix becomes complex. In this case, it describes both the capacitance and the conductance between the conductors and is denoted by here $\underline{\mathbf{C}}$. The real quantities of capacitance \mathbf{C} and conductance \mathbf{G} can be obtained as

$$\mathbf{C} = \Re(\underline{\mathbf{C}}), \quad (\text{E.57a})$$

$$\mathbf{G} = -\Im(\underline{\mathbf{C}}) / \omega. \quad (\text{E.57b})$$

E.5.5 Proof of Equivalence With TWA

For Two Conductors in Homogeneous Medium

For two conductors in homogeneous medium, the equation system reduces to

$$\begin{bmatrix} 1 & 0 \\ 0 & 1 \end{bmatrix} \begin{bmatrix} \phi_1 \\ \phi_2 \end{bmatrix} = \frac{1}{2\pi\epsilon} \begin{bmatrix} -\ln a_1 & -\ln \rho_{1,2} \\ -\ln \rho_{2,1} & -\ln a_2 \end{bmatrix} \begin{bmatrix} \lambda_1 \\ \lambda_2 \end{bmatrix} \quad (\text{E.58})$$

Using $-\lambda_1 = \lambda_2 = \lambda$ and $\rho_{2,1} = \rho_{1,2} = \rho$, one obtains

$$\phi_2 - \phi_1 = \frac{1}{2\pi\epsilon} (\ln \rho_{2,1} - \ln a_2 - \ln a_1 + \ln \rho_{1,2}) \lambda = \frac{\ln \left(\frac{\rho^2}{a_1 a_2} \right)}{2\pi\epsilon} \lambda \quad (\text{E.59})$$

Therefore,

$$C' = \frac{\lambda}{\phi_2 - \phi_1} = \frac{2\pi\epsilon}{\ln \left(\frac{\rho^2}{a_1 a_2} \right)} \quad (\text{E.60})$$

For equal radii $a_1 = a_2 = a$ this reduces to

$$C' = \frac{\lambda}{\phi_2 - \phi_1} = \frac{\pi\epsilon}{\ln \left(\frac{\rho}{a} \right)} \quad (\text{E.61})$$

For N Conductors in Homogeneous Medium

In case of only the first mode used in the method of the preceding sections, the equation system can be written in the block-form

$$\begin{pmatrix} \phi_n \\ \phi_0 \end{pmatrix} = \frac{1}{2\pi\epsilon} \begin{pmatrix} \mathbf{P}^{(n,n)} & \mathbf{P}^{(n,0)} \\ \mathbf{P}^{(0,n)} & P^{(0,0)} \end{pmatrix} \begin{pmatrix} \boldsymbol{\lambda}_n \\ \lambda_0 \end{pmatrix} \quad (\text{E.62})$$

where the normalized coefficients of potential are given by

$$\mathbf{P}_{i,j}^{(n,n)} = \begin{cases} -\ln(a_i) & (i = j) \\ -\ln(\rho_{i,j}) & (i \neq j) \end{cases} \quad (\text{E.63a})$$

$$\mathbf{P}_i^{(n,0)} = -\ln(\rho_{i,0}) \quad (\text{E.63b})$$

$$\mathbf{P}_j^{(0,n)} = -\ln(\rho_{0,j}) \quad (\text{E.63c})$$

$$P^{(0,0)} = -\ln(a_0) \quad (\text{E.63d})$$

The condition that the charge on the reference conductor being of equal magnitude but opposite sign to the sum of all other charges can be expressed as

$$\lambda_0 = - \underbrace{\begin{pmatrix} 1 & 1 & \cdots & 1 \end{pmatrix}}_{\text{length } n} \boldsymbol{\lambda}_n = -\mathbf{J}_{1,n} \boldsymbol{\lambda}_n \quad (\text{E.64})$$

From the second row of (E.62) and with (E.64)

$$\phi_0 = \frac{1}{2\pi\epsilon} (\mathbf{P}^{(0,n)} \boldsymbol{\lambda}_n + P^{(0,0)} \lambda_0) = \frac{1}{2\pi\epsilon} (\mathbf{P}^{(0,n)} - P^{(0,0)} \mathbf{J}_{1,n}) \boldsymbol{\lambda}_n \quad (\text{E.65})$$

Using the first row of (E.62) with (E.64) and (E.65)

$$\begin{aligned} \phi_n - \phi_0 &= \phi_n - \mathbf{J}_{n,1} \phi_0 = \frac{1}{2\pi\epsilon} (\mathbf{P}^{(n,n)} \boldsymbol{\lambda}_n + \mathbf{P}^{(n,0)} \lambda_0 - \mathbf{J}_{n,1} \phi_0) \\ &= \frac{1}{2\pi\epsilon} (\mathbf{P}^{(n,n)} - \mathbf{P}^{(n,0)} \mathbf{J}_{1,n} - \mathbf{J}_{n,1} (\mathbf{P}^{(0,n)} - P^{(0,0)} \mathbf{J}_{1,n})) \boldsymbol{\lambda}_n \\ &= \frac{1}{2\pi\epsilon} \underbrace{(\mathbf{P}^{(n,n)} - \mathbf{P}^{(n,0)} \mathbf{J}_{1,n} - \mathbf{J}_{n,1} \mathbf{P}^{(0,n)} + \mathbf{J}_{n,1} P^{(0,0)} \mathbf{J}_{1,n})}_{\tilde{\mathbf{P}}} \boldsymbol{\lambda}_n \end{aligned} \quad (\text{E.66})$$

From this it follows

$$\begin{aligned} \tilde{P}_{i,j} &= \frac{1}{2\pi\epsilon} \begin{cases} -\ln(a_i) + \ln(\rho_{i,0}) + \ln(\rho_{0,j}) - \ln(a_0) & (i = j) \\ -\ln(\rho_{i,j}) + \ln(\rho_{i,0}) + \ln(\rho_{0,j}) - \ln(a_0) & (i \neq j) \end{cases} \\ &= \frac{1}{2\pi\epsilon} \begin{cases} \ln\left(\frac{\rho_{i,0}\rho_{0,j}}{a_0 a_i}\right) & (i = j) \\ \ln\left(\frac{\rho_{i,0}\rho_{0,j}}{a_0 \rho_{i,j}}\right) & (i \neq j) \end{cases}, \end{aligned} \quad (\text{E.67})$$

which is equivalent to (7.1b).

E.6 Generalized Capacitance Matrix

A generalized capacitance matrix can be defined that allows for a choice of the reference conductor with a comparatively simple computation. The computation of this generalized capacitance matrix is based on partial capacitances for an arbitrary reference point. The enforcement of the conditions for the currents and voltage for the reference conductor then leads to the capacitance matrix for a chosen reference conductor. The relation with the capacitance matrix for a specific reference conductor can be found e.g. in [98, Sec. 3.1.4]. The following derivation is analog to [98, Sec. 3.1.4], but based on a matrix notation with implicit sums instead of explicit sums.

Consider a generalized capacitance matrix that can be written with blocks as

$$\begin{bmatrix} q_r \\ \mathbf{q}_s \end{bmatrix} = \underbrace{\begin{bmatrix} \mathcal{C}_{rr} & \mathcal{C}_{rs} \\ \mathcal{C}_{sr} & \mathcal{C}_{ss} \end{bmatrix}}_{\mathcal{C}} \begin{bmatrix} \phi_r \\ \boldsymbol{\phi}_s \end{bmatrix} \quad (\text{E.68})$$

where \mathbf{q}_s , \mathcal{C}_{sr} , and $\boldsymbol{\phi}_s$ are column vectors, \mathcal{C}_{rs} is a row vector, and \mathcal{C}_{ss} is a (square) matrix. Index r refers to the (single) reference conductor and index s to the signal (non-reference) conductors. The conditions of the sum of the charges on the signal conductors to be equal in magnitude and opposite in sign to the charge on the reference conductor can be written in matrix notation and applied to the first row of (E.68) as

$$q_r = - \underbrace{\begin{bmatrix} 1 & 1 & \cdots & 1 \end{bmatrix}}_{\mathbf{J}_{1,s}} \mathbf{q}_s = \mathcal{C}_{rr}\phi_r + \mathcal{C}_{rs}\boldsymbol{\phi}_s \quad (\text{E.69})$$

A similar form can be obtained for the second row of (E.68) if both side are multiplied (from the left) with $\mathbf{J}_{1,s}$:

$$\mathbf{J}_{1,s}\mathbf{q}_s = \mathbf{J}_{1,s}(\mathcal{C}_{sr}\phi_r + \mathcal{C}_{ss}\boldsymbol{\phi}_s) \quad (\text{E.70})$$

Summing up (E.69) and (E.70) one obtains

$$0 = \mathcal{C}_{rr}\phi_r + \mathcal{C}_{rs}\boldsymbol{\phi}_s + \mathbf{J}_{1,s}(\mathcal{C}_{sr}\phi_r + \mathcal{C}_{ss}\boldsymbol{\phi}_s) \quad (\text{E.71})$$

The voltages of the signal conductors are related to the potentials as $\boldsymbol{\phi}_s = \mathbf{V}_s - \phi_r$ or in

size compliant vector notation and rearranged for ϕ_s

$$\phi_s = \underbrace{\begin{bmatrix} 1 \\ \vdots \\ 1 \end{bmatrix}}_{\mathbf{J}_{s,1}} \phi_r + \mathbf{V}_s \quad (\text{E.72})$$

By inserting (E.72) into (E.71), and rearranging for ϕ_r one obtains

$$\phi_r = \frac{-(\mathbf{C}_{rs} + \mathbf{J}_{1,s}\mathbf{C}_{ss})}{\mathbf{C}_{rr} + \mathbf{C}_{rs}\mathbf{J}_{s,1} + \mathbf{J}_{1,s}\mathbf{C}_{sr} + \mathbf{J}_{1,s}\mathbf{C}_{ss}\mathbf{J}_{s,1}} \mathbf{V}_s \quad (\text{E.73})$$

The denominator of (E.73) can be identified as the sum of all elements of matrix \mathbf{C} for which in the following the shorthand notation $\sum \mathbf{C}$ will be used. By inserting (E.73) and (E.72) into the second row of (E.68)

$$\begin{aligned} \mathbf{q}_s &= \mathbf{C}_{sr}\phi_r + \mathbf{C}_{ss}\phi_s \\ &= \mathbf{C}_{sr}\phi_r + \mathbf{C}_{ss}(\mathbf{J}_{s,1}\phi_r + \mathbf{V}_s) \\ &= \mathbf{C}_{ss}\mathbf{V}_s + (\mathbf{C}_{sr} + \mathbf{C}_{ss}\mathbf{J}_{s,1})\phi_r \\ &= \left(\mathbf{C}_{ss} - \frac{(\mathbf{C}_{sr} + \mathbf{C}_{ss}\mathbf{J}_{s,1})(\mathbf{C}_{rs} + \mathbf{J}_{1,s}\mathbf{C}_{ss})}{\sum \mathbf{C}} \right) \mathbf{V}_s \end{aligned} \quad (\text{E.74})$$

In the last nominator, the first multiplicand of the product can be identified as the sums for each of the rows of \mathbf{C} (except for the one of the reference conductor). Correspondingly, the second multiplicand can be identified as the sums of all columns of \mathbf{C} (except for the one of the reference conductor).

E.7 Network Parameters of Transmission Lines

E.7.1 Chain Parameter Matrix for the General Case

In general, the frequency domain characterization of the transmission line by computation of network parameters involves an explicit or implicit modal transformation. A transformation matrix is computed which diagonalized the product of the per-unit-length matrices $\hat{\mathbf{Y}}\hat{\mathbf{Z}}$.

From [98, Eq. 4.45b] the following chain parameter matrix that relates voltages and cur-

rents² at the ends of the transmission line can be given

$$\begin{bmatrix} \hat{V}(\mathcal{L}) \\ \hat{I}(\mathcal{L}) \end{bmatrix} = \begin{bmatrix} \hat{\Phi}_{11}(\mathcal{L}) & \hat{\Phi}_{12}(\mathcal{L}) \\ \hat{\Phi}_{21}(\mathcal{L}) & \hat{\Phi}_{22}(\mathcal{L}) \end{bmatrix} \begin{bmatrix} \hat{V}(0) \\ \hat{I}(0) \end{bmatrix}, \quad (\text{E.75})$$

with the entries given as [98, Eq. 4.70]

$$\hat{\Phi}_{11}(\mathcal{L}) = \frac{1}{2} \hat{\mathbf{Y}}^{-1} \hat{\mathbf{T}} (e^{\hat{\gamma}\mathcal{L}} + e^{-\hat{\gamma}\mathcal{L}}) \hat{\mathbf{T}}^{-1} \hat{\mathbf{Y}}, \quad (\text{E.76a})$$

$$\hat{\Phi}_{12}(\mathcal{L}) = -\frac{1}{2} \hat{\mathbf{Z}}_C \hat{\mathbf{T}} (e^{\hat{\gamma}\mathcal{L}} - e^{-\hat{\gamma}\mathcal{L}}) \hat{\mathbf{T}}^{-1}, \quad (\text{E.76b})$$

$$\hat{\Phi}_{21}(\mathcal{L}) = -\frac{1}{2} \hat{\mathbf{T}} (e^{\hat{\gamma}\mathcal{L}} - e^{-\hat{\gamma}\mathcal{L}}) \hat{\mathbf{T}}^{-1} \hat{\mathbf{Z}}_C^{-1}, \quad (\text{E.76c})$$

$$\hat{\Phi}_{22}(\mathcal{L}) = \frac{1}{2} \hat{\mathbf{T}} (e^{\hat{\gamma}\mathcal{L}} + e^{-\hat{\gamma}\mathcal{L}}) \hat{\mathbf{T}}^{-1}, \quad (\text{E.76d})$$

where the exponential function operates element-wise on the matrix arguments and a characteristic impedance matrix is defined as [98, Eq. 4.67]

$$\hat{\mathbf{Z}}_C = \hat{\mathbf{Z}} \hat{\mathbf{T}} \hat{\gamma}^{-1} \hat{\mathbf{T}}^{-1}. \quad (\text{E.77})$$

For the computation of the modal transformation matrix $\hat{\mathbf{T}}$ and its inverse $\hat{\mathbf{T}}^{-1}$, several options exist. The most relevant case for TSV modeling seems to be the one of perfect conductors in inhomogeneous media discussed in [98, Sec. 4.4.3].

E.7.2 Approximations for Short Transmission Lines

For short sections of transmission lines, lumped-element representations can be applicable. The symmetric representations are the (lumped) pi-circuit and (lumped) T-circuit which are illustrated in Fig. E.4. The corresponding chain parameter matrices are computed from the per-unit-length admittance and impedance matrices $\hat{\mathbf{Y}}$ and $\hat{\mathbf{Z}}$, respectively, as [98, Eq. 4.149]

$$\Phi_\pi = \begin{bmatrix} \mathbf{1}_n + \frac{1}{2} \hat{\mathbf{Z}} \hat{\mathbf{Y}} \left(\frac{\mathcal{L}}{N}\right)^2 & -\hat{\mathbf{Z}} \frac{\mathcal{L}}{N} \\ -\hat{\mathbf{Y}} \frac{\mathcal{L}}{N} - \frac{1}{4} \hat{\mathbf{Y}} \hat{\mathbf{Z}} \hat{\mathbf{Y}} \left(\frac{\mathcal{L}}{N}\right)^3 & \mathbf{1}_n + \frac{1}{2} \hat{\mathbf{Y}} \hat{\mathbf{Z}} \left(\frac{\mathcal{L}}{N}\right)^2 \end{bmatrix} \quad (\text{E.78})$$

$$\Phi_T = \begin{bmatrix} \mathbf{1}_n + \frac{1}{2} \hat{\mathbf{Z}} \hat{\mathbf{Y}} \left(\frac{\mathcal{L}}{N}\right)^2 & -\hat{\mathbf{Z}} \frac{\mathcal{L}}{N} - \frac{1}{4} \hat{\mathbf{Z}} \hat{\mathbf{Y}} \hat{\mathbf{Z}} \left(\frac{\mathcal{L}}{N}\right)^3 \\ -\hat{\mathbf{Y}} \frac{\mathcal{L}}{N} & \mathbf{1}_n + \frac{1}{2} \hat{\mathbf{Y}} \hat{\mathbf{Z}} \left(\frac{\mathcal{L}}{N}\right)^2 \end{bmatrix} \quad (\text{E.79})$$

²Note that this current definition is conventionally assuming a flow inside each terminal (except for the reference conductor) at the beginning of the MTL and outside each terminal (except for the reference conductor) at both end of the MTL, cf. [98, Fig. 4.3]

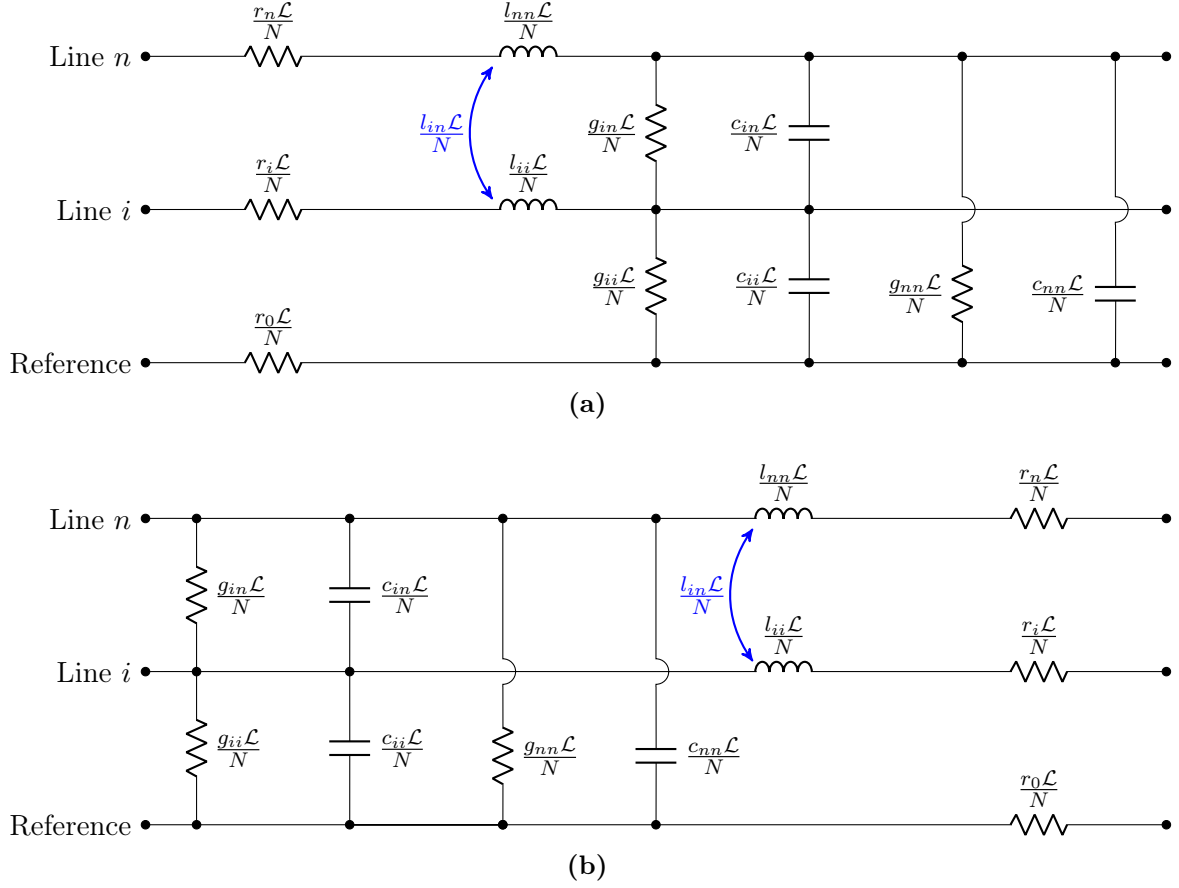


Figure E.3: Short transmission line (of length L/N) represented as (a) lumped Γ - and (b) lumped T -circuit. Figure adapted from [98, Fig. 4.12].

where \mathcal{L} is the total length of the MTL, N is the number of segments (of equal length), and $\mathbf{1}_n$ is an identity matrix of size n that is equal to the number of terminals (except for the reference conductor).

The lumped Γ - and lumped T -circuit are depicted in Fig. E.3 and can be characterized correspondingly as [98, Eq. 4.149]

$$\Phi_\pi = \begin{bmatrix} \mathbf{1}_n & -\hat{\mathbf{Z}} \frac{\mathcal{L}}{N} \\ -\hat{\mathbf{Y}} \frac{\mathcal{L}}{N} & \mathbf{1}_n + \hat{\mathbf{Y}} \hat{\mathbf{Z}} \left(\frac{\mathcal{L}}{N}\right)^2 \end{bmatrix}, \quad (\text{E.80})$$

$$\Phi_T = \begin{bmatrix} \mathbf{1}_n + \hat{\mathbf{Z}} \hat{\mathbf{Y}} \left(\frac{\mathcal{L}}{N}\right)^2 & -\hat{\mathbf{Z}} \frac{\mathcal{L}}{N} \\ -\hat{\mathbf{Y}} \frac{\mathcal{L}}{N} & \mathbf{1}_n \end{bmatrix}. \quad (\text{E.81})$$

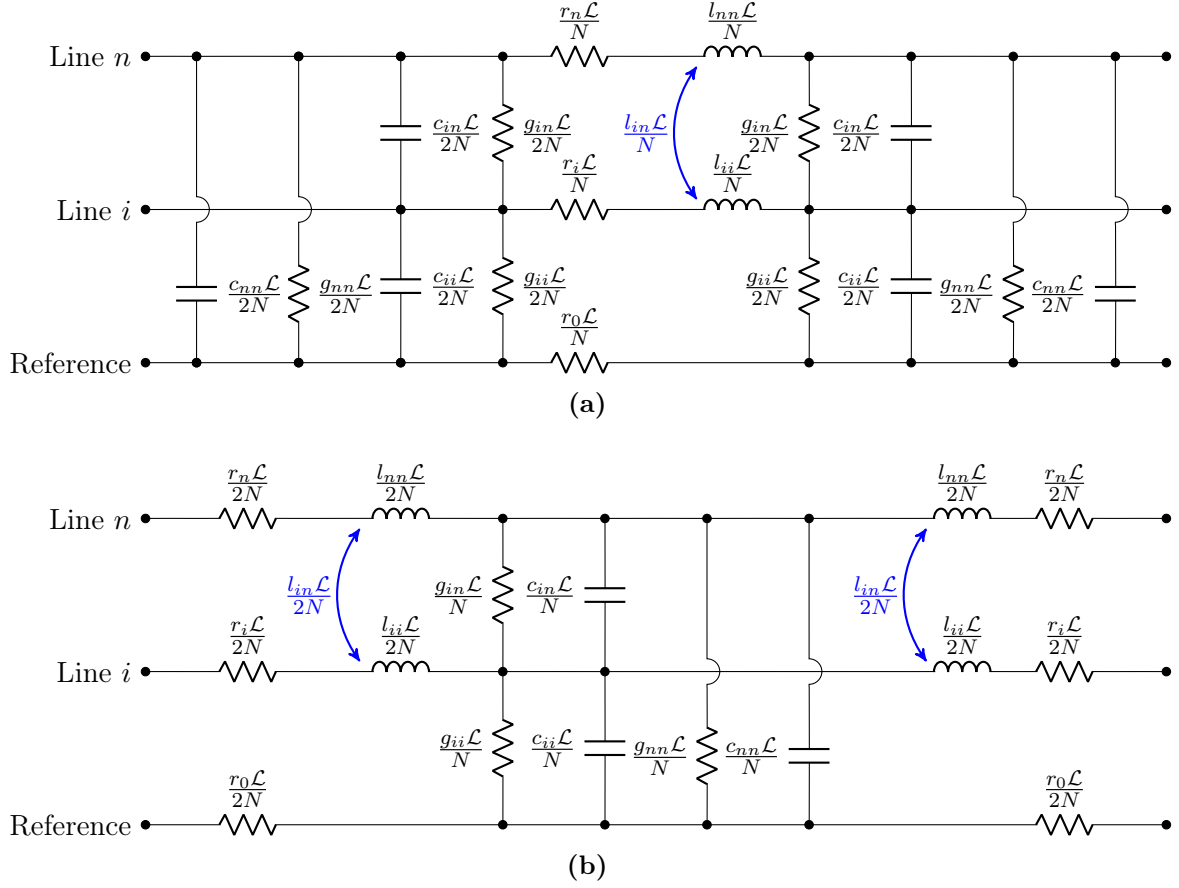


Figure E.4: Short transmission line (of length L/N) represented as (a) lumped pi-circuit and (b) lumped T-circuit. Figure adapted from [98, Fig. 4.12].

E.7.3 Assignment of Several Reference Conductors

The basic multi-conductor transmission line theory assumes a single reference conductor which is unambiguously defined by a normalization of all voltages to the reference conductor voltage and by setting the current along the reference conductor equal in magnitude and opposite in sign to the sum of currents along all conductors (except for the reference conductor). It is of interest in various cases to assign several reference conductors. As these reference conductors are not connected in the plane that is transverse to the conductor axes and thereby create a single conductor out of the disjoint conductors, the problem needs further discussion.

Consideration in Terms of Per-Unit-Length Parameters for Short Transmission Lines

Short two-conductor transmission lines are characterized by a guided wavelength of the mode of interest, here the TEM- or quasi-TEM mode, which is significantly shorter than the geometrical length of the transmission line. Usually a ratio above 10 of guided wavelength to geometrical length is considered a short line. In an analog manner, short multiconductor transmission lines are characterized by guided wavelengths of all TEM- or quasi-TEM-modes which are significantly shorter than the geometrical length of the MTL. Short MTLs can with good accuracy be modeled by lumped element circuits as those discussed in Appendix E.7.2. Following the general procedure, a first reference conductor must be chosen. From these circuit descriptions in Appendix E.7.2, it can be reasoned that a short-circuiting at the ends of signal conductors with the reference conductors is equivalent to short circuiting the descriptions in terms of the corresponding longitudinal impedance matrix and the transverse admittance matrix. Consider the Pi-circuit in Fig. E.4 for the case where the i th conductor is short-circuited with the reference conductor at both ends of the line with a total length \mathcal{L} and $N = 1$ segments. The transverse capacitances and admittances are then short-circuited and the longitudinal inductance and resistances of all reference conductors (the first, initial one with index 0 and the newly added one with index i) are in parallel. This can easily also be seen for the lumped T- and the lumped Γ -circuit in Fig. E.3. For the T-circuit (also shown in Fig. E.4), in contrast, a similar simplification is not possible. When short-circuiting conductors i and 0, there remains a series connection of elements from the longitudinal impedance elements and from the transverse admittance elements. Nevertheless, the technique should be applicable because, for short lines, all lumped element representations should give similar results.

Short-circuiting of per-unit-length parameters (in terms of the corresponding longitudinal impedance and the transverse admittance matrices) is e.g. described in [145, Appendix C]. For the case of actually connected conductors (that constitute a model for a conductor with skin-effect) a similar approach is given in [98, Sec. 3.6.2.3] and this method is analog to the one for the generalized capacitance matrix [98, Sec. 3.1.4]. For the longitudinal impedance, the self inductances and the resistances of all reference conductors are in parallel. The mutual inductances of the reference conductors to the signal conductors (or “non-reference conductor”) are in parallel and the original mutual inductances of the reference conductors to the first reference conductor disappear. For the transverse admittance, the conductances and resistances to the first reference conductor are short-circuited and disappear while those to the signal conductors are in parallel.

In the following, the case with $\hat{\mathbf{R}} = 0$ is considered. Consider first the transverse admittance

matrix $\hat{\mathbf{Y}} = \hat{\mathbf{G}} + j\omega\hat{\mathbf{C}}$ where $\hat{\mathbf{G}}$ and $\hat{\mathbf{C}}$ are the per-unit-length conductance matrix and capacitance matrix, respectively. As can be seen from the relation with the generalized capacitance matrix in Appendix E.6 for the capacitance matrix, the charge on the reference conductor is given as the sum of charges of one row or column of the matrix. Consequently, by using a square sub-matrix of the per-unit-length capacitance matrix addressed with an index set s (for signal conductors), the remaining conductors from the disjoint index set r are assigned as reference conductors. This can be expressed analogously for the admittance matrix as

$$\begin{bmatrix} \mathbf{I}_s \\ \mathbf{I}_r \end{bmatrix} \begin{bmatrix} \hat{\mathbf{Y}}_{ss} & \hat{\mathbf{Y}}_{sr} \\ \hat{\mathbf{Y}}_{rs} & \hat{\mathbf{Y}}_{rr} \end{bmatrix} \begin{bmatrix} \mathbf{V}_s \\ \mathbf{V}_r \end{bmatrix}, \quad (\text{E.82})$$

from which by requiring $\mathbf{V}_r = 0$ one obtains simply

$$\hat{\mathbf{Y}}_{\text{red.}} = \hat{\mathbf{Y}}_{ss} \quad (\text{E.83})$$

as the admittance matrix for the case of additional assigned reference conductors.

For the longitudinal impedance matrix $\hat{\mathbf{Z}} = j\omega\hat{\mathbf{L}}$, the relation with the capacitance matrix for the conductors with all dielectrics replaced by vacuum can be used. After computation of this capacitance matrix and application of the reduction as in (E.82)–(E.83), the inductance matrix $\hat{\mathbf{L}}$ is obtained from this reduced capacitance matrix for the vacuum case $\mathbf{C}_{\text{vac.}}$ as [98, Eq. 3.4]

$$\hat{\mathbf{L}} = \mathbf{C}_{\text{vac.}}^{-1} \varepsilon_0 \mu_0. \quad (\text{E.84})$$

Consideration in Terms of Network Parameters of the MTL for General Transmission Line

For the general transmission line with a geometric length that is no necessarily shorter than the guided wavelengths, the assignment of several reference conductors can only be performed in terms of the ports for the network parameters. Physically this corresponds to relevant currents that are induced due to the loop that the different reference conductor (short-circuited only at their ends) constitute. For the chain parameters in (E.75) this computation can be carried out as follows. Consider the following organization of the chain parameter matrix with indices r for conductors that are subsequently assigned as reference conductors, indices s for conductors that are subsequently used as signal conductors, and an equal ordering of all voltage and current vectors for both ends of the MTL:

$$\begin{bmatrix} \hat{\mathbf{V}}_s(\mathcal{L}) \\ \hat{\mathbf{V}}_r(\mathcal{L}) \\ \hat{\mathbf{I}}_s(\mathcal{L}) \\ \hat{\mathbf{I}}_r(\mathcal{L}) \end{bmatrix} = \begin{bmatrix} \hat{\Phi}_{11}^{ss} & \hat{\Phi}_{11}^{sr} & \hat{\Phi}_{12}^{ss} & \hat{\Phi}_{12}^{sr} \\ \hat{\Phi}_{11}^{rs} & \hat{\Phi}_{11}^{rr} & \hat{\Phi}_{12}^{rs} & \hat{\Phi}_{12}^{rr} \\ \hat{\Phi}_{21}^{ss} & \hat{\Phi}_{21}^{sr} & \hat{\Phi}_{22}^{ss} & \hat{\Phi}_{22}^{sr} \\ \hat{\Phi}_{21}^{rs} & \hat{\Phi}_{21}^{rr} & \hat{\Phi}_{22}^{rs} & \hat{\Phi}_{22}^{rr} \end{bmatrix} \begin{bmatrix} \hat{\mathbf{V}}_s(0) \\ \hat{\mathbf{V}}_r(0) \\ \hat{\mathbf{I}}_s(0) \\ \hat{\mathbf{I}}_r(0) \end{bmatrix} \quad (\text{E.85})$$

where for all Φ the evaluation for the length \mathcal{L} is assumed. By enforcing $\hat{V}_r(\mathcal{L}) = 0$ and $\hat{V}_r(0) = 0$, the second row of (E.85) gives the relation for the currents on the “new” reference conductors as

$$\hat{I}_r(0) = - \left(\hat{\Phi}_{12}^{rr} \right)^{-1} \left(\hat{\Phi}_{11}^{rs} \hat{V}_s(0) + \hat{\Phi}_{12}^{rs} \hat{I}_s(0) \right) \quad (\text{E.86})$$

Insertion into (E.85) then gives for the remaining signal conductors

$$\begin{bmatrix} \hat{V}_s(\mathcal{L}) \\ \hat{I}_s(\mathcal{L}) \end{bmatrix} = \begin{bmatrix} \left\{ \hat{\Phi}_{11}^{ss} - \hat{\Phi}_{12}^{sr} \left(\hat{\Phi}_{12}^{rr} \right)^{-1} \hat{\Phi}_{11}^{rs} \right\} & \left\{ \hat{\Phi}_{12}^{ss} - \hat{\Phi}_{12}^{sr} \left(\hat{\Phi}_{12}^{rr} \right)^{-1} \hat{\Phi}_{12}^{rs} \right\} \\ \left\{ \hat{\Phi}_{21}^{ss} - \hat{\Phi}_{22}^{sr} \left(\hat{\Phi}_{12}^{rr} \right)^{-1} \hat{\Phi}_{11}^{rs} \right\} & \left\{ \hat{\Phi}_{22}^{ss} - \hat{\Phi}_{22}^{sr} \left(\hat{\Phi}_{12}^{rr} \right)^{-1} \hat{\Phi}_{12}^{rs} \right\} \end{bmatrix} \begin{bmatrix} \hat{V}_s(0) \\ \hat{I}_s(0) \end{bmatrix}. \quad (\text{E.87})$$

It can be observed that the elements from the second column and those from the last row of (E.85) are not required for (E.87). Alternatively, corresponding termination procedures can be carried out after a conversion to impedance or admittance parameters. The conversions can be found in [98, Sec. 4.6], the terminations can be derived analog to the derivation shown here.

Appendix F

Mathematical Appendix

F.1 Derivatives in 2D Cartesian Coordinates

F.1.1 Directional Derivative of Scalar Field

Given a general scalar field $v(\boldsymbol{\rho})$, the directional derivative with respect to a direction given by the normalized vector \boldsymbol{d} can be computed as [146, Sec. 13.2.1.2]

$$\frac{\partial v}{\partial \boldsymbol{d}} = \langle \boldsymbol{d}, \nabla v \rangle = \langle \nabla v, \boldsymbol{d} \rangle \quad (\text{F.1})$$

F.1.2 Normal Derivative of Euclidean Norm

One applies (F.1) with $v(\boldsymbol{\rho}) = |\boldsymbol{\rho}| = \|x\boldsymbol{e}_x + y\boldsymbol{e}_y\|_2$ and $\boldsymbol{d} = \hat{\boldsymbol{n}} = \boldsymbol{n}$ to obtain

$$\frac{\partial |\boldsymbol{\rho}|}{\partial \boldsymbol{n}} \stackrel{(\text{F.1})}{=} \langle \nabla |\boldsymbol{\rho}|, \hat{\boldsymbol{n}} \rangle \stackrel{(\text{F.3})}{=} \langle \hat{\boldsymbol{\rho}}, \hat{\boldsymbol{n}} \rangle \quad (\text{F.2})$$

F.1.3 Gradient of Euclidean Norm

For the case that $\boldsymbol{\rho} = (x, y)^T = x\boldsymbol{e}_x + y\boldsymbol{e}_y$:

$$\begin{aligned} \nabla |\boldsymbol{\rho}| &= \nabla \left\| \begin{pmatrix} x \\ y \end{pmatrix} \right\|_2 = \begin{pmatrix} \partial/\partial x \\ \partial/\partial y \end{pmatrix} \|x\boldsymbol{e}_x + y\boldsymbol{e}_y\|_2 = \begin{pmatrix} \partial/\partial x \\ \partial/\partial y \end{pmatrix} \sqrt{x^2 + y^2} \\ &= \frac{1}{2\sqrt{x^2 + y^2}} \begin{pmatrix} 2x \\ 2y \end{pmatrix} = \frac{\boldsymbol{\rho}}{|\boldsymbol{\rho}|} = \hat{\boldsymbol{\rho}} \end{aligned} \quad (\text{F.3})$$

F.2 Symmetries of Harmonic Functions for Complex Arguments

From the well known addition theorems for harmonic functions and the relation to the hyperbolic functions one can derive

$$\begin{aligned}\sin(x + jy) &= \sin(x) \cosh(y) + j \cos(x) \sinh(y) \\ &= -\sin(-x) \cosh(-y) - j \cos(-x) \sinh(-y) = -\sin(-(x + jy)),\end{aligned}\tag{F.4a}$$

$$\begin{aligned}\cos(x + jy) &= \cos(x) \cosh(y) - j \sin(x) \sinh(y) \\ &= \cos(-x) \cosh(-y) - j \sin(-x) \sinh(-y) = \cos(-(x + jy)).\end{aligned}\tag{F.4b}$$

As can be seen from the representation as harmonic and hyperbolic functions of the real and imaginary part, sine and cosine functions of complex arguments are odd and even functions, respectively.

F.3 Derivatives of Bessel Functions

For any Bessel function of order n , $\mathcal{F}_n(x)$, the following relations for its derivative hold [96, Appendix D]:

$$\mathcal{F}'_n(x) = -\mathcal{F}_{n+1}(x) + \frac{n}{x} \mathcal{F}_n(x)\tag{F.5a}$$

$$\mathcal{F}'_n(x) = \mathcal{F}_{n-1}(x) - \frac{n}{x} \mathcal{F}_n(x)\tag{F.5b}$$

For the special case of $n = 0$, this reduces to

$$\mathcal{F}'_0(x) = -\mathcal{F}_1(x)\tag{F.6}$$

The sum of the two relations in (F.5) leads to the recurrence

$$\mathcal{F}'_n(x) = \frac{1}{2} (\mathcal{F}_{n-1}(x) - \mathcal{F}_{n+1}(x))\tag{F.7}$$

which can be advantageous in comparison to both (F.5a) or (F.5b) for $x \rightarrow 0$.

Appendix G

Network Parameters

G.1 Concatenation of Admittance Parameters

G.1.1 General case

Assume the following organization of the matrices of the admittance parameters $\mathbf{Y}^{(a)}$ and $\mathbf{Y}^{(b)}$ that are to be concatenated:

$$\begin{pmatrix} \mathbf{I}_u^{(a)} \\ \mathbf{I}_c^{(a)} \end{pmatrix} = \underbrace{\begin{pmatrix} \mathbf{Y}_{uu}^{(a)} & \mathbf{Y}_{uc}^{(a)} \\ \mathbf{Y}_{cu}^{(a)} & \mathbf{Y}_{cc}^{(a)} \end{pmatrix}}_{\mathbf{Y}^{(a)}} \begin{pmatrix} \mathbf{V}_u^{(a)} \\ \mathbf{V}_c^{(a)} \end{pmatrix}, \quad (\text{G.1a})$$

$$\begin{pmatrix} \mathbf{I}_u^{(b)} \\ \mathbf{I}_c^{(b)} \end{pmatrix} = \underbrace{\begin{pmatrix} \mathbf{Y}_{uu}^{(b)} & \mathbf{Y}_{uc}^{(b)} \\ \mathbf{Y}_{cu}^{(b)} & \mathbf{Y}_{cc}^{(b)} \end{pmatrix}}_{\mathbf{Y}^{(b)}} \begin{pmatrix} \mathbf{V}_u^{(b)} \\ \mathbf{V}_c^{(b)} \end{pmatrix}. \quad (\text{G.1b})$$

where indices u mark the unconnected ports of each of the network parameter sets and indices c mark the connected port with the same ordering for a and v inside the respective matrix blocks. It is desired to obtain a concatenated result $\mathbf{Y}^{(ab)}$ with the ordering as

$$\begin{pmatrix} \mathbf{I}_u^{(a)} \\ \mathbf{I}_u^{(b)} \end{pmatrix} = \mathbf{Y}^{(ab)} \begin{pmatrix} \mathbf{V}_u^{(a)} \\ \mathbf{V}_u^{(b)} \end{pmatrix}. \quad (\text{G.2})$$

Using the conditions $\mathbf{I}_c^{(a)} = -\mathbf{I}_c^{(b)}$ and $\mathbf{V}_c^{(a)} = \mathbf{V}_c^{(b)}$ one can find in accordance with [140, Sec. 3.2.3] that

$$\mathbf{Y}^{(ab)} = \begin{pmatrix} \mathbf{Y}_{uu}^{(a)} & \mathbf{0} \\ \mathbf{0} & \mathbf{Y}_{uu}^{(b)} \end{pmatrix} - \begin{pmatrix} \mathbf{Y}_{uc}^{(a)} \\ \mathbf{Y}_{uc}^{(b)} \end{pmatrix} (\mathbf{Y}_{cc}^{(a)} + \mathbf{Y}_{cc}^{(b)})^{-1} \begin{pmatrix} \mathbf{Y}_{cu}^{(a)} & \mathbf{Y}_{cu}^{(b)} \end{pmatrix}. \quad (\text{G.3})$$

For many cases, simplifications of special cases lead to similar results but if, e.g., only network b has only connected ports, network b terminates several ports of network a .

Concatenation of Per Port and Common Series Admittance

The case of concatenating of a common series impedance Z_r to the common reference conductor path of a multiport is illustrated in Fig. G.1. The matrix \mathbf{Y}_1 that is concatenated has a symmetric structure of the following form

$$\mathbf{Y}_1 = \begin{pmatrix} \mathbf{Y}_{aa} & -\mathbf{Y}_{aa} \\ -\mathbf{Y}_{aa} & \mathbf{Y}_{aa} \end{pmatrix}. \quad (\text{G.4})$$

For the matrix \mathbf{Y}_{aa} , the diagonal entries are as follows

$$Y_{ii} = \frac{1}{Z_i + Z_{i||}}, \quad (\text{G.5})$$

where $Z_{i||}$ is the impedance of the parallel circuit of all impedances including the common impedance and except for the impedance Z_i given by

$$Z_{i||} = \left(Y_r + \sum_{k=1, k \neq i}^N Y_k \right)^{-1} = \left(\frac{1}{Z_r} + \sum_{k=1, k \neq i}^N \frac{1}{Z_k} \right)^{-1} \quad (\text{G.6})$$

The off-diagonal entries ($i \neq j$) of \mathbf{Y}_{aa} are given by

$$Y_{ij} = \frac{-1}{Z_i \left(\frac{Z_j}{Z_{j||}} + 1 \right)} \quad (\text{G.7})$$

where $Z_{j||}$ is defined analogously to $Z_{i||}$ in (G.6).

For the case that all $N + 1$ impedances are equal, i.e. $Z = Z_1 = Z_2 = \dots = Z_N = Z_r$, all $Z_{i||}$ are also equal and given by

$$Z_{i||} = Z/N. \quad (\text{G.8})$$

The expressions for the entries of \mathbf{Y}_{aa} for this case reduces to

$$Y_{ii} = \frac{1}{Z + Z/N} = \frac{1}{Z(1 + \frac{1}{N})}, \quad (\text{G.9})$$

$$Y_{ij} = \frac{-1}{Z \left(\frac{Z}{Z/N} + 1 \right)} = \frac{-1}{Z(N + 1)} \quad (i \neq j). \quad (\text{G.10})$$

Using (G.3) and (G.4), the concatenation of matrices \mathbf{Y}_1 and \mathbf{Y}_2 can be given as

$$\mathbf{Y}_{12} = \mathbf{Y}_{aa} - \mathbf{Y}_{aa}(\mathbf{Y}_{aa} + \mathbf{Y}_2)^{-1}\mathbf{Y}_{aa}. \quad (\text{G.11})$$

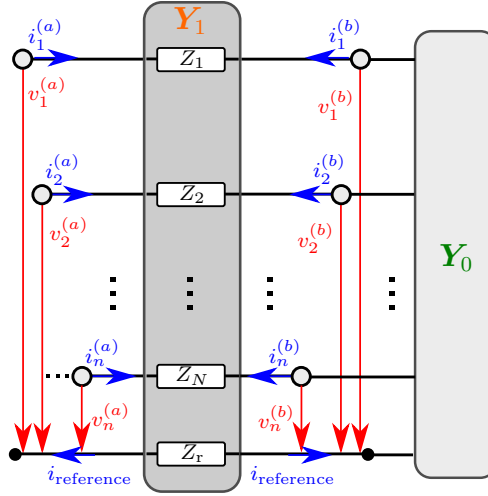


Figure G.1: Concatenation of single series impedances and a common impedance.

G.2 Concatenation of Impedance Parameters

G.2.1 General Case

Assume the following organization of the matrices of the impedance parameters $\mathbf{Z}^{(a)}$ and $\mathbf{Z}^{(b)}$ that are to be concatenated:

$$\begin{pmatrix} \mathbf{V}_u^{(a)} \\ \mathbf{V}_c^{(a)} \end{pmatrix} = \underbrace{\begin{pmatrix} \mathbf{Z}_{uu}^{(a)} & \mathbf{Z}_{uc}^{(a)} \\ \mathbf{Z}_{cu}^{(a)} & \mathbf{Z}_{cc}^{(a)} \end{pmatrix}}_{\mathbf{Z}^{(a)}} \begin{pmatrix} \mathbf{I}_u^{(a)} \\ \mathbf{I}_c^{(a)} \end{pmatrix}, \quad (\text{G.12a})$$

$$\begin{pmatrix} \mathbf{V}_u^{(b)} \\ \mathbf{V}_c^{(b)} \end{pmatrix} = \underbrace{\begin{pmatrix} \mathbf{Z}_{uu}^{(b)} & \mathbf{Z}_{uc}^{(b)} \\ \mathbf{Z}_{cu}^{(b)} & \mathbf{Z}_{cc}^{(b)} \end{pmatrix}}_{\mathbf{Z}^{(b)}} \begin{pmatrix} \mathbf{I}_u^{(b)} \\ \mathbf{I}_c^{(b)} \end{pmatrix}. \quad (\text{G.12b})$$

where indices u mark the unconnected ports of each of the network parameter sets and indices c mark the connected port with the same ordering for a and v inside the respective matrix blocks. It is desired to obtain a concatenated result $\mathbf{Z}^{(ab)}$ with the ordering as

$$\begin{pmatrix} \mathbf{V}_u^{(a)} \\ \mathbf{V}_u^{(b)} \end{pmatrix} = \mathbf{Z}^{(ab)} \begin{pmatrix} \mathbf{I}_u^{(a)} \\ \mathbf{I}_u^{(b)} \end{pmatrix}. \quad (\text{G.13})$$

Using the conditions $\mathbf{I}_c^{(a)} = -\mathbf{I}_c^{(b)}$ and $\mathbf{V}_c^{(a)} = \mathbf{V}_c^{(b)}$ one can find in accordance with [140,

Sec. 3.2.2] that

$$\mathbf{Z}^{(ab)} = \begin{pmatrix} \mathbf{Z}_{uu}^{(a)} & \mathbf{0} \\ \mathbf{0} & \mathbf{Z}_{uu}^{(b)} \end{pmatrix} + \begin{pmatrix} \mathbf{Z}_{uc}^{(a)} \\ -\mathbf{Z}_{uc}^{(b)} \end{pmatrix} (\mathbf{Z}_{cc}^{(a)} + \mathbf{Z}_{cc}^{(b)})^{-1} \begin{pmatrix} -\mathbf{Z}_{cu}^{(a)} & \mathbf{Z}_{cu}^{(b)} \end{pmatrix}. \quad (\text{G.14})$$

G.2.2 Concatenation of Single Series Impedances Per Port

The case of appending single series impedances to every port of a multiport is illustrated in Fig. G.2a. The matrix of the overall impedance can be obtained as

$$\mathbf{Z}_1 = \mathbf{Z}_0 + \begin{pmatrix} Z_1 & 0 & \cdots & 0 \\ 0 & Z_2 & \cdots & 0 \\ \vdots & \vdots & \ddots & 0 \\ 0 & 0 & 0 & Z_N \end{pmatrix}. \quad (\text{G.15})$$

In the case where $Z_{\text{series}} = Z_1 = Z_2 = \dots = Z_N$ this reduces to

$$\mathbf{Z}_1 = \mathbf{Z}_0 + Z_{\text{series}} \cdot \mathbf{1}_N, \quad (\text{G.16})$$

where $\mathbf{1}_N$ is the identity matrix of size $N \times N$.

G.2.3 Concatenation of a Common Series Impedance

The case of concatenating of a common series impedance Z_r to the common reference conductor path of a multiport is illustrated in Fig. G.2b. In this network parameter representation the condition

$$i_{\text{reference}} = \sum_{k=1}^N i_k \quad (\text{G.17})$$

holds. The matrix of the overall impedance can be obtained as

$$\mathbf{Z}_1 = \mathbf{Z}_0 + Z_r \cdot \begin{pmatrix} 1 & 1 & \cdots & 1 \\ 1 & 1 & \cdots & 1 \\ \vdots & \vdots & \ddots & 1 \\ 1 & 1 & 1 & 1 \end{pmatrix}. \quad (\text{G.18})$$

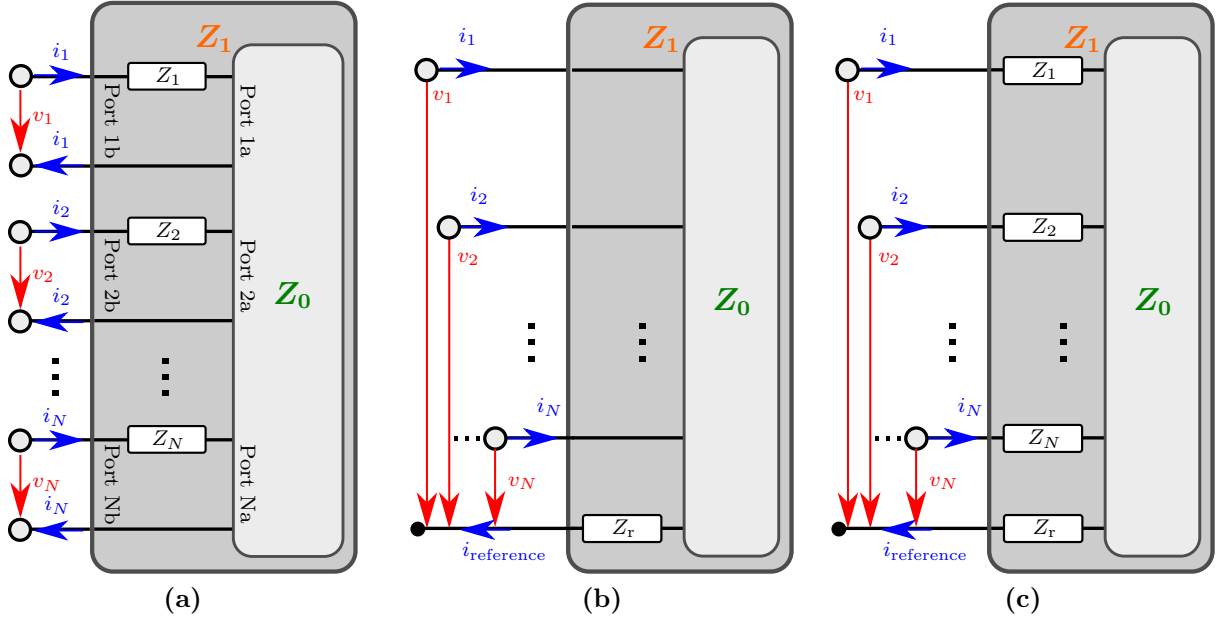


Figure G.2: (a) Concatenation of single series impedances. (b) Concatenation of a common impedance. (c) Concatenation of single series impedances and a common impedance.

G.2.4 Concatenation of Per Port and Common Series Impedances

The cases from sections G.2.2 and G.2.3 can be combined, leading to the case illustrated in Fig. G.2c. The matrix of the overall impedance can be obtained as

$$\mathbf{Z}_1 = \mathbf{Z}_0 + \mathbf{Z}_r \cdot \begin{pmatrix} 1 & 1 & \cdots & 1 \\ 1 & 1 & \cdots & 1 \\ \vdots & \vdots & \ddots & \vdots \\ 1 & 1 & 1 & 1 \end{pmatrix} + \begin{pmatrix} Z_1 & 0 & \cdots & 0 \\ 0 & Z_2 & \cdots & 0 \\ \vdots & \vdots & \ddots & \vdots \\ 0 & 0 & 0 & Z_N \end{pmatrix}. \quad (\text{G.19})$$

For the special case that $Z_{\text{series}} = Z_r = Z_1 = Z_2 = \dots = Z_N$ this leads to

$$\mathbf{Z}_1 = \mathbf{Z}_0 + Z_{\text{series}} \cdot \begin{pmatrix} 2 & 1 & \cdots & 1 \\ 1 & 2 & \cdots & 1 \\ \vdots & \vdots & \ddots & \vdots \\ 1 & 1 & 1 & 2 \end{pmatrix}. \quad (\text{G.20})$$

G.3 Conversion Between Single-Ended and Mixed-Mode Network Parameters

In this section, a short motivation and the relevant application of mixed-mode network parameters are discussed.

In many electronic systems differential signaling is used because it is more robust in terms of signal integrity. Differential signaling is typically used with multi-conductor systems where pairs of signal conductors show a symmetry with respect to the reference conductor and are to some degree coupled, both “physically” and “mathematically”. The reference conductor is defined as the conductor carrying the total current of all other conductors with inverted sign, thus leading to a net zero current of the overall multi-conductor system. Apart from this mixed-mode analysis can also be carried out for non-symmetrical system and for systems in which no or almost no coupling between signal conductors occurs.

G.3.1 On the Use of Block-Diagonal Matrices

The conversion between single-ended and mixed-mode network parameters consist in weighted superpositions of scattering parameters. These conversion can be written in compact form with multiplications using matrices. If sparse matrices are used, operations (i.e. multiplications) with these matrices even represent a viable option for the actual implementation of a numerical code. These matrices are block-diagonal matrices if one certain port ordering is used and they consist of four diagonal blocks if another certain port ordering is used. As the matrices are sparsely populated, the use of algorithms for sparse matrices can improve the numerical efficiency during the practical application. Alternatively, the corresponding/effective operations that amount to a weighted summation of two matrix rows or columns can be carried out directly using adapted functions.

In the conversion between single-ended and mixed-mode network parameters, block-diagonal matrices need to be inverted if the following port ordering is chosen: Adjacent indices of the single-ended ports form a mixed-mode port. The differential and common mode ports are adjacent in the mixed-mode ordering. For this ordering, the conversion matrices take the following block-diagonal form

$$\mathbf{A} = \begin{pmatrix} \mathbf{A}_1 & \mathbf{0} & \cdots & \mathbf{0} \\ \mathbf{0} & \mathbf{A}_2 & \cdots & \mathbf{0} \\ \vdots & \vdots & \ddots & \mathbf{0} \\ \mathbf{0} & \mathbf{0} & \mathbf{0} & \mathbf{A}_n \end{pmatrix} \quad (\text{G.21})$$

where all submatrices \mathbf{A}_k ($\mathbf{A}_1, \mathbf{A}_2, \dots, \mathbf{A}_n$) are identical 2×2 matrices, i.e.

$$\mathbf{A}_k = \mathbf{A}_1 = \mathbf{A}_2 = \dots = \mathbf{A}_n = \begin{pmatrix} A_{11}^{(k)} & A_{12}^{(k)} \\ A_{21}^{(k)} & A_{22}^{(k)} \end{pmatrix}. \quad (\text{G.22})$$

As $\det(\mathbf{A}_k) = 1$ for all conversion matrices (from which follows also $\det(\mathbf{A}) = 1$), the inverse can be given for each block as:

$$\mathbf{A}_k^{-1} = \begin{pmatrix} A_{22}^{(k)} & -A_{12}^{(k)} \\ -A_{21}^{(k)} & A_{11}^{(k)} \end{pmatrix}. \quad (\text{G.23})$$

The inverse of the block-diagonal matrix is then given as

$$\mathbf{A}^{-1} = \begin{pmatrix} \mathbf{A}_k^{-1} & \mathbf{0} & \dots & \mathbf{0} \\ \mathbf{0} & \mathbf{A}_k^{-1} & \dots & \mathbf{0} \\ \vdots & \vdots & \ddots & \mathbf{0} \\ \mathbf{0} & \mathbf{0} & \mathbf{0} & \mathbf{A}_k^{-1} \end{pmatrix}. \quad (\text{G.24})$$

Secondly, the following port ordering is considered: The n -th element for the two blocks of the single-ended ports form a mixed-mode port. The differential and common mode ports are organized in two blocks in the mixed-mode ordering. For this ordering, the conversion matrices take the following form with four diagonal blocks:

$$\mathbf{A} = \begin{pmatrix} A_{11} & \mathbf{0} & \dots & \mathbf{0} & A_{12} & \mathbf{0} & \dots & \mathbf{0} \\ \mathbf{0} & A_{11} & \dots & \mathbf{0} & \mathbf{0} & A_{12} & \dots & \mathbf{0} \\ \vdots & \vdots & \ddots & \mathbf{0} & \vdots & \vdots & \ddots & \mathbf{0} \\ \mathbf{0} & \mathbf{0} & \mathbf{0} & A_{11} & \mathbf{0} & \mathbf{0} & \mathbf{0} & A_{12} \\ A_{21} & \mathbf{0} & \dots & \mathbf{0} & A_{22} & \mathbf{0} & \dots & \mathbf{0} \\ \mathbf{0} & A_{21} & \dots & \mathbf{0} & \mathbf{0} & A_{22} & \dots & \mathbf{0} \\ \vdots & \vdots & \ddots & \mathbf{0} & \vdots & \vdots & \ddots & \mathbf{0} \\ \mathbf{0} & \mathbf{0} & \mathbf{0} & A_{21} & \mathbf{0} & \mathbf{0} & \mathbf{0} & A_{22} \end{pmatrix} = \begin{pmatrix} A_{11}\mathbf{1}_n & A_{12}\mathbf{1}_n \\ A_{21}\mathbf{1}_n & A_{22}\mathbf{1}_n \end{pmatrix} \quad (\text{G.25})$$

where $\mathbf{1}_n$ is an identity matrix of size $n \times n$. From reordering of ports of the results for the previously considered ordering, the following inverse can be obtained

$$\mathbf{A}^{-1} = \begin{pmatrix} A_{22}\mathbf{1}_n & -A_{12}\mathbf{1}_n \\ -A_{21}\mathbf{1}_n & A_{11}\mathbf{1}_n \end{pmatrix} \quad (\text{G.26})$$

The inverse is again a matrix consisting of four diagonal block. Here, the necessary but not sufficient condition $\det(\mathbf{A}) = 1$ can be used for a check of applicability.

G.3.2 Scattering Parameter Conversion for Uncoupled, Balanced Port Pairs

From the single-ended network parameters \mathbf{S}_{se} , the mixed-mode parameters \mathbf{S}_{mm} can be obtained as [147, 148]

$$\mathbf{S}_{\text{mm}} = \mathbf{M} \mathbf{S}_{\text{se}} \mathbf{M}^{-1} \quad (\text{G.27})$$

where \mathbf{M} for the orderings in (G.21) and (G.25) has entries

$$\begin{pmatrix} A_{11} & A_{12} \\ A_{21} & A_{22} \end{pmatrix} = \frac{1}{\sqrt{2}} \begin{pmatrix} 1 & -1 \\ 1 & 1 \end{pmatrix} \quad (\text{G.28})$$

and the inverse \mathbf{M}^{-1} can be obtained using (G.24) and (G.26), respectively.

Appendix H

Additional Discussions and Data Related to Measurements

In this appendix an additional discussion regarding the design of test structures, additional detailed data on both test structures and measurement setups, and an overview of the geometries of the test structures designed at the Institute of Electromagnetic Theory (TET), Hamburg University of Technology, are provided.

H.1 Design for Practical Measurability

The main design objective has been to create structures with only a few TSVs and small interaction with adjacent structures on the wafer coupon that optimally capture the effects due to the TSVs. Most of the marginal conditions are caused by the way the structures can be measured. For the practical measurement it must be taken into account which type of probing/contacting, calibration, and de-embedding is (commercially) available or feasible. Custom solutions for measurement of this kind of device under test (DUT) exist such as test fixtures for high frequency substrates [149, Sec. 3.3.3] and specialized interposers for printed circuit boards [150], but these require adapted calibration standards and are not flexible with regard to their applicability. Therefore, the most commonly used option in this domain is the measurement with micro-probes [151, 152]. These micro-probes provide the transition from the coaxial cable connector to a fine-pitched tip with the aim to minimize reflections and thereby achieve a high remaining sensitivity for the measurement of the DUT. A three tip coplanar layout with GSG (ground–signal–ground) layout can be advantageous compared to the two tip layout because it can lead to an even lower discontinuity at the transition from probe tip to the signal launch of the DUT and has a higher shielding of the signal path [153, Sec. 2.6.1]. A signal launch with probe tips is illustrated in Fig. 7.15a. Therefore, every signal launch that is used in the following has three contact pads (cases

without plane metallizations) or contact areas (case of plane metallizations). Along the signal path also three TSVs in parallel can be used to route the signal but other layouts are possible, e.g., the layout of the type depicted in Fig. 7.10a is also used with a lesser number of ground vias.

The properties of TSVs can be isolated to a high degree if contacting of such a TSV triplet is possible. This type of probing is feasible as shown in [128] but very difficult due to several reasons: It requires an adapted mechanical setup to hold and support the thin wafer and permit probing from both sides. The alignment of all mechanical parts is more difficult and requires microscopes both above and below the level at which the wafer coupon is located. Further, a non-standard calibration is required. A turning of probes between a planar calibration and a vertical measurement can be used but leads to uncertain effects on the calibration, e.g., due to cable movement/connector strain. As discussed in [128], a SOLR calibration could be used with a reciprocal “thru” in form of a very short via.

A de-embedding is also feasible as shown in [154]: By stacking a first interposer with TSVs on a second interposer with a coplanar line that routes the bottom side connection of the TSVs to a location where it is not underneath the first interposer, a contacting with micro-probes from exclusively the top side can be used. A similar effort has not been undertaken for the presented investigations.

H.2 Details on the Test Structures and Measurement Setups

Parameter	Structure IDs:		
	V13	V5	V10
w_{plane} (width of plane)	1000 μm	–	1300 μm
l_{plane} (length of plane)	800 μm	–	800 μm
l_{pad} (length of probing pad)	100 μm	150 μm	100 μm
w_{pad} (width of probing pad)	50 μm	50 μm	50 μm
l_{strip1} (length of top side line)	100 μm	0 μm	100 μm
w_{line} (width of line, top and bottom)	20 μm	20 μm	20 μm
l_{strip2} (length of bottom side line)	200 μm	250 μm	500 μm
d_{gnd} (pitch to ground)	200 μm	100 μm	200 μm
w_{clear} (width of clearances)	10 μm	–	10 μm
r_{pad} (radius of pad)	15 μm	15 μm	15 μm
number of ground vias	2	4	4

Table H.1: Parameter values of the test structures considered in the following. For geometry definitions, see Fig. 7.10a. Structure IDs are not be confused with the Variation names V1–V5 from Section 7.2.

Layer description	Nominal Value	Estimated value	Simulated values
Silicon	100 μm	80 μm	80 μm – 100 μm
WPR polymer	4.5 μm	3.5 μm	3 μm – 5 μm
SiO_2	200 nm	–	180 nm – 300 nm
	500 nm	–	500 nm

Table H.2: Relevant values of the layers thicknesses. The nominal values are the values for which the designs were planned. The estimated values are values estimated from the microsection in Fig. 7.9a. The simulated values specify the range of values used for the fits in the FEM full-wave simulations for correlation with the measurements.

	Structure V5	Structure V10	Structure V13
Wafer W09	–	–	→ Fig. 7.19
Wafer W10A	–	–	→ Fig. 7.20
Wafer W23B	→ Fig. 7.18	→ Fig. 7.16	→ Fig. 7.17

Table H.3: Overview of the simulated structures (combinations wafer ID–structure ID) with references to the corresponding figures. Structure IDs are not be confused with the Variation names V1–V5 from Section 7.2.

Setup identifiers	Measurement Setups 1a/1b	Measurement Setups 2a/2b
Location	Institute of Electromagnetic Theory, Hamburg University of Technology	Fraunhofer Institute for Reliability and Microintegration (IZM), Berlin
Probing station	custom	CASCADE Microtech SUMMIT 11651B-HT
Illustration	→ Fig. 7.13	→ Fig. 7.14
Mechanical support	Custom plastic chuck	Metal chuck + plastic card
Network analyzer	1a) Anritsu Vector Network Analyzer 37397D (40 MHz – 65 GHz) 1b) Agilent PNA Microwave Network Ana- lyzer E8364C (10 MHz – 50 GHz)	Agilent PNA Network Analyzer N5227A (10 MHz – 67 GHz)
Frequency extension	none	Agilent N5262A + Agilent N5251AR20 (110 GHz)
Calibration software	1a) built-in of VNA 1b) MMSNT Ver. 3.1 [125]	2a) built-in of PNA 2b) WinCal XE 4.5 (up to 110 GHz) [155]
Calibration type	LRM (including lumped short and load standards)	LRM (including lumped short and load standards)
Microprobe type	GGB Picoprobe 67A-GSG-100-DS	2a) GGB Picoprobe 67A-GSG-100-DS 2b) CASCADE Microtech ACP110-A-GSG-100
Calibration substrate	GGB CS-5	2a) GGB CS-5 2b) CASCADE Microtech P/N 101-190
Contact substrate	none	CASCADE Microtech P/N 005-018

Table H.4: Table of measurement setup configurations.

H.3 Fabricated Structures

This chapter presents, in the form of drawings, additional data on the geometries of more of the fabricated and measured structures. Fig. H.1 depicts the wafer coupon with markings of the areas for which the detailing drawings are given in Figs. H.2 and H.3.

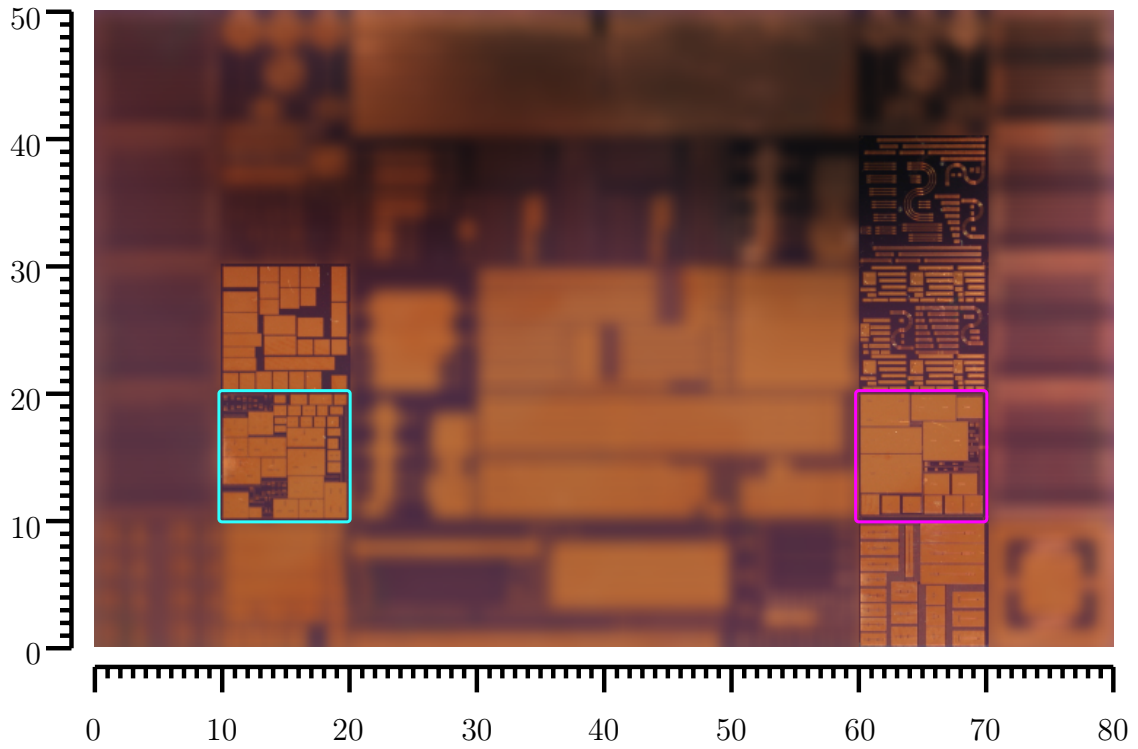


Figure H.1: Photo of the wafer coupon with marking of the structures documented in from of drawings in Fig. H.2 and Fig. H.3. Dimensions are given in mm.

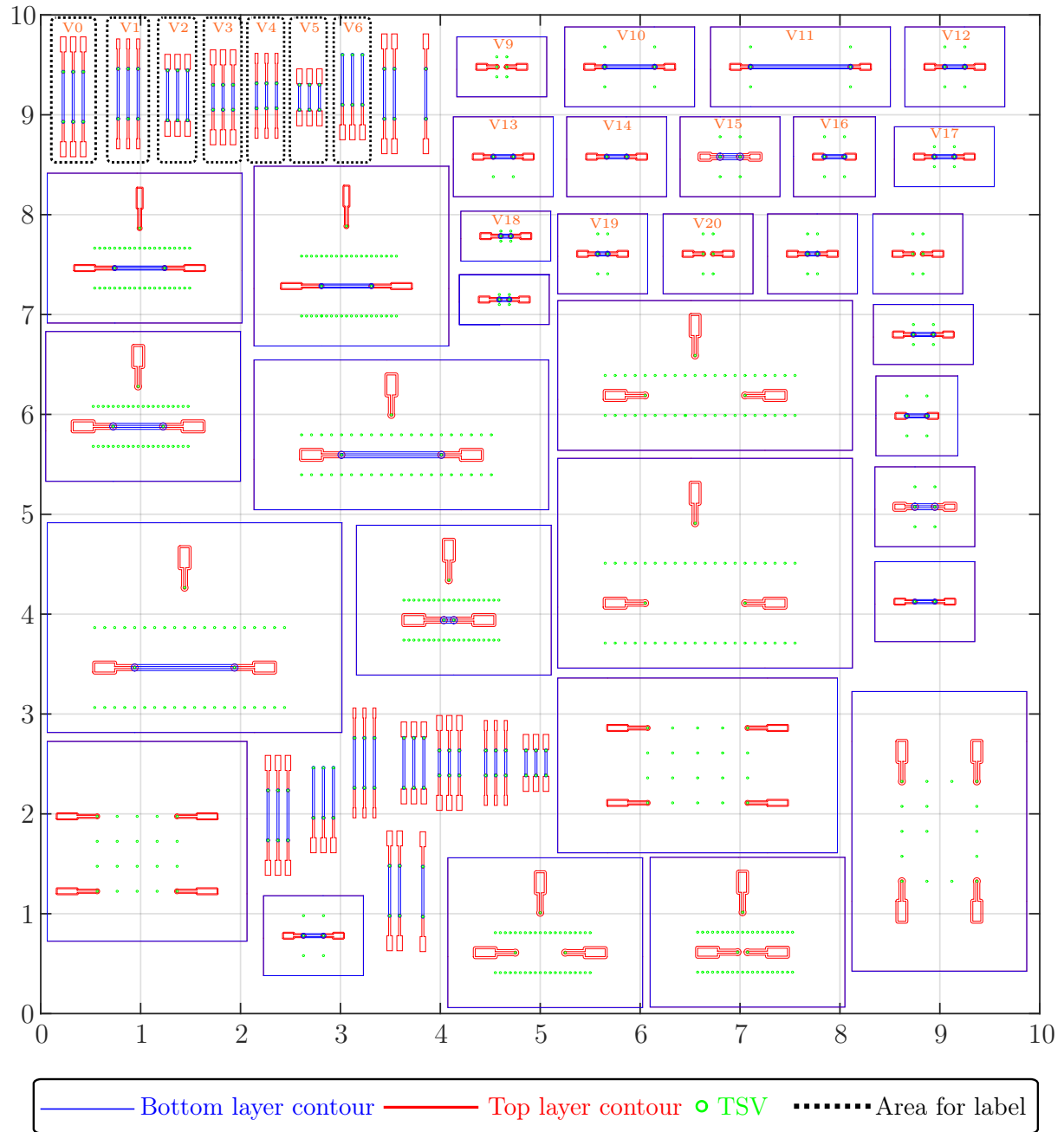


Figure H.2: Part 3 of the fabricated structures. All dimensions and coordinates given in mm. Outermost contours mark metallized areas. The contours inside these alternate between cutouts and metallized areas from outside to inside. Refer also to the photos (overview and detail) given in Fig. 7.12. If not stated otherwise, two port measurements have port 1 at the respective higher coordinate.

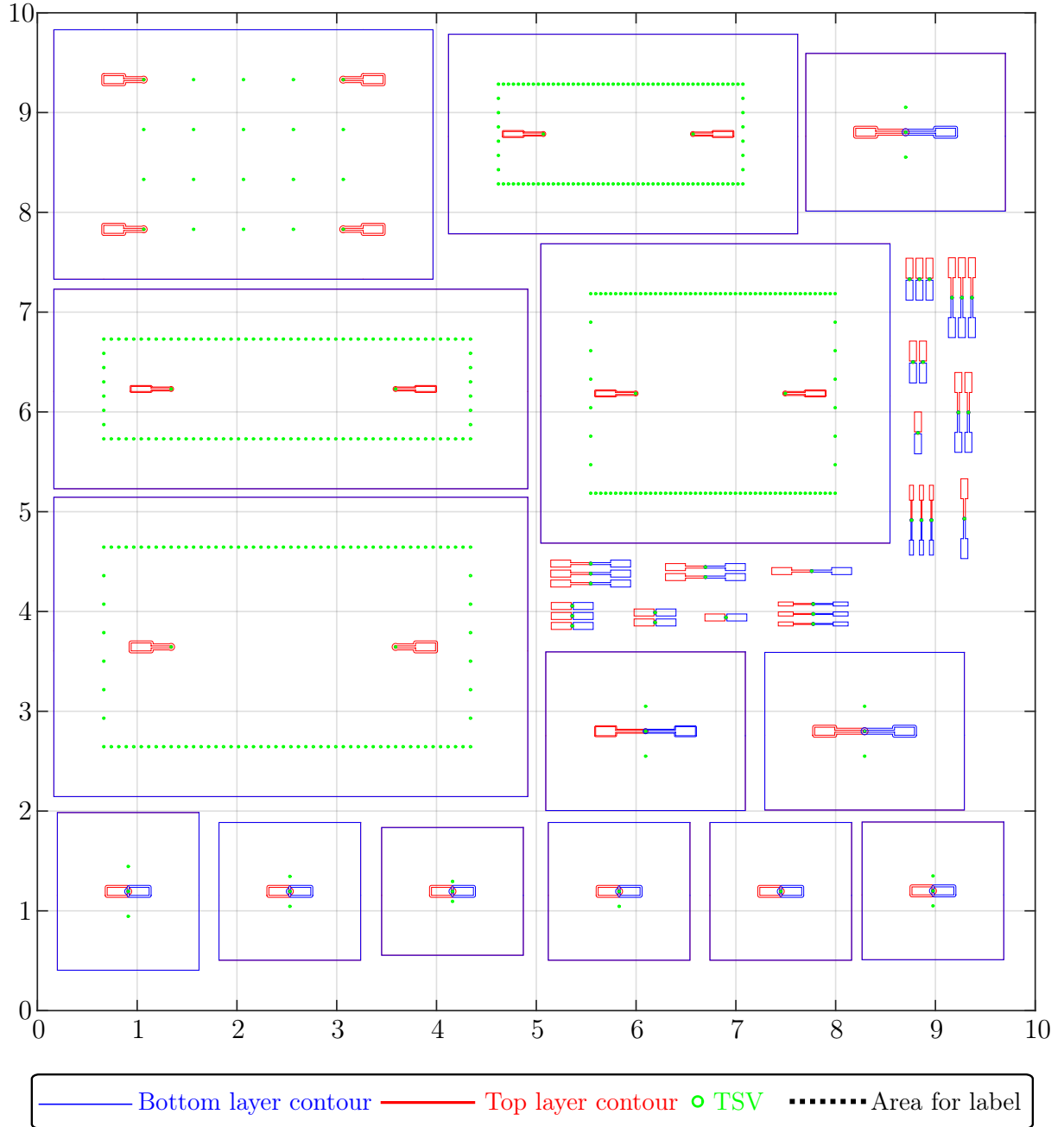


Figure H.3: Part 4 of the fabricated structures. All dimensions and coordinates given in mm. Outermost contours mark metallized areas. The contours inside these alternate between cutouts and metallized areas from outside to inside. Refer also to the photo (overview) given in Fig. 7.12.

References

- [1] International Technology Roadmap for Semiconductors (ITRS) 2.0 Home Page. [Online]. Available: <http://www.itrs2.net/>
- [2] C. Maxfield, *Bebop to the Boolean Boogie: An Unconventional Guide to Electronics*, 3rd ed., Newnes (Elsevier), 2009.
- [3] Fraunhofer Institute for Reliability and Microintegration IZM, Working Group Chip- and Wirebonding. [Online]. Available: https://www.izm.fraunhofer.de/en/abteilungen/system_integrationinterconnectionstechnologies/arbeitsgruppen/chip-_und_wire-bonding.html
- [4] H. Veenstra and J. R. Long, *Circuit and interconnect design for RF and high bit-rate applications*, Springer Science & Business Media, 2008.
- [5] I. Ndip, A. Öz, S. Guttowski, H. Reichl, K.-D. Lang, and H. Henke, “Modeling and minimizing the inductance of bond wire interconnects,” *IEEE Workshop on Signal and Power Integrity (SPI)*, May 2013.
- [6] I. Ndip, A. Öz, H. Reichl, K.-D. Lang, and H. Henke, “Analytical models for calculating the inductances of bond wires in dependence on their shapes, bonding parameters, and materials,” *IEEE Transactions on Electromagnetic Compatibility*, vol. 57, no. 2, pp. 241–249, Apr. 2015.
- [7] M. S. Bakir, C. King, D. Sekar, H. Thacker, B. Dang, G. Huang, A. Naeemi, and J. D. Meindl, “3D heterogeneous integrated systems: Liquid cooling, power delivery, and implementation,” *IEEE Custom Integrated Circuits Conference*, Sep. 2008.
- [8] D. Dahl, X. Duan, A. Beyreuther, I. Ndip, K.-D. Lang, and C. Schuster, “Application of the transverse resonance method for efficient extraction of the dispersion relation of arbitrary layers in silicon interposers,” *IEEE Workshop on Signal and Power Integrity (SPI)*, May 2013.
- [9] D. Dahl, X. Duan, A. Beyreuther, I. Ndip, K.-D. Lang, and C. Schuster, “Applying a physics-based via model for the simulation of Through Silicon Vias,” *IEEE Conference on Electrical Performance of Electronic Packaging and Systems (EPEPS)*, Oct. 2013.

- [10] D. Dahl, A. Beyreuther, X. Duan, I. Ndip, K.-D. Lang, and C. Schuster, "Analysis of wave propagation along coaxial through silicon vias using a matrix method," *IEEE Workshop on Signal and Power Integrity (SPI)*, May 2014.
- [11] D. Dahl, T. Reuschel, X. Duan, I. Ndip, K. D. Lang, and C. Schuster, "On the upper bound of total uncorrelated crosstalk in large through silicon via arrays," *IEEE Workshop on Signal and Power Integrity (SPI)*, May 2016.
- [12] D. Dahl, I. Ndip, K. D. Lang, and C. Schuster, "Effect of 3D stack-up integration on through silicon via characteristics," *IEEE Workshop on Signal and Power Integrity (SPI)*, May 2017.
- [13] D. Dahl, X. Duan, I. Ndip, K. D. Lang, and C. Schuster, "Efficient computation of localized fields for through silicon via modeling up to 500 GHz," *IEEE Transactions on Components, Packaging and Manufacturing Technology*, vol. 5, no. 12, pp. 1793–1801, Dec. 2015.
- [14] D. Dahl, T. Reuschel, J. B. Preibisch, X. Duan, I. Ndip, K. D. Lang, and C. Schuster, "Efficient total crosstalk analysis of large via arrays in silicon interposers," *IEEE Transactions on Components, Packaging and Manufacturing Technology*, vol. 6, no. 12, pp. 1889–1898, Dec. 2016.
- [15] D. Dahl, S. Müller, and C. Schuster, "Effect of layered media on the parallel plate impedance of printed circuit boards," *IEEE Electrical Design of Advanced Packaging Systems Symposium (EDAPS)*, Dec. 2014.
- [16] A. Hardock, D. Dahl, H.-D. Brüns, and C. Schuster, "Efficient calculation of external fringing capacitances for physics-based PCB modeling," *IEEE Workshop on Signal and Power Integrity (SPI)*, May 2015.
- [17] T. Reuschel, M. Kotzev, D. Dahl, and C. Schuster, "Modeling of differential striplines in segmented simulation of printed circuit board links," *IEEE International Symposium on Electromagnetic Compatibility (EMC)*, Jul. 2016.
- [18] A. Abed-Alhak, "Simulation of substrate integrated waveguides with a contour integral method," B.S. thesis, Hamburg University of Technology (TUHH), 2014.
- [19] A. Savic, "Simulation von Durchkontaktierungen in Silizium auf Basis der Mehrleitertheorie," B.S. thesis, Hamburg University of Technology (TUHH), 2015.
- [20] M. Robaszkiewicz, "Multiconductor ports for transitions between packages and printed circuit boards," M.S. thesis, Hamburg University of Technology (TUHH), 2016.

-
- [21] M. Doose, “Design of delay lines using meanders,” B.S. thesis, Hamburg University of Technology (TUHH), 2017.
- [22] X. Duan, M. Böttcher, S. Dobritz, D. Dahl, C. Schuster, I. Ndip, and K. D. Lang, “Comparison of passivation materials for high frequency 3D packaging application up to 110 GHz,” *European Microelectronics Packaging Conference (EMPC)*, Sep. 2015.
- [23] X. Duan, M. Boettcher, D. Dahl, C. Schuster, C. Tschoban, I. Ndip, and K. D. Lang, “High frequency characterization of silicon substrate and through silicon vias,” *IEEE Electronic Components and Technology Conference (ECTC)*, May 2016.
- [24] X. Duan, D. Dahl, C. Schuster, I. Ndip, and K.-D. Lang, “Efficient analysis of wave propagation for Through-Silicon-Via pairs using multipole expansion method,” *IEEE Workshop on Signal and Power Integrity (SPI)*, May 2015.
- [25] X. Duan, D. Dahl, I. Ndip, K. D. Lang, and C. Schuster, “A Rigorous Approach for the Modeling of Through-Silicon-Via Pairs Using Multipole Expansions,” *IEEE Transactions on Components, Packaging and Manufacturing Technology*, vol. 6, no. 1, pp. 117–125, Jan. 2016.
- [26] G. E. Moore, “Cramming more components onto integrated circuits,” *Proceedings of the IEEE*, vol. 86, no. 1, pp. 82–85, Jan. 1998.
- [27] W. Arden, M. Brillouët, P. Coge, M. Graef, B. Huizing, and R. Mahnkopf, “More-than-Moore,” White Paper, International Technology Roadmap for Semiconductors (ITRS), 2010.
- [28] V. F. Pavlidis and E. G. Friedman, *Three-dimensional integrated circuit design*, Morgan Kaufmann (Elsevier), 2010.
- [29] R. Tummala, *System on package*, McGraw-Hill Professional, 2008.
- [30] Fraunhofer Institute for Reliability and Microintegration IZM, Berlin. (2016) Prinzipieller Ablauf des TSV Prozesses. [Online]. Available: http://www.izm.fraunhofer.de/content/dam/izm/de/images/Abteilungen/High_Density_Interconnect_Wafer_Level_Packaging/Leistungsangebot/gr_vertikale_Durchkontaktierungen.jpg
- [31] P. Garrou, C. Bower, and P. Ramm, *Handbook of 3D Integration, Vol. 1 and 2*, Wiley-VCH, 2008.
- [32] P. Garrou, C. Bower, and P. Ramm, *Handbook of 3D Integration, Vol. 3*, Wiley-VCH, 2014.

- [33] Z. Zhang and C. P. Wong, "Recent advances in flip-chip underfill: materials, process, and reliability," *IEEE Transactions on Advanced Packaging*, vol. 27, no. 3, pp. 515–524, Aug. 2004.
- [34] C. S. Selvanayagam, J. H. Lau, X. Zhang, S. K. W. Seah, K. Vaidyanathan, and T. C. Chai, "Nonlinear thermal stress/strain analyses of copper filled TSV (through silicon via) and their flip-chip microbumps," *Electronic Components and Technology Conference*, May 2008.
- [35] J. Rautio, "Electromagnetic analysis for microwave applications," *Computational Electromagnetics and Its Applications*. Springer, 1997, pp. 80–96.
- [36] B. Curran, I. Ndip, S. Guttowski, and H. Reichl, "The impacts of dimensions and return current path geometry on coupling in single ended Through Silicon Vias," *Electronic Components and Technology Conference (ECTC)*, May 2009.
- [37] I. Ndip, B. Curran, S. Guttowski, and H. Reichl, "Modeling and quantification of conventional and coax-TSVs for RF applications," *European Microelectronics and Packaging Conference (EMPC)*, Jun. 2009.
- [38] I. Ndip, B. Curran, K. Löbbicke, S. Guttowski, H. Reichl, K.-D. Lang, and H. Henke, "High-Frequency Modeling of TSVs for 3-D Chip Integration and Silicon Interposers Considering Skin-Effect, Dielectric Quasi-TEM and Slow-Wave Modes," *IEEE Transactions on Components, Packaging and Manufacturing Technology*, vol. 1, no. 10, pp. 1627–1641, Oct. 2011.
- [39] A. Engin and S. Narasimhan, "Modeling of Crosstalk in Through Silicon Vias," *IEEE Transactions on Electromagnetic Compatibility*, vol. 55, no. 1, pp. 149–158, Feb. 2013.
- [40] I. Ndip, K. Zoschke, K. Löbbicke, M. Wolf, S. Guttowski, H. Reichl, K.-D. Lang, and H. Henke, "Analytical, Numerical-, and Measurement-Based Methods for Extracting the Electrical Parameters of Through Silicon Vias (TSVs)," *IEEE Transactions on Components, Packaging and Manufacturing Technology*, vol. 4, no. 3, pp. 504–515, Mar. 2014.
- [41] J. Kim, J. S. Pak, J. Cho, E. Song, J. Cho, H. Kim, T. Song, J. Lee, H. Lee, K. Park, S. Yang, M.-S. Suh, K.-Y. Byun, and J. Kim, "High-Frequency Scalable Electrical Model and Analysis of a Through Silicon Via (TSV)," *IEEE Transactions on Components, Packaging and Manufacturing Technology*, vol. 1, no. 2, pp. 181–195, Feb. 2011.

-
- [42] J. Kim, J. Cho, J. Kim, J.-M. Yook, J. C. Kim, J. Lee, K. Park, and J. S. Pak, "High-Frequency Scalable Modeling and Analysis of a Differential Signal Through-Silicon Via," *IEEE Transactions on Components, Packaging and Manufacturing Technology*, vol. 4, no. 4, pp. 697–707, Apr. 2014.
- [43] K. J. Han and M. Swaminathan, "Polarization mode basis functions for modeling insulator-coated through-silicon via (TSV) interconnections," *IEEE Workshop on Signal Propagation on Interconnects (SPI)*, 2009.
- [44] K. J. Han, M. Swaminathan, and T. Bandyopadhyay, "Electromagnetic Modeling of Through-Silicon Via (TSV) Interconnections Using Cylindrical Modal Basis Functions," *IEEE Transactions on Advanced Packaging*, vol. 33, no. 4, pp. 804–817, Nov. 2010.
- [45] T. Bandyopadhyay, K. J. Han, D. Chung, R. Chatterjee, M. Swaminathan, and R. Tummala, "Rigorous Electrical Modeling of Through Silicon Vias (TSVs) With MOS Capacitance Effects," *IEEE Transactions on Components, Packaging and Manufacturing Technology*, vol. 1, no. 6, pp. 893–903, Jun. 2011.
- [46] K. J. Han and M. Swaminathan, "Consideration of MOS capacitance effect in TSV modeling based on cylindrical modal basis functions," *IEEE Electrical Design of Advanced Packaging and Systems Symposium (EDAPS)*, Dec. 2012.
- [47] K. J. Han, M. Swaminathan, and J. Jeong, "Modeling of Through-Silicon Via (TSV) Interposer Considering Depletion Capacitance and Substrate Layer Thickness Effects," *IEEE Transactions on Components, Packaging and Manufacturing Technology*, vol. 5, no. 1, pp. 108–118, Jan. 2015.
- [48] B. Xie and M. Swaminathan, "FDFD Modeling of Signal Paths With TSVs in Silicon Interposer," *IEEE Transactions on Components, Packaging and Manufacturing Technology*, vol. 4, no. 4, pp. 708–717, Apr. 2014.
- [49] T. M. Winkel, R. Frech, and T. Gneiting, "Effects of partially broken HF signal return on different packaging levels," *IEEE Electrical Performance of Electronic Packaging Conference (EPEP)*, Oct. 2008.
- [50] L. Tsang, H. Chen, C.-C. Huang, and V. Jandhyala, "Modeling of multiple scattering among vias in planar waveguides using Foldy–Lax equations," *Microwave and Optical Technology Letters*, vol. 31, no. 3, pp. 201–208, Nov. 2001.

- [51] C.-C. Huang, L. Tsang, and C. Chan, "Multiple scattering among vias in lossy planar waveguides using SMCG method," *IEEE Transactions on Advanced Packaging*, vol. 25, no. 2, pp. 181–188, May 2002.
- [52] Z. Guo and G. Pan, "On Simplified Fast Modal Analysis for Through Silicon Vias in Layered Media Based Upon Full-Wave Solutions," *IEEE Transactions on Advanced Packaging*, vol. 33, no. 2, pp. 517–523, May 2010.
- [53] B. Wu and L. Tsang, "Signal Integrity Analysis of Package and Printed Circuit Board With Multiple Vias in Substrate of Layered Dielectrics," *IEEE Transactions on Advanced Packaging*, vol. 33, no. 2, pp. 510–516, May 2010.
- [54] X. Gu, B. Wu, M. Ritter, and L. Tsang, "Efficient full-wave modeling of high density TSVs for 3d integration," *Electronic Components and Technology Conference (ECTC)*, Jun. 2010.
- [55] B. Wu, X. Gu, L. Tsang, and M. B. Ritter, "Electromagnetic modeling of massively coupled through silicon vias for 3D interconnects," *Microwave and Optical Technology Letters*, vol. 53, no. 6, pp. 1204–1206, Jun. 2011.
- [56] X. Duan, "Extension of the contour integral method for the electrical design of planar structures in digital systems," Ph.D. dissertation, Hamburg University of Technology (TUHH), 2012.
- [57] R. Abhari, G. Eleftheriades, and E. van Deventer-Perkins, "Physics-based CAD models for the analysis of vias in parallel-plate environments," *IEEE Transactions on Microwave Theory and Techniques*, vol. 49, no. 10, pp. 1697–1707, Oct. 2001.
- [58] C. Schuster, G. Selli, Y. Kwark, M. Ritter, and J. Drewniak, "Progress in representation and validation of physics-based via models," *IEEE Workshop on Signal Propagation on Interconnects (SPI)*, May 2007.
- [59] R. Rimolo-Donadio, A. Stepan, H.-D. Brüns, J. Drewniak, and C. Schuster, "Simulation of Via Interconnects Using Physics-Based Models and Microwave Network Parameters," *IEEE Workshop on Signal Propagation on Interconnects (SPI)*, May 2008.
- [60] R. Rimolo-Donadio, X. Gu, Y. Kwark, M. Ritter, B. Archambeault, F. de Paulis, Y. Zhang, J. Fan, H.-D. Brüns, and C. Schuster, "Physics-Based Via and Trace Models for Efficient Link Simulation on Multilayer Structures Up to 40 GHz," *IEEE Transactions on Microwave Theory and Techniques*, vol. 57, no. 8, pp. 2072–2083, Aug. 2009.

-
- [61] R. Rimolo-Donadio, "Development, validation, and application of semi-analytical interconnect models for efficient simulation of multilayer substrates," Ph.D. dissertation, Hamburg University of Technology (TUHH), 2011.
- [62] R. Rimolo-Donadio, S. Müller, X. Duan, M. Kotzev, H.-D. Brüns, and C. Schuster, "Efficient, physics-based via modeling: Principles and methods," *IEEE Electromagnetic Compatibility Magazine*, vol. 1, no. 1, pp. 55–61, Jul. 2012.
- [63] S. Müller, X. Duan, M. Kotzev, Y.-J. Zhang, J. Fan, X. Gu, Y. Kwark, R. Rimolo-Donadio, H.-D. Brüns, and C. Schuster, "Accuracy of Physics-Based Via Models for Simulation of Dense Via Arrays," *IEEE Transactions on Electromagnetic Compatibility*, vol. 54, no. 5, pp. 1125–1136, Oct. 2012.
- [64] S. Müller, F. Happ, X. Duan, R. Rimolo-Donadio, H.-D. Brüns, and C. Schuster, "Complete Modeling of Large Via Constellations in Multilayer Printed Circuit Boards," *IEEE Transactions on Components, Packaging and Manufacturing Technology*, vol. 3, no. 3, pp. 489–499, Jan. 2013.
- [65] S. Müller, A. Hardock, R. Rimolo-Donadio, H.-D. Brüns, and C. Schuster, "Analytical extraction of via near-field coupling using a multiple scattering approach," *IEEE Workshop on Signal and Power Integrity (SPI)*, May 2013.
- [66] Ansys Inc. High Frequency Structure Simulator (HFSS) Ver. 16. Pittsburgh, USA. [Online]. Available: <http://www.ansys.com/Products/Simulation+Technology/Electromagnetics/Signal+Integrity/ANSYS+HFSS>
- [67] N. Khan, S. Alam, and S. Hassoun, "Through-Silicon Via (TSV)-induced noise characterization and noise mitigation using coaxial TSVs," *IEEE International Conference on 3D System Integration (3DIC)*, Sep. 2009.
- [68] W.-S. Zhao, X.-P. Wang, X.-L. Xu, and W.-Y. Yin, "Electrothermal modeling of coaxial through silicon via (TSV) for three-dimensional ICs," *IEEE Electrical Design of Advanced Packaging Systems Symposium (EDAPS)*, Dec. 2010.
- [69] W.-S. Zhao, Y.-X. Guo, and W.-Y. Yin, "Transmission characteristics of a coaxial through-silicon via (C-TSV) interconnect," *IEEE International Symposium on Electromagnetic Compatibility (EMC)*, 2011.
- [70] W.-S. Zhao, W.-Y. Yin, X.-P. Wang, and X.-L. Xu, "Frequency- and Temperature-Dependent Modeling of Coaxial Through-Silicon Vias for 3-D ICs," *IEEE Transactions on Electron Devices*, vol. 58, no. 10, pp. 3358–3368, Aug. 2011.

- [71] L. Yu, H. Yang, J. Zhang, and W. Wang, "Performance evaluation of air-gap-based coaxial RF TSV for 3D NoC," *IEEE/IFIP International Conference on VLSI and System-on-Chip (VLSI-SoC)*, Oct. 2011.
- [72] Z. Xu and J.-Q. Lu, "Three-Dimensional Coaxial Through-Silicon-Via (TSV) Design," *IEEE Electron Device Letters*, vol. 33, no. 10, pp. 1441–1443, Aug. 2012.
- [73] R. Volant, M. Farooq, P. Findeis, and K. Petrarca, "Coaxial through-silicon via," U.S. Patent US20 110 095 435, Apr. 28, 2011.
- [74] N. Marcuvitz, *Waveguide Handbook*, The Institution of Engineering and Technology (IET), Jan. 1986.
- [75] J. R. Whinnery and H. W. Jamieson, "Equivalent circuits for discontinuities in transmission lines," *Proceedings of the IRE*, vol. 32, no. 2, pp. 98–114, Feb. 1944.
- [76] A. G. Williamson, "Radial-line/coaxial-line junctions: analysis and equivalent circuits," *International Journal of Electronics*, vol. 58, no. 1, pp. 91–104, 1985.
- [77] Y. Zhang, J. Fan, G. Selli, M. Cocchini, and F. de Paulis, "Analytical Evaluation of Via-Plate Capacitance for Multilayer Printed Circuit Boards and Packages," *IEEE Transactions on Microwave Theory and Techniques*, vol. 56, no. 9, pp. 2118–2128, Sep. 2008.
- [78] Y. Zhang, E. Li, A. Chada, and J. Fan, "Calculation of the via-plate capacitance of a via with pad using finite difference method for signal/power integrity analysis," *International Symposium on Electromagnetic Compatibility*, Jul. 2009.
- [79] Y. Zhang, E. Li, Z. Oo, W. Zhang, E. Liu, X. Wei, and J. Fan, "Analytical formulas for the barrel-plate and pad-plate capacitance in the physics-based via circuit model for signal integrity analysis of PCBs," *Asia Pacific Microwave Conference (APMC)*, Dec. 2009.
- [80] Y. Zhang, R. Rimolo-Donadio, J. Fan, C. Schuster, and E. Li, "Extraction of Via-Plate Capacitance of an Eccentric Via by an Integral Approximation Method," *IEEE Microwave and Wireless Components Letters*, vol. 19, no. 5, pp. 275–277, May 2009.
- [81] M. Friedrich, M. Leone, and C. Bednarz, "Exact Analytical Solution for the Via-Plate Capacitance in Multiple-Layer Structures," *IEEE Transactions on Electromagnetic Compatibility*, vol. 54, no. 5, pp. 1097–1104, Oct. 2012.

-
- [82] M. Friedrich, C. Bednarz, and M. Leone, "Exact solution for via-plate capacitances including the finite plate thickness," *International Conference on Electromagnetics in Advanced Applications (ICEAA)*, Sep. 2013.
- [83] M. Friedrich, C. Bednarz, and M. Leone, "Improved Expression for the Via-Plate Capacitance Based on the Magnetic-Frill Model," *IEEE Transactions on Electromagnetic Compatibility*, vol. 55, no. 6, pp. 1362–1364, Dec. 2013.
- [84] R. Keam and A. Williamson, "Analysis of a general coaxial-line/radial-line region junction," *IEEE Transactions on Microwave Theory and Techniques*, vol. 41, no. 3, pp. 516–520, Mar. 1993.
- [85] R. Keam and A. Williamson, "Radial-line to coaxial-line junction to a dielectrically sheathed post," *IEEE Microwave and Guided Wave Letters*, vol. 2, no. 3, pp. 102–104, Mar. 1992.
- [86] Y.-J. Zhang and J. Fan, "An Intrinsic Circuit Model for Multiple Vias in an Irregular Plate Pair Through Rigorous Electromagnetic Analysis," *IEEE Transactions on Microwave Theory and Techniques*, vol. 58, no. 8, pp. 2251–2265, Jul. 2010.
- [87] H. Singer, "Feldstärkeberechnung mit Hilfe von Flächenladungen und Flächenströmen," *Archiv für Elektrotechnik*, vol. 67, no. 5, pp. 309–316, Sep. 1984.
- [88] J. C. Parker, "Via coupling within parallel rectangular planes," *IEEE Transactions on Electromagnetic Compatibility*, vol. 39, no. 1, pp. 17–23, Feb. 1997.
- [89] S. Ramo, J. R. Whinnery, and T. Van Duzer, *Fields and waves in communication electronics*, 2nd ed., Wiley, 1984.
- [90] G.-T. Lei, R. W. Techentin, P. R. Hayes, D. J. Schwab, and B. K. Gilbert, "Wave model solution to the ground/power plane noise problem," *IEEE Transactions on Instrumentation and Measurement*, vol. 44, no. 2, pp. 300–303, Apr. 1995.
- [91] T. Okoshi, *Planar circuits for microwaves and lightwaves*, 1st ed., Springer, 1985.
- [92] X. Duan, R. Rimolo-Donadio, H.-D. Brüns, and C. Schuster, "Circular Ports in Parallel-Plate Waveguide Analysis With Isotropic Excitations," *IEEE Transactions on Electromagnetic Compatibility*, vol. 54, no. 3, pp. 603–612, Jun. 2012.
- [93] X. Duan, R. Rimolo-Donadio, H.-D. Brüns, and C. Schuster, "Extension of the Contour Integral Method to Anisotropic Modes on Circular Ports," *IEEE Transactions on Components, Packaging and Manufacturing Technology*, vol. 2, no. 2, pp. 321–331, Feb. 2012.

- [94] S. Müller, X. Duan, R. Rimolo-Donadio, H.-D. Brüns, and C. Schuster, “Non-uniform currents on vias and their effects in a parallel-plate environment,” *IEEE Electrical Design of Advanced Packaging Systems Symposium (EDAPS)*, Dec. 2010.
- [95] P. C. Sharma and K. Gupta, “Desegmentation Method for Analysis of Two-Dimensional Microwave Circuits,” *IEEE Transactions on Microwave Theory and Techniques*, vol. 29, no. 10, pp. 1094–1098, Oct. 1981.
- [96] R. F. Harrington, *Time-harmonic electromagnetic fields*, McGraw-Hill, Jun. 1961.
- [97] R. E. Collin, *Field Theory of Guided Waves*, McGraw-Hill, Dec. 1960.
- [98] C. R. Paul, *Analysis of multiconductor transmission lines*, John Wiley & Sons, 2008.
- [99] T. Tamir and A. Oliner, “Guided complex waves. Part 1: Fields at an interface,” *Proceedings of the Institution of Electrical Engineers*, vol. 110, no. 2, pp. 310–324, Feb. 1963.
- [100] T. Itoh, *Numerical Techniques for Microwave and Millimeter-Wave Passive Structures*, John Wiley & Sons, May 1989.
- [101] E. Anemogiannis and E. Glytsis, “Multilayer waveguides: efficient numerical analysis of general structures,” *Journal of Lightwave Technology*, vol. 10, no. 10, pp. 1344–1351, Oct. 1992.
- [102] J. Quine, H. Webster, Glascock, II, H.H., and R. Carlson, “Characterization of via connections in silicon circuit boards,” *IEEE Transactions on Microwave Theory and Techniques*, vol. 36, no. 1, pp. 21–27, Jan. 1988.
- [103] Ansys Inc. High Frequency Structure Simulator (HFSS) Ver. 13. Pittsburgh, USA. [Online]. Available: <http://www.ansoft.com/products/hf/hfss/>
- [104] H. Hasegawa, M. Furukawa, and H. Yanai, “Properties of microstrip line on Si–SiO₂ system,” *IEEE Transactions on Microwave Theory and Techniques*, vol. 19, no. 11, pp. 869–881, Nov. 1971.
- [105] The MathWorks Inc. MATLAB. Natick, MA, USA. [Online]. Available: <http://www.mathworks.com>
- [106] J. C. Rautio, “A new definition of characteristic impedance,” *IEEE MTT-S International Microwave Symposium*, Jul. 1991.
- [107] A. Taflove and S. C. Hagness, *Computational electrodynamics*, Artech House, 2005.

-
- [108] V. Kollia and A. Cangellaris, "A Domain Decomposition Approach for Efficient Electromagnetic Analysis of the Power Distribution Network of Packaged Electronic Systems," *IEEE Transactions on Electromagnetic Compatibility*, vol. 52, no. 2, pp. 320–331, May 2010.
- [109] Ansys Inc. ANSYS Q3D Extractor Ver. 11.0. Canonsburg, PA, USA. [Online]. Available: <http://www.ansys.com>
- [110] D. K. Cheng, *Field and wave electromagnetics*, 2nd ed., Addison-Wesley, 1989.
- [111] J. B. Preibisch, X. Duan, and C. Schuster, "An Efficient Analysis of Power/Ground Planes With Inhomogeneous Substrates Using the Contour Integral Method," *IEEE Transactions on Electromagnetic Compatibility*, vol. 56, no. 4, pp. 980–989, Aug. 2014.
- [112] Ansys Inc. High Frequency Structure Simulator (HFSS) Ver. 15. Pittsburgh, USA. [Online]. Available: <http://www.ansys.com/Products/Simulation+Technology/Electromagnetics/Signal+Integrity/ANSYS+HFSS>
- [113] T. H. Hubing, J. L. Drewniak, T. P. V. Doren, and D. M. Hockanson, "Power bus decoupling on multilayer printed circuit boards," *IEEE Transactions on Electromagnetic Compatibility*, vol. 37, no. 2, pp. 155–166, May 1995.
- [114] The MathWorks Inc. MATLAB Release 2014b. Natick, MA, USA. [Online]. Available: <http://www.mathworks.com>
- [115] T. Reuschel, S. Müller, H.-D. Brüns, and C. Schuster, "Investigation of long range differential crosstalk on printed circuit boards," *IEEE Workshop on Signal and Power Integrity (SPI)*, May 2014.
- [116] R. C. Nongpiur, D. J. Shpak, and A. Antoniou, "Average power sum of the near-end crosstalk couplings after near-end crosstalk cancellation," *IEEE International Symposium on Circuits and Systems (ISCAS)*, May 2006.
- [117] N. Marlow, "A normal limit theorem for power sums of independent random variables," *Bell System Technical Journal*, vol. 46, no. 9, pp. 2081–2089, May 1967.
- [118] A. Sanders, "Statistical Simulation of Physical Transmission Media," *IEEE Transactions on Advanced Packaging*, vol. 32, no. 2, pp. 260–267, May 2009.
- [119] D. Timmermann, R. Rimolo-Donadio, Y. Kwark, T.-M. Winkel, C. Siviero, H. Harrer, and C. Schuster, "Methods for calculation of eye diagrams for digital links with

- multiple aggressors having unknown time offsets,” *IEEE Workshop on Signal and Power Integrity (SPI)*, May 2012.
- [120] T. Winkel, H. Harrer, T. Strach, R. Rimolo-Donadio, Y. Kwark, X. Duan, and C. Schuster, “Framework for co-simulation of signal and power integrity in server systems,” *IEEE Conference on Electrical Performance of Electronic Packaging and Systems (EPEPS)*, Oct. 2012.
- [121] S. Müller, T. Reuschel, R. Rimolo-Donadio, Y. Kwark, H.-D. Brüns, and C. Schuster, “Energy-Aware Signal Integrity Analysis for High-Speed PCB Links,” *IEEE Transactions on Electromagnetic Compatibility*, vol. 57, no. 5, pp. 1226–1234, Oct. 2015.
- [122] S. Kay, *Intuitive probability and random processes using MATLAB®*, Springer Science & Business Media, 2006.
- [123] C. R. Paul, “Useful Matrix Chain Parameter Identities for the Analysis of Multi-conductor Transmission Lines (Short Papers),” *IEEE Transactions on Microwave Theory and Techniques*, vol. 23, no. 9, pp. 756–760, Sep. 1975.
- [124] D. Lu and C. Wong, *Materials for advanced packaging*, Springer, 2009.
- [125] HFE High Frequency Engineering Sagl. MMSNT Ver. 3.1. Grono, Switzerland. [Online]. Available: <http://www.hfemicro.com>
- [126] G. Katti, M. Stucchi, J. V. Olmen, K. D. Meyer, and W. Dehaene, “Through-silicon-via capacitance reduction technique to benefit 3-D IC performance,” *IEEE Electron Device Letters*, vol. 31, no. 6, pp. 549–551, Jun. 2010.
- [127] H. Saito, Y. Hagihara, and H. Ikeda, “Semiconductor chip and semiconductor device,” U.S. Patent US 20 060 145 301, Jul. 6, 2006.
- [128] K.-C. Lu, Y.-C. Lin, T.-S. Horng, S.-M. Wu, C.-C. Wang, C.-T. Chiu, and C.-P. Hung, “Vertical interconnect measurement techniques based on double-sided probing system and short-open-load-reciprocal calibration,” *IEEE Electronic Components and Technology Conference (ECTC)*, May 2011.
- [129] E. Zeidler, H. Schwarz, W. Hackbusch, B. Luderer, J. Blath, A. Schied, S. Dempe, G. Wanka, J. Hromkovič, and S. Gottwald, *Springer-Taschenbuch der Mathematik*, Springer-Verlag, 2013.
- [130] P. D. Proinov and S. I. Ivanov, “On the convergence of Halley’s method for simultaneous computation of polynomial zeros,” *Journal of Numerical Mathematics*, vol. 23, no. 4, pp. 379–394, 2015.

-
- [131] J. S. Kasten, M. B. Steer, and R. Pomerleau, "Enhanced through-reflect-line characterization of two-port measuring systems using free-space capacitance calculation," *IEEE Transactions on Microwave Theory and Techniques*, vol. 38, no. 2, pp. 215–217, Feb. 1990.
- [132] I. J. Bahl and S. S. Stuchly, "Analysis of a microstrip covered with a lossy dielectric," *IEEE Transactions on Microwave Theory and Techniques*, vol. 28, no. 2, pp. 104–109, Feb. 1980.
- [133] E. Yamashita and R. Mittra, "Variational method for the analysis of microstrip lines," *IEEE Transactions on Microwave Theory and Techniques*, vol. 16, no. 4, pp. 251–256, Apr. 1968.
- [134] P. Yeh, A. Yariv, and E. Marom, "Theory of Bragg fiber," *Journal of the Optical Society of America*, vol. 68, no. 9, pp. 1196–1201, Sep. 1978.
- [135] Y. Xu, R. K. Lee, and A. Yariv, "Asymptotic analysis of Bragg fibers," *Optics Letters*, vol. 25, no. 24, pp. 1756–1758, Dec. 2000.
- [136] R. Rimolo-Donadio, H.-D. Brüns, and C. Schuster, "Hybrid approach for efficient calculation of the parallel-plate impedance of lossy power/ground planes," *Microwave and Optical Technology Letters*, vol. 51, no. 9, pp. 2051–2056, Sep. 2009.
- [137] R. Rimolo-Donadio, H.-D. Brüns, and C. Schuster, "Erratum: Hybrid approach for efficient calculation of the parallel-plate impedance of lossy power/ground planes," *Microwave and Optical Technology Letters*, vol. 52, no. 1, pp. 247–247, Jan. 2010.
- [138] P. C. Sharma and K. Gupta, "An Alternative Procedure for Implementing the De-segmentation Method," *IEEE Transactions on Microwave Theory and Techniques*, vol. 32, no. 1, pp. 1–4, Jan. 1984.
- [139] P. Sharma and K. Gupta, "A generalized method for de-embedding of multiport networks," *IEEE Transactions on Instrumentation and Measurement*, vol. IM-30, no. 4, pp. 305–307, Dec. 1981.
- [140] K. C. Gupta and M. D. Abouzahra, *Analysis and design of planar microwave components*, IEEE, 1994.
- [141] M. D. Janezic and J. A. Jargon, "Complex permittivity determination from propagation constant measurements," *IEEE Microwave and Guided Wave Letters*, vol. 9, no. 2, pp. 76–78, Feb. 1999.

- [142] C. Qu, R. Ding, X. Liu, and Z. Zhu, “Modeling and optimization of multiground TSVs for signals shield in 3-D ICs,” *IEEE Transactions on Electromagnetic Compatibility*, vol. 59, no. 2, pp. 461–467, Apr. 2017.
- [143] X. Duan, H.-D. Brüns, and C. Schuster, “Efficient DC Analysis of Power Planes Using Contour Integral Method With Circular Elements,” *IEEE Transactions on Components, Packaging and Manufacturing Technology*, vol. 3, no. 8, pp. 1409–1419, Aug. 2013.
- [144] G. Lehner, *Electromagnetic field theory for engineers and physicists*, Springer-Verlag, 2010.
- [145] A. Cozza, “Railways EMC: Assessment of infrastructure impact,” Ph.D. dissertation, Université des Sciences et Technologie de Lille–Lille I and Politecnico di Torino, 2005.
- [146] I. N. Bronshtein and K. A. Semendyayev, *Handbook of mathematics*, Springer-Verlag, 2015.
- [147] W. Fan, A. Lu, L. L. Wai, and B. K. Lok, “Mixed-mode S-parameter characterization of differential structures,” *Electronics Packaging Technology Conference (EPTC)*, Dec. 2003.
- [148] D. E. Bockelman and W. R. Eisenstadt, “Pure-mode network analyzer for on-wafer measurements of mixed-mode S-parameters of differential circuits,” *IEEE Transactions on Microwave Theory and Techniques*, vol. 45, no. 7, pp. 1071–1077, Jul. 1997.
- [149] M. Hiebel, *Grundlagen der vektoriellen Netzwerkanalyse*, Rhode & Schwarz, 2007.
- [150] M. Kotzev, Y. Kwark, C. Baks, X. Gu, and C. Schuster, “Electrical performance of a multiport interposer for measurements of dense via arrays,” *IEEE Workshop on Signal Propagation on Interconnects (SPI)*, May 2011.
- [151] S. Wartenberg, “Selected topics in RF coplanar probing,” *IEEE Transactions on Microwave Theory and Techniques*, vol. 51, no. 4, pp. 1413–1421, Apr. 2003.
- [152] A. Rumiantsev and R. Doerner, “RF probe technology: History and selected topics,” *IEEE Microwave Magazine*, vol. 14, no. 7, pp. 46–58, Nov. 2013.
- [153] V. Teppati, A. Ferrero, and M. Sayed, *Modern RF and microwave measurement techniques*, Cambridge University Press, 2013.

- [154] H. Kim, J. Cho, M. Kim, K. Kim, J. Lee, H. Lee, K. Park, K. Choi, H.-C. Bae, J. Kim, and J. Kim, "Measurement and Analysis of a High-Speed TSV Channel," *IEEE Transactions on Components, Packaging and Manufacturing Technology*, vol. 2, no. 10, pp. 1672–1685, Oct. 2012.
- [155] Cascade Microtech, Inc. WINCAL XE Ver. 4.5. Beaverton, OR, USA. [Online]. Available: <https://www.cascademicrotech.com>

References

Curriculum Vitea

Name	Dahl
Vorname	David
Staatsangehörigkeit	deutsch
Geburtsdatum	17.02.1986
Geburtsort, -land	Mölln, Deutschland
08.1992 – 07.1996	Grundschule in Nusse
08.1996 – 05.2005	Lauenburgische Gelehrtenschule (Gymnasium) in Ratzeburg
10.2005 – 08.2009	Studium der Allgemeinen Ingenieurwissenschaften an der Technischen Universität Hamburg-Harburg (TUHH), Abschluss: Bachelor of Science
10.2009 – 05.2012	Studium der Elektrotechnik an der Technischen Universität Hamburg-Harburg (TUHH), Abschluss: Master of Science
09.2010 – 01.2011	Studium im Rahmen des Erasmus-Programmes an der École nationale supérieure d'électrotechnique, d'électronique, d'informatique, d'hydraulique et des télécommunications (ENSEEIHT) in Toulouse, Frankreich im Studiengang Elektrotechnik
Seit 10.2012	Wissenschaftlicher Mitarbeiter am Institut für Theoretische Elektrotechnik der Technischen Universität Hamburg-Harburg (TUHH)